A Thermodynamic Rate of Ablation for Iceberg Keels

by

Elise Athena Marie

A thesis submitted to the Faculty of Graduate and Postdoctoral Studies of

The University of Manitoba

in partial fulfilment of the requirements of the degree of

Master of Science

Department of Environment and Geography

University of Manitoba

Winnipeg

This page intentionally left blank.

Abstract

Glaciers melt in contact with seawater and this contributes to sea level change and affects water circulation, mixing, and hydrography. Estimating the rate of melting is therefore key to improving the representation of this input in global coupled circulation models. The goal of this project was to determine how fast vertical ice walls melt as a function of water salinity and temperature. Hitherto there was only one model that included both variables. Based on analytical fluid dynamics work from the 1970s, it is very expensive computationally and only applicable over a limited range of conditions. Several simple models are also available but they generally take the form of a power of temperature times the first power of a second variable that may or may not be broadly relevant. I collected experimental data from the literature, then used a benchtop-scale version of an experimental method first used in situ in Greenland in 1879 to conduct a more thorough investigation of the full domain of applicable temperature and salinity. I fitted a bivariate quadratic model which fit both my data and the legacy data. Finally I developed an easy model of glacier density and bubble pressure with depth to create a model iceberg, and applied my thermodynamic ablation model to the model iceberg with water conditions obtained from a reanalysis product. My main findings were that there is in fact an intrinsic thermodynamic rate of phase change, independently of fluid dynamics, and that it can be both measured and calculated very cheaply; but also that the bubbles in icebergs, when released by melting, add considerable buoyancy to the melt, which increases the rate of ablation by contributing additional energy to the ice interface as momentum flux. My model provides both a fast equation in salinity and temperature which can be applied anywhere in the sea, as required, but also an inexpensive model of the ice for more detailed descriptions at the level of an iceberg or ice face, and a basis for further work on the effects of pressure, stress, momentum transfer, the ice's thermal history, bubbles, solar radiation, and more.

Acknowledgements

All praise is due to God, the compassionate, the merciful, creator of worlds. He says to a thing "be", and it is, and He is of all things knowing.

The experimental work in this thesis was done with Winnipeg city water, obtained through the Shoal Lake aqueduct that was built at a great human cost and injustice to the people of Shoal Lake 40 First Nation.

This project was proposed and advised by Dr. Jens Ehn (CEOS). The committee members were Dr. Tim Papakyriakou (CEOS) and Dr. Shawn Clark (Department of Engineering). The original research question was suggested by Dr. Sergei Kirillov (CEOS).

Contents

List of Tables

List of Figures

List of Symbols

The use of symbols may vary locally in the text and this will be noted wherever it is not evident from context. Some usage departs from tradition, generally to privilege the common oceanography usage over other disciplines. For example, S is salinity and p is pressure, though in physics typically S is entropy, p is momentum, and pressure is P. Units are indicated where appropriate.

Lowercase Roman

a, $\mathbf{a}$	$\mathrm{m\ s^{-2}}$	acceleration (scalar, vector)
c_p	$\mathrm{J\ kg^{-1}\ K^{-1}}$	specific heat capacity at constant pressure
d		derivative
g, $\mathbf{g}$	$\mathrm{m\ s^{-2}}$	acceleration due to gravity (scalar, vector)
h	$\mathrm{J\ s^{-1}\ m^{-2}\ K^{-1}}$	heat transfer coefficient
k	variable	in Arrhenius equations, the reaction rate constant
k	none	in a logistic function, the logistic growth rate
ℓ	m	a characteristic length
m	kg	mass
n	none	number of occurrences
o		subscript denoting bubbles
p	Pa	pressure
q	$\mathrm{J\ s^{-1}\ m^{-2}}$	heat flux
r	m	radius
r	none	Pearson correlation coefficient (for a single predictor, may be positive or negative)
r^2	none	coefficient of determination for a single predictor
t	°C	temperature in °C
v	$\mathrm{m\ s^{-1}}$	velocity
x	none	a generic unknown

z	m	position along the z axis

Uppercase Roman

A	m^2	area
A	variable	Arrhenius factor
$\mathcal{A}$	kg m^{-2} day^{-1}	ablation rate
$\hat{\mathcal{A}}$	kg m^{-2} day^{-1}	modelled ablation rate
$\mathcal{A}_c$	m water $year^{-1}$	accumulation rate for Herron-Langway model
$\hat{\mathcal{A}}_g$	m water $year^{-1}$	Agassiz rate
C	mol L^{-1}	concentration
C_{sz}	none	non-dimensionalized concentration parameter (eq.1.29, p.47)
D	m^2 s^{-1}	diffusivity
$\mathcal{D}$	m	diameter
E	J K^{-1}	entropy
E_a	J mol^{-1}	in an Arrhenius equation, the molar activation energy
F	kg	apparent weight
H	J	enthalpy
$\mathbf{K}$	none	Kenora coefficient matrix
L	J kg^{-1}	latent heat
M	kg	mass
$\dot{M}$	kg s^{-1}	rate of change of mass with time
N	none	number of occurrences
O	none	order of magnitude
Q	J	total heat supplied to a system
$\dot{Q}$	J $^{-1}$	heat flow rate
R	J kg^{-1} mol^{-1}	the universal gas constant
R	m s^{-1}	in ice melting literature, recession rate of the ice-water interface

R	none	in normal usage, the correlation coefficient in a system with multiple predictors
R^2	none	coefficient of determination for multiple predictors
R_{sz}	none	non-dimensionalized temperature parameter (eq.1.28, p.41)
S	variable	salinity
S_A	g kg^{-1}	absolute salinity
S_B	g kg^{-1}	bench salinity (see definition on p.64)
S_P	psu	practical salinity
T	K	temperature
T_d	K	thermal driving
U	J	internal energy
V	m^3	volume
Z	m	the thickness of a glacier in the glacier model

Lowercase Greek

α	(alpha)	m $^{-2}$	thermal diffusivity
α			subscript denoting an initial state or condition
β	(beta)	K^{-1}	coefficient of thermal expansion
β			subscript denoting the snow-firn transition in the glacier model
γ	(gamma)	none	geometric factor of Agassiz model
δ	(delta)		infinitesimal
ϵ	(epsilon)		error
ζ	(zeta)	m	thickness of bubble wall at failure (eq.3.43, p.116)
ι	(iota)		subscript denoting an intermediate state or condition, or the firn-ice transition in the glacier model
κ	(kappa)	J s^{-1} m^{-1} K^{-1}	thermal conductivity

κ	none	polytropic index
λ (lambda)		eigenvalue
μ (mu)	N m^{-2} s	dynamic viscosity
μ		mean (first statistical moment)
ν (nu)	m^2 s^{-1}	kinematic viscosity
π (pi)		the number pi
ρ (rho)	kg m^{-3}	density
σ (sigma)		standard deviation (second statistical moment)
τ (tau)	s	time
ω (omega)		subscript denoting a final state or condition, or the maximum density of ice in the glacier model

Uppercase Greek

Δ	(delta)	difference
Λ	(lambda)	least upper bound of logistic function
Π	(pi)	product operator
Σ	(sigma)	sum operator

Other

∞	infinity; subscript denoting far-field conditions
Gr	Grashof number (eq.1.16, p.22)
Le	Lewis number (eq.1.14, p.21)
Nu	Nusselt number (eq.1.15, p.22)
Pr	Prandtl number (eq.1.12, p.21)
Ra	Rayleigh number (eq.1.17, p.22)
Ra_S	solutal Rayleigh number (eq.1.19, p.22)
Ra_T	thermal Rayleigh number (eq.1.18, p.22)

Re	Reynolds number (eq.1.10, p.20)
Sc	Schmidt number (eq.1.13, p.21)
Ste	Stefan number (eq.1.11, p.21)

Introduction

On 14 December 2022, the 77th session of the United Nations' General Assembly adopted a resolution "to declare 2025 the International Year of Glaciers' Preservation" and invite stakeholders to observe it "through activities aimed at raising awareness of the importance of glaciers, snow and ice in the climate system and the hydrological cycle, and the economic, social and environmental impacts of the impending changes in the Earth's cryosphere, and to share best practices and knowledge in this regard" (Resolution 77/158, 2022). The resolution notes that "glaciers are a critical component of the hydrological cycle and that the current accelerated melting and retreat of glaciers have severe impacts on the climate, the environment, the maintenance of human well-being and health and sustainable development."

Interest in the melting of glaciers and icebergs is much more ancient than the United Nations, but has always had a connection to climate concerns. The early 1850s, for example, were meteorologically strange. There seems to have been a particularly strong El Niño in 1851–52, judging by ship captains' logs (Barrett et al., 2018). The winter would likely have been warm and dry in Alaska, cool and wet in California. In western Europe it was warm and extremely wet. Then in the winter of 1853-54, the East Asian winter monsoon failed, and Lake Suwa in central Japan did not freeze (Hirano et al., 2021). Across the Pacific, an ice ship supplying San Francisco found no suitable ice to load at Sitka in Alaska, and went into the fjords to load ice from Baird Glacier instead (Keithahn, 1967, cited in Weeks & Campbell, 1973). On 14 November 1854, apparently a cyclone hit the Crimean Peninsula where British, French and Russian forces were engaged in the absurdity of the Crimean War. For several months in 1854-55 there was a considerable increase reported in the number of icebergs in the Southern Ocean (Towson, 1859, cited in Budd et al., 1980), suggesting warm weather, but in western Europe there was a prolonged period of very dry cold weather, particularly in Febrary 1855.

Iceberg production spiked again in 1888-97 (Russell, 1895 and 1897, cited in Budd et al., 1980), and this time the ice trade was ready to profit from the situation: between 1890 and 1900, they transported whole icebergs by sailing and towing from Lake San Rafael (Aysén, Chile, 45°S),

where they calve into the lake from the San Rafael Glacier, to Valparaiso and even as far north as Callao (Peru, 12°S).

The ice trade died out in the early twentieth century when technology for the manufacture of ice became widely available, but in the 1960s the concept of towing icebergs was revived, this time as a source of fresh water for growing populations in dry climates such as California, Australia, and the Middle East (Weeks & Campbell, 1973). In 1978, a conference on iceberg utilization was convened in Ames, Iowa, USA, with sponsorship from the government of Saudi Arabia (Zaffarano, 1979). Desalination proved easier to implement, but recently new articles on towing icebergs for drinking water have appeared (Condron, 2023; Qadir & Siriwardana, 2022).

Despite climate change, the enduring desire to drink icebergs, the United Nations' urgency, and more than 140 years of research on how fast ice melts in seawater, at the time of Resolution 77/158, there were essentially two generally accepted models of iceberg melting, both inadequate in practice: a one-factor power law from 1973 (Weeks & Campbell), or a complex computational fluid dynamics simulation based on partial differential equation models from 1971 (Gebhart & Pera). Both were created by engineers working from fluid dynamics. The simple model has no salinity term; the more sophisticated one applies only over a limited range of water conditions, requires numerous assumptions and some arbitrary parameters, and is not known to scale from the laboratory to icebergs that are larger by six orders of magnitude, much less glaciers. Almost all the data used to validate it was generated from a small number of laboratory experiments done between 1976 and 1982, and only a half-dozen experimental points exist at low temperatures, where the salt content of seawater contributes more energy than its heat content. Thus there is currently no model that can produce a computationally cheap yet sufficiently accurate estimate of mass loss from vertical ice walls in high-latitude seas, which is an important factor in ocean models because it contributes to sea-level change and also affects water circulation, mixing, and hydrography.

For this M.Sc. thesis, I was desired to provide "estimates of the real-world dissolving rates (mainly for the icebergs' vertical walls)" (Sergei Kirillov, personal communication) for "the regions and depth ranges where the water temperatures are in the dissolution range (i.e. -1.8 to

0°C)" (Jens Ehn, personal communication). I started from a thermodynamic perspective instead of fluid dynamics and adapted the oldest of the ice melting experiments, first tried in a West Greenland fjord in 1879 (Hammer, 1883; Steenstrup, 1883), into a fast and inexpensive benchtop experiment, described in chapter 2, which produced enough data to generate empirical relations relating the rate of melting of ice in seawater to its salinity and temperature. It was not possible to investigate the pressure dependence of the melt rate with this apparatus and improvements to the method are being made for future work. The rate of mass loss in icebergs also depends on many more factors than in a manufactured ice sample in the laboratory, including but not limited to the density of the ice and the air pressure in the bubbles it contains. I created a model of density and bubble pressure in icebergs, described in chapter 3. The density profile is sufficiently complete to use as an input in a melt model, but more work is needed on the bubbles and other factors like differential stress, momentum flux, and the ice's history.

This work advances our ability to reflect the melting of glaciers in coupled ocean-atmosphere models by providing computationally inexpensive equations that require only a few easily obtained inputs. It did not exactly answer the brief given by Drs. Ehn and Kirillov, however. For a more realistic model, we need equations not only for the effect of water pressure and bubble pressure, but also the thermal history of the ice, momentum flux from moving water, and differential stresses caused by the iceberg's shape.

Chapter 1

Review of existing work

1.1 Mathematical methods

The freezing of a body of water has been fairly well understood mathematically since Stefan (1891). The melting of ice in water is more complicated because the geometry of the interface is much more variable from one case to another, as well as variable in time for each individual case. The situation is further complicated by the movement induced in the water by the heat and mass exchange, which in turn is complicated by the non-monotonic, salinity-dependent dependence of the water density on temperature. This "causes a phenomenon called convective inversion" (Merk, 1954). The study of the melting problem has therefore historically focused heavily on the attendant convection.

Merk (1954) began on a solution, but most of the progress can be attributed to Dr. Benjamin Gebhart and his colleagues in the 1970s. They used a fluid mechanics approach that depends on the use of dimensionless numbers, and came to the conclusion that the general problem is not solvable, but a solution can be found for part of the domain of water properties, if enough simplifying assumptions and parametrizations are made. Their solution, expanded on by several later researchers, is the one used in computational fluid dynamics (CFD) solutions today.

1.1.1 The Buckingham Π *theorem and dimensionless numbers*

Suppose we want to describe the position Z of an object falling in a frictionless vacuum. We know that it will depend on its original position Z_0, original velocity V_0, time elapsed τ, and the acceleration due to gravity, g. Therefore we can write a function,

$$Z = f(Z_0,\ V_0,\ \tau,\ g) \tag{1.1}$$

which will be in the form of a product of a constant, K, and each variable to some power:

$$Z = K\ Z_0^a\ V_0^b\ \tau^c\ g^d \tag{1.2}$$

Because this equation describes a physical reality, it has to be dimensionally homogenous, and K has to be dimensionless, not a repository of missing dimensions created ad hoc to make a regression cohere to a model. We can write equation 1.2 in terms of its units, m and s, instead of variable names:

$$\mathrm{m} = \mathrm{m}^{a} \left(\frac{\mathrm{m}}{\mathrm{s}}\right)^{b} \mathrm{s}^{c} \left(\frac{\mathrm{m}}{\mathrm{s}^2}\right)^{d} \tag{1.3}$$

$$\mathrm{m}^{1} \cdot \mathrm{s}^{0} = \mathrm{m}^{a+b+d} \cdot \mathrm{s}^{c-b-2d} \tag{1.4}$$

hence

$$\begin{cases} a + b + d = 1 \\ c - b - 2d = 0 \end{cases} \tag{1.5}$$

Since we have two equations in four unknowns, we can solve any two in terms of the other two, for example

$$\begin{cases} c = b + 2d \\ a = 1 - b - d \end{cases} \tag{1.6}$$

Putting this into equation 1.2 we have

$$\begin{aligned} Z &= K \cdot Z_0^{1-b-d} \cdot V_0^{b+2d} \cdot \tau^{b+2d} \cdot g^{d} \\ &= K \cdot Z_0 \cdot \left(\frac{V_0 \tau}{Z_0}\right)^{b} \cdot \left(\frac{V_0^2 \tau^2 g}{Z_0}\right)^{d} \end{aligned} \tag{1.7}$$

$$\frac{Z}{Z_0} = K \cdot \left(\frac{V_0 \tau}{Z_0}\right)^b \cdot \left(\frac{V_0^2 \tau^2 g}{Z_0}\right)^d \tag{1.8}$$

so instead of having Z as a function of four variables, we have now described the relation between Z and Z_0 as a function of only two similarity variables:

$$\frac{Z}{Z_0} = f\left(\frac{V_0 \tau}{Z_0}, \frac{V_0^2 \tau^2 g}{Z_0}\right) \tag{1.9}$$

Note that Z / Z_0 is dimensionless since it is a ratio of two lengths, and likewise the ratios in the brackets are both dimensionless. These two groups are called Πs, because they are products. This derivation, adapted from White (1979, pp.280-283), is a basic example, obviously not a proof, of the *Buckingham* Π *theorem*, which states that if a physically meaningful relation has n variables in p dimensions, they can be grouped into at most $k = n - p$ dimensionless products. The Πs are not uniquely defined, since the system of equations in 1.5 has $\binom{4}{2} = 6$ possible solutions. The other five are left to the reader as an exercise.

Since the relation between Z and Z_0 is a function of the two ratios we derived, if either ratio changes, so does the relation. For example, in this situation, if g changes, the freefall behaviour of a body will change, hence we cannot do a freefall experiment on the Moon and extrapolate it to a lander on Mars. Likewise in the fluid dynamics problem that arises in the conversation on melting icebergs, many dimensionless numbers are used as similarity variables to reduce dimensionality, and therefore the solutions are only applicable for the specific conditions on the dimensionless numbers, for which they are established.

Probably the most famous dimensionless number in geophysics is the Reynolds number, which relates inertia and viscosity:

$$\mathrm{Re} = \frac{\rho v \ell}{\mu} \tag{1.10}$$

where ρ is density, v is the flow velocity, ℓ is a characteristic length, and μ is the dynamic viscosity. The Reynolds number is often used in meteorology, but not that much in the iceberg problem. Likewise the Stefan number (Lock, 1969, p.288)

$$\text{Ste} = \frac{c_p \, \Delta T}{L} \tag{1.11}$$

which relates sensible heat and latent heat, is more used in sea ice problems than iceberg problems. Here L is the latent heat of the phase transition being studied, and c_p is the specific heat capacity at constant pressure; in a freezing problem, c_p is that of the solid phase, and in a melting problem, c_p is that of the liquid phase.

In the study of icebergs we often see the Prandtl number, which relates the dissipation and conduction of heat in a convective flow (White, 1979, p.280):

$$\text{Pr} = \frac{\mu c_p}{\kappa} \tag{1.12}$$

where κ is the thermal conductivity. It is often in company with the Schmidt number, for which I have not found an origin story, and which relates the viscous diffusion rate to the molecular diffusion rate:

$$\text{Sc} = \frac{\mu}{\rho D} \tag{1.13}$$

where D is the molecular diffusivity. The ratio of the two is the Lewis number, which relates the thermal diffusivity to the mass diffusivity:

$$\text{Le} = \frac{\text{Sc}}{\text{Pr}} = \frac{\alpha}{D} \tag{1.14}$$

where α is the thermal diffusivity. Finally we come to the two most important numbers in the iceberg world. One is the Nusselt (1930) number, which relates convective and conductive heat

transfer normal to a boundary:

$$\mathrm{Nu} \;=\; \frac{h\ell}{\kappa} \tag{1.15}$$

In the case of a sphere, the characteristic length ℓ is simply the diameter of the sphere (Dumoré et al., 1953).

The other key number is the Grashof number, or rather numbers, which are various ways of relating buoyancy and viscosity. One version (White, 1979, p.280) is

$$\mathrm{Gr} \;=\; \frac{\beta\ \Delta T\ g\ \ell^3\ \rho^2}{\mu^2} \tag{1.16}$$

where β is the coefficient of thermal expansion of the fluid. Notice that we have ℓ^3 in the numerator. This characteristic length, for an iceberg, is going to be of the order of 10^2 m, so $\ell^3 \;= O(10^6)$, whereas in the laboratory we are limited to scales of 10^{-1} m, or $\ell^3 \;= O(10^{-3})$, nine orders of magnitude smaller. This scale dependence is a very significant problem in trying to investigate icebergs with benchtop models.

From there, the Rayleigh number relates the time scales of diffusion and convection:

$$\mathrm{Ra} \;=\; \mathrm{Gr} \;\times\; \mathrm{Pr} \tag{1.17}$$

As there are many definitions of the Grashof number, so the Rayleigh number can be defined variously, for example the thermal Rayleigh number for heat transport:

$$\mathrm{Ra}_T \;=\; \frac{g\beta_T \Delta T^2 \ell^3}{2\nu\alpha_T} \tag{1.18}$$

and the solutal Rayleigh number for solute transport:

$$\mathrm{Ra}_S \;=\; \frac{g\beta_S \Delta S \ell^3}{\nu\alpha_S} \tag{1.19}$$

where the diffusivity (α) and coefficient of expansion (β) relate to T in the thermal case and S in the solutal case, as indicated by the subscripts (Yang et al., 2023). While mathematically highly useful, the dimensionless numbers introduce another cognitive and computational cost which can make it difficult to appreciate at a glance the meaning and utility of a model, so I have tried to work away from them and use only quantities we can measure in the field.

1.1.2 The similarity solution for vertical walls

Dr. Benjamin Gebhart (1923–2009), an icon in mechanical engineering and heat transfer over his 46-year academic career, worked with many colleagues on the general problem in which a flow is affected by differences of heat, chemical composition, and phase. In the attempt to write an analytical solution, Gebhart and Pera (1971) had to start by neglecting various effects, including stratification and viscous dissipation. They also used simplifying assumptions such as the Boussinesq approximation, which ignores density differences unless they are multiplied by the acceleration due to gravity. This is difficult to defend in a problem that is heavily dependent on density. Even so they found that not much could be done in any case where the Schmidt and Prandtl numbers are not approximately equal, or in other words, when the heat and salt transport do not proceed at approximately the same speed. Once they discarded enough of the complexity, however, they arrived at what they are pleased to call a "convenient similarity form", which is shown as equation A.1 (p.142). Although this equation has become a focal point of ice melting research, it does not describe how fast ice melts, but how the liquid moves along the interface as its temperature and concentration change. It is only applicable when $\mathrm{Pr} \approx \mathrm{Sc}$, and even so one has to guess the parameters P and Q. In a simple system like a laboratory experiment, one can measure C_0, C_∞, T_0, and T_∞ and use them to calculate c_p, k, D, μ, ν, β, β^*, and ρ. In the case of an iceberg at sea, the measurements are complicated by advection, by the iceberg's movement, and by the fact that neither atmospheric nor hydrostatic pressure are constant. In fact the solution is not even applicable to icebergs generally because they rarely if ever have flat, smooth, vertical walls.

In a subsequent paper, Pera and Gebhart (1973) put it more bluntly: where the temperature and composition diffusion regions do not have the same distribution, $\mathrm{Pr} \neq \mathrm{Sc}$, and these solutions

are not applicable. In those cases, which include iceberg melting since heat diffuses much faster than salt, it remains necessary to integrate the eighth-order set of coupled momentum, energy, and mass diffusion equations, which I have not reproduced in this thesis. There is no way to do this but numerically, and later work has relied heavily on computational methods. In practice, however "convenient" Gebhart and Pera found their solution, later workers mostly focused on calculating and manipulating the dimensionless numbers, particularly the Nusselt number to look for equilibrium points in the model, rather than working out the complete solution.

Gebhart and Mollendorf (1978) continued the analysis, using a new density equation of state they had published the previous year, which accounted for the non-monotonic temperature dependence of the density of water. This allowed them to present a single model that includes the effects of high salinity and pressure across "the vast majority of terrestrial surface water". They noted that "salinity and pressure levels in the flow field also have considerable effects". The effect of the density maximum was particularly significant as, under some conditions, it can cause the buoyancy of the melt to decrease to zero and then reverse. Their model for the buoyancy density difference is shown as equation A.10 (p.144).

1.1.3 A model for a horizontal ice sheet

While Gebhart's team was working on the vertical ice walls, Gade (1979) investigated the melt situation under a horizontal ice surface such as an ice sheet, inspired not by the iceberg problem but apparently by an ancient argument in papers published from 1900 to 1912 by Drs. Otto Pettersson and Fridtjof Nansen, two legendary figures of oceanography. I have not been able to access the said papers, but according to Gade, Pettersson thought that melt from the bottom of an ice sheet would convect down, whereas Nansen thought it would produce a stably stratified fresh or nearly fresh layer on top of the salty field water, which would insulate the ice from the sea and inhibit further melting. Gade assumed a laterally infinite sheet of homogeneous, isotropic ice of time-invariant thickness, floating on a reservoir of seawater, the inside of the ice being always below its melting point temperature, and the upper surface at a constant temperature. Assuming a diffusive boundary layer in contact with the ice and a convective turbulent layer further out, he wrote

a system of five partial differential equations, shown as equation A.20 (p.146). He was thwarted, in applying his solution, by the lack of data for the constants and parameters in his system, any of which may or may not in fact be constant. Making a number of simplifying assumptions, he managed to reproduce to his relative satisfaction the observations of Nansen, and those of Matthews and Quinlan (1975) along the Muir Glacier. Fresh layers under sea ice have factually been observed, for example by Ehn et al. (2004) under the ice in Santala Bay, Gulf of Finland, in the spring, and by Ehn et al. (2011) in Franklin Bay and Darnley Bay in June 2008, and is also seen in the experiments of Russell-Head (1980) reviewed in Subsection 1.2.3 (p.38). This much of the analysis, therefore, is well established.

1.1.4 Melting and dissolving

Much of the theory on the melting of ice in seawater comes from the collaborators of geophysicist Dr. Herbert E. Huppert, because it is analogous to the melting of magmas which they were studying. Woods (1991) describes an experiment involving melting a solid under a binary liquid, which may be of little interest for iceberg keels, but is very relevant in the case of rock melting under an overlying magma. The experiments were done with ice at approximately -15°C, frozen in a 10 cm-layer in the bottom of a tank 10 cm × 10 cm × 30 cm deep. Over that was poured a solution of aqueous sodium carbonate (Na_2CO_3) at 20°C in different concentrations. The instrumentation included a shadowgraph, thermometers, and a refractometer to measure concentration from various samples. He found that the melting shows two clear regimes: either very slow when the density difference is below a critical value, or vigorous above the critical value, but not something in between.

The companion paper (Woods, 1992) develops a theoretical description of the processes at the interface between a pure solid and binary liquid. Woods shows that if the excess of heat above the freezing point in the liquid (*melt superheat*) is much greater than the deficit of heat below the melting point of the solid (*solid supercooling*), the solid phase will melt, the rate of the phase transition is determined by the thermal diffusivity, and the composition of the melt is that of the solid. However if the melt superheat is too low, the source of energy for the phase transition

from solid to liquid shifts from the heat in the solution to the chemical potential of the solute, and therefore the rate of phase change becomes limited by the rate at which solute molecules can diffuse to the interface. The composition of the melt, therefore, evolves away from that of the melt towards that of the far-field, and the phase change becomes driven by chemical rather than thermal energy; that is to say, the solid *dissolves* instead of melting. Further, since seawater freezes at lower temperatures than fresh ice melts, we can have a situation where liquid seawater is in contact with solid fresh water that is at a *higher* temperature. Note that we cannot talk about the "freezing point of seawater" because, being a solution, it has a freezing *range*, and this freezing range varies with salinity. The mathematical construct developed by Woods describes the melt superheat, and is shown in equation A.21 (p.146).

Kerr (1994a, 1994b), also a graduate of Huppert, further developed the melting-and-dissolving model. I mention it for completeness because his work is somewhat foundational to current approaches, but I am not using it myself and did not include it in the appendix.

1.1.5 At the iceberg scale

The mathematical work described in the previous subsections is scale-less, but would necessarily have to be applied over small distances because of the assumption that the properties of the solution are constant. There are also a few investigations intended specifically for geophysical scales. Responding to the iceberg-towing problem, Weeks and Campbell (1973) derived a model for the rate of melting of the submerged face of an iceberg under tow, which is still in use in current literature and is simply

$$R \;=\; 6.74 \;\times\; 10^{-6} \cdot \frac{v^{0.8} \Delta T}{\ell^{0.2}} \tag{1.20}$$

where R is the recession of the ice face in m s^{-1}, v is the tow velocity, ℓ is the length of the iceberg along the tow direction, and ΔT is the temperature difference between the ice and the water. The use of "R" for this measure is unfortunate since it conflicts not only with the much older use in statistics but also with the usage developed at the same time by Gebhart and colleagues for a

different measure for the same problem. However, because it is very common in the iceberg melting literature, I am leaving it as is. This equation is no doubt useful for engineering purposes, though long-distance iceberg towing never really caught on, but it does not convey any information about the physical chemistry at the sea-ice interface and is much too rough for modern climate modelling.

Another paper in the conversation on iceberg utilization is that of Neshyba (1977), though he had no interest in towing icebergs and was concerned with finding out how much upwelling they cause in the Weddell Sea. In his estimation, the Grashof number (Gr) would be of the order of 10^{17}. As the transition from laminar to turbulent flow takes place when Gr is of the order of 10^8 to 10^9, this indicates vigorous turbulence which he thought would entrain a lot of saltwater into the mix. This certainly interrogates the applicability of any of our mathematical models to the melting of iceberg keels, since the turbulence would invalidate most of our assumptions.

Wells and Worster (2008), also academic descendants of Huppert, expanded the differential models to geophysical scales. Their model is represented by fourteen equations and takes an entire journal page, not counting the definition of symbols. I have omitted it from the appendix. The key finding we need to retain is that whereas in the laboratory, the laminar layer of melt adjacent to the ice is dominated by its own buoyancy, at geophysical scales it is driven by the shear imposed on it by the outer layer which is more buoyant. So again, this questions the scalability of laboratory models. Wells and Worster (2011) incorporated Woods's (1992) melting and dissolving, and found that "melting is faster and generates a stronger flow than dissolving". They also noted the interesting result that the fluid flow is independent of the ratio of densities of the solid and liquid phases, or, "the mass flux of fluid released by ablation is equal to the ratio of the heat flux into the interface and the latent heat per unit mass L required to change phase, independent of the density of the solid". Once again their model is too large to reproduce in the appendix, but they do provide a simple criterion for the boundary between melting and dissolving:

$$\frac{1}{\mathrm{Ste}} = \frac{c_l(T_\infty - T_m)}{L} = O\left(\left[\frac{D}{\kappa_l}\right]^{1/2}\right) \tag{1.21}$$

where Ste is the Stefan number, c_l is the specific heat of the liquid, κ_l is its thermal conductivity, D is the diffusivity of the salt, T_∞ is the far-field temperature, and T_m is the extremum temperature for the ambient conditions (defined in Gebhart and Mollendorf, 1978).

Finally, for the sake of completeness, I will mention the paper of Marschall (1977), which, in four pages, sets up a differential system to represent "melting of pure ice in saline water under the condition of natural convection", states that it admits a similarity solution that "provides local heat and mass transfer rates, velocity, temperature, and concentration distributions near the melting surface, and other pertinent information", and gives none of the solution.

1.2 Experiments

In-situ measurements of the rate of melting of icebergs are hardly possible, because of the danger of approaching them and the difficulty in any case of devising instrumentation for such a chaotic environment, though recently Weiss (2024) used a remotely operated vehicle to mount instruments to an iceberg face below the water line, and Johnson (2025, chapter 1) demonstrated a similar approach attached just below the water line on small growlers by working from a boat. Both, however, are expensive and produce limited numbers of data points. Field experiments are possible but rare. Laboratory experiments, on the other hand, are multitudes, but there are many experimental methods, each used too few times, and the results are reported differently by each author. A recent review of laboratory approaches by McCutchan and Johnson (2020) was very helpful in starting my research. It is well agreed in the literature that the ice ablation problem depends on the geometry of the ice-sea interface, and mathematical approaches are always predicated on a certain geometry, so experiments are normally compared with others of like geometry. Three categories interest me here: spherical, horizontal, and vertical.

1.2.1 Field experiments

According to Loewe (1961), the first reported experiments on the rate of melting of ice in seawater are Steenstrup (1883) and Hammer (1883). From 1878 to 1880, Steenstrup was working in West Greenland, then as now a largely self-governing territory of Denmark. Between March

and October 1879, I believe around Uummannaq, he did some experiments in melting blocks of ice in the sea. Four were bubbly glacier ice, with initial weights of 8 kg to 11.25 kg. In the October experiment he sank one to 100 feet and simultaneously floated another on the surface. In April he also melted a 12.5-kg block of sea ice. Hammer (1883) also melted blocks of ice in the sea in spring 1880 around Jakobshavn (present-day Ilulissat). He mentions that he could not determine the surface area of the blocks, but that they were as close to cubes as he could make them. Neither one describes the experimental protocol, but evidently they sank the blocks and retrieved them from time to time to weigh them. This is unfortunate because, as I learned in my own experiments, recovering and re-inserting the test piece can significantly change the results. In my opinion this is due to mostly to the drag exerted by the water on the interface as the ice moves through the water.

Taking all the data from both researchers together, a systematic effect is discernible in Figure 1.1. In particular, the two October sets, represented as the darkest shade of red, ran concurrently, one floating at the surface and one at 100 feet depth. The temperature was -0.5°C at the surface and -0.2°C at depth, a difference that should have a very minor effect in my experience, so the greater rate of ablation for the deep block is very likely due to some combination of depth and the disturbance of raising and sinking the block. The whole set could be fitted to a polynomial in temperature t and depth z, thusly:

$$\mathcal{A} = 466.6 + 148.9\,t + 1.849\,z - 33.7\,t + 6.378\,tz \tag{1.22}$$

the result having units of kg m^{-2} day^{-1}. Despite the roughness of the method, the goodness of fit is $R^2 = 0.7555$. Also of interest, the measurements of 10 and 11 June 1880, represented in greenish-blue in Figure 1.1, include five separate blocks, all melted floating on the surface in different air temperatures and times of day. When plotted against time as shown in Figure 1.2, this series shows some relation between the melt rate and solar elevation, which cannot have been caused by air or water temperature if the measurements are reliable. Given that the site is on the west coast of Greenland, I am unsure how to explain why the melt rate would be higher in the

Figure 1.1
Temperature and depth effects in the observations of Steenstrup (1883) and Hammer (1883).

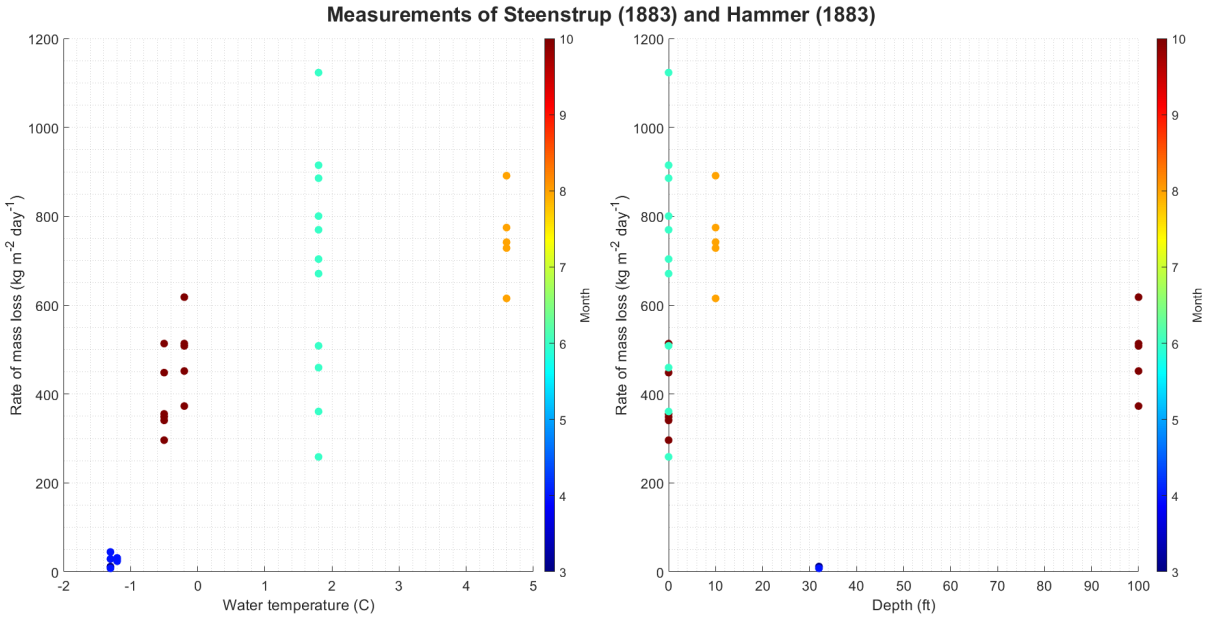

Note. In these field experiments in a fjord in Greeland, cubes of ice were submerged to various depths, from the surface to 100 feet. The left panel shows the rate of mass loss against water temperature, the right panel against depth. The temperature dependence is discernible, but the depth dependence is obscured by the scatter and the temperature effect. This figure is discussed in the text on p.29.

morning in colder air than in the evening. My best hypothesis is that the evening of 10 June was cloudy, clearing overnight, and the increased rate of melt on 11 June was due to sunlight. The fact that solar radiation interacts with seasonal sea ice is well established (e.g. Ehn, 2008).

Loewe (1961) further reports that, according to unpublished notes made available to him by Keith Jack, who had been of the Ross Sea party of the Imperial Trans-Antarctic Expedition in 1914-17, this team also conducted ice-melting experiments. According to Loewe, they cut ice blocks with side lengths of 15 to 20 cm from the glacier at Cape Evans and sank them. Whereas Steenstrup had been quite certain that ice does not form under the sea, this experiment reports that blocks submerged from 9 August to 26 August, 1915, gained mass, and those sunk on 3 October 1916 grew until 18 October and then lost mass, but by 16 November were still heavier than they started. Mass gain was greater at greater depths. In December, two sets of blocks “disappeared from

Figure 1.2
Effect of time of day in the observations of Hammer (1883).

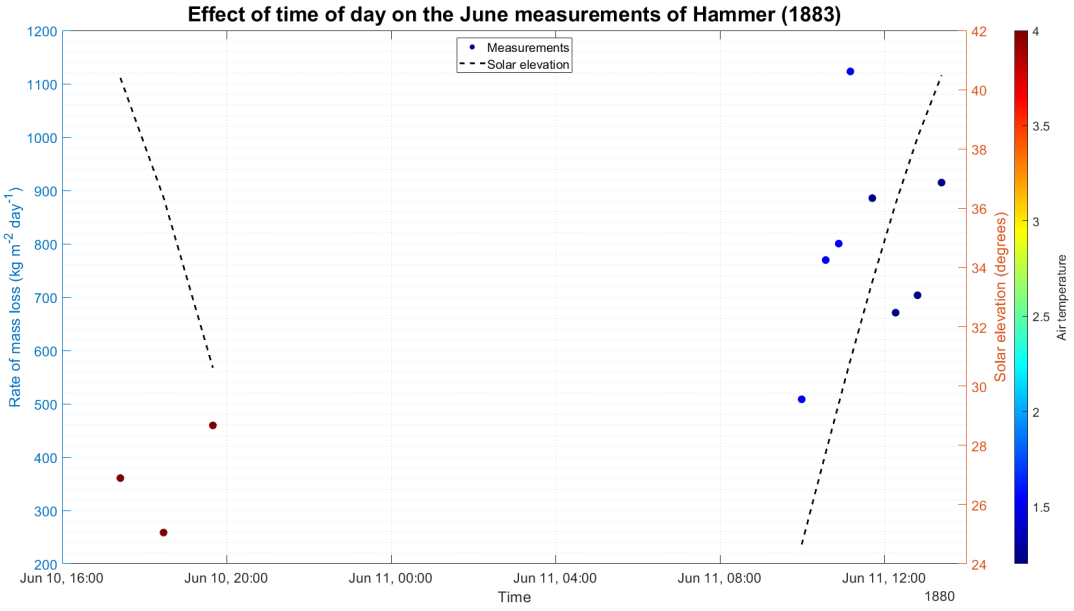

Note. Melt data: Hammer (1883); code for calculating solar elevation: Dozier (2025). Surprisingly, the melt rate is higher in the morning than in the evening despite the temperature being colder and the site being on the west coast of Greenland, where it probably receives more evening light. This figure is discussed in the text on p.29.

their lashings", and thereafter the blocks were "enclosed in netting". One can therefore imagine that the experiment was typically done by tying a line about the blocks and the other end to a weight, knot-tying being at the time a self-evident life skill. In late December, the water temperature being -1.7°C, a 6-kg block immersed at 9 m was reduced from 6 kg to "a very small remnant" in 53 hours, and one on the surface, from 9 kg to 2 kg. Assuming the ice density was 916.7 kg m^{-3}, this yields melt rates of 11.5 kg m^{-2} day^{-1} at the surface and 12.9 kg m^{-2} day^{-1} at 9 m depth. Unfortunately the unsystematic way in which the experiment is reported, whether by Loewe or the expedition notes, means only these two points have enough data for any kind of use. Both blocks melted faster than Steenstrup's (1883) sea ice block despite the water being colder.

A different kind of field experiment was reported by Stolfi et al. (1978), from the US Navy's Naval Postgraduate School in Monterey CA, USA. Being energetic people with access to a good deal of hardware, they tried to address the flow scaling problem by making a huge block of ice and

having a boat tow it in the sea. They managed to contract to have an ice block made with dimensions 4.9 m × 1.2 m × 0.46 m. Their contractor, however, struggled significantly with the project, so the blocks were frozen from the outside in, resulting in much warping and cracking. Nonetheless, shortly after sunrise on 23 September 1977, they had a 41-foot rescue boat from the US Coast Guard lower such an ice block into the water of Monterey Bay and tow it at a speed of approximately 1.2 knots, which was as slow as the coxswain could manage. After 25 minutes, however, the towing bollard pulled out of the ice block, which shortly fell apart in the water. On 2 October 1977 they made a second attempt, which they stopped soon enough to recover the ice block and observe its decay. These experiments did not produce any numerical data, but I am including them for completeness, and because ice manufacturing has progressed since and iceberg-towing is in fact well established on Canada's east coast, so one could certainly do this experiment again with more adequate expertise and climate, given sufficient funding.

1.2.2 Spherical experiments

Kranse and Schenk (1966) report investigating thermal free convection by "melting solid benzene spheres in excess liquid benzene", a horrifying thought since benzene is flammable, toxic, teratogenic, and carcinogenic. The word "solid" here refers to the solid phase of the benzene; the spheres themselves were not solid, but a hollow copper shell with a diameter of 3.2 cm, into which a cold liquid could be introduced so that the liquid benzene in which they were immersed would slowly freeze onto the surface, producing a 3 mm-thick bubble-free coating. This sphere was then immersed in an insulated glass vessel containing approximately 30 L of liquid benzene, and photographed at intervals through a window in the insulation. This paper does not describe how the test piece was held in place in the tank. The analysis was mostly concerned with quantifying the heat transfer as a function of the angular distance from the highest point of the sphere. Neither the method nor the results are applicable to my brief, but I include it here for completeness and because their comment that "general experience has taught us that the exact shape of the surface has no considerable effect upon convective transfer processes" agrees with my experience.

There are some references in the literature to Oborin (1967) having allegedly done a

spherical experiment. In reality the experiment is so tersely described that I cannot even make a drawing of it, but it certainly was not made with ice. It involved “some tests for a sphere and a cylinder”, from which he plotted the Nusselt number and found it to have the same form reported by, among others, Gebhart and Wang (1982, p.212). His result is “an analytical expression of the law of displacement of heat-transfer minimum as a function of the value and sign of the temperature head”. The *temperature head* is the interface temperature less the far-field temperature, and the function is

$$t_\infty = \frac{16 - t_s}{3} \tag{1.23}$$

where t_∞ is the far-field temperature of minimum heat transfer and t_s is the interface temperature, in °C. Thus for $t_s = 0$°C, the calculated temperature of minimum heat transfer is $t_\infty = 5.3$°C.

Schenk and Schenkels (1968) extended the method of Kranse and Schenk (1966) to use liquid and solid water instead of benzene. They were particularly keen to prevent disturbances to the flow pattern from external vibrations, so they “attached the sphere to a support that was mounted on a heavy steel column”, but they did not explain how. Their main contribution to method, according to themselves, was to image the movement of water using “the small dust particles present in ordinary tap water”, which were easily visible when lit with a focused beam from a high-pressure mercury lamp against a dark background. The measuring tool was a film camera with exposure times from 1.5 to 5 s. They found three regimes: one when the water was below 4°C, in which a small upward-flowing boundary layer formed near the surface of the sphere; one when the water was above 6°C, in which the boundary layer flowed downward instead; and one in between, where the flow was upward at the liquid-solid interface but slowed and reversed as distance from the interface increased. At 5.3°C, they “observed a small layer with practically stagnant water along the surface of the sphere”. This temperature is the same that was reported by Oborin (1967), and the authors note that “when the present paper was finished and the manuscript sent to the editor a paper by Oborin on related subjects appeared”, so apparently this result was arrived at independently from

different experimental and mathematical methods.

Vanier and Tien (1970) describe an experiment using an ice sphere with a lead core. In 1968, the same authors had presented at a symposium "an accurate numerical method to solve the similarity equations for a semi-infinite vertical plate at a constant temperature (T_w) immersed in an indefinitely large volume of water at bulk temperature T_∞". They noted that the equation must be solved separately for every combination of T_w and T_∞. They did so, then mapped the solutions and found two regions where "the similarity equations become quite intractable". The melting vertical ice wall problem is a special case of this problem and "theoretical solutions have shown the associated heat transfer rates to be closely similar to (but somewhat less than) the nonmelting case".

They also noted that spheres are "a more practical geometry" for experiments than flat plates and that "measurements of this kind can be carried out by continuous photography of the body profile or by apparent weight recordings", which remains the case, but, they add, their instrument produced tiny (~.01 g) noise polluted weight changes", and the analysis is complicated by "heat conduction losses within the ice". Their experimental design, of which a scale drawing is shown in Figure 1.3, involved molding ice balls with a lead core, so that the average density of the ball would be 1300 kg m^{-3}. They made no attempt to prevent bubbles. The molds were made of copper and had internal diameters of 2, 3, and 4 inches. The test pieces were frozen at -10°C, then warmed to -0.4°C before demolding. They were suspended from a balance arm by a nichrome wire extending out from the lead core, into a stainless steel tank 50.8 cm × 50.8 cm × 61.0 cm tall which was insulated with cooling oil. The experiments were done at a room temperature of +25°C, so the water temperature rose by 0.2°C hr^{-1}, but for runs of 30 minutes or less, the variation in T_∞ was small enough that the error would be no more than ±5%. Three mercury thermometers monitored the water temperature. The scale was "an Ainsworth type 15 high speed null-restoring balance", on which I have found no information, but evidently by its description it was a balance scale, with the test piece suspended from one arm and "precision analytical weights" on the other arm. The weight change was recorded continuously by an electronic device which produced a lot of noise,

Figure 1.3
Scale drawing of the experiment of Vanier and Tien (1970).

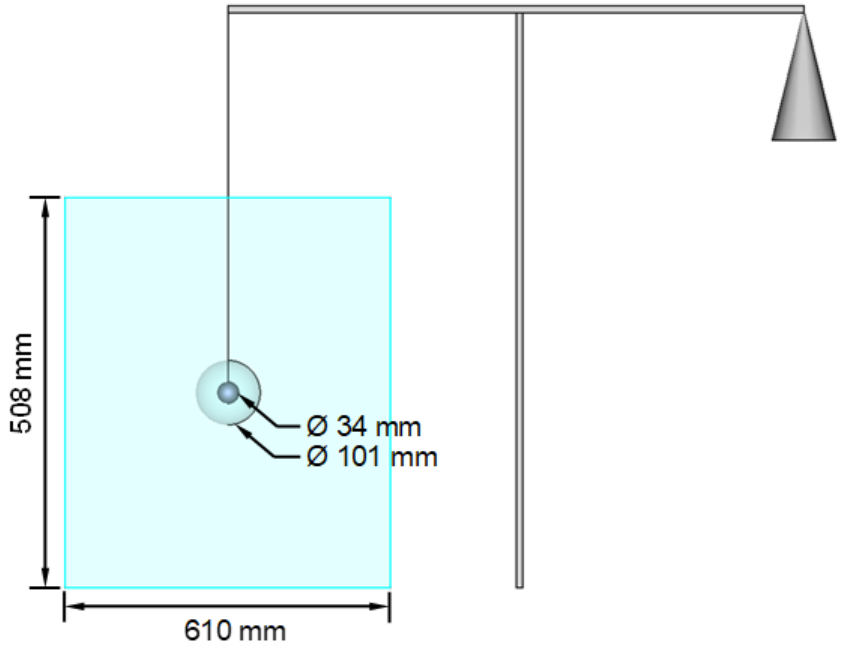

Note. This experiment used ice balls of various diameters molded around a lead core to obtain an overall density of approximately 1300 kg m^{-3}, suspended from a balance. It is discussed in the text on p.34.

in addition to disturbance of the balance itself by any ambient vibration. Their correction for this was that "the best line is drawn by eye through the middle of such oscillations." Also, there is a period at the beginning of each melt where measurements are not available while the ice piece is submerged and the system recovers from the disturbance. Vanier and Tien extrapolated from the rest of the experiment to cover that twilight zone. They do not mention how many trials they made, but a label on one of their diagrams reads "run 103", so clearly they had a fairly large body of data, relative to other experiments on this problem.

Vanier and Tien called the measured quantity "apparent weight", F, and found that $F(\tau)$ fit equally well a linear, quadratic, or exponential model. They selected the quadratic, integrated it,

and used the result to calculate a heat transfer coefficient, $\bar{h}$, as

$$\bar{h} = \left(\frac{\rho_s}{\rho_l - \rho_s}\right)\left(\frac{L}{\pi \mathcal{D}^2 (T_\infty - T_w) g}\right)\frac{dF}{dt} \tag{1.24}$$

where $\mathcal{D}_0$ is the starting diameter and $\mathcal{D} < \mathcal{D}_0$ is the change in diameter, calculated as

$$\mathcal{D} = \left[\mathcal{D}_0^3 - \frac{6\,\Delta F}{\pi g(\rho_l - \rho_s)}\right]^{1/3} \tag{1.25}$$

They plotted the Nusselt number for their experimental data along with a theoretical curve for a vertical plate, and found them to be nearly identical, from which they concluded that "a melting sphere behaves very similarly to a melting flat plate" but that approximately 11% more heat would be transferred by convection to the flat plate than to the sphere, the difference being due to the effect of the curvature on the flow velocities. Unfortunately the paper does not include a table of the data they collected, and as of the time of this writing, my efforts to locate this data have not (yet) succeeded. Obviously it would have been of great interest.

Merk (1954), Kranse and Schenk (1966), Schenk and Schenkels (1968), and Vanier and Tien (1970) all refer to a paper of Dumoré et al. (1953) which allegedly melted ice spheres in water. Unfortunately it is a short communication in *Nature* which only states that "by submerging a sphere of ice in water of temperature T_∞ and studying the gradual decrease of its diameter or its change of weight in the course of time, we have found the experimental points, as shown in the graph." The analysis is similar to the other sources here.

1.2.3 Horizontal experiments

Yen (1968) used a highly controlled experimental apparatus to investigate convection in the water below a melting horizontal ice surface and compare the heat transfer to the Stefan solution. His goal was not to measure the melt rate, but because he reported the time of the onset of convection and the position of the ice-water interface at that time, it is possible to calculate the ablation rate anyway. Of particular interest for our purpose here is the fact that he could control the temperature

Figure 1.4
Results of Yen (1968) for melting a horizontal ice surface from below.

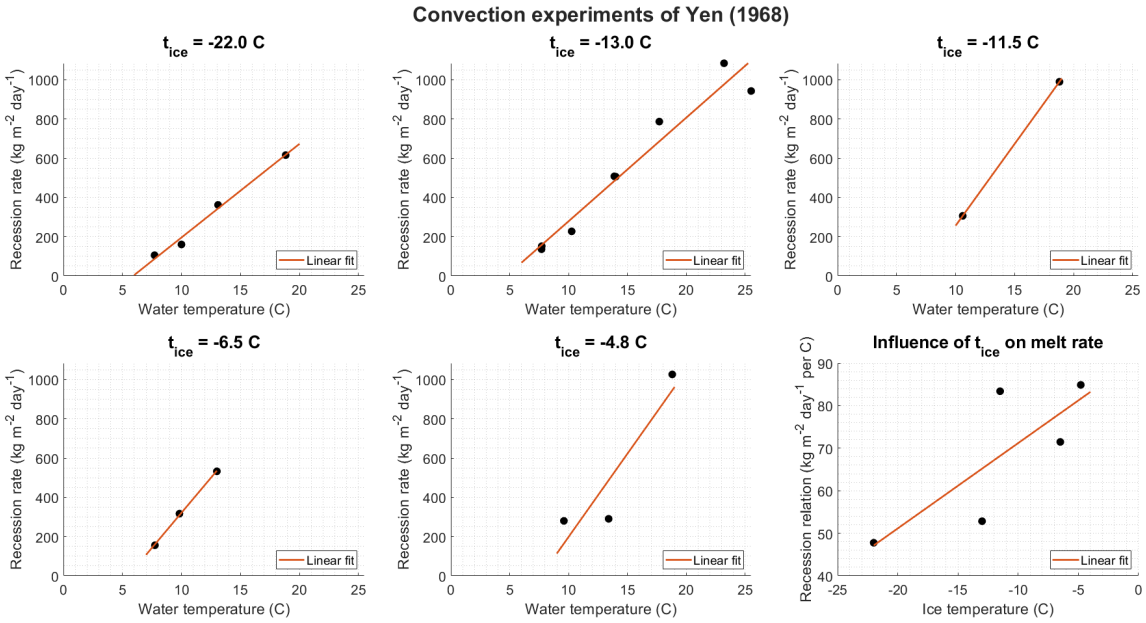

Note. In the first five panels, a straight line was fitted for each temperature using a standard Matlab solver. In the bottom right panel, the slope of the five linear fits was plotted against their respective ice temperature, and the Matlab solver was used to fit a straight line. This figure is discussed in the text on p.37.

of the ice as well as the water, and he made several runs at each of several ice temperatures, with water at different temperatures. He reported that the ice temperature had no significant effect on the onset of convection. However, when the recession rate is plotted against water temperature as shown in Figure 1.4, it becomes apparent that the ice temperature does have a detectable effect on the recession rate. Also, while Yen observed convection in all his experiments, if his results are extrapolated to 4°C as shown in Figure 1.5, the time to onset would be approximately 194 days. With colder saltwater under the melt instead of fresh, the melt layer would indeed be stable over the lifespan of a sheet of seasonal sea ice.

Yen and Galea (1969) then used a similar apparatus to investigate convection in water above a melting horizontal ice surface. Those results are less directly useful to me, in part because the water temperature was up to nearly 40°C, but two qualitative observations are relevant: one, that convection causes the “scallops” in the ice frequently observed on icebergs, and two, that the

Figure 1.5
Log of time to onset of convection in a layer of melt under an ice sheet, from Yen (1968).

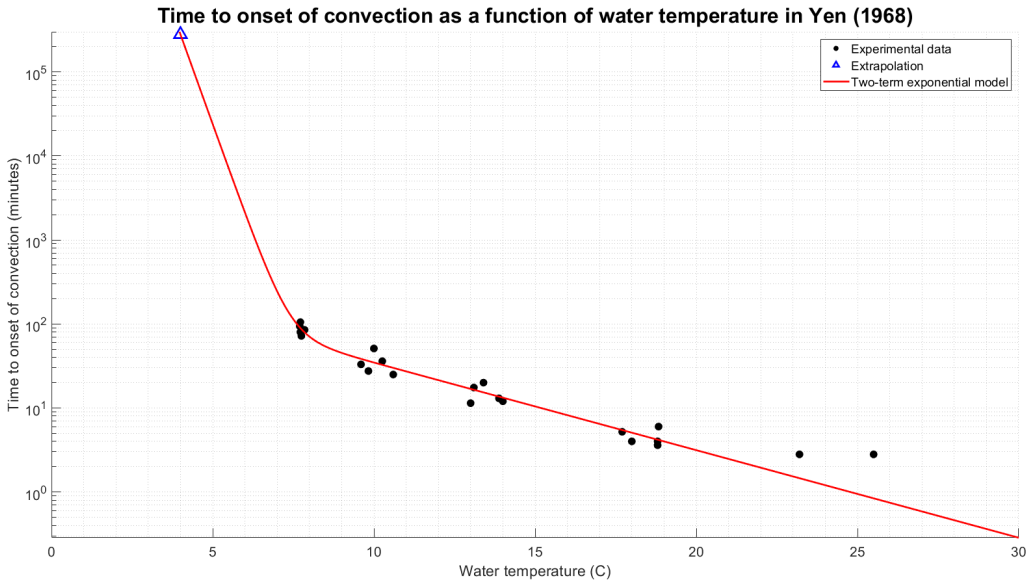

Note. The scale is decimal on the abscissa and logarithmic on the ordinate, hence the elbow in what is in fact an exponential curve. The model was fitted with a standard Matlab solver, and the extrapolation was obtained simply by evaluating the exponential fit at the desired temperature. This figure is discussed in the text on p.37.

temperature gradient in the water varied non-linearly as a function of time, which makes numerical solutions based on a steady-state assumption suspect.

Russell-Head (1980) used a water tank with dimensions of 0.9 m × 0.45 × 0.45 m and one of 2.0 × 1.2 × 1.0 m, therefore capable of containing 182 L and 2400 L of water, respectively, filled with a solution of table salt in tap water. He made ice blocks with an aspect ratio of 1:2:4, to model the geometry of tabular icebergs. He had two molds with the long side 0.5 m and 1.0 m, so the ice blocks were 15.6 or 125 L. The model bergs floated on the surface of the tank but were restrained from moving laterally by a wire system. The tank was not insulated and this allowed photography to be used as the principal measurement, beside some thermistors to monitor temperatures. He found that the rate of melting along the bottom of the sheet was essentially constant with time and also varied little with water salinity from 17.5‰ to 35‰. Confirming once again the prediction of Nansen and the calculation of Gade (1979), the melt formed a stable layer under the ice, which was

colder than the field water and fresh, and thus somewhat insulated the ice from further melting. However, the bottom edges of the block, exposed to the bulk water from the side, melted much faster, and as they receded we can infer that melt moved up the slope so created, causing more field to well up to the ice surface and so sustaining the rate of melting of the bottom. Russell-Head fitted his melt rates for the base with a power law:

$$R = (1.8 \times 10^{-2} \text{ m day}^{-1}) \cdot T_d^{1.5} \tag{1.26}$$

where T_d is *thermal driving*, a term commonly used in this context to refer to the temperature difference between the far-field water and conditions at the interface. Although I have retained the symbol, I think the term is both superfluous and misleading, as we already have *melt superheat*, the difference between the far-field's temperature and its freezing point temperature, and *temperature head*, the difference between the far-field temperature and the temperature at the wall. Russell-Head noted that this agreed tolerably well with Morgan and Budd's (1978) calculated rate for the natural deterioration of icebergs around Antarctica.

Kerr (1994a, 1994b) describes horizontal experiments with the ice either above or below the water, and with a sloped ice surface. All these experiments use solutions that are compositionally very different from the melt, to force vigorous compositional convection. The composition of the solutions was not designed to reflect polar oceanographic reality and the experiments are not directly applicable to my brief, but some of the qualitative information remains relevant. For example, figure 7 on p.262 of 1994b shows cavities growing upward into an ice sheet sitting on a solution with considerable thermal and chemical potential, a result I also obtained. For a sloped ice surface underlying the solution, as might happen with the wave-cut terraces around melting icebergs, the shadowgraph results show that when compositional convection is weak, thermal stratification develops and tends to slow ablation. 1994a found that where dissolution is the main ablation process, it is accompanied by "the release of a significant heat of solution", another effect I reproduced easily. In both cases, and in Josberger (1979) which we will see below, compositional

differences result in much greater irregularity developing in the surface over time, which I also observed.

There are many other horizontal experiments in the literature, but I will not review them here because my assignment was specifically to investigate vertical walls, and because the horizontal case is fairly straightforward compared to the vertical problem.

1.2.4 Vertical experiments

1.2.4.1 The Atlantic experiment

Beside their extensive mathematical work, Gebhart and his collaborators developed an experimental method, which I call the "Atlantic" experiment since they were based in New York State on the Atlantic seaboard. Bendell and Gebhart (1976) made a sheet of ice 30.3 cm high × 14.8 cm wide × 3 cm thick, formed inside an insulated acrylic frame that was frozen from the top and the bottom simultaneously at -20°C, causing bubbles to be trapped in the centre of the sheet. This was done by design, to prevent them being released during the experiment. The frame was then weighted down with stainless steel weights and suspended vertically into a tank of fresh water from "a hook assembly inside of a Sartorius model 2257 balance" so that the rate of melting could be measured by the changing weight; unfortunately the authors do not explain how they arranged to suspend a load from a scale that is designed to be top-loading. The water tank was 0.61 m × 0.61 m × 0.86 m deep, or 320 L, insulated with two inches of rigid and a sheet of plywood, and filled with distilled water cooled to the desired temperature by a circulating chiller. Thermocouples in the ice and in the water monitored the temperature. A scale drawing of the apparatus is shown in Figure 1.6. Data recording and analysis were, in comparison to later iterations, somewhat simple: a series of instantaneous weight readings was recorded for each run, and "the straight line which was thought to be most representative of the data was drawn through the points". The slope of this line was then converted to a melting rate from the densities of water and ice. The density of the water was calculated from its temperature using an equation of state current at the time. The melting rate was

Figure 1.6
Scale drawing of the "Atlantic" experiment used by Gebhart and collaborators.

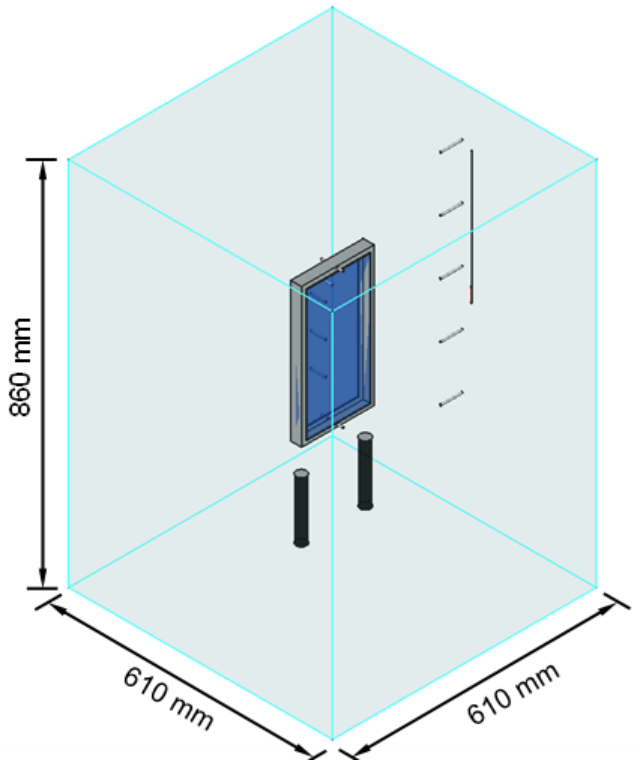

Note. In this experiment, ice was molded inside an acrylic frame, weighted down with steel weights, and suspended from a scale. This figure is discussed in the text on p.40.

then converted to the Nusselt number as

$$\mathrm{Nu} = \frac{h\ell}{\kappa} = \frac{\ell}{\kappa}\left(\frac{\delta m}{\delta t}\frac{L}{A\Delta T}\right) \tag{1.27}$$

Here I rewrote their equation 2 (p.1084) to use our notation conventions. ℓ is the length of the ice face (in this case its vertical dimension), κ is the thermal conductivity of the ice, L is its latent heat of fusion, and A is the surface area, which includes both sides of the ice sheet.

Bendell and Gebhart also defined a parameter to quantify the proximity of the conditions to the density anomaly, thusly:

$$R_{sz} = \frac{t_m(S_\infty) - t_\infty}{t_0(S_0) - t_\infty} \tag{1.28}$$

where the 0 subscripts indicate the conditions at the interface, ∞ the bulk conditions, and $t_m(S)$ is the extremum temperature, that is to say, the temperature of maximum density for a given salinity. Bendell and Gebhart called this parameter R, but because of the competing use by Weeks and Campbell (1973) and others, here I am calling it "R_{sz}", because it compares the heat gradients on both sides of the boundary and therefore affects the propagation of heat across the boundary, somewhat similarly to the way different properties affect the propagation of heat or light across a boundary. The words for "propagation" in Polish and Hungarian starts with "sz", and as I am running out of letters, this seems like a reasonable option. Values of R_{sz} near zero indicate the far field is close to the density anomaly.

Johnson's (1978) Master's thesis, supervised by Mollendorf, used the same apparatus as Bendell and Gebhart (1976), but with salinity $S = 35 \pm 0.5$ and -1.08°C $\leq t \leq$ 24.4°C. He provides some additional information about this design, which was used for years by different workers. The variables measured are the far-field temperature, the interface temperature, and the instantaneous weight. As in Bendell and Gebhart (1976), what is reported is not the instantaneous weight but the melt rate, which is calculated by fitting a straight line to the instantaneous weight and using an inferred density to convert the weight to a mass. Temperatures were measured by five thermocouples embedded in the ice at different heights, three along the vertical centre line of the ice, and two closer to the water-ice interface. It seems from the write-up that the ice came quite rapidly to an equilibrium temperature, and this is what is reported as "interface temperature".

The Ph.D. dissertation of Carey (1981), supervised by Gebhart with Mollendorf on the committee, used the Atlantic method with an ice piece 23.2 cm high × 18.4 cm wide × 3 cm thick, water temperatures from -1°C to +20°C, and salinity from 5 to 26‰ (his p.28). He imaged the flow using an optical camera, a planar beam from a collimated laser shining from above and parallel to the plane of the ice, and glitter made of 40-μm Pliolite® flakes. Pliolite is an acrylic copolymer manufactured by Goodyear Chemical Company, used as a binder in industrial coatings and "virtually insoluble in water" (p.29), so not a choice we would encourage today. Unlike Bendell and Gebhart (1976) and Johnson (1978), Carey did not measure the weight of the ice directly, but

calculated it from the position of the ice-water interface which was measured by reflecting the laser off the surface at an angle. This method was, of his own admission, not particularly accurate, so that "the accuracy of the heat transfer data is limited by the accuracy of the distance measurement to only about ±20%" (p.40). He reported the melt figures in his appendix (pp.143, 145). Confusingly, however, though he describes his experiment as having dimensions of 23.2 cm × 18.4 cm, the table captions read "the average melt rate, $\dot{M}$, is listed for a 1 meter long vertical ice surface". I assume that he multiplied the measured recession of the interface by 1 m^2 and then by the assumed density of the ice. He concluded that "the measured heat transfer agrees with the values predicted by the theory" and with Bendell and Gebhart and Johnson. When I plotted his data, however, I found it quite divergent from his contemporaries, as can be seen in Figure 1.9 (p.51).

Carey and Gebhart (1982) then used the same apparatus with temperatures of 1 to 15°C and salinity of 10‰ and presented an extensive qualitative discussion of the flow patterns, but did not include quantitative results. Sammakia and Gebhart (1983), still using the same experiment, turned their attention to salinities of 14, 17, 22, 30, and 35‰, and temperatures ranging from 1.75°C to +17°C, to reflect actual conditions that occur in situ in the Arctic Ocean. They used a glass tank 0.86 m deep × 0.69 cm × 0.66 cm, so 392 L, filled with de-ionized water mixed with a salt solution that closely matched the conductivity of standard seawater from the Institute of Oceanographic Sciences (Surrey, UK), which was then the custodian of the standard. The tank was insulated with one inch of rigid insulation and three inches of batt. The ice test pieces were made from de-ionized water that was poured into the frame while boiling vigorously. The top and sides were then insulated before putting it in the freezer, to obtain bubble-free ice by freezing from the bottom up. The resulting ice blocks were the same size as Carey's (1981), so 1.28 L, which is only 0.3% of the volume of the tank. The bulk conditions were therefore better controlled than in most other experiments I have reviewed. Sammakia and Gebhart also used the same imaging technique as Carey. The temperature at the interface was measured by embedded thermistors as in previous experiments. Assuming this to be the lowest possible temperature of the liquid, salinity at the interface was inferred from an equation of state. Like other workers, Sammakia and Gebhart

describe extensively the flow patterns they observed but take little interest in the melt rate itself, which they reported for only seven out of their 28 runs.

Johnson and Mollendorf (1984) used the Atlantic apparatus as well with an ice sheet 30.3 cm × 14.8 cm × 3 cm, in either fresh water or a nominal salinity of 35‰, the actual value being between 34.5 and 35.5‰. Imaging was improved with the use of a Schlieren shadowgraph instead of microplastic glitter. Their key observation was that "saline gradients dominate temperature gradients and determine ultimate flow direction." The melt rates from their experiments are not tabulated in the paper but can be read from their figure 3 (p.1931).

1.2.4.2 The Pacific experiment

The Ph.D. dissertation of Josberger (1979) contains a detailed description of the vertical-wall experimental setup he used. I call it the "Pacific" design because Josberger was in Seattle WA, on the USA's Pacific coast, and the same design was then used by Kerr and McConnochie in Australia. A scale drawing is shown in Figure 1.7. Josberger used a clear acrylic tank 1.25 m deep, 1.20 m long, and only 0.45 m wide, filled with water and food-grade salt, in a cold room that cycles around the set temperature with an amplitude of 1°C and a period of 40 minutes. As the tank contained some 675 kg of water, it would take several days to equilibrate to the room temperature, and therefore these small cyclical fluctuations did not significantly affect the water conditions. He used a stirring motor to homogenize temperature and salinity before inserting the ice.

The ice test pieces were bubble-free blocks 0.2 m wide, 0.1 m thick, and from 0.5 to 1.2 m long, with a number of thermistors and rulers mounted onto a plastic support, frozen into it to measure the decay of the ice, and a threaded aluminum rod screwed into the plastic array and clamped to a swiveling support above the tank so it could be aligned vertically along a plumb line. Josberger grew his bubble-free ice by refrigerating water from the bottom and using two stirring motors at the top to shake out the gases. He cut a bevel in one end, to direct melt from the bottom of the block to flow up the back side and not the front, and he planed the front surface smooth with a hot plate. The ice was positioned vertically near one end of the tank, and another array of three thermistors near the other end monitored the temperature of the far field. The water at the far

Figure 1.7
Scale drawing of the "Pacific" experiment used by Josberger (1979).

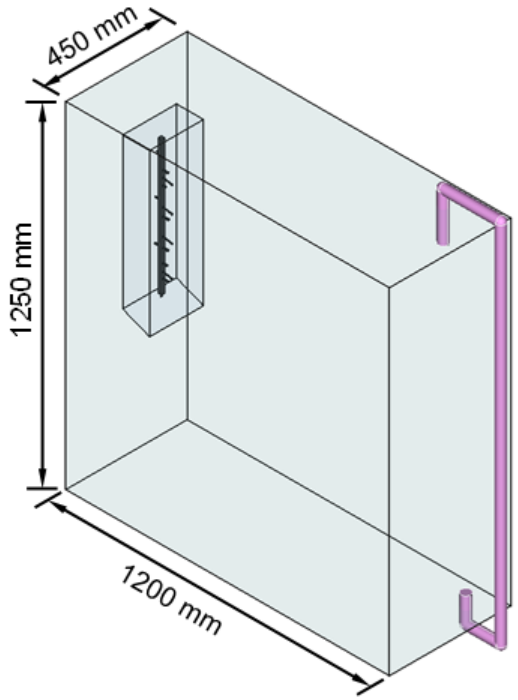

Note. In this experiment, the ice was held down by the rod molded into it, which can also be used to adjust it precisely to the vertical. The bottom of the ice piece is bevelled so melt from the bottom flows up the far side, not the near side that is being measured. This figure is discussed in the text on p.44.

end was also sampled periodically to check its salinity, though the exact method of sampling is not described. A pump with a low flow siphoned water near the surface at the end away from the ice, circulated it through a bath at room temperature, and fed it back into the bottom of the apparatus, to keep the far-field temperature constant.

Josberger used glitter made from commercially available mother-of-pearl flakes, a much more environmentally responsible option than Pliolite, which however required adding 0.2 kg of sodium bicarbonate to his tank, because mother-of-pearl is calcium carbonate and would have a tendency to dissolve in regular water. He projected a planar beam from the narrow end of the tank closest to the ice, through the ice itself, into the boundary layer, where it reflected off the mother-of-pearl glitter. A camera mounted along the long side of the tank took 30-second exposures, and thus captured the movement of the water as light streaks from the illuminated glitter.

However, as he noted, this could only produce qualitative results, because the glitter flakes are flat and rotate in the stream, and are only visible on the photographs when they happen to be at the right angle to reflect light from the slide projector to the camera.

Josberger was also able to measure the velocity of the melt plume by injecting a mixture of India ink and saltwater into the plume and using his own eyes and a stopwatch to time the progress of the dye from one thermistor to another along the vertical dimension of the ice. This method also enabled him to see how far from the surface the plume could mix. Finally, he took photos of the ice block at the end of the experiment. A sample thermistor reading he included shows that the experiments lasted on the order of five hours.

Josberger, like other ice-melting researchers, gives extensive qualitative descriptions of the experimental results, much of which is not relevant to my project. One point of interest was that under certain conditions, the boundary layer flows down below a certain height and up above it, so a horizontal jet of water is drawn from the far field to the ice at the height of the bifurcation. This causes a depression in the ice where the jet is incident. Whether a cause or a consequence, this is also the height where the plume becomes turbulent. At first, small-amplitude waves form in the upper third of the laminar layer, at the interface between the melt and the salt layer. They have horizontal crests across the width of the ice face, a phase speed of the order of 1 mm s^{-1}, and a wavelength of approximately 5 mm. When they reach an amplitude of approximately 3 mm, the waves break, and about 30 mm above the point where they break, the inner flow becomes turbulent. In the upper third of the laminar region, vertical grooves form in the ice, with a width and depth of about 1 mm and about 25 mm apart, indicating the presence of waves or vortices along a vertical axis as well.

Kerr and McConnochie (2015) used the same design as Josberger (1979), except their tank was even narrower, only 20 cm, and the ice was grown directly in the tank by making one short wall a heat exchanger, which was set to -10°C until an ice wall approximately 8 cm thick had formed, and then to -2°C to equilibrate the ice temperature. The remaining fresh water in the tank was then drained and replaced with a solution of 3.44 to 3.60 wt% NaCl and temperatures from 0.3 to

5.4°C. They define a parameter analogous to the R_{sz} of Bendell and Gebhart (1976) in equation 1.28 (p.41), thusly:

$$C_{sz} = \frac{C_i - C_s}{C_f - C_i} \tag{1.29}$$

where C stands for composition, and the subscripts f, i, and s denote the far-field, interface, and solid, respectively. They then fitted the interface temperature and salinity for a dissolving ice face as quadratics, thusly:

$$T_i = T_L(C_f) + 0.251\,T_d - 0.0013\,T_d^2 \tag{1.30}$$

$$C_i = C_f - 4.46\,T_d + 0.0096\,T_d^2 \tag{1.31}$$

where $T_L(C_f)$ is the liquidus temperature at the composition of the far-field, or more simply, the "freezing point" of the solution. Their calculation showed that "the dissolving model breaks down", that is, C_{sz} goes to zero, when the far-field temperature t_f reaches 5.9°C. Recall that Oborin (1967) and Schenk and Schenkels (1968) had found a thermal energy minimum at 5.3°C in fresh water, so this area of the $T - S$ space is problematic in more than one way. Finally they propose a model for the ablation rate due to dissolution, which they call the dissolving velocity:

$$V = 7.8\,T_d^{1.34} \tag{1.32}$$

I mention for completeness McConnochie and Kerr (2016a, 2016b) which continued with the same experimental setup but were concerned respectively with describing the melt plume and adding a salinity gradient, and therefore are not directly relevant to my brief.

Figure 1.8
Scale drawing of the vertical cylinder experiment of Gebhart and Wang (1982).

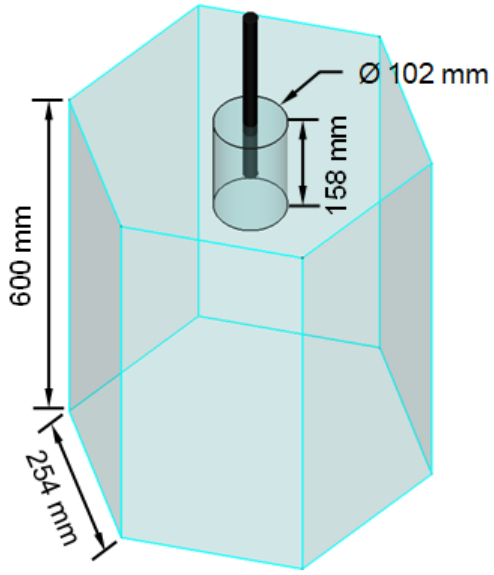

Note. This experiment was a modification of the Atlantic design intended to obtain more realistic flow patterns by eliminating sharp corners and letting the ice face intersect the water-air interface. This figure is discussed in the text on p.48.

1.2.4.3 A vertical cylinder experiment

Gebhart and Wang (1982) changed the geometry of the experiment to reduce confounds on the flow patterns. Instead of a rectangular tank, they used a hexagonal fish tank with sides 25.4 cm wide each and 60 cm tall, therefore a volume of 100.6 L, which they filled with de-ionized water. The ice test piece was a cylinder with a radius of 5.08 cm and length of 15.8 cm, therefore a volume of 1.28 L, or about 1% of the volume of water, which is typical with many of these experiments. A rod was frozen into the ice to keep it in place. No description of the rod is given, and this is unfortunate because the geometry of the rod affects the stresses in the ice piece, which affects the melting. The cylinder was mounted vertically in the center of the tank, with 14 cm in the water and 1.8 cm above the surface. This was probably not intended to mimic the natural floating of ice, since the ice could not move down as it melted, but more to provide a realistic geometry at the air-water-ice interface. A scale drawing of the experiment is shown in Figure 1.8.

The experiment was conducted in a room at +16°C, so that even when the apparatus was

insulated on all sides, the water temperature would rise over time. During the experiments, one side had to be left uninsulated to allow observation. The experiment was illuminated from above by a laser that was spread out into a planar beam, parallel to the observation window and running through the center of the cylinder. As in Carey (1981) and Sammakia and Gebhart (1983), glitter was added to the water in the form of Pliolite flakes. The flakes remained in suspension for a long time and reflected the laser very brightly, and this was imaged with a film camera on a long exposure from 0.1 s to eight minutes. The rate of ablation was determined simply by weighing the cylinder before and after the experiment.

The important result of this experiment was to document the flow patterns around the temperature of maximum density. Since they used only de-ionized fresh water, the maximum density and its associated temperature are known quantities. For water temperatures below 4°C, the melt at 0°C is less dense than the field, and therefore the flow is everywhere upward, except near the surface where interference with the water-air interface causes it to turn. In particular, the melt entrains a column of water upward under the cylinder. For water temperatures above 5.5°C, conversely, the flow is everywhere downward, and water flowing down the sides of the cylinder converges under the bottom and into a downward column of water. Because this downwelling entrains surface water toward the ice, it melts a notch in the cylinder at the sea-air interface, which is not seen in upwelling conditions where cold water moves up and out. In between the two, things are interesting. At 4.2°C the flow is still upward but slowing down. At 4.4°C it reverses down the centre of the column, but this forces a toroidal vortex with a stagnant core around the column. As the temperature increases further the vortex shrinks so that at 5.3°C there is only downward flow, the column forming then a “vigorous and concentrated jet”. This confirmed results about the convective inversion obtained theoretically by Oborin (1967) and experimentally by Schenk and Schenkels (1968). Gebhart and Wang provided not only their own data for the melt rate versus water temperature, but also a correction to Bendell and Gebhart (1976), so the two can be compared.

1.2.5 Other experimental methods

The experimental methods listed above are the most cited in the study of melting icebergs, but there is much more in the literature. The papers of Huppert and Josberger (1980) and Huppert and Turner (1980), frequently cited in this context, are concerned with stratified water, and therefore outside my scope. Machicoane et al. (2013) described melting ice balls either free or restrained by a rod in a turbulent flow produced by impellers in a tank, which must have been interesting but is not applicable here. Li et al. (2016) tried to isolate the heat transfer coefficient using fresh water in a flume tank with low flow velocities. They offer a result as a dimensionless heat transfer coefficient, thusly:

$$C_h = \frac{4594.8}{\rho_w c_w} \tag{1.33}$$

They found $C_h = 1.1 \times 10^{-3}$, which is the same order of magnitude as values they cited from other literature which ranged from 0.16×10^{-3} measured in Liaodong Bay to 3.8×10^{-3} measured in the East Sea.

Understanding the reaction between salt and ice seems rather essential to determining the dissolution rate of icebergs, but is little discussed in that context. In the study of de-icing applications, Klein-Paste and Potapova (2014) tried an experiment in which they added a concentrated solution of NaCl, up to 23.3% wt, to snow they had collected and kept in a freezer at -25°C for some months. They reached the puzzling conclusion that "it is not the melting of ice itself (the transition from solid ice to liquid water) on which the melt rate depends". Further, they commented that "ice-melting rate is much harder to define accurately than ice-melting capacity", which of course anyone can calculate from thermodynamic equations. Just like iceberg researchers, ultimately they had no way to quantify the rate of melting as a function of the amount of salt present.

1.2.5.1 Synthesis of experimental data

All the compatible experimental results reviewed above are tabulated in Appendix B, and plotted in Figure 1.9 along with other available data from various methods. Clearly, much can be

Figure 1.9
Experimental and observational results reviewed.

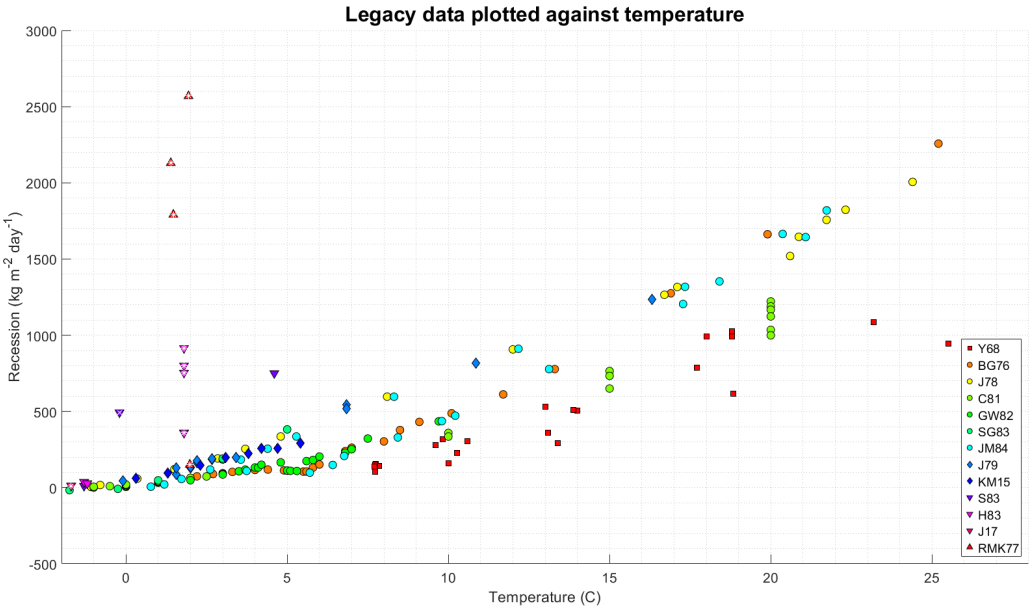

Note. Squares: horizontal experiments. Circles: Atlantic experiment. Diamonds: Pacific experiment. Downward triangle: field experiments. Upward triangles: field observation. Superimposed white stars: ice floating on surface. Superimposed white X: at 30 m depth.
Y68: Yen (1968). BG76: Bendell & Gebhart (1976), J78: Johnson (1978). C81: Carey (1981). GW82: Gebhart & Wang (1982). SG83: Sammakia & Gebhart (1983). JM84: Johnson & Mollendorf (1984). J79: Josberger (1979). KM15: Kerr & McConnochie (2015). S83: Steenstrup (1883). H83: Hammer (1883). J17: Jack 1915-17, cited in Loewe (1961). RMK77: Robe et al. (1977).
This figure is discussed in the text on p.50.

learned from putting the different results into conversation. For example, Yen (1968), which is rarely mentioned, showed the importance of considering the ice temperature (p.36). Moreover it allows us to compare rates for the base and sides of an iceberg. We will see shortly (p.55) that Budd et al. (1980) predicted that the base would melt faster than the sides, whereas in the experiments of Russell-Head (1980) and in my combined plot, the walls clearly melted faster.

1.3 Field observations

While some tried to solve the problem in the lab, others estimated the wastage rate of icebergs from visual field data. For example, Robe et al. (1977) reported on a very large tabular iceberg which was photographed by the aerial International Ice Patrol five times between 12 May

Table 1.1
Dimensions of iceberg, recalculated from Figure 1 of Robe et al. (1977).

Day	Perimeter (m)	Area (m^2)	Mass estimate (10^9 kg)	Temperature (°C)
1	1959	170,635	6.709	1.99
2	2332	178,800	6.802	
20	1991	150,210	5.714	1.47
24	2333	126,490	4.812	1.69
26	2168	120,470	4.583	1.94

Note. This table is discussed in the text on p.51.

and 6 June, 1976. When first spotted it was approximately 680 m × 290 m and, unusually for such a large iceberg, only had 4 to 5 m of freeboard, suggesting a draft of approximately 37 m. According to the authors, its area shrank from approximately 1.9 to 1.09×10^5 m^2 in 25 days at an approximately constant rate. I polygonized the photographs from their figure 1 (p.506) using Matlab, as shown in Figure 1.10, and found the areas and perimeters listed in Table 1.1. The iceberg is visibly larger in the second photograph, and as this cannot be a real physical phenomenon, the photo must be shown at a different scale from the others and I have to exclude it from calculations. I then plotted the ratio of area to perimeter against time. Polynomial and exponential models were inadequate for this data because they are not necessarily strictly decreasing, but a logistic model fits with $r^2 = 0.94$, as shown in Figure 1.11. If we assume incorrectly that the keel depth and sail height remain constant through the observation period, and that the ice density is uniformly 916.7 kg m^{-3}, we can make a mass estimate and therefore a mass loss rate estimate for the vertical walls. Again excluding day 2, the mass loss rate will take a linear fit with $r^2 = 0.90$, but a logistic fit with $r^2 = 0.99$. The mass loss rate and area:perimeter ratio also relate to each other linearly with $r^2 = 0.98$, but we cannot speculate from four data points whether this is a general rule. We can however conclude that approximating the mass loss rate as linear is not appropriate for real icebergs at sea. Robe and colleagues also noted that the mass loss "resulted from wave erosion, undercutting and minor calving" and these processes clearly contributed an order of magnitude more than thermodynamic melting.

Calculating an ablation rate from Robe et al. (1977) is not intuitively obvious. It can be

Figure 1.10
Digitization of the iceberg photographs in Robe et al. (1977, figure 1).

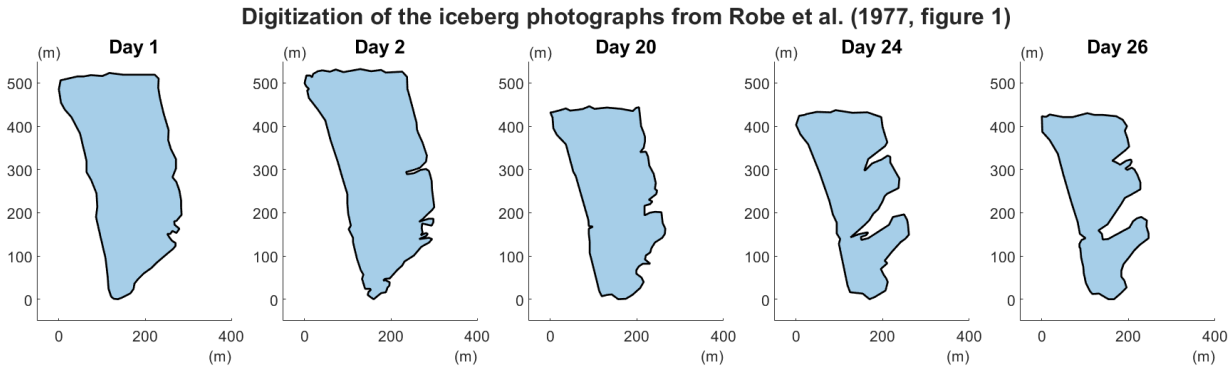

Note. In the black-and-white published photos, the iceberg is very white against a very dark background, making it easy to digitize, and there is no hint of a submerged ice terrace beyond the extent of the sail. Beside the deterioration of the edges, the iceberg surface appears increasingly grainy, likely indicating growing melt ponds on the surface. This figure is discussed in the text on p.51.

shown that

$$\frac{\delta}{\delta\tau}(A\ell\rho) \;=\; \frac{h\Delta T}{L}\,\ell\,\mathcal{P}(\tau) \tag{1.34}$$

where ℓ is the keel depth and $\mathcal{P}$ is the perimeter, hence

$$\frac{h\Delta T}{L} \;=\; \frac{1}{\ell\,\mathcal{P}(\tau)}\frac{\delta}{\delta\tau}(A\ell\rho) \;=\; \frac{\rho}{\mathcal{P}(\tau)}\frac{\delta A}{\delta\tau} \tag{1.35}$$

which has the right units for an ablation rate. When we evaluate this for the four data points we find that the ablation rate is a linear function of time:

$$\mathcal{A}(\tau) \;=\; 93.32\,\tau \;+\; 14.11 \tag{1.36}$$

The thermodynamic ablation is an intrinsic property of ice so it cannot be time-dependent. The depth-averaged water temperature, retrieved from ORAS5 (Zuo et al., 2019) and shown in Table 1.1, do not account for the variation in the rate. Therefore we have to conclude that the rate of ablation

Figure 1.11
Evolution of the area to perimeter ratio of the iceberg in Robe et al. (1977).

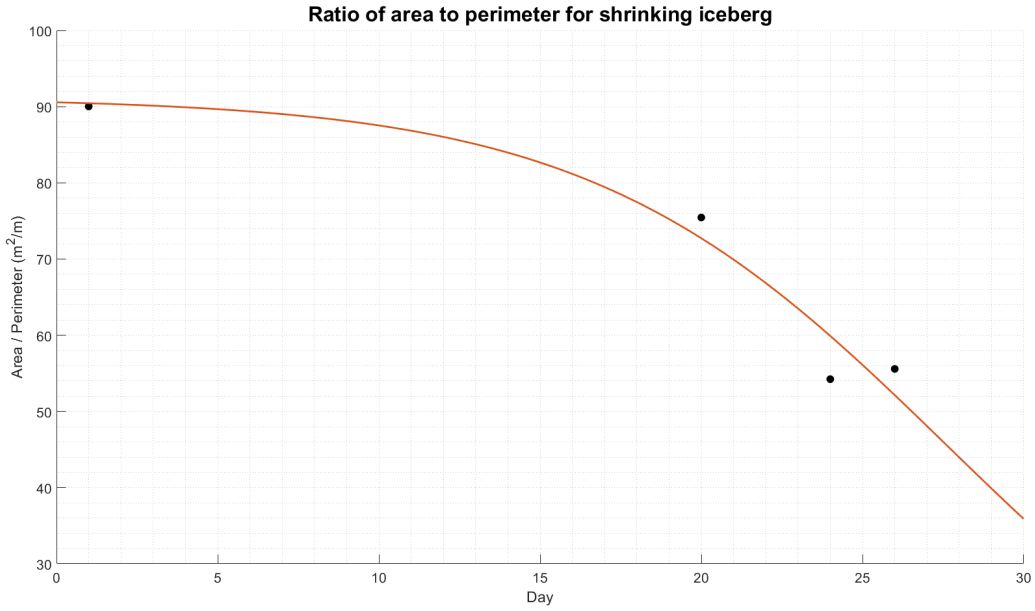

Note. Data (black points) and fitted line (red) with equation $A/P = 91.19/(1 + e^{0.18\times(\tau-27.6)})$. This figure is discussed in the text on p.51.

is driven primarily by the mechanical processes, as the authors themselves did. I have included all four estimated ablation rates in the synthesis plot in Figure 1.9, from which we can see that the thermodynamic ablation rate is in fact consistent with laboratory experiments at the beginning when the iceberg is relatively regular.

Morgan and Budd (1978) and Budd et al. (1980) estimated the melt rate based on iceberg concentrations identified from remote sensing. Though satellite imagery of ice existed since at least 1974 (Kuittinen & Leppäranta, 1989), these authors were still working from aerial and surface photography, which of course limited the scope of their work. Their qualitative comments are however informative. Budd et al. note that

> "In the case of icebergs of large horizontal dimension compared to their thickness, the melt or wastage at the edges makes little difference initially to the change of dimensions, and so their survival is limited by their decrease in thickness until they become so thin

> that they break up. The side wastage does not become a problem until the horizontal dimensions are about twice the thickness."

This, they say, accounts largely for the life histories of very large icebergs, which can survive for years around the Antarctic coast but break up over much shorter periods when they sail into warmer water where their keels melt rapidly. Neshyba and Josberger (1980) disagree, as did the calculations of Neshyba (1977) and Josberger (1978), and the laboratory work of Russell-Head (1980). Based on my current state of knowledge I cannot rule out that they are all right, and that this is simply a result of scale differences, particularly how deviatoric stress scales, which is outside the scope of this thesis.

Greisman (1979) used conductivity-temperature-depth (CTD) measurements along d'Iberville Fiord (80°34' N, 79°0' W) which drains the Agassiz Ice Cap on Ellesmere Island (in present-day Nunavut). This fjord has a small mean tidal range and is (or was then) ice-covered from October to July, and is therefore little disturbed by winds and tides that would otherwise hide the thermohaline circulation signal. Greisman derived a mathematical description of the melt rate of a vertical ice wall in a stratified ocean, thusly:

$$m \propto (\Delta T)^{8/5} \left(\frac{\partial \rho}{\partial z} \right)^{-1/5} \tag{1.37}$$

if the draft of the glacier is less than the vertical scale length given by

$$l_z = \Delta\rho \left(\frac{\delta \rho}{\delta z} \right)^{-1} \tag{1.38}$$

where ρ is the density of the seawater and ΔT is the temperature head, but can be approximated by the far field's superheat. Greisman used temperature measurements to test his model and found that the predicted length scale agreed to within the survey precision of ±1 m. He also derived a condition on the ratio of the volume of seawater entrained to fresh water melted over a given distance on the ice wall, the entrainment ratio, interesting but not directly relevant here.

In 1980, Neshyba and Josberger were starting to wonder: "can various melt rate estimates

of Antarctic icebergs made from laboratory studies, field observations and iceberg distribution statistics be combined, evaluated and/or reconciled to yield a best estimate of actual iceberg melt rate?" Using analytical results from Josberger's older papers, they regressed that the melt rate M_d of an iceberg with draft d is given by

$$M_d = \left(1.55 \times 10^{-2} \text{ m day}^{-1}\right) T_d^{1.6} d^{-1/4} \tag{1.39}$$

They also report a personal communication received from one "D. Topham", according to whom an iceberg was found frozen fast in the pack ice in d'Iberville Fiord, and it was observed that as the keel volume progressively decreased in ambient water at -1.5°C, the decreasing buoyancy of the iceberg distorted the ice surface, from which this D. Topham calculated a melt rate of "two meters per year" at a water temperature of -1.5°C. If we assume that the salinity was 34.5, the liquidus temperature can be calculated, for example from the GSW Toolbox in Matlab (McDougall & Barker, 2011), as -1.88°C, and the thermal driving would therefore be only 0.38°C. We can then solve equation 1.39 and find a draft of 0.14 m, a clearly nonsensical number. We might also question why we are trying to calculate the draft of the iceberg from the alleged melt rate of its vertical walls expressed in inadequate units. Hopefully this can help convince iceberg melt researchers to at least use a unit that makes sense and can be portable from one application to another, such as kg m^{-2} day^{-1}, which I will show is the appropriate unit on p.73 in Subsection 2.2.3.2. As it is now, I am not able to include Topham's measurement in my data set.

1.4 Computational methods

Computational methods have been applied to icebergs at least since White et al. (1980), who used CFD to study the roll stability of icebergs. To a point, models are convenient for phenomena that we cannot measure directly, but not good at singularities and not necessarily effective when we try to extrapolate from known physical processes into ones we do not know. For example, Kim and Yethiraj (2008) modelled the effect of salt on the melting of ice at a molecular level using the TIP5P model, which gives a freezing point for water of 274 K. They noted that this was much better than

other available models like TIP4P, which gives 232 K, and SPC/E, which gives 215 K. However, by definition, the temperature of the triple point of water is 273.16 K (Preston-Thomas, 1990), so even TIP5P is only relatively succesful. The simulation of Kim and Yethiraj involves a model solution of 304 molecules of H_2O, 40 Na^+, and 40 Cl^-, and a crystal of 1536 molecules of H_2O. The simulation temperatures were 260 K, 265 K, and 270 K. The model ran for 50×10^{-9} s and recorded conditions every 400×10^{-15} s. The average number of hydrogen bonds per water molecule differs markedly between ice and water, so a molecule can be classified as being part of the ice or part of the water based on a cutoff value for the number of bonds, which depends on temperature. At any time, molecules near the interface change both from water to ice and vice-versa, regardless of the thermodynamic conditions, but as the relative frequencies of the two changes differ more and more, the reaction favours more and more melting or freezing. At temperatures above 275 K, the model ice melted completely, but at lower temperatures, the ice melts "partially and rapidly" until it reaches an equilibrium. In their simulation, this equilibrium was reached in 40 ns. The proportion of water molecules and salt ions at equilibrium gives a salt concentration, and the relation between temperature and equilibrium concentration can be reversed to obtain the freezing-point depression as a function of the salt concentration.

Recently, Yang et al. (2023) applied CFD to the experiment of Huppert and Turner (1980) with stratified saltwater, using a model previously derived by their group and an advanced computational algorithm. They write that

> "with the parameters of the phase-field model fixed, the system is uniquely determined by six dimensionless control parameters. For these we take the thermal and solutal Rayleigh numbers, the Prandtl number, the Schmidt number, the Stefan number and the density ratio between vertical and horizontal salinity difference... Furthermore, we can define the Lewis number as the ratio of heat and salt diffusivity, as well as the density ratio between temperature and horizontal salinity difference... Because the parameter space is so large, some of the control parameters have to be fixed in order to make the study feasible."

In addition, "since salt diffuses much more slowly than heat, the resolution for the salinity is more demanding than that for the temperature, which limits the simulations to moderate" Rayleigh numbers. This may explain why it was novel to them that, in their simulation, the ablation rate first decreases as salinity increases, then increases. They explain that "the physical origin of this non-monotonic dependence is the competition between thermally-driven buoyancy and salt-driven buoyancy, as well as the stable stratification due to the vertical salinity gradient." While the general shape of the result agrees with my findings, we will see later that it does not actually depend on the stratification. Be that as it may, Dr. Detlef Lohse, senior author of Yang et al. (2023), was the 2019 recipient of the Max Planck medal for extraordinary achievements in theoretical physics, as well as the editor of the *Journal of Fluid Mechanics*. Clearly, the best minds and computational resources of the moment are being applied to the CFD approach, and if it looks unlikely to succeed for them, surely there is little use in my trying the same.

A good deal of effort has also been invested into modelling water flows at larger scales. Cenedese and Straneo (2023) reviewed many such papers at the scale of the iceberg, including the iceberg-ocean-climate interaction. The review of Malyarenko et al. (2020) looks mostly at papers at the scale of glaciers to entire ice shelves. Of course none of this work resolves the physical processes at the iceberg-sea interface, but its existence does show the considerable interest from the climate community in the development of a usable thermodynamic melt model to help parametrize their work.

1.5 Bubbles

While the question of the melt rate of manufactured ice in saltwater is intractable, real glacier ice is only more so due to the presence of bubbles. The literature on this is much more sparse. Bader (1950) wrote that "in my reading on glaciology I was surprised to find a general lack of curiosity concerning air bubbles in glacier ice" and accordingly cited no other works. He conducted experiments on ice of the Malaspina Glacier in Alaska, but because this is a temperate glacier, the air bubbles were associated with a quantity of liquid water, which complicates matters and is not entirely relevant to the major iceberg-producing glaciers in Greenland and Antarctica,

which are cold. In 1956, Scholander and colleagues wrote that "the gas is usually under pressure and is liberated with a fizzing sound when a piece of berg ice melts in a pail of water... The pressure is also manifested by the way chips almost fly off the ice at the slightest fracture. This is undoubtedly caused by the release of compressed air from the bubbles into the fracture." Their experiment on iceberg pieces from Greenland glaciers involved drawing mercury into a syringe and closing the nozzle with their finger; I will not be trying it at home. They found the bubbles to be under pressure, ranging from 2 to 6 atm in a single iceberg, and were perplexed to find such large pressure gradients. They concluded that "if such pressure gradients can persist in the bergs for a long time they might reflect something of the history of the berg such as the depth in the glacier from which it came."

Scholander and Nutt (1960) described a mercury-free method for measuring bubble pressure in glacier ice, which is accurate at both high and low pressures and suitable for field work. "The instrument was built in the machine shop of the ship from porthole windows and other available materials" and consisted in a glycerol bath, chilled to 0°C, set on top of a tire inner tube that absorbed vibrations. A piece of ice would be immersed in the glycerol and the top closed with a heavy glass window and an O-ring seal, so it could be observed from above with a microscope. The ice would slowly melt, releasing its air bubbles. The measurement is achieved by pressurizing the glycerol chamber with a pump until, when the bubbles open, the gas meniscus is only very slightly curved. At this point the chamber pressure is equal to the bubble pressure and can be read with a gauge. Using this apparatus, Scholander and Nutt measured bubble pressure in different icebergs around West Greenland, and found that even in a small piece of ice, pressure can vary by 2 to 5 atm between bubbles, and this was consistent within and between icebergs, as Scholander et al. (1956) had reported. The absolute pressure, however, varies considerably between icebergs, from 2 to over 20 atm, and this, as Bader (1950) hypothesized, reflects their history in the parent glacier.

Leaving aside some works on temperate glaciers that are not applicable to my purpose, we then come to the paper of Gow (1968), who, working on cores from Byrd and Little America V in Antarctica, 308 m and 254 m long respectively, showed that below the pore closure depth,

densification is almost entirely due to compression of the air bubbles, while relaxation when confining pressure is released is not due to expansion of the bubbles, as had been generally thought at the time. Gow concluded that as a result the bubble pressure can be used to determine in situ ice density more effectively than direct measurement of the recovered core.

Urick (1971), working for the US Navy, used sonobuoys dropped from an aircraft around icebergs in about 365 m of water off Newfoundland, and measured the radiated noise power from the bergs, which he attributed to the bubbles. In the 0.1-10 kHz band he measured 0.1 W for one iceberg, 0.03 W for another, and no detectable noise for a third. If the noise is in fact due to bubble pressure, this is consistent with Scholander and Nutt's (1960) observation that each berg has its own pressure signature. Urick also relays the information that "apparently authentic iceberg ice can be purchased in some Washington area supermarkets".

None of this work on iceberg bubble pressure was much used in later research until the last 15 years or so. Since 2014 the literature shows a surge of interest in the sound of glaciers, spearheaded by Dr. Grant Deane at Scripps Institution of Oceanography, with a view to monitoring melting under marine-terminating glaciers. This developing corpus includes Glowacki et al. (2016), Deane et al. (2019), Vishnu et al. (2020, 2023, 2025), and Johnson (2025), and shows good promise for the development of techniques and models to understand the behaviour of bubbles in melting glacial ice. An attempt at an experimental method has also been made by Wengrove et al. (2023), in which they melted two identically-shaped blocks of ice, one clear and one cut from a glacier, in water with temperature $T = 4.1°\mathrm{C}$ and salinity $S = 28$, for 1.5 hour, and reported that the glacier ice lost mass 2.25 times faster than the clear ice. The small sample size, and the fact that they did not report the bubble pressure, make it of course impossible to generalize this result at this time.

1.6 Discussion

This lengthy yet regrettably incomplete tour d'horizon of the iceberg melting literature has shown us that the problem has been attacked diligently with every resource available, up to and including the US Navy, for the past 145 years or more, and yet an answer is still lacking. Before I proceed, therefore, I want to synthesize the lessons learned from the ancients. The main takeaways

are as follows:

a. Analytical fluid dynamics cannot succeed because the general problem is not solvable.

b. Computational fluid dynamics cannot be integrated with coupled circulation models because of the computational cost, time, and expertise involved.

c. Field surveys, for example from remote sensing, are unlikely ever to succeed because non-thermodynamic mass loss exceeds thermodynamic mass loss by at least an order of magnitude and is not sufficiently systematic to be filtered out from the signal.

d. Experimental data, even rough, can be integrated from many sources, and efforts towards FAIR management and stewardship of this data (Wilkinson et al., 2016) could contribute significantly to better modelling.

Interoperability in particular proved to be problematic, as authors frequently reported insufficient details, and even more frequently, inconsistent units. For an ice melting experiment to be usable, a measurement or reasonable estimate must be available for:

1. the far-field temperature,
2. the far-field salinity,
3. the temperature of the ice,
4. the geometry of the ice piece, including all dimensions,
5. the mass or density of the ice piece,
6. the duration of the experiment, and
7. a measure of the mass loss in appropriate units.

The Nusselt number can be considered to have “appropriate units” if the length, temperature, and salinity are given, but since it must be calculated from these quantities, it makes more sense to report the measurements.

Another important lesson is that controlling and measuring melt experiments precisely is difficult, but also relatively unnecessary if enough data points can be collected to average out the nonsystematic noise. Statistically, the univariate sampling distribution from any population with a finite mean and variance approaches normal if the number of independent observations approaches infinity; for a quantity that depends on four or more variables, the distribution tends to be normal even for small numbers of variables (Roddick, 1987). Since our dependent variables depends on at least four variables (salinity, far-field temperature, ice temperature, density), the assumption of a normal error distribution is probably realistic, and collecting more data rather than more accurate data is a valid approach. Indeed, the science of thermodynamics is entirely based on the average behaviour of systems. Further, as Christie et al. (2005) wrote, "the availability of data is a significant issue for complex systems" (p.11) and "it is essential to make full use of all possible sources of information — even those that provide only indirect information" (p.15). That being said, it is now time for me to join the ancient international brotherhood of graduate students who melt ice, and add my own contribution to the data inventory.

Chapter 2

Thermodynamic experiment

2.1 Introduction

In planning an experiment, we have to answer two questions: what can we measure, and how can we use that measurement to calculate the quantity we are investigating? As we saw in Section 1.1, the established mathematical model for the phenomenon under study here is extremely involved and computationally costly. Being a physicist, not an engineer or a mathematician, I tried instead to create the simplest situation possible. The simplicity of the method allowed me to make a thousand trials in under a year, of which enough were comparable to smooth out much of the spurious variations from effects that could not be controlled, measured, and/or treated mathematically. The resulting data fit a simple bivariate quadratic model, either in temperature and salinity or in enthalpy and density, which is also consistent with the legacy data I have been able to obtain. Many choices had to be made in arriving at this model and other researchers could produce different ones. At the suggestion of my advisor Dr. Jens Ehn, I named this one "Agassiz", after the proglacial lake that covered our experiment site in the Pleistocene (Teller, 1975, figure 1).

2.2 Method

2.2.1 Experiment

2.2.1.1 General procedure

My experiment is a benchtop version of Hammer (1883) and Steenstrup's (1883). In contrast to the Atlantic and Pacific methods reviewed previously, I call it the Manitoba experiment. A scale drawing of the experiment is shown in Figure 2.1, and a comparison with older designs in Figure 2.2. My test tanks were tall resin containers. Two were opaque flower planters with the same geometry, and two were clear acrylic food storage containers with sealing tops and different cross-sections. The test solution was made from Winnipeg city water, weighed with a kitchen scale with a precision of 0.1 g. For "fresh" water, the water was used as delivered. Its reported average properties include conductivity 296 µS, pH 7.50, and hardness 80.8 ppm (City of Winnipeg, 2025). Higher salinities were obtained by adding a measured weight of Instant Ocean™ salt (Spectrum

Brands, Inc., 2025), which is commonly used to make artificial seawater because of its accessibility and affordability (e.g. Tison et al., 2002). The ratio of the weight of salt to the total weight of solution was used to calculate what I call "bench salinity", S_B. For "cold" trials the solution was kept in a household refrigerator, and its temperature varied with the refrigerator's duty cycle, but was generally between 1.3 and 2.9°C. For "warm" trials the tank was moved to the bench at room temperature and left to warm by conduction from the ambient air. For "very cold" runs, the solution was transferred to an insulated cooler, the top of which was covered with a poly film, and stored in the freezer, so that it cooled and eventually froze from the top down; the melt was then done in the refrigerator, with the cooler's insulated lid on and a thermal blanket wrapped around it.

The test pieces were also made from Winnipeg city water. Most tests were made with ice balls molded with a silicone mold available from a household goods store, with a nominal diameter of 45 mm, which was frozen in the freezer of the aforementioned household refrigerator for at least eight hours. No attempt was made to control air bubbles. This low-technology approach to molding introduced some variability in the geometry of the test pieces, including flashing at the mold seam, over- or underfill at the gate, some variation in diameter and in the amount and geometric distribution of air bubbles, and bulging, occasionally quite pronounced, resulting from the bubble formation process. Balls that were too irregularly shaped were discarded; the ones that were acceptable were also weighed with a kitchen scale, originally with 0.1 g precision and later upgraded to one with 0.001 g precision and accuracy ± 0.003 g.

To conduct a trial, the solution would first be stirred vigorously with a non-metallic utensil. Its temperature was measured with an older model of the Traceable® Digital Thermometer 4000CC (Control Company, n.d.) with a maximum resolution of 0.001 K, though the temperature was only recorded to 0.1°C, and accuracy ± 0.05 K. Conductivity was measured with a Xylem 330i handheld conductivity probe (WTW GmbH, 2008) that measures temperature with a precision of 0.1 K and accuracy of ± 0.1 K, and conductivity with a maximum precision of 1 µS and accuracy of ± 0.5%. Both probes were verified against a Thermo Scientific Orion Star A210 meter (Thermo Scientific, 2015) with a more recent calibration, graciously lent by Dr. Zou Zou Kuzyk. Then, an ice ball was

Figure 2.1
Scale drawing and detail photo of the Manitoba experimental design.

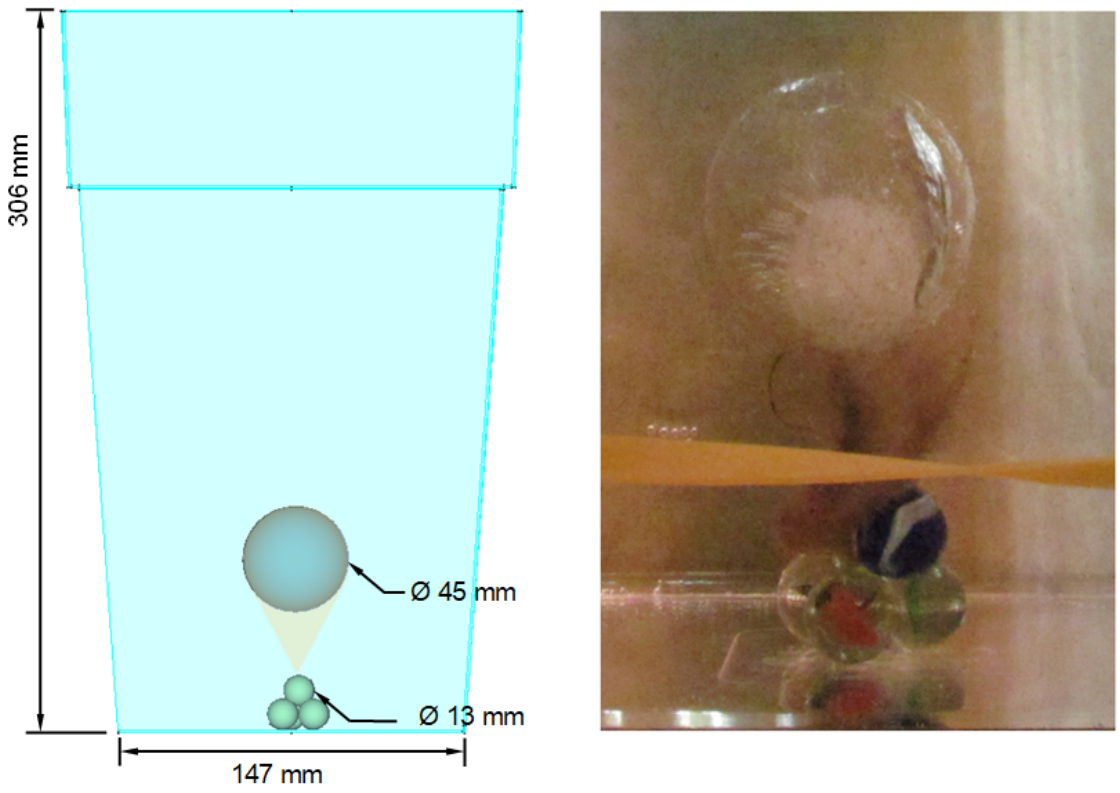

Note. The Manitoba method consists in submerging an ice piece of known geometry, most commonly a ball with nominal diameter 45 mm, in the solution, by restraining it in a very fine polymer net weighed down with glass marbles approximately 13 mm in diameter. The photo is at a larger scale than the drawing and is typical of the clarity and contrast in the imaging setup. The ice-solution interface and the bubbles in the ice are clearly visible. The thermal cleavage plane visible as a shiny area on the right side of the ball, and the fact that the ice is clear, show that the water in this example is warm. In cold water the ice stays cloudy for a long time and does not crack. This figure is discussed in the text on p.63.

removed from the freezer, weighed, and wrapped in a very fine polymer net (Flair Beauty Canada, n.d.) weighted with glass marbles from a toy store. The weighted ball was dropped into the solution and the timer on a Timex Ironman watch was started. The watch manufacturer describes the accuracy of the quartz movement as "a few seconds a month" (Timex, 2026). If we assume that "a few" is $O(2)$, this suggests an accuracy of $\pm\ 4 \times 10^{-5}$ %. Different melt durations were used, generally 90 minutes for very cold runs, 45 minutes for cold, and 4 minutes for warm runs. Late in the experiment I established that the four-minute runs were too short for temperatures below 10°C and the melt time was increased to either 10 or 15 minutes for that range. For cold and very cold

Figure 2.2
Scale drawing of past and current experimental designs.

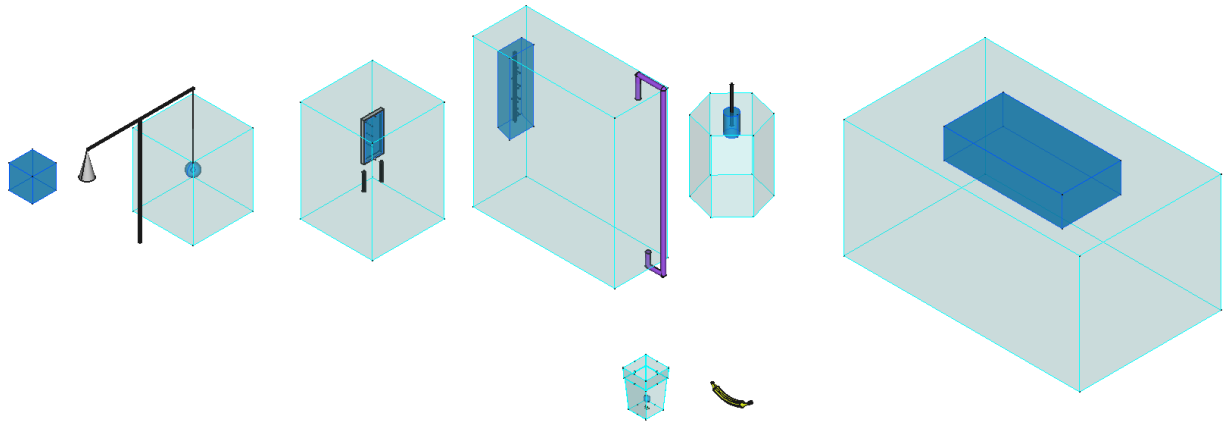

Note. Back row from left: typical ice cube of the Ross Sea Party (Jack, cited in Loewe, 1961); Vanier & Tien (1970); "Atlantic" method (Bendell & Gebhart, 1976; Johnson, 1978); "Pacific" method (Josberger, 1979); Gebhart & Wang (1982); Russell-Head (1980). Front row: "Manitoba"; banana for scale. This figure is discussed in the text on p.63.

runs, the tank was moved back to the refrigerator immediately after the test piece was submerged; for warm runs it was left on the bench.

After the required time elapsed, the test piece was recovered with a non-metallic utensil and weighed again. The remnant was then discarded. The melt weight was added to the weight of the solution, and this new total weight was used to calculate the amount of salt to add to obtain the desired bench salinity for the next run.

2.2.1.2 Ice cylinders

Early in the data collection, I obtained cylindrical molds and made a few trials to see how much the geometry affected the results. The cylinders did not sit vertically in the net and melted very roughly, including in some cases forming a cavity where the water broke through to the bubble space, and in others, a groove parallel to the axis of revolution on the downward-facing part of the cylinder. In all cases the edge between the bases and the cylindrical face became rounded. Nonetheless, the results were consistent with the ball melts. After the main data collection on the balls was complete, I made numerous paired trials, melting first a ball and immediately after a

cylinder, to compare the two. This allowed me to determine a correction factor between the two geometries. The cylinder tests are therefore included in the analysis with this correction.

2.2.1.3 Testing the assumption that the recession is linear

2.2.1.3.1 Melting in air at room conditions

Processing the data collected in this experiment depends on the assumption that the radius of the test piece changes linearly with time, which is supported by Bendell and Gebhart (1976, p.1083, figure 3). They plotted the weight loss, measured in real time by hanging their test piece from a scale. Since the test piece was a flat sheet of bubble-free ice, the weight is a multiple of the recession rate, and since their weight loss rate was linear, so was the recession. Nonetheless, since I used a different geometry and at the suggestion of my committee member Dr. Shawn Clark, I tested the assumption again for my experimental method. This cannot be done by retrieving the test piece periodically and submerging it again, as in the field experiments of Steenstrup (1883) and Hammer (1883) (see Subsection 1.2.1, p.28), because the repeated disruptions corrupted the results. The method of Vanier and Tien (1970) (see Subsection 1.2.2, p.34) was not practical given the time, budget, and engineering constraints of the present study, and also biases the results. As a proxy, I melted some ice balls in air at room temperature. The apparatus for this was a hair net stretched over the top of a kitchen strainer, which sat on top of a glass container. The test piece would sit on the hair net, so it was exposed to the ambient air on all sides and had no contact with heat-conducting materials. Melt would flow through the net and strainer into the glass container. Measurements were taken every five minutes, first by recording the total weight of the apparatus, and then by moving the strainer to a dry container and recording the weight with the dry container. Thus the wet measurement included both the solid and liquid phase, which could be used to determine whether any mass was gained from or lost to the atmosphere; while the dry measurement recorded only the mass of solid remaining. I made three trials, each lasting approximately four hours.

Each weight series was non-dimensionalized by dividing the instantaneous mass by the maximum mass. The weights where then converted to a radius by assuming a constant non-dimensionalized mass density of 1, and the radius curves were fitted to polynomials of different degrees. The time

Figure 2.3
Mass loss behaviour of ice balls in air at room conditions.

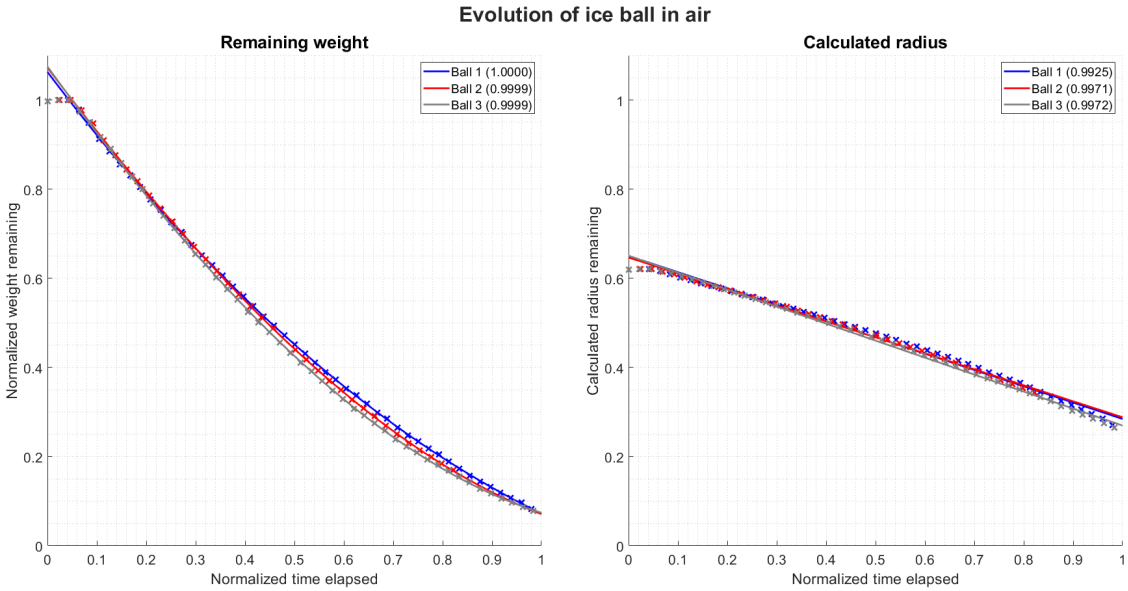

Note. Fit lines are third-degree polynomials in the left panel and first-degree in the right panel. r^2 for each line is in brackets in the legend. This figure is discussed in the text on p.68.

was non-dimensionalized by first fitting the time as a cubic of the weight rather than vice-versa, and then dividing the mean of the four coefficients for each run by the mean of the four coefficients for the first run. This arbitrary choice stretched the curves horizontally so they all occupy the same domain in time. All three were then divided by 240 minutes to obtain a dimensionless time axis.

With the three air trials thus stretched to occupy the same time and weight domains, as plotted in Figure 2.3, we can see that all three trials started with a small mass gain before melting set on. When this mass gain period was excluded, the goodness of fit of a cubic to the instantaneous weight was better than 99.9% in all cases, and the fit of a straight line to the radius was always better than 99%. Although the calculated radius does have a small systematic deviation from linear, the assumption of linearity is adequate here.

2.2.1.3.2 Melting in air with high relative humidity

Surmising from the recession test in air that the initial mass gain depends on relative humidity, I then repeated the experiment in air at approximately +28°C and relative humidity greater than 90%. This was achieved by moving the experiment into a bathroom and running the shower at maximum temperature with the fan off. In this case the reading from the scale was typed into a Matlab code on my laptop every time the display on the scale changed, so that the code recorded simultaneously the temperature reading and the time of the reading. This experiment ran for only a short time to avoid getting too much condensation on the laptop, but I observed that (a) the ice piece gained mass much more rapidly than in normal humidity, (b) the mass gain was in the form of clearly discernible white frost spicules, and (c) the bottom of the ball changed to a clear appearance with liquid water dripping down before all the frost at the top had disappeared. This explains Scholander and Nutt's (1960) observation that freshly cut or calved iceberg ice turns white fairly quickly. They attributed this change to warming up in the sunshine, but in my experiments ice always turns from cloudy to clear as it warms up, and only the high-humidity experiment produced a white surface due to frosting. I did an additional run at room temperature and normal humidity, using the same recording method, to obtain a comparable data set in dry air. The normal and high-humidity conditions are plotted in Figure 2.4. This observation has little bearing on the current work but will be useful information for some later iceberg-modelling work.

2.2.1.3.3 Imaging

To check that the recession is linear in water as well as in air, I ran the larger clear tank on the bench and took photos continuously with a Canon PowerShot SX30i camera (Canon Inc., 2010). To make sure the ice ball was centered in the tank and get a reference scale in the photographs, after stirring and measuring initial conditions, I positioned a 17-inch long cylindrical clear acrylic tube vertically in the centre of the container. I then dropped the weighted ice ball into the solution through the tube and waited for it to settle at the bottom before carefully removing the tube. The outer diameter of the tube is clearly visible in the pictures and can be measured, with a caliper on

Figure 2.4
Mass gain of ice balls in steam and dry conditions.

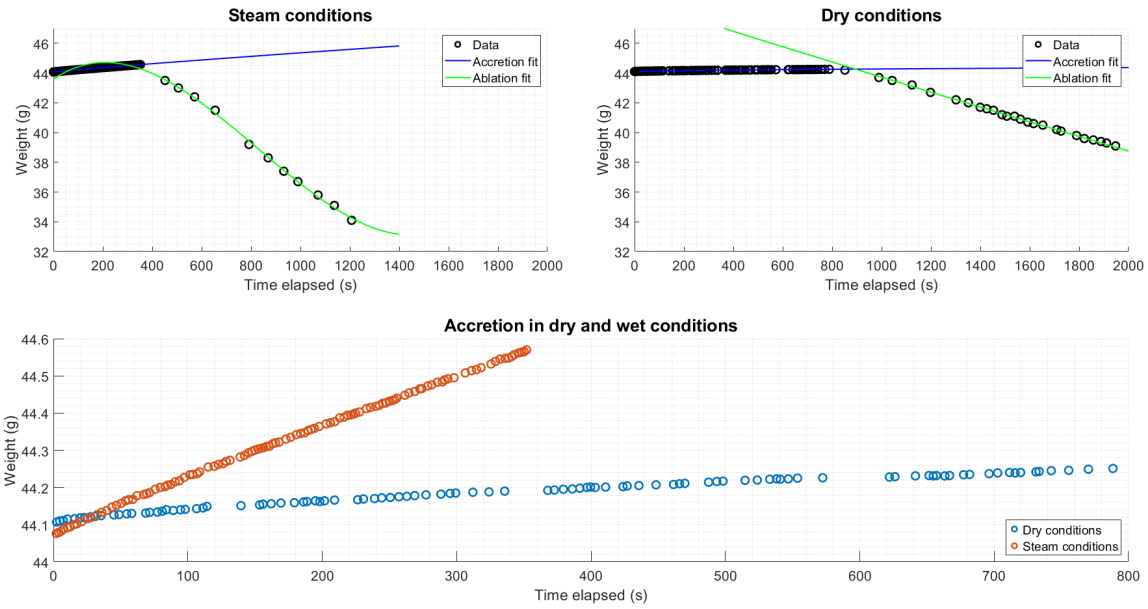

Note. The accretion phase is fitted with a power model and the ablation phase with a cubic. This figure is discussed in the text on p.69.

the actual object and as a number of pixels in the photograph. This yields a scaling factor for each experimental run. The apparent diameter of the ball can then be measured as a number of pixels in each frame, and converted to a length with the scaling factor. Obviously this diameter can be used to calculate the volume of the ball, and since we know its weight, this gives us its density. Measuring the diameter of the ice ball on the bench, on the other hand, was unsuccessful because contact with measuring instruments immediately causes melting, and photographing it next to a reference item gave consistently poor results. Only very much later did I realize I could have been photographing the ball inside the tube on the bench as I did in the water.

I made 45 trials initially to check that the melt was linear. Three were lost due to mistakes in handling the digital files. The remaining 42 are plotted in Figure 2.5 . We can see at a glance that in almost all cases, the ablation is linear or nearly so. A few, notably runs 33 and 40, showed a pronounced drop at first, then a rebound, then a sustained decline. Although the ball is free to

Figure 2.5
Change in apparent diameter of ice balls under various conditions, from imaging.

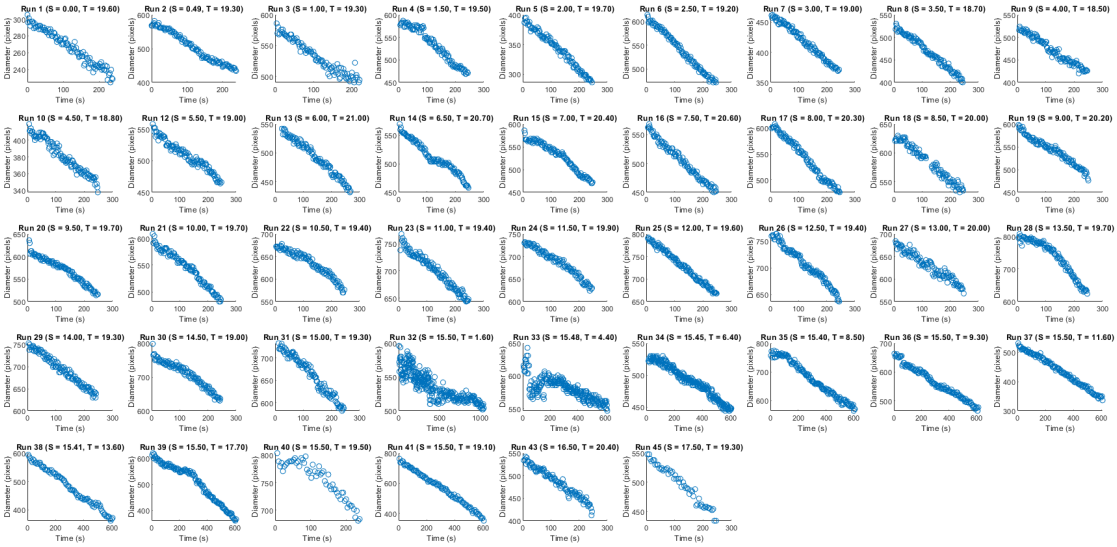

Note. Each plot shows time on the abscissa and apparent radius on the ordinate, for a single imaging run. Salinity, temperature, and scale vary between plots. This graphic is intentionally presented at a very small scale so the general impression of shape is perceived without overthinking the thermodynamic meaning, from which it is apparent that the recession is mostly linear most of the time, but not always. The interested reader can zoom in using their pdf reader's functionality and may find Run 33 particularly curious. This figure is discussed in the text on p.70.

rotate in any direction and often does so, this is not likely to be the explanation, because I have never observed either a slow rise followed by a sharp drop, or a sharp rise followed by a slow decline. I think a more likely hypothesis is that due to the differences among the various rates of energy transfer involved, a phase of rapid ablation can occur, resulting in the formation of a supercooled volume that freezes again until the energy mismatch is resolved. More work is needed on this, however, and for the time being I had to exclude points that are likely to be affected by this phenomenon. For the rest, I conclude that the assumption of a linear ablation rate with time is reasonable.

2.2.2 Density

I made no direct measurements of the volume of the ice balls since I had no equipment capable of it. The imaging in water, described in Subsection 2.2.1.3.3 above, provided an

approximate measurement of the diameter compared to an object of known dimensions. (One should really say *a* diameter since the ball is never strictly spherical.) I also tried the ice ball and an object of known dimension together in air on the bench before and after the melt runs. The first method was more convincing because it created less parallax between the ball and the reference object. With a sample size of $N = 42$, this yielded an average ρ_α = 788 kg m^{-3}. The second method, with $N = 29$, did not produce absolute results, but can be scaled to have the same mean as the first method. Between the two sets I get $N = 71$, and estimate the initial density of the ice to be $\overline{\rho}_\alpha = 788 \pm 95$ kg m^{-3}. The geometry of the ball remnant after melting was too irregular to yield meaningful volume estimates from imaging.

2.2.3 Mathematical treatment of measurements

2.2.3.1 Calculating surface recession

Since the test pieces are approximately spherical, their volume is given by

$$V = \frac{4}{3}\pi r^3 \tag{2.1}$$

where r is the radius, and conversely

$$r = \left(\frac{3V}{4\pi}\right)^{1/3} = \left(\frac{3m}{4\pi\rho}\right)^{1/3} \tag{2.2}$$

where m is the mass and ρ is the density. The mass was measured for each ball, and I used the average density calculated in Subsection 2.2.2. Since melting is a surface process and not a bulk process, the ice loss was expressed as the recession of the ice-solution interface:

$$\delta r = r_\alpha - r_\omega \tag{2.3}$$

where α and ω denote the initial and final positions, respectively. Thus the recession is

$$\delta r = \left(\frac{3m_\alpha}{4\pi\rho}\right)^{1/3} - \left(\frac{3m_\omega}{4\pi\rho}\right)^{1/3} \tag{2.4}$$

The calculation for the cylinders follows the same method except that for a right cylinder,

$$V = \pi \ell r^2 \tag{2.5}$$

where ℓ is the height of the cylinder. If we assume all faces recede at the same rate,

$$r_\omega = r_\alpha - \delta r \tag{2.6}$$

and

$$\ell_\omega = \ell_\alpha - 2\delta r \tag{2.7}$$

so

$$\delta V = \left(\pi \ell r^2 \right)_\alpha - \left(\pi \ell r^2 \right)_\omega = \pi \ell_\alpha r_\alpha^2 - \pi (\ell_\alpha - 2\delta r)(r_\alpha - \delta r)^2 \tag{2.8}$$

Now that we only have α subscripts we can omit them to improve legibility, and rearrange the equation to have the δr terms on the left:

$$(\ell - 2\delta r)(r - \delta r)^2 = \ell r^2 - \frac{\delta m}{\pi \rho} \tag{2.9}$$

This is not nearly as convenient as the ball equation since we have a third-degree polynomial in δr on the left that we will have to solve. Cylinders are the easiest shape of ice to harvest in the field, however, so we need to be able to handle it. The equation can be solved numerically in Matlab.

2.2.3.2 The units of ablation

Historically, workers reported the rate of phase change either as the rate of mass change, denoted $\dot{M}$ and having units of mass per time, or the recession rate, denoted R and having units of

distance per time. However, neither is tenable theoretically. Consider that

$$\dot{M} = \frac{\delta m}{\delta \tau} = \frac{\delta}{\delta \tau}(V\rho) \tag{2.10}$$

where τ denotes time. For a flat surface, as used in most of the previous experiments,

$$\delta V = A\delta r \tag{2.11}$$

where A is the surface area of the interface, so

$$\dot{M} = \frac{\delta}{\delta \tau}(Ar\rho) \tag{2.12}$$

Assuming that A and ρ are constant as the ice ablates, as in a vertical wall, this becomes

$$\frac{\delta m}{A\delta t} = \rho \frac{\delta r}{\delta t} \tag{2.13}$$

which we can then write in legacy notation as

$$\frac{\dot{M}}{A} = R\rho \tag{2.14}$$

Thermodynamically it is somewhat obvious that the total mass that changes phase is equal to the total flow of heat into the ice, Q, divided by the latent heat of fusion of the ice, L:

$$\delta m = \frac{Q}{L} \tag{2.15}$$

and of course the total flow of heat is the time integral of the heat flow rate, which is usually given as

$$\dot{Q} = hA\Delta T \tag{2.16}$$

where h is the heat transfer rate and ΔT is the temperature differential across which heat flows. Since I am looking for a relation in (S, T) and not just T, I replace the term $h\Delta T$ with some function $f(S, T)$, which has units of J m^{-2} s. Hence

$$\dot{Q} = Af \tag{2.17}$$

and the time integral is therefore

$$Q = \int \dot{Q} \mathrm{d}\tau = \int Af \, \mathrm{d}\tau = A \int f \mathrm{d}\tau \tag{2.18}$$

assuming that A is time-invariant. We can combine this with equation 2.15:

$$L\delta m = A \int f \mathrm{d}\tau \tag{2.19}$$

hence

$$\frac{\delta m}{A} = \frac{\int f \mathrm{d}\tau}{L} \tag{2.20}$$

We divide both sides by the time elapsed, $\delta\tau$:

$$\frac{\delta m}{A\delta\tau} = \frac{\int f \mathrm{d}\tau}{L\delta\tau} \tag{2.21}$$

If f is also time-invariant, this becomes

$$\frac{\delta m}{A\delta\tau} = \frac{f}{L} \tag{2.22}$$

Here, everything on the left side is a quantity we can measure, and on the right side we know L, so f is fully resolved. Therefore this equation tells us what we need from the experiment in order to calculate our quantity of interest. It also implies that the natural units of the rate of ablation are

neither mass per time nor distance per time, but mass per area per time. The same units are used in Gebhart and Wang's table 1 (1982, p.213), and was made explicit by Wells and Worster (2011) as we saw in Subsection 1.1.5 (p.27). Going back to equation 2.13, therefore, I calculated the ablation rate, $\mathcal{A}$, from the experimental data as

$$\mathcal{A} = \rho \frac{\delta r}{\delta \tau} = \frac{\rho}{\delta \tau} \left(\frac{3}{4\pi\rho} \right)^{1/3} \left({m_\alpha}^{1/3} - {m_\omega}^{1/3} \right) = \frac{\rho^{2/3}}{\delta \tau} \left(\frac{3}{4\pi} \right)^{1/3} \left({m_\alpha}^{1/3} - {m_\omega}^{1/3} \right) \tag{2.23}$$

or similarly for the cylinder tests. As noted above, the density is taken as the average of the imaging runs.

2.2.4 Fitting

The fitting procedure is illustrated in Figure 2.6. Panel A shows the data points scattered in $S - T$ space. The measured ablation rate $\mathcal{A}$ is a third dimension and is not depicted here. Fitting starts by excluding unreliable point categories. This includes 33 melts with $t < 7$°C and duration less than 10 minutes, which are questionable because of the non-linear melt behaviour in cold water, and 15 cold melts where a weight gain was recorded. The remaining data were separated into two sets, above and below 0°C. In the above-zero set, I selected those at the refrigerator range of temperatures, 274.5 K $< T <$ 276.0 K. This set, bounded by the box in panel B, was the densest and most comparable series; I call it the "Dryden" set. I fit a third-degree polynomial in (S, T) to this data, thus creating a low-temperature constraint line. I call this line, shown as a yellow line in panel C, the Dryden line.

I also determined the effective freezing point temperature by selecting the lowest temperatures recorded in the very cold points, where the water contained a lot of frazil[1] and the temperature was equilibrated between the water and the frazil. I fitted a straight line to these points and called it the

[1] Ice forms in the insulated cooler as a solid surface layer, while the solution becomes measurably supercooled. The cooler is then removed from the freezer, the ice layer is broken with a non-metallic utensil, and the whole cooler is shaken vigorously to mix. The necessary conditions for the formation of frazil, supercooling and turbulence, are therefore met, and the term is appropriate here.

Figure 2.6
Kenora fitting procedure.

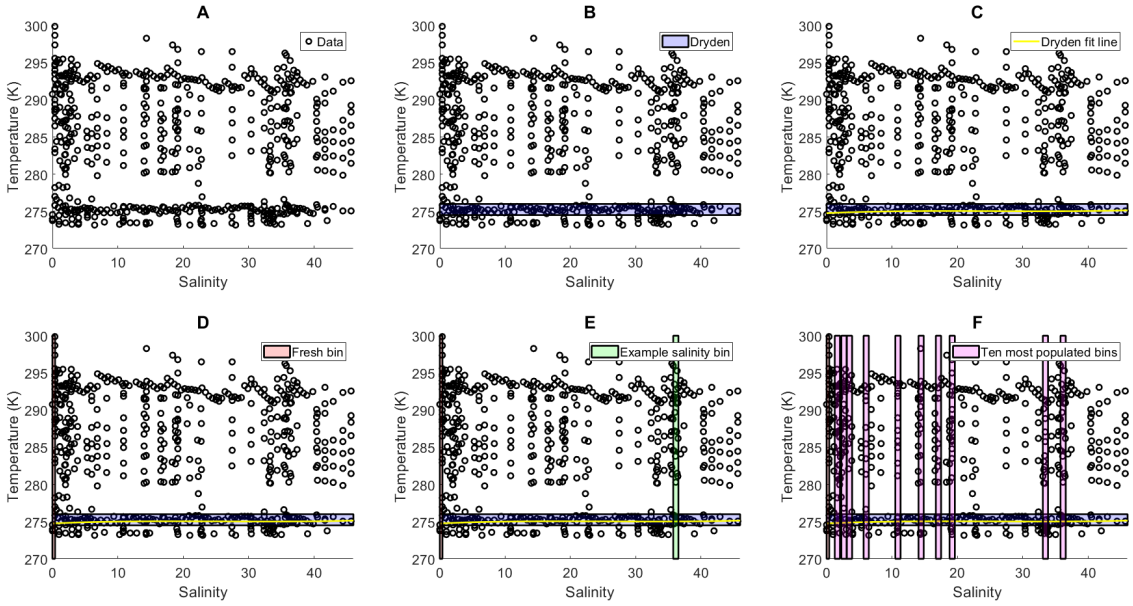

Note. The Kenora fitting procedure first separates the data into bins of approximately constant salinity and fits each bin as a quadratic of temperature, constrained to the best-controlled values at the refrigerator temperature (Dryden band) and the experimental freezing point temperature, then fits the sets of values so obtained for the quadratic coefficients as quadratics of salinity, constrained to the best-controlled values for freshwater. This figure is discussed in the text on p.76.

Vauban line[2]. Its equation is

$$T_{f0} = 273.54\ \mathrm{K} - 6.248\ \mathrm{K} \cdot \mathrm{kg} \cdot \mathrm{g}^{-1} \tag{2.24}$$

I then binned the data by salinity, starting with the "fresh" bin, shown in panel D, for salinities below 0.4. For higher salinities, I identified the most populated bins recursively using a sliding window of a given width, until it was not possible to make any more bins with three or more points. An example salinity bin is shown in panel E. This binning approach was the motivation for selecting certain bench salinities repeatedly during the data gathering rather than scattering them

[2]Vauban's fortifications were a system of defensive installations built in the seventeenth century to secure France's northeast border. The twelve surviving installations were included in the UNESCO World Heritage List in 2008 (UNESCO World Heritage Centre, n.d.). I used the name here because I was happy to have found something I could depend on.

Table 2.1
Performance of bin widths in Kenora fitting.

Bin width	Number of bins	Points not binned
0.1	46	215
0.2	42	180
0.3	38	159
0.4	34	163
0.5	29	178
0.6	37	102
0.7	35	91
0.8	37	62
0.9	36	60
1	32	82

Note. This table is discussed in the text on p.78.

randomly through the $S - T$ space, hence the pattern of vertical streaks in the scatter. Table 2.1 shows how well each bin width covers the data set, which shows that 0.8 and 0.9 are the most inclusive choices. I selected 0.8 arbitrarily out of the two to get one more bin. Panel F shows the top ten most populated bins.

Having thus binned the salinity data, for each bin of salinity S I fitted the recession to a quadratic of the water temperature T in K, using the Dryden and Vauban lines to constrain each such polynomial. For each salinity bin, therefore, I have an equation of the form

$$\mathcal{A}_S(T) \;=\; a_1\,T^2 \;+\; a_2\,T \;+ a_3 \tag{2.25}$$

I then took the set of values obtained for each coefficient a_i, and fitted it to a quadratic of the salinity, using the "fresh" bin as a constraint, so that

$$\hat{a}_i(S) \;=\; b_{i,1}\,S^2 \;+\; b_{i,2}\,S \;+\; b_{i,3} \tag{2.26}$$

The ablation is therefore modelled as a quadratic of temperature, each coefficient of which is a

quadratic of salinity. Put more simply,

$$\mathcal{A}(S,T) = \begin{bmatrix} T^2 & T & 1 \end{bmatrix} \begin{bmatrix} b_{11} & b_{12} & b_{13} \\ b_{21} & b_{22} & b_{23} \\ b_{31} & b_{32} & b_{33} \end{bmatrix} \begin{bmatrix} S^2 \\ S \\ 1 \end{bmatrix} \tag{2.27}$$

I call equations fitted with this method "Kenora equations". They provide very good fits to the data over specific temperature ranges, but I could not fit a single Kenora form equally well throughout the experimental domain; hence the division of the set into above- and below-zero domains. The below-zero set was constrained to the Vauban line only. I tried to connect the above- and below-zero fits with a cubic spline interpolation, but the results were not satisfactory. It later came to my attention that cold-water chemistry expert Dr. Feiyue Wang from our department, my committee member Dr. Tim Papakyriakou, and colleagues, have established the existence of a discontinuity at 0°C in the rate equations for other reactions in seawater (e.g. Bailey et al., 2018; Polcwiartek et al., 2025). The regime change in my observations is therefore also probably a property of the seawater solution and not an artifact of my data. This does bring into question the validity of using the Vauban line as a constraint for fitting the above-zero model, but since it works so well, I decided not to change the fitting procedure.

2.2.5 Pressure

Finally, keeping in mind the Euler relation (Steane, 2017, p.171) according to which

$$U = TE - pV + \mu N \tag{2.28}$$

that is to say, the internal energy of a system is equal to its temperature times entropy (normally denoted S, but in oceanography we use S for salinity), less its volume times pressure, plus the chemical potential of its components times the number of moles, I attempted to fit the residual in the model to high-resolution pressure data provided by an Environment Canada station about 900 m

from my experiment site. This however did not produce any improvement in the fit, and estimates of the effect size from enthalpy calculations suggest that it is much too small, over the range of naturally occurring atmospheric pressures at our site, to be detected by the Manitoba method. On the scale of an iceberg, however, pressure cannot be neglected, and further investigation is necessary. It is also possible that the rate of change in atmospheric pressure may have an effect. I therefore include the pressure only as error terms in my model.

2.2.6 Alternate model

In thermodynamics, enthalpy (H) is the potential used to study phase changes at constant pressure. It therefore stands to reason that we should be able to express the rate of phase change as a function of enthalpy, and indeed this turned out to be the case. The ablation rate can be fitted as a quadratic of enthalpy, and following a suggestion by committee member Dr. Tim Papakyriakou, I found that the residual of that model varies with salinity. As salinity is the main determinant of density, I fitted a quadratic model in enthalpy and density, thus connecting my work not only to principles of thermodynamics but also to some extent to the foregoing fluid dynamics work.

2.3 Results

2.3.1 The Agassiz salinity-temperature ($S-T$) model

As I mentioned in the introduction, the name "Agassiz" was selected for prehistorical reasons. Since I am using $\mathcal{A}$ for ablation, I denote the Agassiz model ablation $\hat{\mathcal{A}}_g$. The result has units of kg m^{-2} day^{-1}, as discussed in Subsection 2.2.3.2. The model's final form is shown in equations 2.29 and 2.30, and plotted as contours in $S-T$ space in Figures 2.7 and 2.8.

$$\gamma \cdot \hat{\mathcal{A}}_g(S,T,p) = \begin{bmatrix} T^2 & T & 1 \end{bmatrix} \mathbf{K} \begin{bmatrix} S^2 \\ S \\ 1 \end{bmatrix} + \epsilon_p + \epsilon_{dp} \tag{2.29}$$

Figure 2.7
The Agassiz model as contours in $S - T$ space.

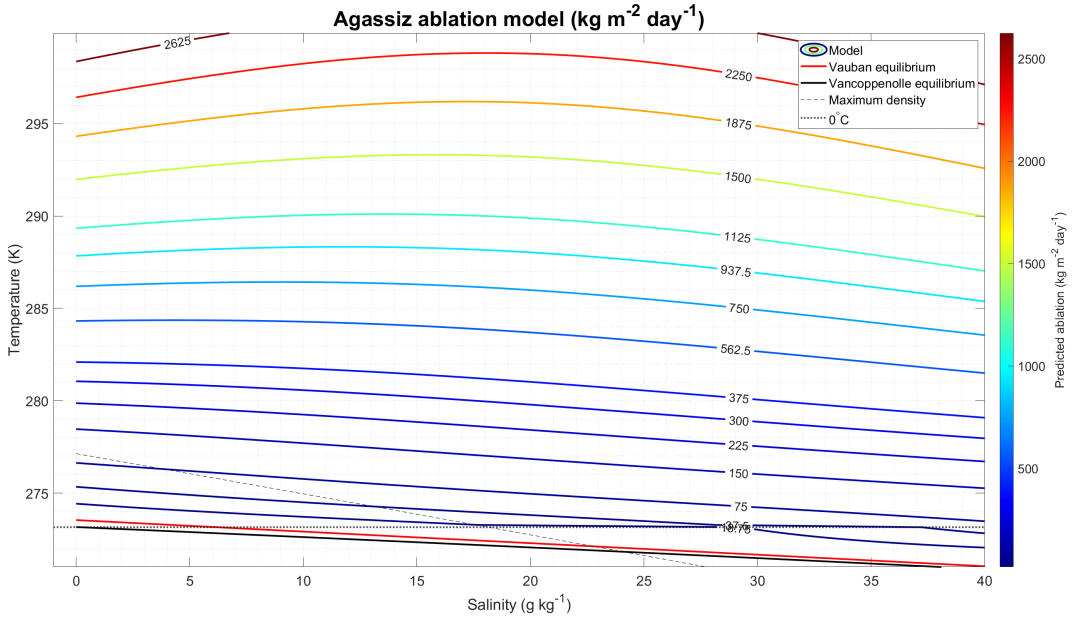

Note. The Vauban line is the experimental freezing point temperature. The Vancoppenolle line is the freezing point temperature determined computationally by Vancoppenolle et al. (2018). This figure is discussed in the text on p.80.

where ϵ_p and ϵ_{dp} are the hitherto undetermined contributions from pressure and pressure change, γ is the geometric correction factor, listed in Table 2.2, and

$$\mathbf{K} = \begin{cases} \begin{bmatrix} 4.58 \times 10^{-3} & -0.27 & 3.84 \\ -2.47 & 1.47 \times 10^{2} & -2.09 \times 10^{3} \\ 3.33 \times 10^{2} & -2.00 \times 10^{4} & 2.84 \times 10^{5} \end{bmatrix}, & t < 0°\text{C} \\ \begin{bmatrix} 2.69 \times 10^{-3} & -0.13 & 3.84 \\ -1.48 & 71.21 & -2.09 \times 10^{3} \\ 2.04 \times 10^{2} & -9.90 \times 10^{3} & 2.84 \times 10^{5} \end{bmatrix}, & \text{otherwise.} \end{cases} \tag{2.30}$$

Figure 2.8
The Agassiz model as contours in $S - T$ space for low temperatures.

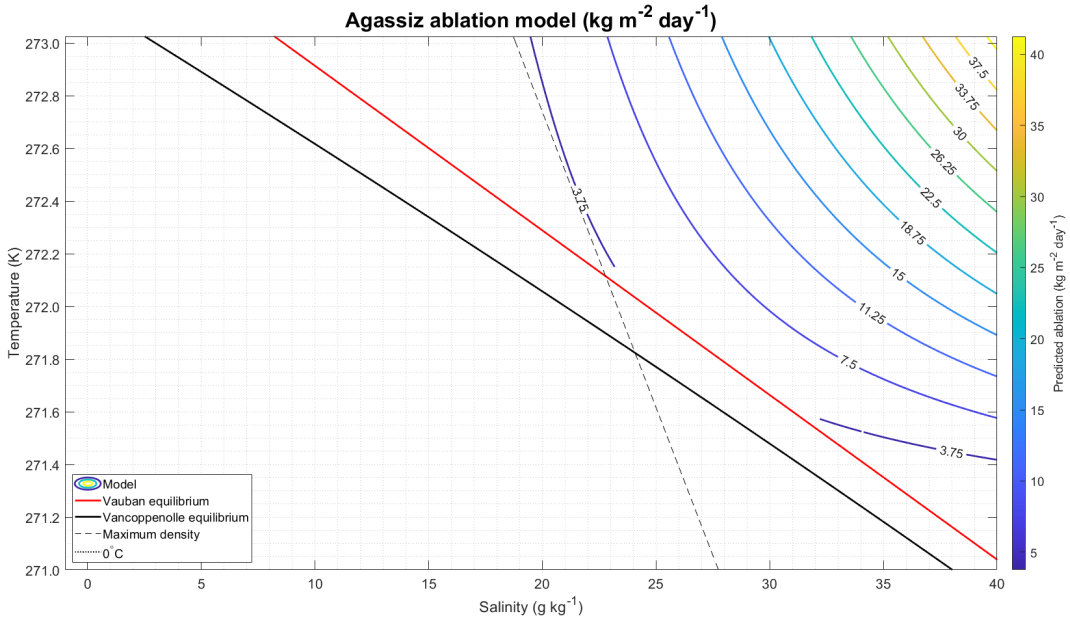

Note. The Vauban line is the experimental freezing point temperature. The Vancoppenolle line is the freezing point temperature determined computationally by Vancoppenolle et al. (2018). This figure is discussed in the text on p.80.

Notice that the third column of coefficients is the same in both matrices. This is because this column vector, taken by itself, describes the behaviour at $S = 0$, which is constrained to the same freshwater bin in both cases. Again this may be questionable given that the freshwater froze, in practice, somewhat above 0°C, and therefore the value used as a constraint in the fitting below zero is an unphysical extrapolation. Ideally, the below-zero part of the model should be constrained to a different salinity bin, for example $S = 42$, once sufficient data of good quality can be obtained there.

This model fits all data, including balls, cylinders, and legacy data, with $r^2 = 0.9848$. The variables S, T, and p, are listed here in the order in which they are entered in the TEOS-10 GSW Toolbox in Matlab (McDougall & Barker, 2011), which I used for most saltwater calculations. Since it is an empirical formula, and the coefficients are therefore regressed from data rather than derived, they do not have logical units.

Table 2.2
Geometric correction factors for Agassiz model.

Geometry (nominal)	Factor	Source
Vertical wall	0.90	Vanier and Tien, 1970
Sphere, 45 mm diameter	1	this study
Cylinder, 38 mm diameter × 42 mm high	1.13	this study

Note. This table is discussed in the text on p.80.

Table 2.3
Enthalpy model.

Term	Coefficient	Lower 95%	Upper 95%
H^2	1.23×10^{-7}	1.13×10^{-7}	1.33×10^{-7}
H	9.37×10^{-3}	8.44×10^{-3}	1.03×10^{-2}
1	14.41	− 0.59	29.41

Note. This table is discussed in the text on p.83.

2.3.2 Enthalpy-density ($H - \rho$) model

Where enthalpy can be calculated, using for example the Thermodynamic Equation of seawater (TEOS-10) instantiated in the Gibbs seawater (GSW) Oceanographic Toolbox (McDougall & Barker, 2011) in Matlab as I did, one can use instead a simple quadratic function of enthalpy. I fitted the model over the whole set using a built-in Matlab solver that returns 95% confidence intervals; the coefficients and 95% bounds are listed in Table 2.3. The complete data set includes $N = 1065$ points; the model fits the data over its entire domain with $R^2 = 0.9607$, and is plotted in Figure 2.9. The solid black line is the fit for all data, and the dotted line is for my data only, so they are very similar but the combined set gets closer to the measured values when enthalpy is negative. The boundary between the good fit and bad fit areas is clearly zero enthalpy, which corresponds to $t = 0$°C. Woods' (1992) dichotomy between melting and dissolving, and the energy minimum of Oborin (1967) and Schenk and Schenkels (1968), do not yield divisions of the data set that significantly improved the results. The marker colour shows salinity, so we can see with the naked eye that the residual must have a pronounced salinity dependence, and since the density of seawater depends mostly on salinity, I fitted the whole data set to a second-degree polynomial

Figure 2.9
Measured recession speed versus specific enthalpy for my data and legacy data, with quadratic model.

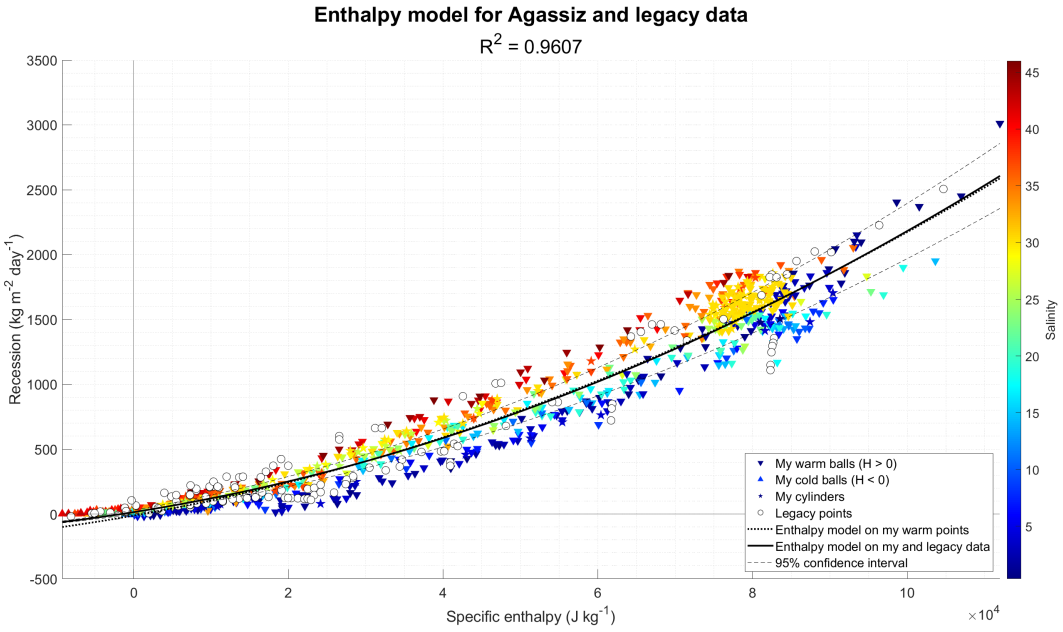

Note. Coloured triangles: my data. Coloured stars: my cylinders. White circles: legacy data. The colour gradient makes it obvious that the residual in the quadratic enthalpy model is driven by salinity. This figure is discussed in the text on p.83.

in (H, ρ), again using a built-in linear solver in Matlab. The coefficients and 95% bounds of the quad-quad model are listed in Table 2.4. This model fits the data with $R^2 = 0.9794$. Finally, the coefficients of determination and root mean squared error (RMSE) for the Agassiz, enthalpy, and quad-quad models are listed in Table 2.5, for the whole set and my cold points only. Clearly, over the whole experimental domain, the combined data is highly coherent, all three models are good predictors of the thermodynamic ablation rate, and Agassiz is the best one. For $t < 0$°C the Agassiz fit is not very good, and if the legacy data is included it decreases to $R^2 = 0.59$. The enthalpy and quad-quad models, which are fitted over the whole set rather than piecewise, are very poor in the cold range.

Table 2.4
Enthalpy-density model.

Term	Coefficient	Lower 95%	Upper 95%
H^2	1.31×10^{-7}	1.23×10^{-7}	1.40×10^{-7}
H	-0.14	-0.17	-0.12
$H\rho$	1.50×10^{-4}	1.28×10^{-4}	1.72×10^{-4}
ρ	-8.28×10^{2}	-9.95×10^{2}	-6.61×10^{2}
ρ^2	0.41	0.33	0.49
1	4.18×10^{5}	3.33×10^{5}	5.02×10^{5}

Note. This table is discussed in the text on p.83.

Table 2.5
Comparison of fitted models.

Model	All points		$t < 0$°C points	
	R^2	RMSE	R^2	RMSE
Agassiz	0.9848	84.39	0.7346	5.52
Enthalpy	0.9607	147.98	0.1198	28.00
Quad-quad	0.9794	109.20	0.2936	47.75

Note. This table is discussed in the text on p.84.

2.4 Discussion

2.4.1 Appropriateness of experimental method

The ball geometry was selected because it is the simplest. It has no edges, which would create differential melting, and no horizontal surfaces that would trap melt. And because the ball diameter is only 45 mm, it is much smaller than the distance required for turbulent flow to develop, which Josberger (1979) had found to be at least 20 cm.

The method of weighting the ice piece down with a fine net is superior to that of Vanier and Tien (1970) with the lead core for several reasons. One, it is much easier to mold. Two, the metal components would have introduced thermodynamic effects, one because of the presence of three metals (steel, lead, and nichrome) in a solution, and another because the nichrome wire would have conducted heat from the atmosphere at +25°C into the lead core, thus adding a heat source inside the ice. The hair net, on the other hand, normally made no impression on the ice surface, except in

a few cold melts where I retrieved the ball before it had lost a measurable amount of mass. In such cases there was occasionally a *raised* impression of the net on the ball. Although a thermodynamic explanation cannot be ruled out from what I observed, it is also possible that the net was still wet from an earlier run and it was that water remnant that froze onto the ball.

Third and most importantly, the method of Vanier and Tien (1970) introduces stress in the ice, and this changes the melt behaviour. Figure 2.10 illustrates this phenomenon. The colour gradients show the normal internal stresses calculated with the demo version of FEATool (Precise Simulation, 2025), a finite element analysis (FEA) utility in Matlab, in the horizontal direction in the left panel marked "x-stress", and in the vertical direction in the right panel marked "y-stress". Red indicates tensile stress, and blue indicates compressive stress. The inner circle is the lead core, and all the other outlines relate to the ice. Of course the lead core is drawn downward by gravity, while the ice is pushed upward by buoyancy. Where the bottom of the core touches the ice, there is therefore a zone of compression, as we would expect. The outer solid black circle in both panels is the original shape of the ice ball drawn by Vanier and Tien in their figure 3 (1970, p.78), which I traced using Matlab's image processing toolbox and scaled to overlay the stress diagram. Vanier and Tien show two other outlines, one being an ellipse fit to the remnant of the ball after some amount of time, and one being a concavity that consistently formed in the bottom of their ice balls. I traced both with ellipses which are likewise scaled and overlain on the stress plots. In each panel one of the ellipses is in bold dashes and the other is in light dots. In the x-stress panel, therefore, we can see that the concavity in the bottom of the ice, shown by the bold dashes, coincides with the highest tensile normal x-stresses. In the y-stress panel, on the other hand, the areas of greater ablation in the iceball coincide with both high normal tensile and high normal compressive y-stresses, whereas the "sides" of the ball, where the tangent surface is vertical, show little to no ablation. This melt pattern matches exactly my observations, except that I never had a concavity in the bottom, whereas they always did. The difference therefore has to be introduced by the different weighting methods. If it was due to thermodynamic effects it would be self-correcting as melt would be trapped in the concavity and isolate it from the solution; there is also no plausible

Figure 2.10
Differential stress and differential ablation in the experiment of Vanier and Tien (1970) using lead-core ice balls suspended in saltwater.

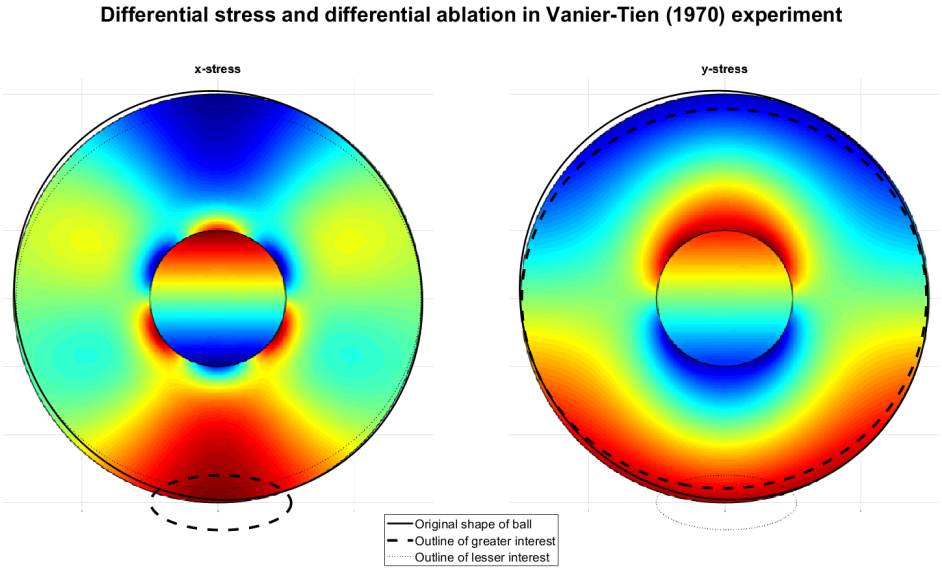

Note. The inner circle is the lead core. The remaining lines are traced from the original published figured and overlain on the stress diagram produced by FEATool. Red indicates tensile stress, blue indicates compressive stress. x-stress (in the horizontal direction) ranges from -3.2 (blue) to +3.2 (red). y-stress (in the vertical direction) ranges from -10.5 (blue) to +10.5 (red). This figure is discussed in the text on p.86.

reason for a thermodynamic anomaly to form in the solution at that spot. I conclude from this that stress is highly relevant to the melting of ice, but given the differences between the two panels, it looks like differential tensile stress has a much greater effect than any other pattern. Differential stress is known to increase the rate of melt reactions in rock (Wheeler, 2014), and ice is particularly weak in tension (Petrovic, 2003); the melt pattern is coherent with these facts. More research is clearly needed on this point.

2.4.2 Sources of error in the experiment

The molded balls were more or less strictly spherical with a clustered and generally excentric distribution of air bubbles, an example of which is visible in Figure 2.1. The spherical shape was essentially but not strictly maintained even with extensive recession. No attempt was made to control or quantify any of these variations. Since they clearly have no relation to the temperature

or salinity of the solution, there cannot be any covariance, and therefore the errors in geometry are random noise and do not affect the results in a systematic way.

The assumption that the ice surface recedes at a constant speed was tested in several ways, as we saw above. Except for short melts in cold water, the change in radius was found to fit a first-degree function of time elapsed with $R^2 > 0.95$, and a third-degree function improved the coefficient of determination by only 1% on average. This was true whether the radius was measured directly or calculated from the mass. Significant deviations from linearity occurred only at the beginning of melts in water colder than approximately 10°C, in which case there was some mass gain before the onset of mass loss. The time elapsed from the start of the experiment until the test piece returned to its starting radius was approximated by a linear function of temperature which could be used to correct the melt times; but for greater certainty, short melts at low temperatures were excluded.

The most intractable source of error is the measurement of salinity. The solution of Instant Ocean and tap water, which is commonly used as a substitute for seawater in experiments due to its low cost and accessibility, is known to undergo a reaction in which the calcium in the tap water reacts with the salt to produce gaseous CO_2 and a solid $CaCO_3$ precipitate (Tison et al., 2002). Some of the ions in the tap water also precipitated out during freezing, and the accumulation of this product in the experimental solution over repeated melts caused increasing turbidity. These reactions change the relation between conductivity and absolute salinity, so it was never entirely clear how my experimental salinity compares to actual seawater of the same nominal salinity in terms of chemical potential. Also, whenever salt is added to the solution, there is a period of evolution of the salinity and temperature as the hydration reaction proceeds. I made at least three measurements with the conductivity probe before every run, because it takes a little time to stabilize, and I thought at the time that this was sufficient, but much later it came to my attention that the reaction is much longer-lived than the time between my measurements, and therefore it is not impossible that there was a drift in salinity over the course of the longer melts if the experiment started too soon after salt was added. Given the good agreement between my results and legacy

data, however, I doubt that this made much of a difference. The legacy experiments also used a variety of solutions, including seawater from different locations, tap water with table salt, and distilled water with standard sea salt. The legacy measurement techniques were likewise variable, including then-current technology from 1879 to 2015. Yet, all laboratory results using the Atlantic, Pacific, and Manitoba methods are consistent with each other. The diversity of methods may in fact be a strength of the combined data set in that the average bias will be less pronounced than the effect in each single experiment.

2.4.3 Sources of error in the fitting method

The Kenora fitting method could be open to argument because it is not a standard procedure. The need for it arises partly from the uneven distribution of data points in salinity-temperature space, and more importantly from the need to isolate the salinity effect from the stronger temperature effect. Historically, workers have focused heavily on either freshwater or ocean-salinity water, and almost no data was available in the middle. A linear solver would therefore fit the two ends of the salinity domain well and largely neglect the middle. The binning method I devised ensures that salinity is nearly equally weighted throughout its domain. The temperature could be deprioritized because it is much easier to vary and its effect on the ablation rate is well documented and monotonic above the temperature of maximum density of the solution. So while the Kenora method obviously does not weigh all points equally, this is a strength of the design and not a weakness. As we saw in Table 2.1, a lot of points were excluded from the fitting; yet Table 2.5 shows that Agassiz is more successful than the standard linear solvers. Thus the fitting method is clearly appropriate to the data. The downside is of course the lack of a method to evaluate a confidence interval.

2.4.4 Error estimate

To get an idea of the magnitude of the uncertainty in the model coefficients, I devised a brute-force method inspired by the split-half reliability test in psychometrics. The proper way to do this test is to split answers on a psychometric instrument arbitrarily into two halves and calculate the correlation between participants' scores on one half versus the other (Kuder & Richardson, 1937).

Table 2.6
Means and standard deviations of split-half fit coefficients.

Term	All points			$t < 0$ points		
	μ	σ	σ/μ	μ	σ	σ/μ
1	3.80×10^{2}	21.22	0.06	3.31	4.72	1.42
T	-2.79	0.15	-0.05	-1.54×10^{-2}	4.76×10^{-2}	-3.09
T^2	5.11×10^{-3}	2.66×10^{-4}	0.05	1.17×10^{-5}	2.06×10^{-4}	17.55
S	-27.17	2.82	-0.10	59.59	82.48	1.38
ST	0.19	2.01×10^{-2}	0.10	-0.44	0.61	-1.39
ST^2	-3.46×10^{-4}	3.57×10^{-5}	-0.10	8.10×10^{-4}	1.13×10^{-3}	1.39
S^2	0.66	7.91×10^{-2}	0.12	-1.45	2.56	-1.77
S^2T	-4.76×10^{-3}	5.64×10^{-4}	-0.12	1.07×10^{-2}	1.89×10^{-2}	1.77
S^2T^2	8.53×10^{-6}	1.01×10^{-6}	0.12	-1.96×10^{-5}	3.48×10^{-5}	-1.78

Note. This table is discussed in the text on p.89.

The correlation step is necessary because the test measures the internal validity of the instrument. In my case I just need to see if the error is normally distributed so I did something much simpler, which is to draw half the data points at random and use a linear solver to produce a second degree polynomial model. This procedure is computationally very fast so I repeated it 10^6 times and recorded the coefficients, R^2, and RMSE for each trial. Figure 2.11 shows histograms of the nine model coefficients and the goodness of fit. The coefficients are also tabulated in Table 2.6, from which we can see that the standard deviation is generally of the order of 1/10 of the mean, and the RMSE is normally distributed. An error margin of approximately 10% is therefore probably realistic for the warm part of the Agassiz model. As we saw earlier from Roddick (1981), the univariate sampling distribution of the error will approach normal if the number of observations "approaches" infinity, and for four variables or more the number of observations needed is much smaller. Though some improvement is still possible, I have enough observations to be currently quite close to a normal error distribution.

I repeated the procedure for the cold points; the histograms are shown in Figure 2.12 and the numbers are tabulated in Table 2.6. In this case the ratio of σ to μ is of the order of 1.5 in most cases but nearly 20 on the coefficient of T^2. R^2 decreases from 0.99 to 0.81 and the RMSE is no

Figure 2.11
Histogram of coefficients and goodness of fit for split-half test on full data set.

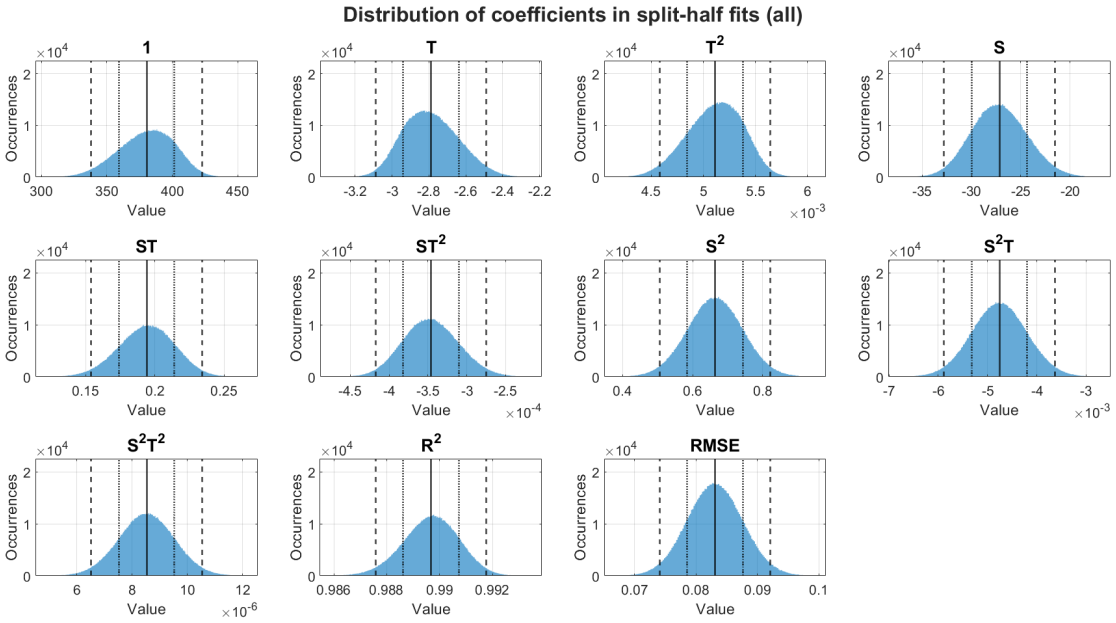

Note. In the absence of a standard method of error analysis for the Kenora fitting method, half the data was selected at random and fitted to a second-order linear function of (S, T). This procedure was repeated 10^6 times. The resulting RMSE is normally distributed. Solid black line: mean (μ); dotted black line: standard deviation (σ); dashed black line: 95% interval (2σ). This figure is discussed in the text on p.89.

longer normally distributed, showing that the error is still dependent on which points are selected. More data points are clearly needed to constrain the low-temperature model better.

2.4.5 Performance of model

To further validate my model, I applied it to the legacy data I had collected from the literature, which is shown in Figure 1.9 (p.51) and includes results from Steenstrup (1883), Hammer (1883), Jack (no date, cited in Loewe, 1961), Yen (1968), Bendell and Gebhart (1976), Robe et al. (1977), Johnson (1978), Carey (1981), Gebhart and Wang (1982), Sammakia and Gebhart (1983), Johnson and Mollendorf (1984), Josberger (1979), and Kerr and McConnochie (2015). This legacy set contains 178 points, of which 133 were obtained by laboratory methods consistent with mine. A histogram of the relative error when applying the Agassiz model to my data and the legacy set is shown in Figure 2.13. Recall that the relative error is the residual over the actual value. This

Figure 2.12
Histogram of coefficients and goodness of fit for split-half test on below-zero data only.

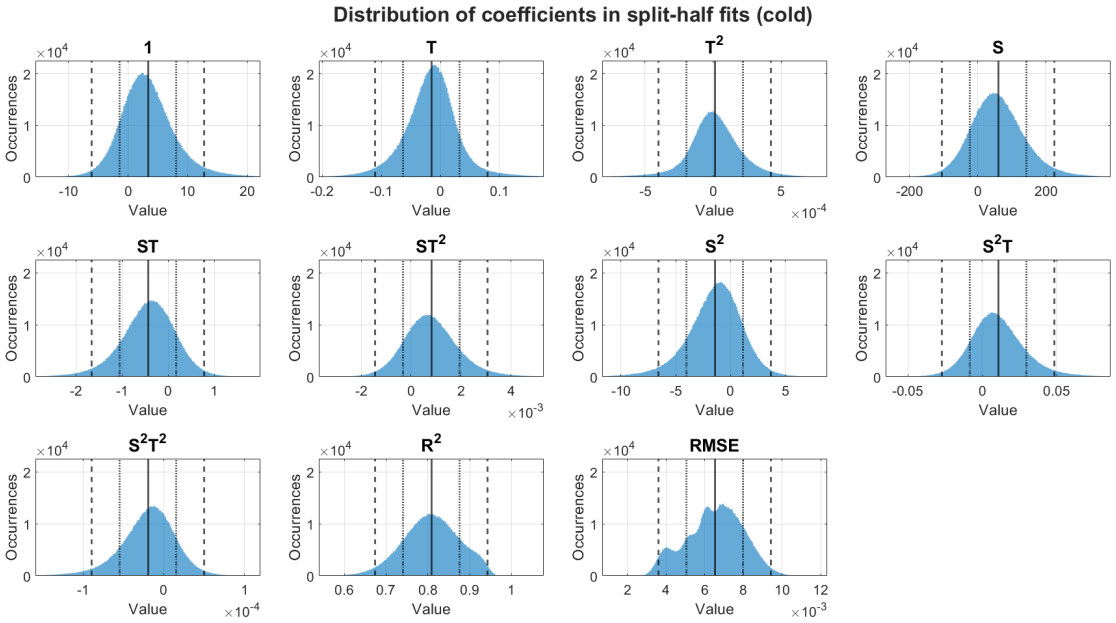

Note. When applied to the below-zero points only, the split-half procedure does not produce a normal error distribution, so more data is needed. Solid black line: mean (μ); dotted black line: standard deviation (σ); dashed black line: 95% interval (2σ). This figure is discussed in the text on p.89.

measure is more useful than the residual itself since the magnitude of the recession varies so much over the experimental domain. However, the relative error goes to infinity when the measured recession goes to zero, as a result of which 6 of my data points had to be excluded as outliers. No legacy points were excluded. A two-sample t-test between the new and legacy data gave a p-value of 0.99, that is, the probability that both error samples are drawn from the same error distribution is 99%.

The success of the Agassiz model on the comparable legacy sets is plotted in Figure 2.14. The measured recession is on the abscissa, the modelled recession is on the ordinate, and the black line is where the two are equal. A straight-line fit between the two gives $r^2 = 0.9695$.

A more detailed synthesis of the results is shown in Figure 2.15. In this graph, salinity is on the abscissa and temperature is on the ordinate. The size and color of the bubbles represent the measured rate of ablation. The circle around each bubble represents the Agassiz model value; a

Figure 2.13
Histogram of error in Agassiz model applied to my data (in blue) and legacy data (in red).

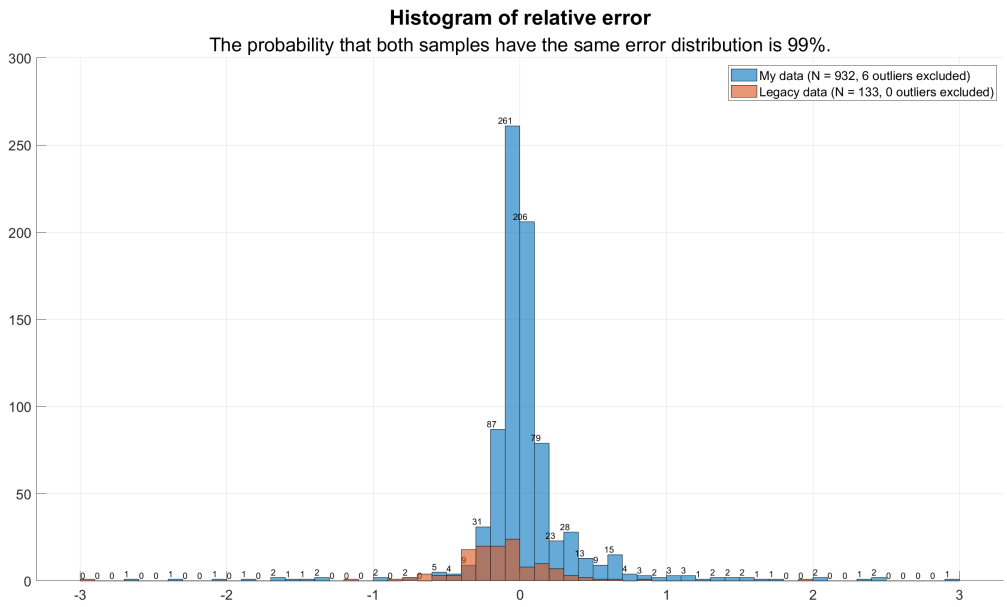

Note. The legacy error distribution is slightly skewed compared to normal. The error distribution in my data is narrow because points near zero recession produce very large relative errors. A two-sample t-test shows that the probably that both samples are drawn from the same error distribution is 99%. This figure is discussed in the text on p.91.

black circle indicates my data, and red is legacy data. The Vancoppenolle (theoretical) and Vauban (measured) freezing point temperatures are indicated, as well as the temperature of maximum density calculated from the GSW Toolbox, and the freezing point temperature of freshwater at 0°C. Perhaps the most striking observation from this diagram is how clustered the legacy data was. As I mentioned, earlier workers focused on freshwater and ocean salinity, leaving the middle empty, and this was probably the main reason why a thermodynamic rate was not obtained sooner. We can also see legacy points clustered around the temperature of maximum density. This range was interesting for reasons of fluid dynamics, but is the most aberrant behaviour of water, and therefore somewhat unhelpful in arriving at a general model. My investigation went perhaps unnecessarily far into the high salinity range. I was aiming for 42, which is the upper limit of correlations on which the TEOS-10 equation is built, but because I only had the bench salinity measure in real time and the actual salinity was calculated later during batch processing of the data, I was further along

Figure 2.14
Performance of the Agassiz model on legacy data obtained by comparable methods.

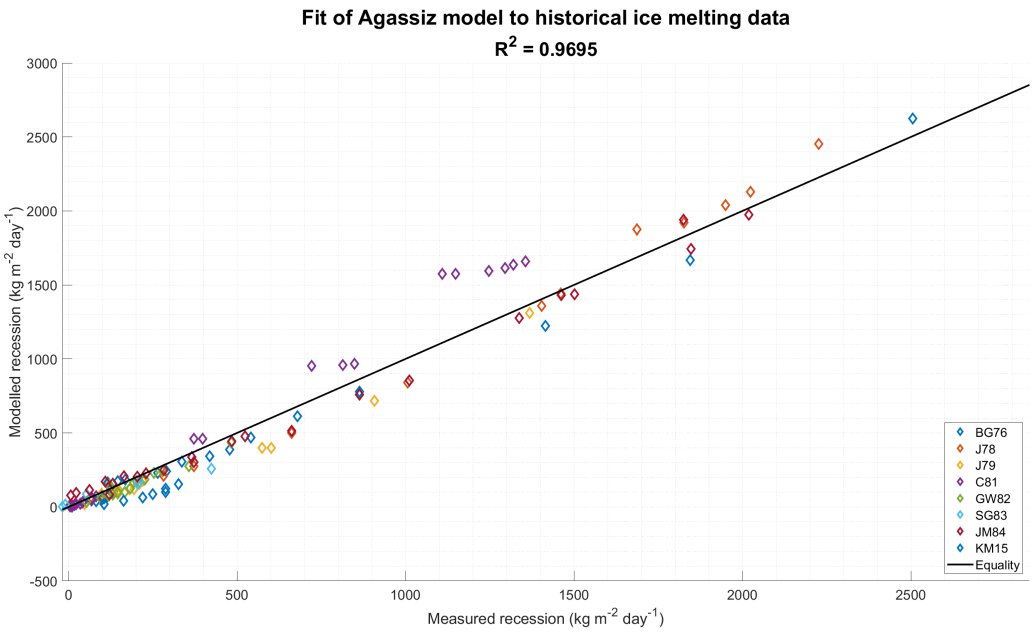

Note. When the Agassiz model, including the geometric correction factor, is applied to the legacy data, a straight-line fit between the measured and modelled recessions gives $r^2 = 0.9695$. This figure is discussed in the text on p.92.

than I expected. For the very cold data, which I gathered last, I stopped at 42.

A similar bubble visualization is applied to the relative error only in Figure 2.16. A particularly interesting observation in this graph is that at low salinities, the model understates recession below the temperature of maximum density and overstates it above. This is consistent with the observations of Gebhart and Wang (1982) and the conclusions of Oborin (1967) and Schenk and Schenkels (1968), and it may be desirable to develop a correction term for this phenomenon, as this part of the domain may be applicable to parts of the Baltic and to river estuaries.

Predictably, the smallest measured recessions have the largest errors. This is unfortunate because of course that is exactly the range where we wanted information for our iceberg problem. Nothing I attempted in partitioning the data or using different model forms and fitting methods was able to fit my very cold points better than $R^2 = 0.81$ and I have to conclude that there is no way to improve it except by collecting more data. Now that we have an effective measurement method,

Figure 2.15
Coverage and goodness of fit of experimental data.

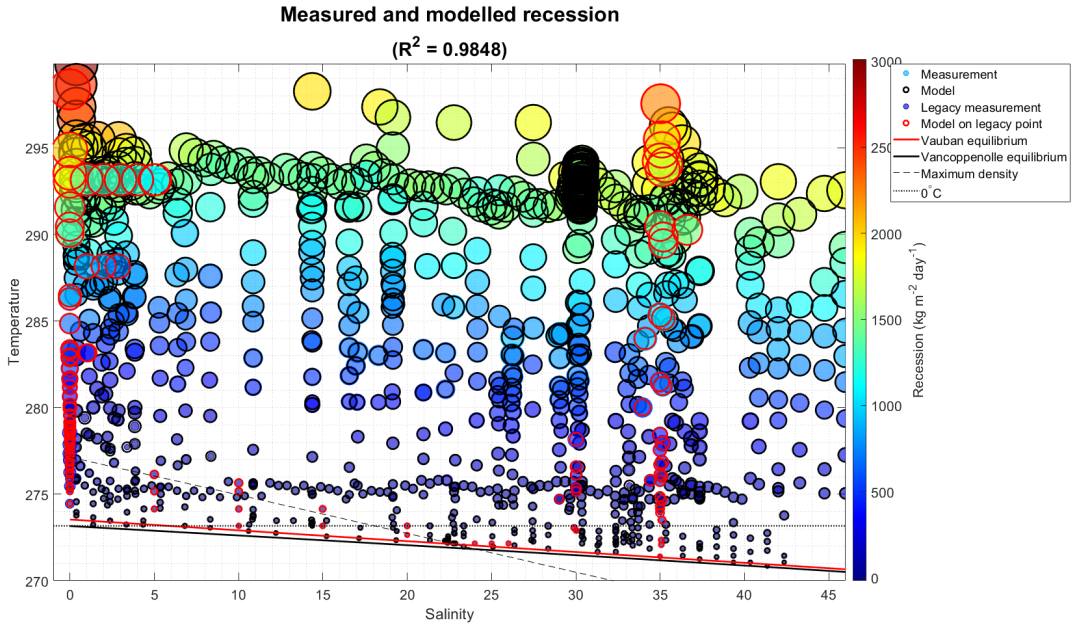

Note. The color and size of the bubbles represents the measured recession; the size of the circles represents the Agassiz model. This figure, discussed in the text on p.92, is the most concise visual summary of the success of the Agassiz model.

this could be easily done in the field with oceanic salinity.

Finally, Figure 2.17 shows the modelled recession by temperature and by salinity. The discontinuity between the two temperature regimes is clearly visible in the lines of equal salinity. The lines of equal temperature show the non-monotonic dependence on salinity that was found by Yang et al. (2023) using a CFD simulation, as we saw earlier. The shape of the equal-temperature curves is similar to that of the Gibbs energy function, the thermodynamic potential that is minimized when a system reaches chemical equilibrium at constant pressure.

Of course this result does not invalidate the legacy work which was based on the density of the solution, ρ_f. Since both $\mathcal{A}$ and ρ_f are functions of $(S,\ T,\ p)$, a transformation could exist from ρ_f to $\mathcal{A}$ such that $\mathcal{A} = \mathcal{A}(\rho_f)$. As Gebhart and Pera (1971) showed, however, this is complicated, and may not in fact be entirely possible given that $\rho_f(S,\ T,\ p)$ is not one-to-one. Likewise the

Figure 2.16
Distribution of relative error.

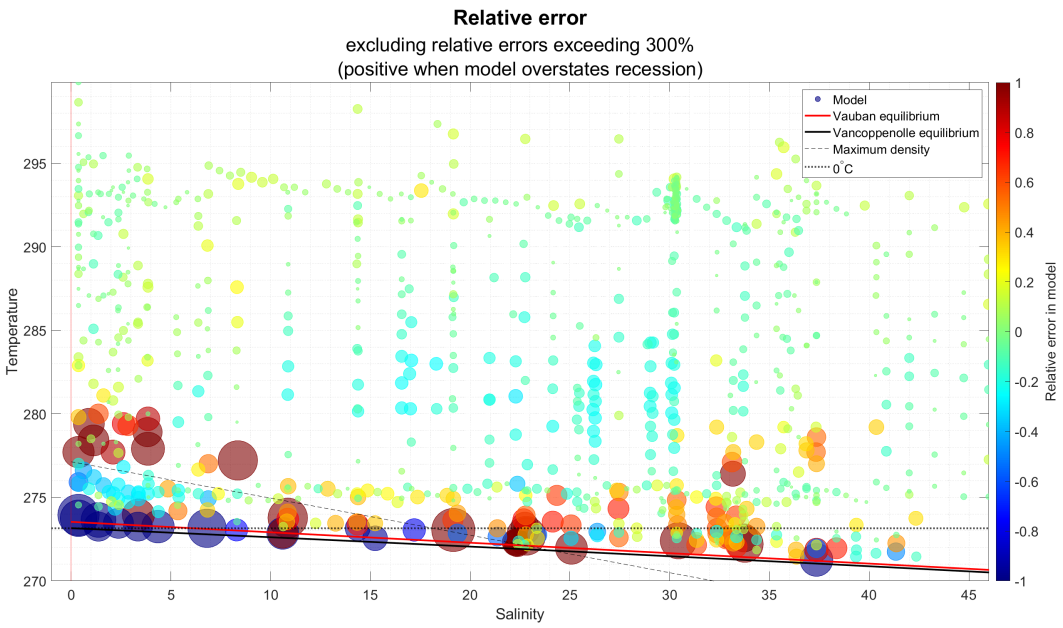

Note. Large relative errors are clustered at below-zero temperatures, where the method needs improvement, and around the temperature of maximum density in low salinity, where the density anomaly of water is known to affect results. These concentrations of error are therefore expected. This figure is discussed in the text on p.94.

enthalpy $H = H(S, T, p)$ so

$$\mathcal{A} = \mathcal{A}(H, \rho, p) = \mathcal{A}(H(S, T, p), \rho(S, T, p), p) = \mathcal{A}(S, T, p) \tag{2.31}$$

Thus my model is simply a much easier way to arrive at a computational formula for the same relation that others derived much more elegantly.

Clearly, my model is coherent with the legacy data as well as my own, despite the fact that the legacy data comes from two different experimental designs both involving a tall vertical ice wall, with a variety of chemistries, instrumentations, and ice manufacturing processes. A strictly thermodynamic model explains better than 98.5% of the ablation rate of ice in water of varying temperature and salinity, and the contribution from fluid dynamics *at the laboratory scale* is negligible. Besides providing an easy and comprehensive computational formula, the greatest

Figure 2.17
Modelled recession as lines of equal salinity versus temperature (left) or equal temperature versus salinity (right).

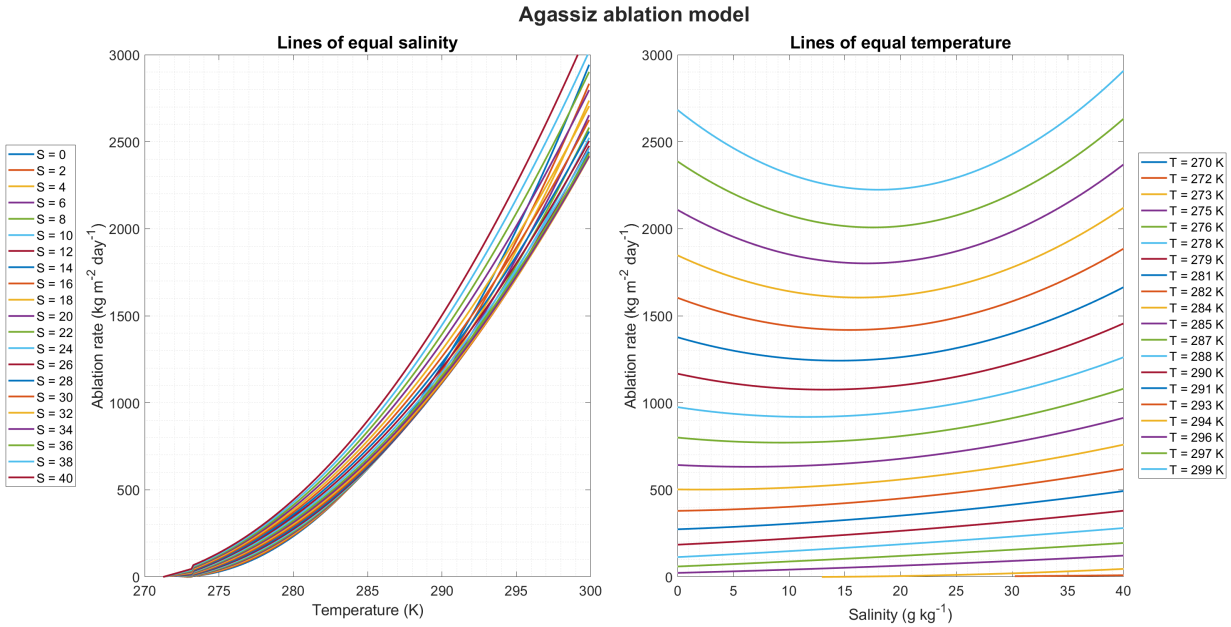

Note. Visualizing the Agassiz model as lines of equal salinity, on the left, makes the discontinuity at 0°C obvious. As lines of equal temperature, on the right, it is similar to the shape of the Gibbs energy function that can be plotted from the GSW Toolbox. This figure is discussed in the text on p.95.

advantages of my model are first, that it uses the variables that are measured directly in the field, second, that it is computationally cheap, and third, that the experiment can be done in the field with a bucket, a pocket scale, and a watch. The main difficulty would be to obtain ice balls, but experiments with cylinders with a diameter of 45 mm, such as can be obtained with a hole saw, show that this geometry is equally applicable, though mathematically less convenient. The enthalpy correlation is also useful in providing a correspondence between the rate of phase change and thermodynamic potentials, which had so far been elusive.

2.5 Conclusion

The original brief of this thesis was to determine experimentally a rate of ablation for vertical ice walls as a function of temperature and salinity. This turned out to be more easily achieved with a fast low-fidelity experiment than the large, well-controlled, slow methods used previously. Using

the Manitoba setup with small balls and cylinders of ice, I was able to collect a large number of points throughout the relevant salinity-temperature space so that the shape of the relation could be seen over the whole domain and hard-to-control sources of error were smoothed out statistically. Integrating as much legacy data as possible contributed to this statistical power and showed that the model is resistant to different geometries of the ice and the water, different molding techniques, different chemistries, and different instrumentations, so it is certainly a property of the phenomenon being investigated and not an artifact of the investigation method.

At the same time, my experiment allowed me to detect several variables that should also be accounted for, including differential stress and momentum transfer from the solution to the ice. The effects of water pressure at depth and of iceberg bubbles could not be reproduced with the available resources, but with the experience accrued here I have been able to design an apparatus for use in the field for future investigations. More controversially, I became convinced that rapid changes in atmospheric pressure can have a measurable effect on the ablation of ice, which currently seems to have no support other than my own opinion, but if it exists I can find a way to measure it. I also hope that more researchers will use the Manitoba method and communicate results that I can add to the data set. Thanks to the success of this experiment, we are now in a better position to study the many factors other than temperature and salinity that affect the rate of mass loss from iceberg keels.

Chapter 3

Application to a model iceberg

3.1 Introduction

Now that we have a thermodynamic rate of melting of ice in saltwater, we need a numerical iceberg to apply it to. We saw previously that the natural units of ablation are kg m^{-2} day^{-1} because the density of the ice being melted affects the melt rate. Therefore, to estimate the melt rate of an iceberg, we need an estimate of its density, and since density varies with depth in glaciers, this estimate has to be a function of depth, $\rho(z)$, rather than a scalar. An additional complication, compared to an ice cube from the freezer, is that the bubbles are pressurized, and this pressure also varies with depth, so we need a profile of bubble pressure as a function of depth, $p(z)$. Finally, we need to quantify the additional ablation due to the bubbles in glacier ice. This last step is incomplete partly because there is essentially no data to work with at this time, and remains for future work, but for the rest I have developed a model that outperforms some commonly used ones in the literature based on data from specific locations shown on the map in Figure 3.1.

3.2 A glacier density profile

3.2.1 The Herron-Langway densification model for snow and firn layers

Icebergs are masses of ice that break off the terminus of a glacier that ends in a body of water. At the time of calving, therefore, their density and temperature profiles are those of the parent glacier. To a first approximation, a young iceberg can therefore be modelled by taking a section of a model of a glacier. A glacier forms over geological time from the progressive compression of the snow pack that accumulates on its surface. Fresh snow is full of air and permeable to air. As it compresses, the snow gradually changes into something called *firn*. Originally defined as "wetted snow that has survived one summer without being transformed to ice," this term now refers to snow that has been modified, without a specific criterion of how and how much (Cuffey & Paterson, 2010, p.11). Accordingly, there is no clearly defined density cut-off between snow and firn. One definite fact about firn, however, is that it is still porous. As compaction continues, the air spaces ultimately become closed off from each other. This transition occurs at approximately 830 kg m^{-3};

Figure 3.1
Locations of data used in model.

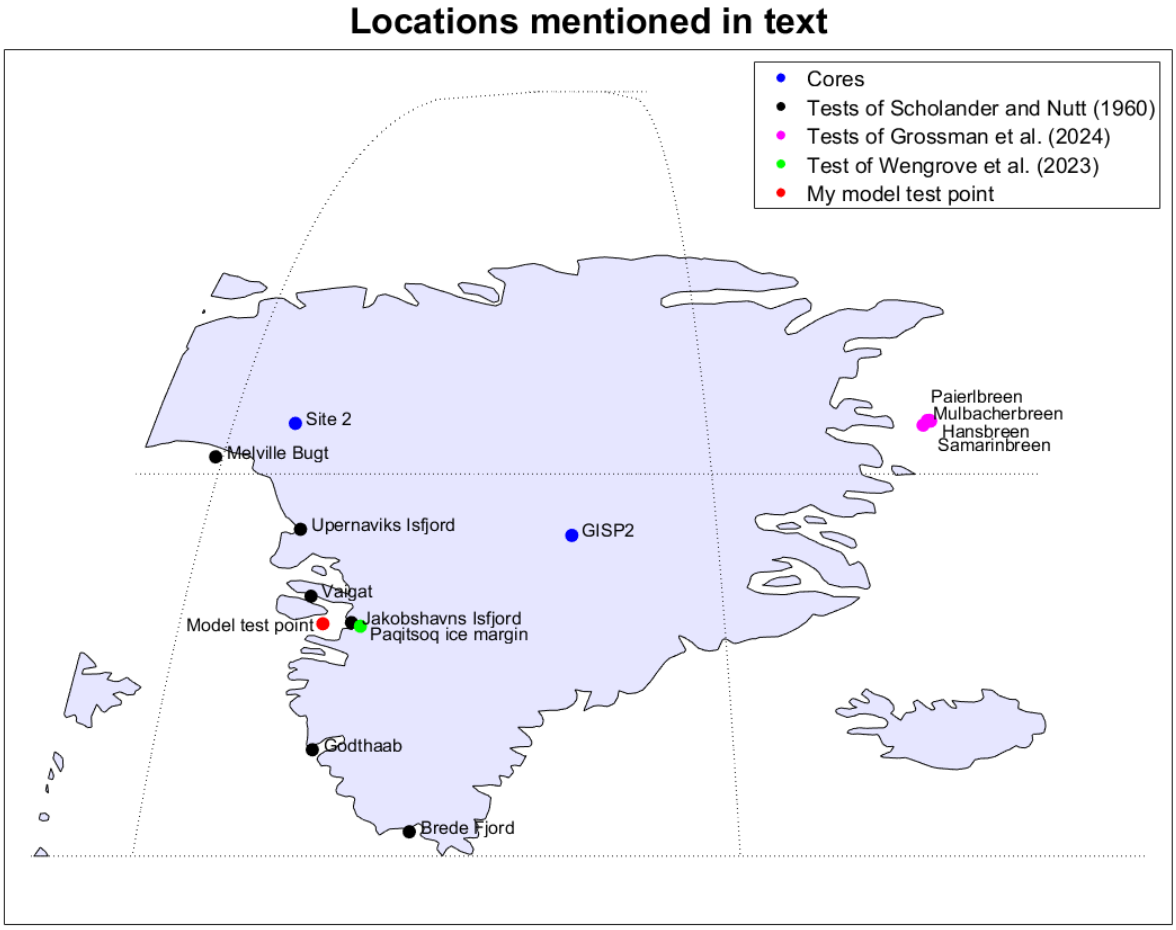

from then on the material is called *ice* and is impermeable. The air in the pores at the point of closure is now trapped and becomes more and more compressed as the ice continues to compact and squeezes the bubbles (Herron & Langway, 1980).

Herron and Langway (1980) produced a mathematical model of the densification of snow and firn that successfully reproduced data from Greenland and Antarctic glaciers. Thirty years later, Cuffey and Paterson (2010, p.24) still found this model to be the most succesful one and it is the one I will be using. Herron and Langway assumed the relation between snow density and depth is invariant with time, and neglected the dependence of the density of ice on temperature and pressure, which would be small at the range of densities involved. They then assumed that the rate

of densification depends on the temperature and the rate of accumulation of snow on the surface, and that the relation has the form of an Arrhenius equation:

$$k \;=\; A\, e^{-E_a/RT} \tag{3.1}$$

where k is the reaction rate constant, A is the Arrhenius, or "pre-exponential", factor, E_a is the molar activation energy for the reaction in question, $R \;=\; 8.314$ J K^{-1} mol^{-1} is the universal gas constant, and T is the absolute temperature. They defined two layers, $n \;=\; 0$ for snow and $n \;=\; 1$ for firn, and described the density profile as

$$\begin{cases} \rho(z) &= \frac{\rho_\omega Z_n}{1 + Z_n} \\ Z_n &= \exp\left(\frac{\rho_\omega k_n (z \;- z_n)}{\mathcal{A}_c^{(n\;-\;1)/2}} \;+\; \ln \frac{\rho_n}{\rho_\omega - \rho_n} \right) \end{cases} \tag{3.2}$$

where z_n is the height of the top of layer n;

ρ_n is the density at the top of layer n;

ρ_ω is the final density of the ice, taken to be 917 kg m^{-3} in their calculations;

k_n is a reaction rate coefficient obtained empirically from Arrhenius plots[1] of the densification process for layer n; and

$\mathcal{A}_c$ is the accumulation rate for the given accumulation site. The values of the inputs are shown in Table 3.1, which also shows the extension of the layer paradigm to the rest of the glacier. The expressions for k in snow and firn are those of Herron and Langway; in ice there is no k coefficient because I am not using an Arrhenius equation. The densities are those assumed for the boundaries between layers, and the question marks denote the values we are trying to determine, namely, the depth of the boundaries. The initial density of the snow pack, ρ_0, has to be assumed.

[1] An Arrhenius plot is the representation of an Arrhenius equation, which describes the dependence of the reaction rate k on temperature T in K, by plotting $\ln(k)$ against $1/T$.

Table 3.1
The four-layer paradigm for the densification model.

Symbol	Snow	Firn	Ice	Ductile ice
n	0	1	2	3
z_n (m)	0	?	?	?
ρ_n (kg m^{-3})	?	550	830	920.5
k_n	11 $e^{-10160/RT}$	575 $e^{-21400/RT}$	n/a	n/a

Note. This table is discussed in the text on p.101.

3.2.2 The ice layer

3.2.2.1 A power-law model from the literature

Herron and Langway's (1980) model only addresses the snow and firn layers. A simple model of the ice layer is given by Shumskiy (1960) as

$$z = a\,\rho^n + c \tag{3.3}$$

where z is the vertical coordinate, positive down;
c is the depth of "the snow or firn layer that would have to lie over the existing surface for densification to occur under the given process from zero to the initial density observed at the surface";
and a and n are arbitrary coefficients of the model, unrelated to the way these symbols were defined above for the Herron-Langway model.

Shumskiy's coefficients are not intrinsically known or derivable from first principles, nor can they be expected to be constant throughout a glacier. Making this equation work also requires expressing density as a unitless number between 0 and 1. Given three or more data points for a given glacier, one could solve for the three coefficients, but the equation would not be generalizable to other glaciers. Worse, a power law is not bounded, so the modelled glacier density can increase to arbitrarily large values at sufficient depth. Power functions are common in the literature because they are the easiest solution to many boundary value problems, but they are not necessarily good

Table 3.2
Value pairs for the logistic densification model.

Source	Subscript	z (m)	ρ (kg m^{-3})
At the surface	α	0	?
At the snow-firn transition	β	z_1	550
At the pore closure depth	ι	z_2	830
At the ice density limit	ω	∞	920.5

Note. This table is discussed in the text on p.103.

representations of physics except at the constraints. Shumskiy's model does not work for my purpose, so I had to make my own.

3.2.2.2 Derivation of a logistic model

To properly approximate the shape of a glacier's density profile, we want a function that tends asymptotically to the density of pure ice as depth goes to $+\infty$. An obvious choice is the logistic function,

$$f(x) = \frac{\Lambda}{1 + e^{-k(x - x_0)}} \tag{3.4}$$

where k is the logistic growth rate, a shape coefficient unrelated to its use in the models above, Λ is the least upper bound, and x_0 is a reference value. For the purpose of this model, the independent variable is the depth z and the dependent variable is the density ρ, so we rewrite the logistic equation as

$$\rho(z) = \frac{\Lambda}{1 + e^{-k(z - z_0)}} \tag{3.5}$$

To create a general model, we need values of z_0, k, and Λ. Since we have three unknowns, we need three known pairs of values for $(z, \rho(z))$. Our options are shown in Table 3.2, where the question marks denote values we do not know right now. At the surface we know the depth but not the density, so we have to assume a characteristic value for fresh snow pack on the glacier. At the snow-firn and firn-ice transitions, we know the density, and we can calculate the depth from the

Herron-Langway model, which also requires an assumption for the density of fresh snow. Only at "infinity" do we know both the depth and density. Note that pure water ice Ih at standard conditions for temperature and pressure (STP) has a density of 916.68 kg m^{-3} (Petrenko & Whitworth, 1999, p.12), but deep in a glacier, ice is under much greater pressure, so its density is higher. For example, Gow and colleagues (1997) reported that the 3053.4 m-long Greenland Ice Sheet Project 2 (GISP2) core originally had a maximum density of $\rho_{max} = 920.5$ kg m^{-3} at approximately 1400 m, and became bubble-free at that depth. Mathematically it is tempting to solve the system using "infinity", the surface, and one transition point, but we get a more general solution and a smoother form using infinity and both transition points, so that is what I will do. Now we are in a position to write our system of equations:

$$\begin{cases} \rho(z_\beta) &= \left(\dfrac{\Lambda}{1 + e^{-k(z - z_0)}} \right)_{z = z_\beta} \\ \rho(z_\iota) &= \left(\dfrac{\Lambda}{1 + e^{-k(z - z_0)}} \right)_{z = z_\iota} \\ \rho(z_\omega) &= \lim_{z \to \infty} \left[\dfrac{\Lambda}{1 + e^{-k(z - z_0)}} \right] \end{cases} \tag{3.6}$$

In the third equation, since z goes to ∞, the exponential goes to zero, so

$$\lim_{z \to \infty} \left[\frac{\Lambda}{1 + e^{-k(z - z_0)}} \right] = \frac{\Lambda}{1 + e^{-\infty}} = \frac{\Lambda}{1 + 0} = \Lambda \tag{3.7}$$

and therefore

$$\Lambda = \rho_\omega \tag{3.8}$$

This leaves us with two equations in two unknowns, both of the form

$$\rho = \frac{\Lambda}{1 + e^{-k(z - z_0)}} \tag{3.9}$$

so

$$1 + e^{-k(z - z_0)} = \frac{\Lambda}{\rho} \tag{3.10}$$

$$e^{-k(z - z_0)} = \frac{\Lambda}{\rho} - 1 \tag{3.11}$$

$$-k(z - z_0) = \ln\left[\frac{\Lambda}{\rho} - 1\right] \tag{3.12}$$

$$k(z_0 - z) = \ln\left[\frac{\Lambda}{\rho} - 1\right] \tag{3.13}$$

$$z_0 = z + \frac{1}{k}\ln\left[\frac{\Lambda}{\rho} - 1\right] \tag{3.14}$$

We still have two unused $(z, \rho(z))$ pairs so we can write a system of two equations in two unknowns:

$$\begin{cases} z_0 = z_\beta + \frac{1}{k}\ln\left[\frac{\Lambda}{\rho_\beta} - 1\right] \\ z_0 = z_\iota + \frac{1}{k}\ln\left[\frac{\Lambda}{\rho_\iota} - 1\right] \end{cases} \tag{3.15}$$

so

$$z_\iota + \frac{1}{k}\ln\left[\frac{\Lambda}{\rho_\iota} - 1\right] = z_\beta + \frac{1}{k}\ln\left[\frac{\Lambda}{\rho_\beta} - 1\right] \tag{3.16}$$

$$k\left(z_\iota - z_\beta\right) = \ln\left[\frac{\Lambda}{\rho_\beta} - 1\right] - \ln\left[\frac{\Lambda}{\rho_\iota} - 1\right] \tag{3.17}$$

and since $\Lambda = \rho_\omega$,

$$k = \frac{1}{z_\iota - z_\beta}\left[\ln\left(\frac{\rho_\omega}{\rho_\beta} - 1\right) - \ln\left(\frac{\rho_\omega}{\rho_\iota} - 1\right)\right] \tag{3.18}$$

Everything on the right is known if we have first used Herron-Langway, so we now know k, and we can find z_0 by substituting this value of k back into either equation in 3.15. Thus we have a complete solution for the logistic curve:

$$\begin{cases} \rho(z) = \dfrac{\rho_\omega}{1 + e^{-k(z - z_0)}} \\ z_0 = z_\beta + \dfrac{1}{k}\ln\left(\dfrac{\rho_\omega}{\rho_\beta} - 1\right) = z_\iota + \dfrac{1}{k}\ln\left(\dfrac{\rho_\omega}{\rho_\iota} - 1\right) \\ k = \dfrac{1}{z_\iota - z_\beta}\left[\ln\left(\dfrac{\rho_\omega}{\rho_\beta} - 1\right) - \ln\left(\dfrac{\rho_\omega}{\rho_\iota} - 1\right)\right] \end{cases} \tag{3.19}$$

This is somewhat unprepossessing to look at but very easy to program, and we can verify that it satisfies the problem constraints.

3.2.3 The ductile layer

Continuing down the GISP2 core, Gow and colleagues (1997) found that the ice density *decreased* below 1400 m, and that the air bubbles, which had gradually disappeared, started to reappear. They noted that the new bubbles were much less regular than the original bubbles, which had been essentially spherical. This deep ice was ductile and relaxed minimally over the three years after its extraction, whereas ice above the density maximum was brittle and relaxed much more extensively. The GISP2 density data from Gow et al. and temperature data from Cuffey et al. (1995) are plotted in Figure 3.2. The density is controlled by the densification process in the top of the glacier but by temperature in the bottom. In between there is a zone of nearly

Figure 3.2
GISP2 density and temperature profiles.

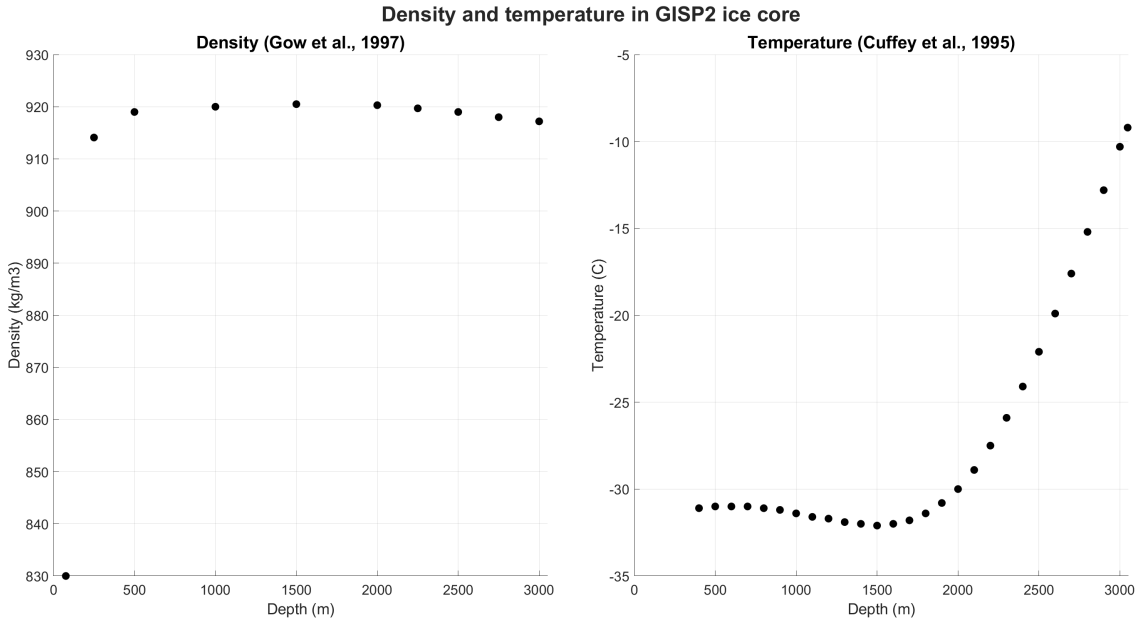

Note. The data, taken from the literature, is represented here by the actual points rather than a smoothed curve. This figure is discussed in the text on p.106.

constant density where the two effects approximately balance. The ductile layer corresponds to the rising temperature region, and presumably this warming is due to heat absorbed from the bedrock at the bottom of the glacier. If we treat the glacier as an isotropic flat plate with a constant heat conductivity, the steady-state temperature profile is given by

$$t(x) \;=\; \frac{t_2 \;-\; t_1}{\ell} x \;+\; t_1 \tag{3.20}$$

(Gebhart, 1971, p.26) where ℓ is the thickness of the slab, t_1 and t_2 are the temperatures of the two surfaces, and x is the distance from the surface that has temperature t_1. Obviously this is simply the equation of a straight line, and therefore describes the rising limb of the temperature curve. In our model situation, the slab thickness ℓ is the distance from the top of the ductile layer, which is z_3 according to our model conventions, to the bottom of the glacier, which I will call Z. The end temperature t_2 is that of the bottom of the glacier; let us denote it t_∞. The starting temperature t_1 is

that of the ductile transition, $t(z_3)$ in the model. In general it depends on the thermal history of the glacier and is not predictable just from physics, so it has to be assumed. Finally the unknown, x, is the distance from the ductile transition depth z_3 to the depth of interest z. Equation 3.21 therefore becomes

$$t(z) = \frac{t_\infty - t(z_3)}{Z - z_3}(z - z_3) + t(z_3) \tag{3.21}$$

As we saw from Gow et al., the density in the ductile layer is primarily controlled by the temperature. The dependence can be fitted by a straight line with approximately $r^2 = 0.94$. Other models can fit even better but give implausibly low values of the density at the bottom, so the straight-line model makes the most sense. We could therefore describe the density of the ductile layer either as

$$\rho(z) = c_1 t(z) + c_2 \tag{3.22}$$

where c_1 and c_2 are the fit coefficients, or as

$$\rho(z) = \frac{Z - z_3}{\rho_\infty - \rho_\omega}(z - z_3) + \rho_\omega \tag{3.23}$$

Since we only have the same data to use either way, 3.23 is simpler than 3.22, so that is what I will use for the ductile layer.

3.2.4 The combined density model

Putting together the Herron-Langway model for the snow and firn layers from equation 3.2 (p.101), the logistic model for the ice from equation 3.19 (p.106), and the conduction model for the

ductile layer from equation 3.23 (p.108), we get the full density model shown in equation 3.24:

$$\begin{cases} \begin{cases} \rho(z) &= \frac{\rho_\omega Z_n}{1 + Z_n} \\ Z_n &= \exp\left(\frac{\rho_\omega k_n (z - z_n)}{\mathcal{A}_c^{(n-1)/2}} + \ln \frac{\rho_n}{\rho_\omega - \rho_n} \right) \end{cases} & , n < 2 \\ \\ \begin{cases} \rho(z) &= \frac{\rho_\omega}{1 + e^{-k(z - z_0)}} \\ z_0 &= z_\beta + \frac{1}{k} \ln\left(\frac{\rho_\omega}{\rho_\beta} - 1 \right) = z_\iota + \frac{1}{k} \ln\left(\frac{\rho_\omega}{\rho_\iota} - 1 \right) \\ k &= \frac{1}{z_\iota - z_\beta} \left[\ln\left(\frac{\rho_\omega}{\rho_\beta} - 1 \right) - \ln\left(\frac{\rho_\omega}{\rho_\iota} - 1 \right) \right] \end{cases} & , n = 2 \\ \\ \rho(z) = \frac{Z - z_3}{\rho_\infty - \rho_\omega}(z - z_3) + \rho_\omega & , n = 3 \end{cases} \tag{3.24}$$

Figure 3.3 shows a solution of this model along with Gow et al.'s (1997) density points. I picked my inputs as close as possible to values available in the literature for GISP2 while still getting a good fit; they are listed in Table 3.3. The model fits with $r^2 = 0.9943$ overall but does not do well where the slope of the curve is changing rapidly. This is no doubt partly due to the choice of model, but probably also depends on the temperature profile in the top of the glacier, which reflects its thermal history and therefore cannot be captured by a theoretical derivation. The fit could be improved by building a solver to optimize the inputs, but that is beyond the scope of this thesis. I just needed a fair approximation of the density in a glacier and this one will do.

3.3 Bubbles

3.3.1 Overburden pressure

The derivation of the density profile was a bit verbose but essentially nothing but trivial algebra. Using it to calculate the glacier's pressure profile is more difficult because the overburden pressure at height z in a glacier is obviously the atmospheric pressure plus the weight of the ice, which is the acceleration due to gravity times the ice density, integrated from the air-ice interface

Figure 3.3
Combined model approximation for GISP2 core.

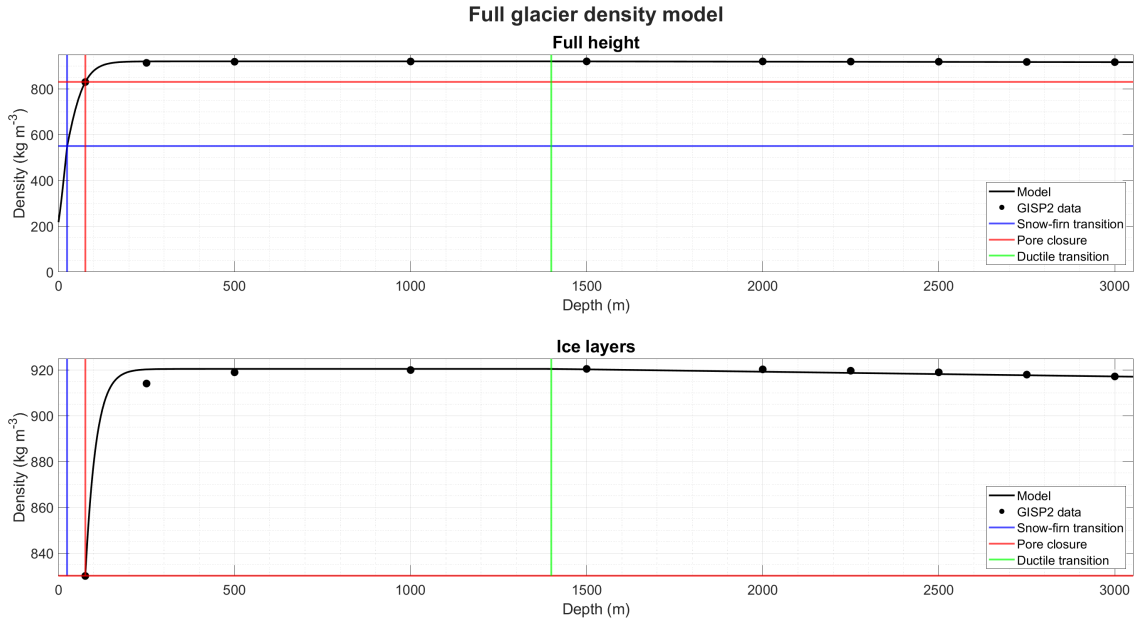

Note. The model in equation 3.24, shown here as the black curve, approximates the GISP2 core well except just below the pore closure depth, where the derivative of the density changes rapidly. The top panel shows the full density scale on the ordinate; the bottom panel starts from the pore closure density. This figure is discussed in the text on p.109.

down to z:

$$p(z) = p_{atm} + g \int_0^z \rho(z)\, dz \tag{3.25}$$

where p_{atm} is the atmospheric pressure at the top of the glacier, which can be estimated from the altitude. Therefore, we need an integral of the whole model in equation 3.24. Ideally we want the integral explicitly, but for lack of space and talent, I had to do it numerically using Matlab for now.

3.3.2 Bubble pressure

Gow (1968) gives an equation relating density and bubble pressure, thusly:

$$P = \frac{(\rho_h - \rho_\iota)\rho}{(\rho_h - \rho)\rho_\iota} P_\iota \tag{3.26}$$

Table 3.3
Inputs for model in Figure 3.3.

Quantity	Value
Altitude of glacier surface (m)	3200
Accumulation rate (m water day^{-1})	0.12
Mean annual temperature (°C)	-32
Initial density of snowpack (m kg^{-3})	285
Depth of ductile transition (m)	1400
Temperature of ductile transition (°C)	-27
Maximum density of ice at ductile transition (m kg^{-3})	920.5
Thickness of glacier (m)	3053
Temperature at bottom of glacier (°C)	-15
Density at bottom of glacier (m kg^{-3})	917.2
Ad hoc parameter for bubble pressure	0.36

Note. This table is discussed in the text on p.109.

where ρ is the density of an ice sample, ρ_h is the density of bubble-free ice at the same conditions of temperature and pressure as the sample, and P_ι is the air pressure at the pore closure. We can rewrite this as a function of z rather than a scalar:

$$P(z) = \frac{(\rho_h(z) - \rho_\iota)\rho(z)}{(\rho_h(z) - \rho(z))\rho_\iota} P_\iota \tag{3.27}$$

and we can calculate P_ι from the atmospheric pressure at the mean annual surface temperature and the altitude of the pore closure, using the barometric equation. The theoretical density of pure ice, ρ_h, can be calculated from in situ temperature and pressure using the GSW Toolbox (McDougall & Barker, 2011). The overburden pressure, density deficit, and bubble pressure, modelled to emulate the GISP2 core, are plotted in Figure 3.4.

3.3.3 Performance of pressure model

As far as I know there is no data set currently available to check the validity of this bubble pressure profile; otherwise I would not have needed to do all this work. My model does have a certain coherence with available facts. Figure 3.5 shows the model pressure from the pore closure to 400 m further down, multiplied by an ad hoc factor of 0.36, which allows it to go through the

Figure 3.4
Overburden pressure, density deficit, and bubble pressure for the model glacier.

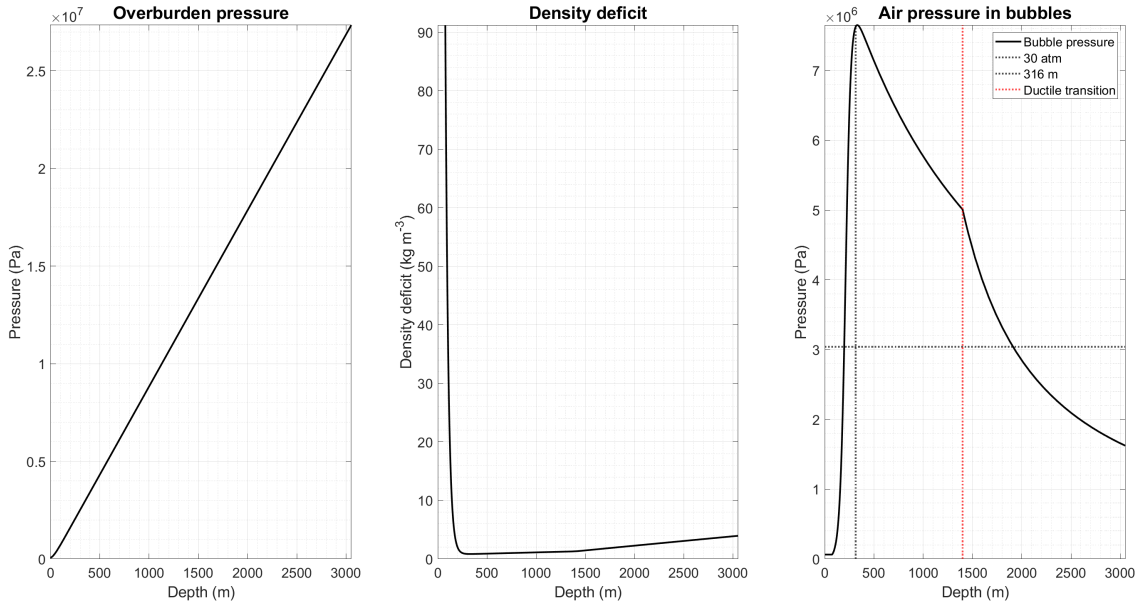

Note. The glacier model shows that the overburden pressure (left panel) increases approximately linearly with depth, but the density deficit (middle panel), being the difference between pure ice Ih at the in situ conditions and the actual glacier density, decreases rapidly at first as bubbles close, to a minimum value that is approximately maintained throughout the brittle layer, and finally rises again slowl through the ductile layer. The bubble pressure (right panel) is calculated from the density deficit using equation 3.26. This figure is discussed in the text on p.110.

value of (z = 360.5 m, p = 27 atm) reported by Langway (1958, cited by Gow, 1968) from Site 2 in Greenland. Recall from the map in Figure 3.1 (p.100) that Site 2 is more than 700 km from GISP2 and therefore conditions are different, but it is the only point I have that gives pressure at a significant depth. Gow, whose equation I am using, notes that "the major point of interest of (Langway's) study was that in most of the samples tested the bubbles were seemingly compressed less than might have been expected from the weight of overlying snow and ice", and therefore it is expected that my values should overstate the known pressure. With the ad hoc factor, the pressure range observed by Scholander and Nutt (1960) of approximately 1 to 20 atm occurs between 120 and 235 m below the pore closure, so it is not surprising that they could find bits of icebergs throughout that range especially when sampling icebergs from different parent glaciers (shown on the map in Figure 3.1). This is also where my density model fits worst, and since the bubble pressure model

Figure 3.5
Detail of bubble pressure model.

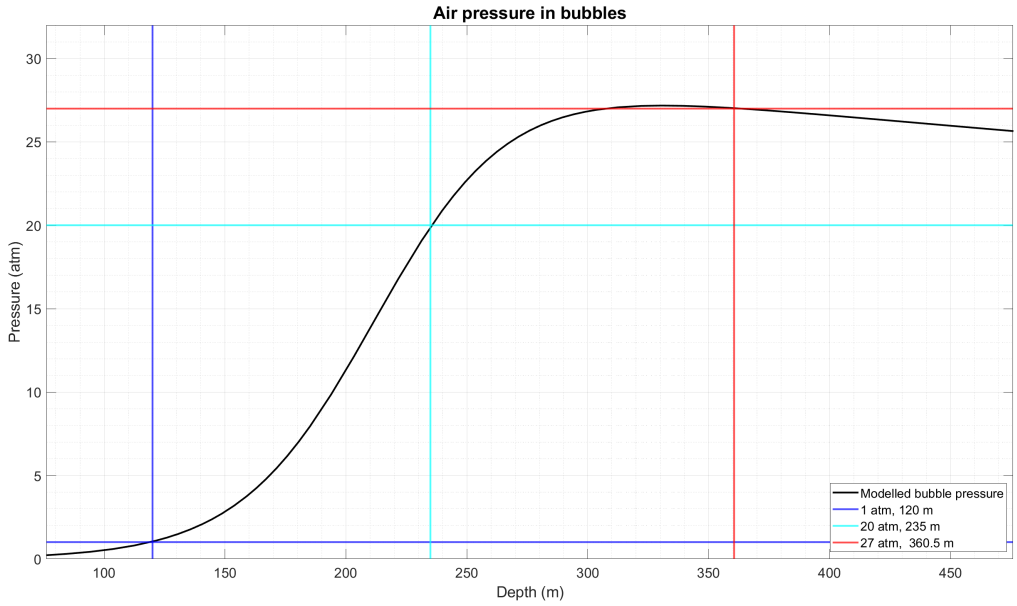

Note. The air bubble pressure from Figure 3.4 is here multiplied by an ad hoc correction factor to match available data, and reported in atmospheres. This figure is discussed in the text on p.111.

is based on the deficit between pure ice and the in situ sample, it is unfortunately where we can expect the worst error. The fact that the values are still broadly realistic is encouraging.

Overall, then, the model is generally realistic but without a statistical measure of goodness of fit. Certainly it could be improved if one had time to work on it, but it is not the central point of this thesis, and this will do for testing my thermodynamic model.

3.3.4 The role of bubbles in ablation

3.3.4.1 Mechanical stress effect

Let us denote ice Ih by the suscript h, air by the subscript a, and glacier ice, consisting of bubbles of air in a matrix of ice Ih, by the subscript g. Obviously the mass of a sample of glacier ice is

$$m_g = m_h + m_a \tag{3.28}$$

so

$$\rho_g V_g = \rho_h V_h + \rho_a V_a \tag{3.29}$$

If we take a unit mass of glacier ice, that is, $m_g = 1$ kg, this becomes

$$\rho_a V_a + \rho_h V_h = 1 \tag{3.30}$$

Equally, the volume is

$$V_g = V_h + V_a = \frac{m_g}{\rho_g} = \frac{1}{\rho_g} \tag{3.31}$$

so we have two equations in two unknowns:

$$\begin{cases} V_h + V_a = \dfrac{1}{\rho_g} \\ \rho_h V_h + \rho_a V_a = 1 \end{cases} \tag{3.32}$$

From the first equation we get

$$V_a = \frac{1}{\rho_g} - V_h \tag{3.33}$$

which we substitute into the second

$$\rho_h V_h + \rho_a \left(\frac{1}{\rho_g} - V_h \right) = 1 \tag{3.34}$$

and solve for V_h:

$$(\rho_h - \rho_a) V_h = 1 - \frac{\rho_a}{\rho_g} \tag{3.35}$$

and finally we have equations for the volumes of ice Ih and air in a unit mass of glacier ice:

$$\begin{cases} V_h &= \dfrac{\rho_g - \rho_a}{\rho_g(\rho_h - \rho_a)} \\ V_a &= \dfrac{1}{\rho_g} - \dfrac{\rho_g - \rho_a}{\rho_g(\rho_h - \rho_a)} \end{cases} \tag{3.36}$$

Let us assume, first, that at the pore closure the bubbles are distributed evenly in space and each bubble is a sphere with a radius of $r_o = 1$ mm; and second, that as the bubbles compress, their geometry in the horizontal plane does not change, and the change in volume is due only to reduction of the vertical radius, r_v. The volume of a single bubble is

$$V_o = \frac{4}{3}\pi r_o^3 = \frac{4}{3}\pi r_v r_o^2 \tag{3.37}$$

and the number density of bubbles is

$$N_o = \frac{V_a}{V_o} = \frac{3}{4\pi r_v r_o^2}\left[\frac{1}{\rho_g} - \frac{\rho_g - \rho_a}{\rho_g(\rho_h - \rho_a)}\right] \tag{3.38}$$

per unit mass of glacier ice.

Recall that the volume of bubbles decreases from V_a at the pore closure to zero at the ductile transition depth where the bubbles disappear, and since we said that only the vertical dimension of the bubbles varies, using equations 3.37 and 3.38, we get

$$\frac{dV_a}{dz} = \frac{d}{dz}(N_0 V_0) = N_0\frac{dV_0}{dz} = \frac{4}{3}\pi\frac{dr_v}{dz}r_o^2 N_o \tag{3.39}$$

since we are assuming that the number of bubbles N_0 does not change as the ice compacts. Mind that in reality, the change in volume is not simply the mass times the change in density, because air mass is gradually lost to enclathratization until it reaches zero; that is to say the bubbles do not close because the air is squeezed into an infinitesimal volume, but because it becomes absorbed into the ice matrix. To solve this problem properly, therefore, we would also need to know the rate

of enclathratization as a function of temperature and pressure, which I, at this time, do not. So to keep making progress, let us just assume that the volume decreases linearly from the pore closure to the ductile transition:

$$\frac{dV_a}{dz} = \frac{0 - V_a(0)}{z_3 - z_2} = \frac{V_a(0)}{z_2 - z_3} \tag{3.40}$$

and therefore

$$\frac{dr_v}{dz} = \frac{3}{4\pi r_o^2 N_o} \frac{V_a}{z_2 - z_3} \tag{3.41}$$

and

$$r_v(z) = r_o + \frac{3}{4\pi r_o^2 N_o} \frac{V_a}{z_2 - z_3} z \tag{3.42}$$

The greatest cross-section surface area of the bubbles in the vertical plane is therefore that of an ellipse with semimajor radius r_o and semiminor radius r_v.

The final piece of information we need is the thickness at which the wall between a bubble and the sea breaks, given the pressure difference between the two. Mechanical engineering provides maximum load formulas for many geometric configurations, but I did not find one for the specific shape of a bubble breaking out of an iceberg. Young and Budynas (2002, p.499, case 32b) provides formulas for the maximum stress in an elliptical plate of constant thickness with fixed edges, with a load uniformly distributed over either the entire surface, thusly:

$$\sigma_{max} = \frac{-3qb^2(1 + \nu\alpha^2)}{\zeta^2(3 + 2\alpha^2 + 3\alpha^4)} \tag{3.43}$$

where q is the force, a is the semimajor radius of the ellipse, b is the semiminor radius, $\alpha = b/a$, ν is the Poisson ratio, and ζ is the thickness of the plate. If we take σ_{max} to be the ultimate tensile strength of ice, ζ is the only unknown and we can easily solve for it, though actually evaluating

Figure 3.6
Investigation of wall failure model.

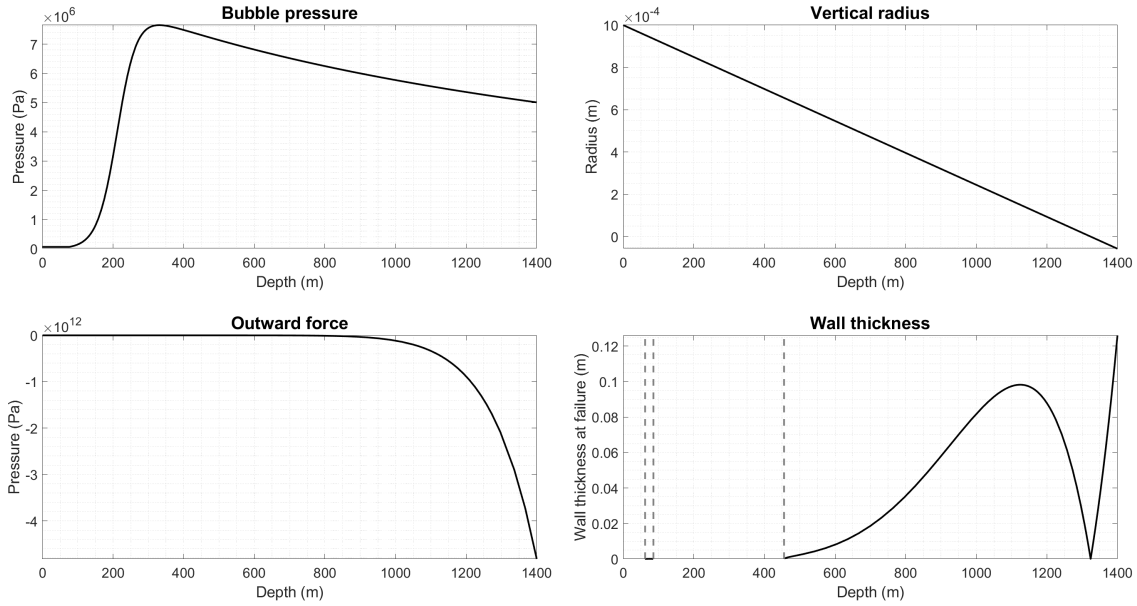

Note. The bubble pressure (top left) is given by the model in subsection 3.3.2. We are assuming that the vertical dimension of the bubbles (top right) decreases linearly. The outward force (bottom left) is the difference between the air pressure inside the bubbles and the water pressure outside (from ORAS5 values). Finally the wall thickness at which failure occurs (bottom right) is calculated by solving equation 3.43. This figure is discussed in the text on p.117.

it over the height of the iceberg profile is computationally not very cheap because of the number of symbolic functions involved in the code so far. Typical values for ice are $\nu = 0.33$ and $\sigma_{max} = 1$ MPa, and the other quantities are obtained from our model.

Using the equation of Picard et al. (2008) for the density of air and a sample water density profile, we can plot the model, as shown in Figure 3.6. The fourth panel shows that there is a very small range of depths, from approximately 62 to 84 m, where the equation returns a plausible value, under a millimeter. Below 450 m the solutions are much too large, and over the rest of the range there is no solution. One possible explanation is that the stress model I chose is not a suitable approximation of the iceberg bubble wall, which is quite possible. Another hypothesis is that the bubble wall does not in fact fail, but melts through. In fact Scholander and Nutt (1960) do not describe the bubbles breaking in their pressure apparatus; rather it seems that they open in

a non-catastrophic way that leaves a meniscus. The sound, therefore, is not caused by mechanical failure of the ice, but more likely by the expansion of the air as pressure is released. A study by Grossman and colleagues (2024) on the sounds made by glaciers in Svalbard identified that approximately 48% of sound events recorded had the acoustic signature of an oscillating bubble, with apparently two distinct populations at different energy spectra. The remaining sounds may or may not have been caused by bubbles, so there may still be some noise from mechanical failure, but I cannot capture it mathematically at this time. Therefore the next question we need to answer is how the expansion of bubbles would contribute to mass loss from the iceberg.

3.3.4.2 Melt density effect

We established in equation 3.36 (p.115) that the volume of air in the ice at the pore closure was

$$V_a = \frac{1}{\rho_g} - \frac{\rho_g - \rho_a}{\rho_g(\rho_h - \rho_a)} \tag{3.44}$$

We can calculate its density ρ_a from the equation of Picard et al. (2008), and therefore we know its mass, m_a. We also know the pore closure density and the density of ice Ih, so we can write

$$\rho_g = \frac{m_a + m_h}{V_a + V_h} \tag{3.45}$$

and solve it for the mass of ice Ih:

$$m_h = \rho_g(V_a + V_h) - m_a \tag{3.46}$$

We can use the ideal gas law (Steane, 2017, p.61) as an approximate equation of state for air:

$$pV = nRT \tag{3.47}$$

from which we can write

$$\frac{V_2}{V_1} = \frac{p_1}{p_2}\frac{n_2 R T_2}{n_1 R T_1} \tag{3.48}$$

When the ice compresses, n actually decreases with increasing depth as air becomes absorbed into clathrates in the ice. When the pressure is released, however, the clathrates would be released as air again, so n can be taken as invariant here. We also assume, not necessarily correctly, that at the time of the phase transition, the ice and the melt are at the same temperature, so that T is also invariant here, and therefore

$$\frac{V_a(z)}{V_a(z_2)} = \frac{p_a(z_2)}{p_a(z)} \tag{3.49}$$

Recall that z_2 is our symbol for the pore closure level, and in this equation $p_a(z)$ is equal to the pressure in the water in which the iceberg melts. Therefore we can easily calculate the volume of air in the melt:

$$V_a(z) = \frac{p_a(z_2)}{p_a(z)} V_a(z_2) \tag{3.50}$$

Johnson (2025, p.56) uses instead a polytropic equation with $\kappa = 7/5$:

$$pV^{\kappa} = C \tag{3.51}$$

where C is a constant. This would give us

$$V_a(z) = \left[\frac{p_a(z_2)}{p_a(z)}\right]^{1/\kappa} V_a(z_2) = \left[\frac{p_a(z_2)}{p_a(z)}\right]^{5/7} V_a(z_2) \tag{3.52}$$

and therefore less expansion.

Meanwhile the volume of water in the melt is given by the mass of water in the glacier ice, which we calculated above, and its density at the hydrostatic pressure at the melting depth, which

Table 3.4
Inputs for model in Figure 3.7.

Quantity	Value
Latitude of test	69.12
Longitude of test	-52.10
Year of test	1958
Month of test	5
Height of iceberg top in parent glacier (m)	80
Vertical size of iceberg (m)	200

Note. This table is discussed in the text on p.120.

we can calculate from the TEOS-10 equation as usual. The density of the melt is therefore

$$\rho_{melt} = \frac{m_a + m_h}{V_a(z) + V_w(z)} \tag{3.53}$$

where the subscript w denotes water. This model requires a water density profile as an input, so we will see the results in the next section.

3.4 The iceberg and the sea

Now that we have a glacier density and pressure model, applying the Agassiz model is trivial. We simply cut a section of the profile, from a desired starting height in the parent glacier to a desired vertical dimension of the iceberg, then pick a likely point in space and time in the ORAS5 reanalyis product (Zuo et al., 2019), calculate the water density from the TEOS-10 equation using the GSW Toolbox (McDougall & Barker, 2011), integrate it to determine how high the iceberg floats, then calculate the Agassiz ablation rate from the Agassiz model and the iceberg density from the profile we just established, multiply the two together, and that gives us the ablation rate with depth, with the caveat that currently there is no pressure term in the Agassiz model. This is easier done than said and a sample test, with the values shown in Table 3.4 is shown in Figure 3.7. I selected a test location off Nuuk (Jakobshavn) in May 1958, shown in red on the map in Figure 3.1. The available depth in ORAS5 at that point is 371 m; as my program is only set up for floating icebergs, it limits the model height to prevent grounding. Since the pore closure depth in the model

Figure 3.7
Test case of Agassiz-bubble model.

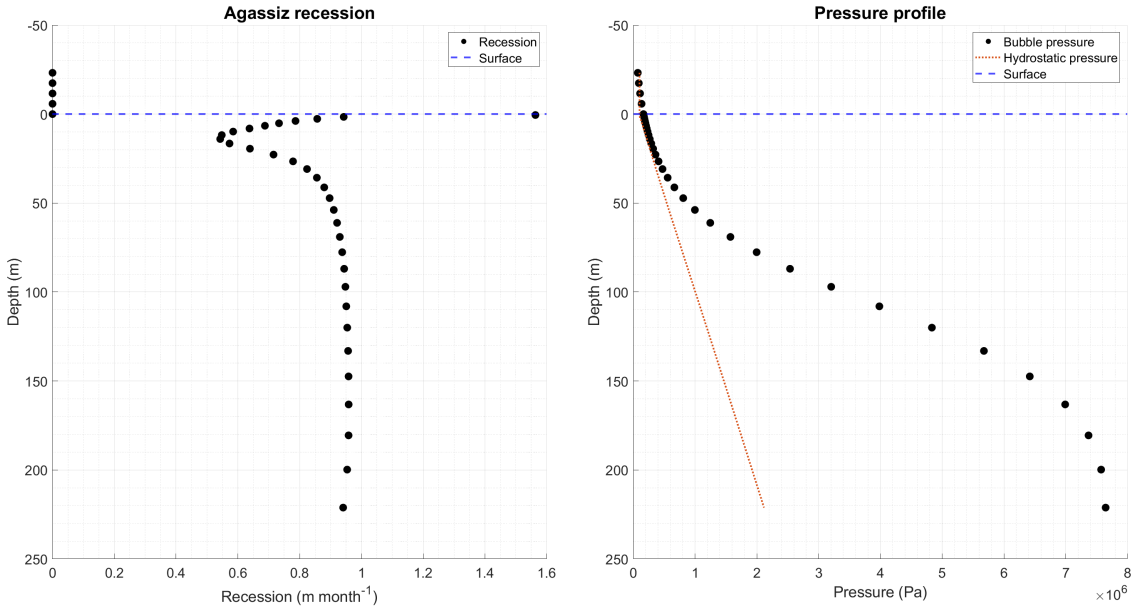

Note. The left panel shows the one month of recession predicted by the Agassiz model using the iceberg density model and sea temperature and salinity from ORAS5. The right panel shows the bubble pressure in the iceberg, compared to the hydrostatic pressure in the sea. Dots represent depth levels, which are not evenly distributed in ORAS5. This figure is discussed in the text on p.120.

glacier is 76 m, I set the top of the iceberg at 80 m to make sure the iceberg is not porous, which would add more problems as the seawater infiltrates submerged firn. Since ORAS5 is a monthly product, I converted the recession into a monthly rather than daily amount. Finally, Figure 3.8 shows the relative contributions of air and water in the melt, and Figure 3.9 shows the resulting buoyancy of the melt compared to non-bubbly melt. Unfortunately, at this point there is simply no data anymore to continue. The only controlled melt experiment I know of involving glacier ice is by Wengrove and colleagues (2023) and involved one single trial with one single piece of glacier ice. Their observation was that the glacier ice melted 2.25 times faster than the bubble-free ice control, but I have no way to use it at this stage of my modelling. Here, therefore, ends my investigation for this thesis. The Matlab code for the whole model is listed in appendix D.

The final programming challenge was to represent the iceberg as a 3D finite element model,

Figure 3.8
Contributions of air and water to the melt.

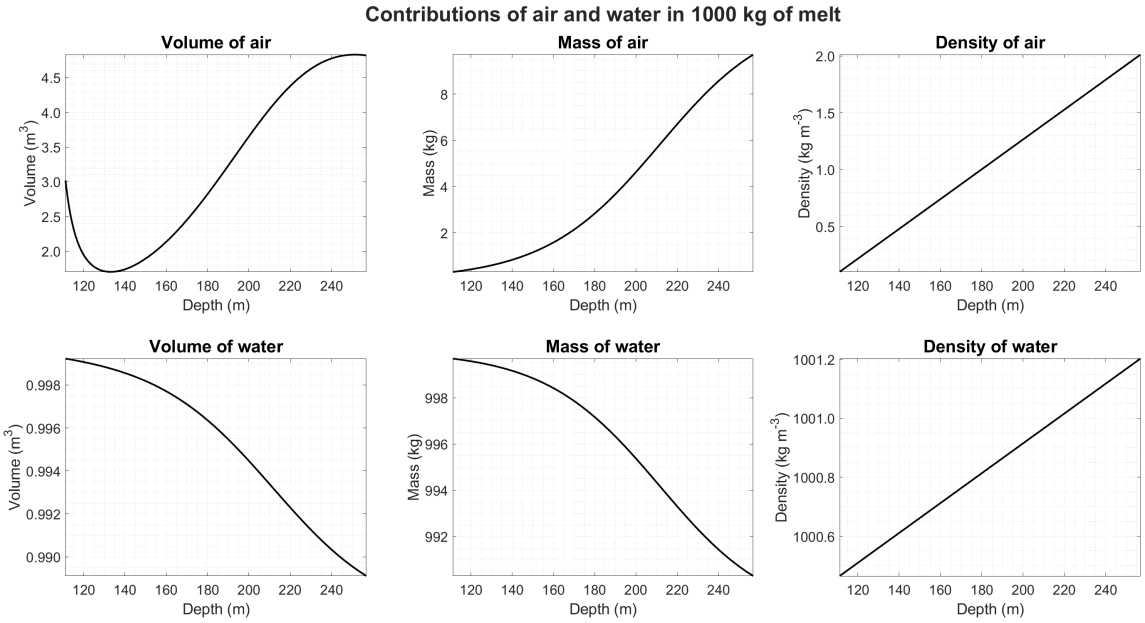

Note. This figure is discussed in the text on p.121.

find a method to round the corners as the surface recedes, and sail the model iceberg along a plausible sea path, adjusting its floating height as the mass loss below the waterline affects its buoyancy. Using a modelled iceberg track by our departmental colleagues Marson et al. (2024), sea conditions from ORAS5 reanalysis (Zuo et al., 2019), the Agassiz model from Chapter 2, the density model from this chapter, and my own programming in Matlab, I generated a movie that illustrates the Agassiz recession for a 100 m-tall iceberg sailing south on the west side of Baffin Bay between 25 August and 27 December 2017. Details of the programming are omitted here as too lengthy and likely of no interest to the reader, but sample frames from the resulting movie are shown in Figures 3.10 to 3.13 (pp.124-125). The model track starts over a year earlier in Greenland where the iceberg would plausibly have been calved, but I picked a starting point well along the track for the sake of making a more exciting movie as the iceberg travels south into more thermodynamically aggressive water. For the same reason, I multiplied the ablation rate by 10. The larger diagram in each view shows the 3D model, with a colour gradient representing the ice density. The smaller

Figure 3.9
Buoyancy of bubbly and bubble-free melt.

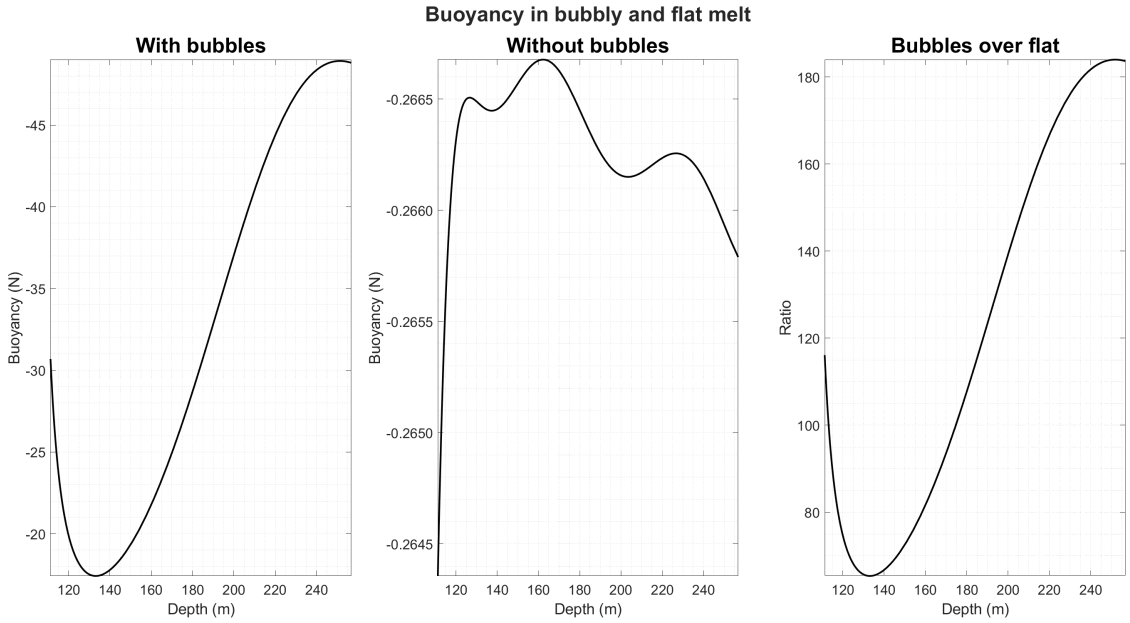

Note. Buoyancy is negative upward. As in the previous figure, depth is with reference to the parent glacier and starts 8 m below the water surface, as the form of the mathematical model produces a vertical asymptote at the surface. This figure is discussed in the text on p.121.

graph at the top right shows the silhouette of the iceberg superimposed on a pseudocolour plot of the Agassiz profile for its current location. The map shows the full predicted path as black dots, and points already traversed as green dots. ORAS5 values are given monthly at its grid points, and therefore the values were interpolated in time and space for each daily time step. The sail does not recede at all in this model because its ablation mechanism is not related to the Agassiz model, and the flat bottom of the iceberg does not recede because none of my work has addressed the situation underneath a horizontal ice sheet. The shape of the bottom of the cantilever in the iceberg profile is an artifact of the gridding.

3.5 Discussion

The glacier density model reproduces quite well the density profile of the GISP2 core. It does require ten inputs, but all of them are physical quantities that can be known or reasonably

Figure 3.10
Sample from iceberg ablation simulation: day 1.

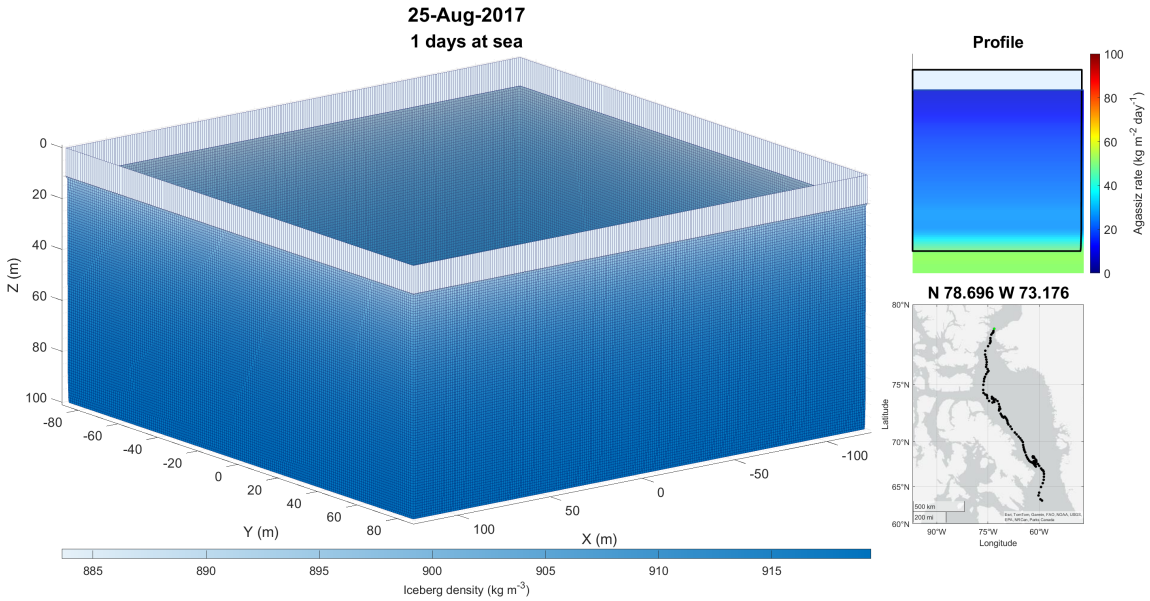

Note. The iceberg encounters a deep layer of warm water. This figure is discussed in the text on p.121.

Figure 3.11
Sample from iceberg ablation simulation: day 25.

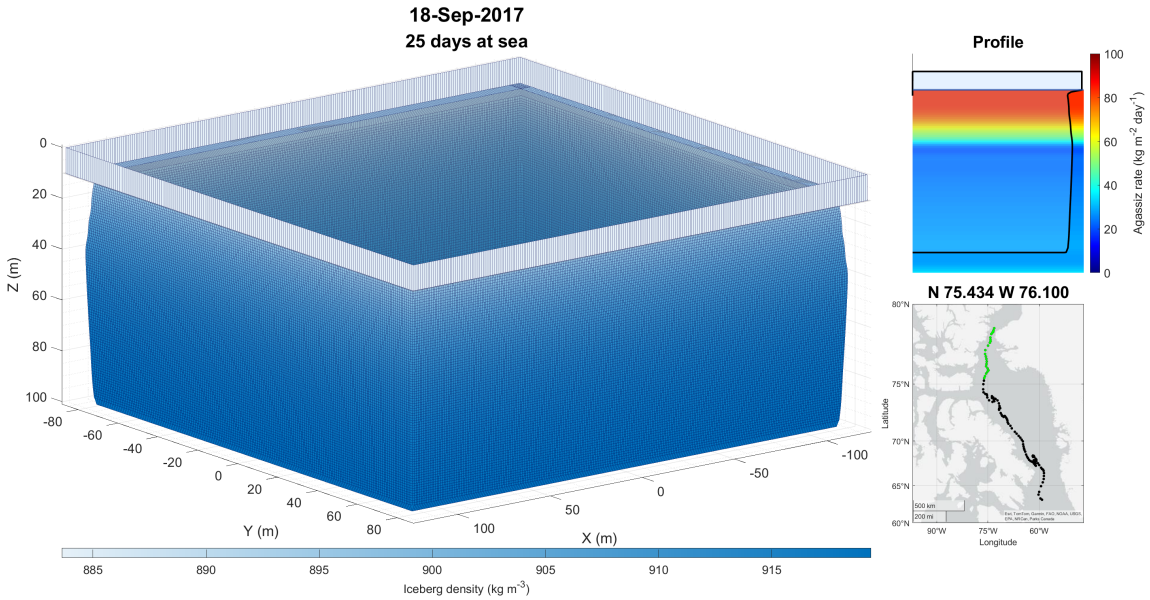

Note. In summer, ablation is faster in the upper layers which are warmed by the sun. This figure is discussed in the text on p.121.

Figure 3.12
Sample from iceberg ablation simulation: day 53.

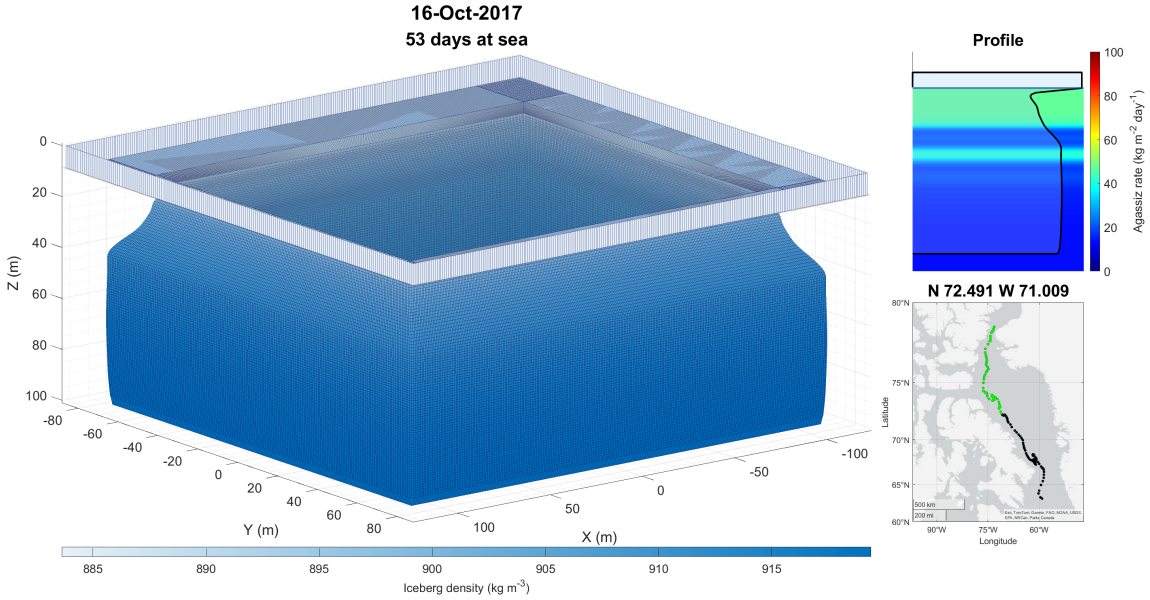

Note. In autumn, the iceberg encounters localized inversions in melt potential. This figure is discussed in the text on p.121.

Figure 3.13
Sample from iceberg ablation simulation: day 124.

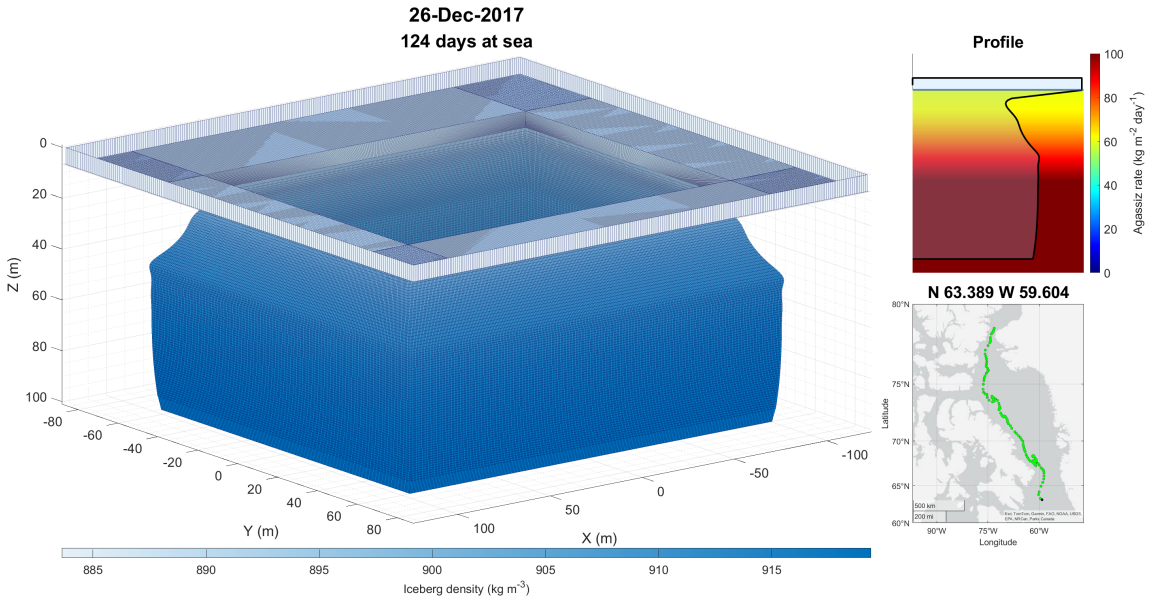

Note. The iceberg crosses into a much more aggressive water mass just as the modelled trail ends. This figure is discussed in the text on p.121.

assumed, and the output is in SI units. On the other hand, the ductile zone was simply fitted empirically to the GISP2 core, and the whole model has only been tested on that core. More work would be needed to create an analytical model of the ductile layer and verify the model against other cores. Overall, though, it is a better approximation than Shumskiy's (1960).

The bubble pressure model significantly overestimated the pressure compared to known values, and the same effect was encountered by other researchers. This may be due in part to the loss of air to enclathratization. Determining the rate at which this happens in the bubbles could therefore be useful. Another factor is the glacier terminus itself, which changes the mechanical and thermodynamic conditions in the ice compared to the summit location where GISP2 was cored. The conditions in icebergs are different still and the ice continues to evolve thermally throughout the iceberg's life, and this could also be investigated further.

The Agassiz ablation model, as we saw in Chapter 2, is only about 80% accurate for water temperatures below zero, and more work is needed to improve this. More importantly when applying it to icebergs, it does not have a pressure term. Establishing this term would be the single greatest improvement we could make to it at this time. Nonetheless the trial results have a certain coherence with observations. In particular, because the melt rate in air is very much slower than in water, the undercut at the water line, which is often attributed to wave erosion, is shown to occur even in the absence of waves. The test also produced a large spur below the surface. This is a known phenomenon in reality, documented for example at the terminus of the Flade Isblink Ice Cap by Bendtsen and colleagues (2017). Compared to the model of Weeks and Campbell (1973) that we saw in equation 1.20 (p.26), as with that of Shumskiy (1960), my model is slower and requires several more inputs, but the inputs are all knowable quantities intrinsic to the iceberg, and the output is considerably more detailed.

Possibly the most important outcome from the model is the huge buoyancy effect the bubbles have on the melt. This will cause the melt to accelerate rapidly upward and produce a much stronger updraft along the interface than in a bubble-free simulation, even ignoring the effect of scale. Ice is very sensitive to momentum flux from the water and melts very much faster in a forced flow than

merely buoyant convection. Quantifying the effect of momentum transfer from the fluid layer on the melt rate would, in my opinion, be the most important improvement to the understanding of ice melting generally, not just deep iceberg keels.

3.6 Conclusion

In this chapter I derived a density model for a glacier which uses the Herron-Langway model to calculate the pore closure depth from assumed climatic conditions at the accumulation site, and produces a logistic curve that tends asymptotically to the maximum density of ice as depth goes to infinity. I integrated this density model to get the overburden pressure profile through the glacier. Finally I used an established method from the literature to calculate the pressure in the bubbles at a given depth in the glacier and showed that the bubbles, when released by the melting of the ice, hugely decrease the density of the melt and therefore create an updraft along the ice interface that will significantly increase the ablation rate. I then took a section of the glacier profile to create a model iceberg, notionally immersed it in a water profile obtained from ORAS5 reanalysis, and applied the Agassiz ablation model developed in Chapter 2 to estimate the rate of ablation. The results are realistic and all this is good progress compared to models currently in use, but happily there is still much opportunity for further work on glacier density profiles; phase changes of air under pressure; the effect of pressure, differential stress, and momentum flux on the melting of ice; programming approaches to the changing floating height of an iceberg at sea; and much more.

Forward

In conclusion, the melting of iceberg keels can be modelled, to a first approximation, with a relatively simple thermodynamic model that uses available data to produce profiles of the ice and the water and calculates the rate of phase change at the interface between the two from thermodynamics only. This is computationally fast and can be conveniently used to feed iceberg melt estimates into larger models of cold seas.

The main weakness in this work comes from the limitations of the data, both in quality and coverage, but this is equally true of any other iceberg melt model. Obtaining thermodynamic profiles whether inside or outside icebergs is at best difficult and dangerous, and a very large number of observations would be needed to establish the statistical distribution of conditions in time and space, which could then be used to improve theoretical models. Even in bench experiments, the temperature distribution is neither well controlled nor thoroughly described. On a positive note, however, this is not a fatal flaw, because thermodynamics is intrinsically a statistical approach which works with averages over large numbers of elements.

The data is also one of the major strengths of this work, because even though more is still needed, I have considerably improved coverage of the salinity-temperature space. The congruence of my data with legacy data obtained with different experimental setups also establishes that the melt rate is not so dependent on geometry that a different model is required for each. Another major strength is that my model does not include any fluid dynamics and therefore is not subject to the scaling issue. The problem of describing the flow of melt remains and is still relevant to local-scale (1 m to 1 km) applications, for example to describe the melt plume from an iceberg or dynamics at a glacier terminus, but it is not necessary to solve it to quantify the influx of fresh water from melting glacial ice.

There are still many ways the thermodynamic modelling of melting icebergs could be improved, including but not limited to

- collecting and using as much interoperable melt data as possible from legacy and new work;
- obtaining more experimental data at temperatures below 0°C to tighten the error range;

- obtaining more data around the density anomaly to constrain rates for low-salinity environments;
- obtaining experimental data for the effect of pressure on the melting of ice in conditions relevant to icebergs;
- improving the glacier density model to be more general, especially for the ductile layer;
- quantifying the rate of enclathratization and exsolution of air in glacier ice;
- including the thermal history of the ice in the iceberg model;
- modelling how the initial temperature profile and thermal evolution of the ice affect the melt rate over time;
- identifying from the previous point under what condition the iceberg gains mass;
- modelling the flow velocity due to the release of bubbles;
- investigating experimentally and computationally the effects of momentum flux and differential stresses on the melt rate; and
- combining all these effects into a model that also adjusts the floating height of the iceberg as melt progresses and includes the decay of the sail.

A key obstacle to progress throughout the history of this investigation has been lack of continuity. Except for the years in which the Gebhart lab worked on the question, the research has been scattered in time and space, with a small number of workers each doing a small number of experiments by their own method. If I never come to answer the remaining questions, I hope this work may at least be useful to the next graduate student who is assigned to figure out how fast an iceberg melts.

References

Bader, H. (1950). The significance of air bubbles in glacier ice. *Journal of Glaciology, 1*(8), 443–451. https://doi.org/10.3189/S002214300001279X

Bailey, N., Papakyriakou, T.N., Bartels, C., & Wang, F. (2018). Henry's Law constant for CO_2 in aqueous sodium chloride solutions at 1 atm and sub-zero (Celsius) temperatures. *Marine Chemistry, 207*, 26–32. https://doi.org/10.1016/j.marchem.2018.10.003

Barrett, H.G., Jones, J.M., & Bigg, G.R. (2018). Reconstructing El Niño Southern Oscillation using data from ships' logbooks, 1815–1854. Part I: methodology and evaluation. *Climate Dynamics, 50*, 845–862. https://doi.org/10.1007/s00382-017-3644-7

Bendell, M.S., & Gebhart, B. (1976). Heat transfer and ice-melting in ambient water near its density extremum *International Journal of Heat and Mass Transfer, 19*, 1081–1087. https://doi.org/10.1016/0017-9310(76)90138-1

Bendtsen, J., Mortensen, J., Lennert, K., Ehn, J.K., Boone, W., Galindo, V., Hu, Y.-B., Dmitrenko, I., Kirillov, S.A., Kjeldsen, K.K., Kristoffersen, Y., Barber, D.G.,, & Rysgaard, S. (2017). Sea ice breakup and marine melt of a retreating tidewater outlet glacier in northeast Greenland (81°N). *Scientific Reports, 7*, 4941. https://doi.org/10.1038/s41598-017-05089-3

Budd, W.F., Jacka, T.H., & Morgan, V.I. (1980). Antarctic iceberg melt rates derived from size distributions and movement rates. *Annals of Glaciology, 1*, 103–112. https://doi.org/10.3189/S0260305500017079

Canon Inc. (2010). *PowerShot SX30 IS Camera* (Model SX30 IS) [Instrument]. https://gdlp01.c-wss.com/gds/5/0300004195/01/PSSX30IS_CUG_EN.pdf

Carey, V.P. (1981). *Transport in vertical mixed convection flows and natural convection flows in cold water* [PhD dissertation]. State University of New York at Buffalo.

Carey, V.P., & Gebhart, B. (1982). Transport near a vertical ice surface melting in saline water: experiments at low salinities *Journal of Fluid Mechanics, 117*, 403–423. https://doi.org/10.1017/S0022112082001682

Carslaw, H.S., & Jaeger, J.C. (1986). *Conduction of heat in solids* (2nd ed.). Oxford University Press.

Cenedese, C., & Straneo, F. (2023). Icebergs melting. *Annual Review of Fluid Mechanics, 55*, 377–402. https://doi.org/10.1146/annurev-fluid-032522-100734

Christie, M.A., Glimm, J., Grove, J.W., Higdon, D.M., Sharp, D.H., & Wood-Schultz, M.M. (2005). Error analysis and simulations of complex phenomena. *Los Alamos Science, 29*.

City of Winnipeg (2025). *2024 Winnipeg distribution system water quality test results* [Webpage]. https://legacy.winnipeg.ca/waterandwaste/water/testResults/Winnipeg.stm

Condron, A. (2023). Towing icebergs to arid regions to reduce water scarcity. *Scientific Reports, 13*. https://doi.org/10.1038/s41598-022-26952-y

Control Company (n.d.). *Traceable Digital Thermometer* (Model 4000CC) [Instrument]. https://www.traceable.com/media/iwd_video/pdf/582b407c6e2d9.pdf

Cuffey, K.M., Clow, G.D., Alley, R.B., Stuiver, M., Waddington, E.D., & Saltus, R.W. (1995). Large Arctic temperature change at the Wisconsin-Holocene glacial transition. *Science, 270*(5235), 455–458. https://www.jstor.org/stable/2889060

Cuffey, K.M., & Paterson, W.S.B. (2010). *The Physics of Glaciers* [3rd ed.]. Butterworth-Heinemann.

Deane, G.B., Glowacki, O., Stokes, M.D., & Pettit, E.C. (2019). The underwater sounds of glaciers. *Acoustics Today, 15*(4), 12–19. https://doi.org/10.1121/AT.2019.15.4.12

Dozier, J. (2025). *Sun Position* [MATLAB Central File Exchange]. Retrieved October 12, 2025 from https://www.mathworks.com/matlabcentral/fileexchange/74939-sun-position

Dumoré, J.M., Merk, H.J., & Prins, J.A. (1953). Heat transfer from water to ice by thermal convection. *Nature, 172*, 460–461. https://doi.org/10.1038/172460b0

Ehn, J. K. (2008). *Solar radiation interactions with seasonal sea ice* [PhD dissertation]. University of Manitoba.

Ehn, J., Granskog, M.A., Reinart, A., & Erm, A. (2004). Optical properties of melting landfast sea ice and underlying seawater in Santala Bay, Gulf of Finland. *Journal of Geophysical*

Research, 109, C09003. https://doi.org/10.1029/2003JC002042

Ehn, J., Mundy, C.J., Barber, D.G., Hop, H., Rossnagel, A., & Stewart, J. (2011). Impact of horizontal spreading on light propagation in melt pond covered seasonal sea ice in the Canadian Arctic. *Journal of Geophysical Research, 116*, C00G02, https://doi.org/10.1029/2010JC006908

Flair Beauty Canada (n.d.). *Pirouette: The Hairnet for Dancers* (Model 2880) [Equipment]. https://flaircanada.com/dance/

Gade, H.G. (1979). Melting of ice in sea water: a primitive model with applications to the Antarctic ice shelf and icebergs. *Journal of Physical Oceanography, 9*(1), 189–198. https://doi.org/10.1175/1520-0485(1979)009<0189:MOIISW>2.0.CO;2

Gebhart, B. (1971). *Heat transfer*. McGraw-Hill.

Gebhart, B., & Mollendorf, J.C. (1978). Buoyancy-induced flows in water under conditions in which density extrema may arise. *Journal of Fluid Mechanics, 89*(4), 673–707. https://doi.org/10.1017/S0022112078002803

Gebhart, B., & Pera, L. (1971). Natural convection flows resulting from the combined buoyancy effects of thermal and mass diffusion. *International Journal of Heat and Mass transfer, 14*, 2025–2050. https://doi.org/10.1016/0017-9310(71)90026-3

Gebhart, B., & Wang, T. (1982). An experimental study of melting vertical ice cylinders in cold water *Chemical Engineering Communications, 13*(4-6), 197–218. https://doi.org/10.1080/00986448208910908

Glowacki, O., Moskalik, M., & Deane, G.B. (2016). The impact of glacier meltwater on the underwater noise field in a glacial bay. *Journal of Geophysical Research: Oceans, 121*, 8455–8470. https://doi.org/10.1002/2016JC012355

Gow, A.J. (1968). Bubbles and bubble pressures in Antarctic glacier ice. *Journal of Glaciology, 7*(50), 167–182. https://doi.org/10.3189/S0022143000030975

Gow, A.J., Meese, D.A., Alley, R.B., Fitzpatrick, J.J., Anandakrishnan, S., Woods, G.A., & Elder, B.C. (1997). Physical and structural properties of the Greenland Ice Sheet Project 2 ice

core: A review. *Journal of Geophysical Research, 102*(C12), 26,559–26,575.

Greisman, P. (1979). On upwelling driven by the melt of ice shelves and tidewater glaciers. *Deep-Sea Research, 26A*, 1051-1065. https://doi.org/10.1016/0198-0149(79)90047-5

Grossman, S., Johnson, H., Stokes, D., & Deane, G. (2024). Toward monitoring submarine glacier melt using hydroacoustics: The role of timescale in the signal of bubble release. *Journal of the Acoustic Society of America, 156*(3), 1820–1838. https://doi.org/10.1121/10.0028628

Hammer, R.R.I. (1883). Undersøgelser ved Jakobshavns Isfjord og nærmeste Omegn i Vinteren 1879-1880. *Meddelelser Om Grønland, 4*, 2–67. https://doi.org/10.7146/mog.v4.139546

Herron, M.M., & Langway, C.C. (1980). Firn densification: An empirical model. *Journal of Glaciology, 25*(93), 373–385.

Hirano, J., Mikami, T., & Zaiki, M. (2022). Analysis of early Japanese meteorological data and historical weather documents to reconstruct the winter climate between the 1840s and the early 1850s. *Climate of the Past, 18*, 327–339. https://doi.org/10.5194/cp-18-327-2022

Huppert, H.E., & Josberger, E.G. (1980). The melting of ice in cold stratified water. *Journal of Physical Oceanography, 10*, 953–960. https://doi.org/10.1175/1520-0485(1980)010<0953:TMOIIC>2.0.CO;2

Huppert, H.E., & Turner, J.S. (1980). Ice blocks melting into a salinity gradient. *Journal of Fluid Mechanics, 100*(2), 367–384. https://doi.org/10.1017/S0022112080001206

Johnson, H.A. (2025). *The release of bubbles and other small-scale processes at the ice-water boundary of marine-terminating glaciers* [PhD dissertation]. University of California San Diego.

Johnson, R.S. (1978). *Transport from a melting vertical ice slab in saline water* [MSc thesis]. University of New York at Buffalo.

Johnson, R.S., & Mollendorf, J.C. (1984). Transport from a vertical surface melting in saline water. *International Journal of Heat and Mass Transfer, 27*(10), 1928–1932. https://doi.org/10.1016/0017-9310(84)90176-5

Josberger, E.G. (1978). A laboratory and field study of iceberg deterioration. In A.A. Husseiny

(Ed.) *Iceberg Utilization: Proceedings of the First International Conference Held at Ames, Iowa*. Pergamon, pp.245–264.

Josberger, E.G. (1979). *Laminar and turbulent boundary layers adjacent to melting vertical ice walls in salt water* [PhD dissertation]. University of Washington.

Keithahn, E.L. (1967). Alaska Ice, In. In M.B. Sherwood [Ed.], *Alaska and its history*. University of Washinton Press, pp.173–186.

Kerr, R.C. (1994a). Dissolving driven by vigorous compositional convection. *Journal of Fluid Mechanics, 280*, 287–302. https://doi.org/10.1017/S0022112094002934

Kerr, R.C. (1994b). Melting driven by vigorous compositional convection. *Journal of Fluid Mechanics, 280*, 255–285. https://doi.org/10.1017/S0022112094002922

Kerr, R.C., & McConnochie, C.D. (2015). Dissolution of a vertical solid surface by turbulent compositional convection. *Journal of Fluid Mechanics, 765*, 211–228. https://doi.org/10.1017/jfm.2014.722

Kim, J.S., & Yethiraj, A. (2008). The effect of salt on the melting of ice: A molecular dynamics simulation study. *The Journal of Chemical Physics, 129*, 124504. https://doi.org/10.1063/1.2979247

Klein-Paste A., & Potapova, J. (2014). Thermal aspects of melting ice with deicer chemicals. *Transportation Research Record, 2440*(1), 69–75. https://doi.org/10.3141/2440-09

Kranse, A.A., & Schenk, J. (1966). Thermal free convection from a solid sphere. *Applied Scientific Research A, 15*, 397–403. https://doi.org/10.1007/BF00411573

Kuder, G.F., & Richardson, M.W. (1937). The theory of the estimation of test reliability. *Psychometrika, 2*(3), 151–160. https://doi.org/10.1007/BF02288391

Kuittinen, R., & Leppäranta, M. (1989). Real-time system for transmitting satellite data products to icebreakers. *Advances in Space Research, 9*(7), 393–397. https://doi.org/10.1016/0273-1177(89)90191-9

Langway, C.C. (1958). Bubble pressures in Greenland glacier ice. *Union Géodésique et Géophysique Internationale. Association Internationale d'Hydrologie Scientifique.*

Symposium de Chamonix, 16-24 sept. 1958, pp.336–349.

Li, N., Tuo, Y.C., Deng, Y., Li, J., Liang, R.F., & An, R.D. (2016). Heat transfer at ice-water interface under conditions of low flow velocities. *Journal of Hydrodynamics, 28*(4), 603–609. https://doi.org/10.1016/S1001-6058(16)60664-9

Lock, G.S.H. (1969). On the use of asymptotic solutions to plane ice-water problems. *Journal of Glaciology, 8*(53), 285–300. https://doi.org/10.3189/S0022143000031269

Loewe, F. (1961). On melting of fresh-water ice in sea-water. *Journal of Glaciology, 3*(30), 1051–1052. https://doi.org/10.3189/S0022143000017457

Machicoane, N., Bonaventure, J., & Volk, R. (2013). Melting dynamics of large ice balls in a turbulent swirling flow. *Physics of Fluids, 25*, 125101. https://doi.org/10.1063/1.4832515

Malyarenko, A., Wells, A.J., Langhorne, P.J., Robinson, N.J., Williams, M.J.M., & Nicholls, K.W. (2020). A synthesis of thermodynamic ablation at ice-ocean interfaces from theory, observations and models. *Ocean Modelling, 154*, 101692. https://doi.org/10.1016/J.OCEMOD.2020.101692

Marschall, E. (1977). Free convection melting of glacial ice in saline water. *Letters in Heat and Mass Transfer, 4*, 381–384. https://doi.org/10.1016/0094-4548(77)90126-6

Marson, J.M., Myers, P.G., Garbo, A., Copland, L. & Mueller, D. (2024). Sea ice-driven iceberg drift in Baffin Bay. *Journal of Geophysical Research: Oceans, 129*, e2023JC020697. https://doi:10.1029/2023JC020697

Matthews, J.B., & Quinlan, A.V. (1975). Seasonal characteristics of water masses in Muir Inlent, a fjord with tidewater glaciers. *Journal of the Fisheries Board of Canada, 32*(10), 1693–1703. https://doi.org/10.1139/f75-203

McConnochie, C.D., & Kerr, R.C. (2016a). The effect of a salinity gradient on the dissolution of a vertical ice face. *Journal of Fluid Mechanics, 791*, 589–607. https://doi.org/10.1017/jfm.2016.62

McConnochie, C.D., & Kerr, R.C. (2016b). The turbulent wall plume from a vertically distributed source of buoyancy. *Journal of Fluid Mechanics, 787*, 237–253.

https://doi.org/10.1017/jfm.2015.691

McCutchan, A.L., & Johnson, B.A. (2022). Laboratory experiments on ice melting: a need for understanding dynamics at the ice-water interface. *Journal of Marine Science and Engineering, 10*, 1008. https://doi.org/10.3390/jmse10081008

McDougall, T.J., & Barker, P.M. (2011). Getting started with TEOS-10 and the Gibbs Seawater (GSW) Oceanographic Toolbox. *SCOR/IAPSO WG127*. https://www.teos-10.org/pubs/gsw/v3_04/pdf/Getting_Started.pdf

Merk, H.J. (1954). The influence of melting and anomalous expansion on the thermal convection in laminar boundary layers. *Applied Scientific Research, 4*(5-6), 435–452. https://doi.org/10.1007/BF03185255

Morgan, V.I., & Budd, W.F. (1978). The distribution, movement and melt rates of Antarctic icebergs. In Husseiny, A.A. (Ed.) *Iceberg Utilization: Proceedings of the First International Conference Held at Ames, Iowa*. Pergamon Press, pp.220–228.

Neshyba, S. (1977). Upwelling by icebergs. *Nature, 267*, 507–508. https://doi.org/10.1038/267507a0

Neshyba, S., & Josberger, E.G. (1980). On the estimation of Antarctic iceberg melt rate. *Journal of Physical Oceanography, 10*, 1681–1685. https://doi.org/10.1175/1520-0485(1980)010<1681:OTEOAI>2.0.CO;2

Nusselt, W. (1930). Eine neue Formel für den Wärmedurchgang im Kreuzstrom. *Technische Mechanik und Thermodynamik, 1*, 417–422. https://doi.org/10.1007/BF02640212

Oborin, L.A. (1967). Special features of free convection in water at temperatures below 277°K. *Journal of Engineering Physics, 13*(6), 837–841. https://doi.org/10.1007/BF00828966

Pera, L., & Gebhart, B. (1973). On the stability of natural convection boundary layer flow over horizontal and slightly inclined surfaces. *International Journal of Heat and Mass Transfer, 16*, 1147–1163. https://doi.org/10.1016/0017-9310(73)90127-0

Petrenko, V.F., & Whitworth, R.W. (1999). *Physics of ice*. Oxford University Press.

Petrovic, J.J. (2003). Review: Mechanical properties of ice and snow. *Journal of Materials*

Science, 38, 1–6. https://doi.org/10.1023/A:1021134128038

Picard, A., Davis, R.S., Gläser, M., & Fujii, K. (2008). Revised formula for the density of moist air (CIPM-2007). *Metrologia, 45*, 149–155. https://doi.org/10.1088/0026-1394/45/2/004

Polcwiartek, K., Stern, G.A., & Wang, F. (2025). Incorporation and distribution of polycyclic aromatic hydrocarbons in experimental sea-ice. *Environmental Science & Technology, 59*(14), 7310–7319. https://doi.org/10.1021/acs.est.4c13839

Precise Simulation (2025). FEATool Multiphysics - MATLAB FEA and CFD Toolbox [Software]. https://github.com/precise-simulation/featool-multiphysics/releases/tag/1.17.5

Preston-Thomas, H. (1990). The International Temperature Scale of 1990 (ITS-90). *Metrologia, 27*, 3–10. https://doi.org/10.1088/0026-1394/27/1/002

Qadir, M., & Siriwardana, N. (2022). Water transportation via icebergs towing. In M. Qadir, V. Smakhtin, S. Koo-Oshima, & E. Guenther (Eds.) *Unconventional Water Resources*. Springer, pp.199–212. https://doi.org/10.1007/978-3-030-90146-2_9

Resolution 77/158. *International Year of Glaciers' Preservation, 2025*, 77th Session, United Nations General Assembly, 2022 (adopted 14 December 2022). https://digitallibrary.un.org/record/3998543

Robe, R.Q., Maier, D.C., & Kollmeyer, R.C. (1977). Iceberg deterioration. *Nature, 267*, 505–506. https://doi.org/10.1038/267505a0

Roddick, J.C. (1987). Generalized numerical error analysis with applications to geochronology and thermodynamics, *Geochimica et Cosmochimica Acta, 51*, 2129–2135. https://doi.org/10.1016/0016-7037(87)90261-4

Russell, H.C. (1895). Icebergs in the Southern Ocean. *Journal and Proceedings of the Royal Society of New South Wales, 29*, 221–251.

Russell, H.C. (1897). Iceberrgs in the Southern Ocean, no.2. *Journal and Proceedings of the Royal Society of New South Wales, 31*, 221–251.

Russell-Head, D.S. (1980). The melting of free-drifting icebergs. *Annals of Glaciology, 1*, 199–122. https://doi.org/10.3189/S0260305500017092

Sammakia, B., & Gebhart, B. (1983). Transport near a vertical ice surface melting in water of various salinity levels. *International Journal of Heat and Mass Transfer, 26*(10), 1439–1452. https://doi.org/10.1016/S0017-9310(83)80045-3

Schenk, J., & Schenkels, F.A.M. (1968). Thermal free convection from an ice sphere in water. *Applied Scientific Research, 19*, 465-476. https://doi.org/10.1007/BF00383941

Scholander, P.F., & Nutt, D.C. (1960). Bubble pressure in Greenland icebergs. *Journal of Glaciology, 3*(28), 671–678. https://doi.org/10.1017/S0022143000017950

Scholander, P.F., Kanwisher, J.W., & Nutt, D.C. (1956). *Science, 123*(3186), 104–105. https://www.jstor.org/stable/1749646

Shumskiy, P. (1960). Density of glacier ice. *Journal of Glaciology, 3*(27), 568–573. https://doi.org/10.3189/S0022143000023686

Spectrum Brands, Inc. (2025). Instant Ocean [Reagent]. https://www.instantocean.com/products/sea-salt-mixes/sea-salt

Steane, A.M. (2017). *Thermodynamics*. Oxford University Press.

Steenstrup, K.J.V. (1883). Bidrag til Kjendskab til Bræerne og Bræ-Isen i Nord-Grønland. Meddelelser Om Grønland, 4, 69–112. https://doi.org/10.7146/mog.v4.139528

Stefan, J. (1891). Ueber die Theorie der Eisbildung, insbesondere über die Eisbildung im Polarmeere. *Annalen Der Physik, 278*(2), 269—286. https://doi.org/10.1002/andp.18912780206

Stolfi, R., Fuhs, A., Wang, P., Bourke, R., Denner, W., Erman, R., & Clifford, W. (1978). Ice moving in sea water. In A.A. Husseiny (Ed.) *Iceberg Utilization: Proceedings of the First International Conference Held at Ames, Iowa*. Pergamon, pp.199–219.

Teller, J.T. (1975). Lake Agassiz deposits in the main offshore basin of southern Manitoba. *Canadian Journal of Earth Sciences, 13*(1), 27–43. https://doi-org.uml.idm.oclc.org/10.1139/e76-003

Thermo Scientific (2015). *Thermo Scientific Orion Star A210 Series* [Instrument]. https://documents.thermofisher.com/TFS-Assets/LED/manuals/

Orion-Star-A210-Series-Benchtop-Meter-User-Manual-EN.pdf

Timex (2026). *Mechanical vs quartz movements*. Timex. https://timex.ca/pages/mechanical-vs-quartz-movements

Tison, J.-L., Haas, C., Gowing, M.M., Sleewaegen, S., & Bernard, A. (2002). Tank study of physico-chemical controls on gas content and composition during growth of young sea ice *Journal of Glaciology, 48*, 177–191. https://doi.org/10.3189/172756502781831377

Towson, J.T. (1859). Icebergs in the Southern Ocean: A paper read before the Historic Society of Lancashire and Cheshire on the 19th November, 1857, and corrected from reports of more recent dates. Liverpool: T. Brakell, Printer.

UNESCO World Heritage Centre (n.d.). *Fortifications of Vauban*. https://whc.unesco.org/en/list/1283/

Urick. R.J. (1971). The noise of melting icebergs. *The Journal of the Acoustical Society of America, 50*(1), 337–341. https://doi.org/10.1121/1.1912637

Vancoppenolle, M., Madec, G., Thomas, M., & McDougall, T.J. (2018). Thermodynamics of sea ice phase composition revisited. *Journal of Geophysical Research: Oceans, 124*, 615–634. https://doi.org/10.1029/2018JC014611

Vanier, C.R., & Tien, C. (1970). Free convection melting of ice spheres. *AIChE Journal, 16*(1), 76–81. https://doi.org/10.1002/aic.690160116

Vishnu, H., Deane, G.B., Chitre, M., Glowacki, O., Stokes, D., & Moskalik, M. (2020). Vertical directionality and spatial coherence of the sound field in glacial bays in Hornsund Fjord. *Journal of the Acoustic Society of America, 148*(6), 3849–3862. https://doi.org/10.1121/10.0002868

Vishnu, H., Deane, G.B., Glowacki, O., Chitre, M., Johnson, H., Moskalik, M. & Stokes, D. (2023). Depth-dependence of the underwater noise emission from melting glacier ice. *JASA Express Letters, 3*(2), 020801. https://doi.org/10.1121/10.0017348

Vishnu, H., Chitre, M., Glowacki, O., Stokes, D., Johnson, H., Moskalik, M., & Deane, G.B. (2025). Acoustic activity indicates submarine melt at tidewater glaciers. *Journal of*

Glaciology, 71(e83), 1–16. https://doi.org/10.1017/jog.2025.10061

Weeks, W.F., & Campbell, W.J. (1973). Icebergs as a fresh-water source: an appraisal. *Journal of Glaciology, 12*(65), 207–233. https://doi.org/10.3189/S0022143000032044

Wells, A.J., & Worster, M.G. (2008). A geophysical-scale model of vertical natural convection boundary layers. *Journal of Fluid Mechanics, 609*, 111–137. https://doi.org/10.1017/S0022112008002346

Wells, A.J., & Worster, M.G. (2011). Melting and dissolving of a vertical solid surface with laminar compositional convection. *Journal of Fluid Mechanics, 687*, 118–140. https://doi.org/10.1017/jfm.2011.322

Weiss, K. (2024). *Direct measurements of melt rate and boundary layer characteristics at Alaskan icebergs* [MSc thesis]. Oregon State University.

Wengrove, M.E., Pettit, E.C., Nash, J.D., Jackson, R.H., & Skyllingstad, E.C. (2023). Melting of glacier ice enhanced by bursting air bubbles. *Nature Geoscience, 16*, 871–876.

Wheeler, J. (2014). Dramatic effects of stress on metamorphic reactions. *Geology, 42*(8), 647–650. https://doi.org/10.1130/G35718.1

White, F.M. (1979). *Fluid mechanics*. McGraw-Hill, Inc.

White, F.M., Spaulding, M.L., & Gominho, L. (1980). *Theoretical estimates of the various mechanisms involved in iceberg deterioration in the open ocean environment* (Report No. CG-D-62-80). United States Coast Guard.

Wilkinson, M.D., Dumontier, M., Aalbersberg, I.J., Appleton, G., Axton, M., Baak, A., Blomberg, N., Boiten, J.W., Bonino da Silva Santos, L., Bourne, P.E., Bouwman, J., Brookes, A., Clark, T., Crosas, M., Dillo, I., Dumon, O., Edmunds, S., Evelo, C.T., Finkers, R., Gonzalez-Beltran, A., ... & Mons, B. (2016). The FAIR Guiding Principles for scientific data management and stewardship. *Scientific Data, 3*, 160018. https://doi.org/10.1038/sdata.2016.18

Woods, A.W. (1991). Fluid mixing during melting. *Physics of Fluids, 3*, 1393–1404. https://doi.org/10.1063/1.858018

Woods, A.W. (1992). Melting and dissolving. *Journal of Fluid Mechanics, 239*, 429–448. https://doi.org/10.1017/S0022112092004476

WTW GmbH (2008). *Handheld Conductivity Meter* (Model 330i) [Instrument]. https://www.xylemanalytics.com/en/File%20Library/Resource%20Library/WTW/01%20Manuals/ba52302e04_Cond_330i-340i.pdf

Yang, R., Howland, C.J., Liu, H.-R., Verzicco, R., & Lohse, D. (2023). Ice melting in salty water: layering and non-monotonic dependence on the mean salinity *Journal of Fluid Mechanics, 969*, R2-1-R2-12. 0.1017/jfm.2023.582https://doi.org/0.1017/jfm.2023.5820.1017/jfm.2023.582

Yen, Y.-C. (1968). Onset of convection in a layer of water formed by melting ice from below. *The Physics of Fluids, 11*(6), 1263–1270. https://doi.org/10.1063/1.1692096

Yen, Y.-C., & Galea, F. (1969). Onset of convection in a water layer formed continuously by melting ice. *The Physics of Fluids, 12*(3), 509–516. https://doi.org/10.1063/1.1692513

Young, W.C., & Budynas, R.G. (2002). *Roark's formulas for stress and strain* (7th ed.). McGraw-Hill.

Zaffarano, D.J. (1979). Introduction. In A.A. Husseiny (Ed.) *Iceberg Utilization: Proceedings of the First International Conference Held at Ames, Iowa* (p.xix). Pergamon.

Zuo, H., Balmaseda, M.A., Tietsche, S., Mogensen, K., & Mayer, M. (2019). The ECMWF operational ensemble reanalysis-analysis system for ocean and sea ice: A description of the system and assessment. *Ocean Science, 15*, 779–808. https://doi.org/10.5194/os-15-779-2019

Appendix A

Selected mathematical models of phase change

A.1 Similarity solution for flow along a vertical ice wall (Gebhart & Pera, 1971)

This model, referred to in literature as "the similarity solution" describes the flow of an aqueous solution with composition C and temperature T along a vertical ice wall, using the dimensional numbers Nusselt (Nu), Grashof (Gr), Prandtl (Pr), and Schmidt (Sc), and can take two forms. The form for temperature is

$$\frac{\mathrm{Nu}_{x,T}}{\sqrt[4]{\mathrm{Gr}_{x,T}}} = C\sqrt[4]{\mathrm{Pr}\left[1 + N\frac{\mathrm{Pr}}{\mathrm{Sc}}\right]} \tag{A.1}$$

where

$$\mathrm{Gr}_{x,T} = \frac{g\beta x^3 (R_0 - T_\infty)}{\nu^2} \tag{A.2}$$

and

$$\mathrm{Nu}_{x,T} = -\frac{\phi'(0)}{\sqrt{2}}\sqrt[4]{P \cdot \mathrm{Gr}_{x,T} + Q \cdot \mathrm{Gr}_{x,C}} \tag{A.3}$$

The form for concentration is

$$\frac{\mathrm{Nu}_{x,C}}{\sqrt[4]{|\mathrm{Gr}_{x,C}|}} = C\sqrt[4]{\mathrm{Sc}\left|1 + N\frac{\sqrt{\frac{\mathrm{Sc}}{\mathrm{Pr}}} + N}{N}\right|} \tag{A.4}$$

where

$$\mathrm{Gr}_{x,C} = \frac{g\beta^* x^3 (C_0 - C_\infty)}{\nu^2} \tag{A.5}$$

and

$$\mathrm{Nu}_{x,C} \;=\; -\frac{C'(0)}{\sqrt{2}}\sqrt[4]{P \cdot \mathrm{Gr}_{x,T} \;+\; Q \cdot \mathrm{Gr}_{x,C}} \tag{A.6}$$

In both cases,

$$N \;=\; \frac{\mathrm{Gr}_{x,C}}{\mathrm{Gr}_{x,T}} \;=\; \frac{\beta^{*}\,(C_0 \;-\; C_\infty)}{\beta\,(T_0 \;-\; T_\infty)} \tag{A.7}$$

$$\mathrm{Pr} \;=\; \frac{\mu c_p}{k} \tag{A.8}$$

$$\mathrm{Sc} \;=\; \frac{\mu}{\rho D} \tag{A.9}$$

The remaining symbols are as follows:

x is the vertical distance along the wall,

k, μ, and ν are the thermal conductivity, kinematic viscosity, and dynamic viscosity of the solution,

c_p is the specific heat of the solution at constant pressure,

ρ is its density,

D is the molecular diffusivity of the solute in the solution,

β is the volumetric coefficient of thermal expansion, and β^{*} is the volumetric coefficient of expansion with concentration,

ϕ is a dimensionless temperature and ϕ' is its first time derivative,

C is a dimensionless concentration and C' is its first time derivative,

C_0 and C_∞ are the concentration at the interface and the far field, respectively, and likewise

T_0 and T_∞ for temperature,

and P and Q are parameters.

A.2 Model for non-monotonic density (Gebhart & Mollendorf, 1978)

Gebhart and Mollendorf (1978) give the buoyancy density difference as

$$\begin{aligned} \frac{\rho_\infty - \rho}{\rho_m(s_\infty, p)\alpha(s_\infty, p)\,|t_0 - t_\infty|^q} &= [1 + AS][1 + BS]\,|\phi - R - QS|^q - |R|^q - PS \\ &= W(\eta, \phi, S, A, B, R, P, Q, q) \end{aligned} \tag{A.10}$$

where

$$R = \frac{t_m(s_\infty, p) - t_\infty}{t_0 - t_\infty} = \frac{T_m - t_\infty}{t_0 - t_\infty} \tag{A.11}$$

$$S = \frac{s - s_\infty}{s_0 - s_\infty} \tag{A.12}$$

$$A' \equiv \frac{A}{\Delta s_0} \equiv \frac{g_1(p)\rho_m(0,1)}{\rho_m(s_\infty, p)} \tag{A.13}$$

$$B' \equiv \frac{B}{\Delta s_0} \equiv \frac{g_2(p)\alpha(0,1)}{\alpha(s_\infty, p)} \tag{A.14}$$

$$Q' \equiv \frac{Q\Delta t_0}{\Delta s_0} \equiv g_3(p)t_m(0,1) \tag{A.15}$$

$$P' \equiv \frac{P|\Delta t_0|^q}{\Delta s_0} \equiv \frac{g_1(p)\rho_m(0,1)}{\alpha(s_\infty,p)\rho_m(s_\infty,p)} = \frac{A'}{\alpha(s_\infty,p)} \tag{A.16}$$

$$\alpha(s,p) = \alpha(s_\infty,1)\ [1 + B(s_0,s_\infty,p)S + B'(s_0,s_\infty,p)\ S(S+E)] \tag{A.17}$$

$$t_m(s,p) = t_m(s_\infty,p)\ [1 + C(s_0,s_\infty,p)\ S + C'(s_0,s_\infty,p)\ S(S+E)] \tag{A.18}$$

$$q(s,p) = q(s_\infty,p)\ [1 + D(s_0,s_\infty,p)\ S + D'(s_0,s_\infty,p)\ S(S+E)] \tag{A.19}$$

t, s, and p are temperature, salinity, and pressure (in atm),

ρ is density,

the subscripts 0, ∞, and m denotes the interface, the far field and a maximum, respectively,

T_m is the extremum temperature for the conditions of the local ambient medium,

(0, 1) indicates the condition of zero salinity and one atmosphere,

ϕ is the non-dimensional temperature function of Gebhart and Pera (1971),

η is a similarity variable,

g_1, g_2, and g_3 are quadratics of pressure, the coefficients of which are given in the appendix of the paper,

and A to E are coefficients that arise in the solution.

A.3 Solution for a horizontal interface (Gade, 1979)

Gade (1979) wrote a system of five equations of which the first relates to the ice, the second and third to the boundary layer under the ice, and the last two to the turbulent layer, thusly:

$$\begin{cases} \dfrac{\partial T}{\partial z} - \dfrac{w\rho c_i}{\kappa}(T - T_0) = 0 \\ \dfrac{\partial T}{\partial z} - \dfrac{w\rho c_w}{k}\left(T - T_1 + \dfrac{c_i}{c_w}(T_1 - T_0) + \dfrac{L}{c_w}\right) = 0 \\ \dfrac{\partial}{\partial z}(\rho S) - \dfrac{w\rho S}{k_s} = 0 \\ \dfrac{\partial T}{\partial \zeta} - \dfrac{w\rho c_w}{K}\left(T - T_1 + \dfrac{c_i}{c_w}(T_1 - T_0) + \dfrac{L}{c_w}\right) = 0 \\ \dfrac{\partial}{\partial \zeta}(\rho S) - \dfrac{w\rho S}{K_s} = 0 \end{cases} \tag{A.20}$$

where

T and S are temperature and salinity,

w denotes the velocity caused by melting or thermal expansion or contraction,

ζ is a vertical coordinate originating at the lower limit of the boundary layer,

κ is the thermal conductivity of the ice,

k and k_s are the conductivity of heat and molecular diffusion of salt in the boundary layer,

K and K_s are the eddy conductivity and diffusivity in the outer region,

ρ is density,

c is specific heat,

and the subscripts i and w refer to ice and water, but are omitted where the context is obvious.

A.4 Equation for melt superheat (Woods, 1992)

Woods (1992) obtained an equation for the non-dimensionalized imposed melt superheat, thus:

$$\hat{T}_m = F(-\lambda)\left(\lambda \cdot \mathrm{Ste} - \hat{T}_s \frac{\mu K}{F(\lambda\,/\,K)} + \left(\frac{1}{F(-\lambda)} + \frac{\mu K}{F(\lambda\,/\,K)}\right)\left(\frac{\lambda F(-\lambda\,/\,\epsilon)}{\epsilon + \lambda F(-\lambda\,/\,\epsilon)}\right)\right) \tag{A.21}$$

where

$$\text{Ste} = \frac{\rho_s L}{\rho_m c_m \Gamma C_m} \tag{A.22}$$

is the Stefan number,

$$K = \left(\frac{\kappa_s}{\kappa_l}\right)^{1/2} \tag{A.23}$$

$$\mu = \frac{\rho_s c_s}{\rho_m c_m} \tag{A.24}$$

$$\epsilon = \left(\frac{D_l}{\kappa_l}\right)^{1/2} \ll 1 \tag{A.25}$$

$$F(x) = \pi^{1/2}\, e^{z^2} \operatorname{erfc} x \tag{A.26}$$

and is tabulated, according to Woods, in *Conduction of Heat in Solids* by Carslaw and Jaeger (1986, p.485), which I have not verified,

$\hat{T}_s$ is the imposed solid temperature,

C_m is the composition of the melt,

L is latent heat,

D_l is the compositional diffusivity in the liquid phase,

κ is thermal diffusivity and ρ is density,

the subscripts l, s, and m denote liquid, solid, and melt,

and λ is the rate of phase change. I did not find a definition of Γ.

Appendix B

Legacy data

Temperature is in °C, salinity is as listed in the original, recession rates are converted from original units to kg m^{-2} day^{-1}, and Agassiz model rates are in kg m^{-2} day^{-1}. Sources are as follows:

- BG76: Bendell and Gebhart (1976)
- J78: Johnson (1978)
- J79: Josberger (1979)
- C81: Carey (1981)
- GW82: Gebhart and Wang (1982)
- SG83: Sammakia and Gebhart (1983)
- JM84: Johnson and Mollendorf (1984)
- KM15: Kerr and McConnochie (2015)

Table B.1
Legacy data.

Index	Source	Temperature	Salinity	Recession	Agassiz rate
1	BG76	2.2	0.000	82.029	37.998
2	BG76	2.7	0.000	98.679	51.055
3	BG76	3.0	0.000	105.006	59.810
4	BG76	3.3	0.000	114.663	69.255
5	BG76	4.0	0.000	128.427	93.981
6	BG76	4.4	0.000	131.535	109.798
7	BG76	4.9	0.000	125.097	131.296
8	BG76	5.0	0.000	122.988	135.826
9	BG76	5.5	0.000	116.439	159.627
10	BG76	5.6	0.000	117.105	164.617
11	BG76	5.8	0.000	145.854	174.828

Index	Source	Temperature	Salinity	Recession	Agassiz rate
12	BG76	6.0	0.000	168.387	185.345
13	BG76	6.8	0.000	265.290	230.486
14	BG76	7.0	0.000	290.598	242.538
15	BG76	8.0	0.000	336.663	307.405
16	BG76	8.5	0.000	419.136	342.716
17	BG76	9.1	0.000	478.632	387.622
18	BG76	10.1	0.000	541.569	468.604
19	BG76	11.7	0.000	678.987	614.137
20	BG76	13.3	0.000	863.025	779.315
21	BG76	16.9	0.000	1415.250	1222.792
22	BG76	19.9	0.000	1845.486	1668.328
23	BG76	25.2	0.000	2505.714	2624.229
24	J78	24.4	35.039	2226.799	2453.136
25	J78	22.3	35.110	2023.833	2127.993
26	J78	21.7	35.116	1950.345	2039.255
27	J78	20.9	35.319	1826.699	1919.873
28	J78	20.6	35.144	1686.722	1874.952
29	J78	17.1	36.612	1461.592	1443.348
30	J78	16.7	35.179	1404.435	1357.336
31	J78	12.0	35.175	1006.667	839.526
32	J78	8.1	35.152	662.557	498.874
33	J78	4.8	35.129	372.105	273.909
34	J78	3.7	35.118	282.287	211.792
35	J78	2.9	35.116	212.298	168.228
36	J78	1.5	35.102	134.145	106.892
37	J78	0.3	35.094	65.323	62.296
38	J78	-0.8	35.083	18.664	18.415
39	J78	-1.1	35.081	4.666	13.636
40	J79	-0.1	29.900	47.952	19.019
41	J79	1.6	29.000	97.822	90.643
42	J79	1.6	29.000	145.774	90.643
43	J79	2.0	30.000	149.610	111.898
44	J79	2.0	30.000	145.774	111.898
45	J79	2.0	30.000	147.692	111.898
46	J79	2.2	30.000	181.259	120.367
47	J79	2.2	30.000	194.685	120.367
48	J79	2.7	34.400	206.194	156.385

Index	Source	Temperature	Salinity	Recession	Agassiz rate
49	J79	2.7	34.400	210.989	156.385
50	J79	3.4	30.000	220.579	176.215
51	J79	6.8	33.950	601.318	398.394
52	J79	6.8	33.950	574.465	398.394
53	J79	10.8	34.100	908.211	717.563
54	J79	16.3	35.200	1368.550	1310.393
55	C81	1.0	5.000	35.236	21.114
56	C81	2.0	5.000	68.414	44.176
57	C81	3.0	5.000	98.928	73.766
58	C81	0.0	10.000	11.588	7.624
59	C81	1.0	10.000	41.169	28.953
60	C81	2.0	10.000	71.199	55.934
61	C81	2.5	10.000	81.491	71.543
62	C81	0.0	15.000	17.558	12.470
63	C81	1.0	15.000	44.923	38.006
64	C81	-0.5	20.000	10.619	3.208
65	C81	0.0	20.000	22.159	19.119
66	C81	-1.0	24.000	4.371	4.372
67	C81	-1.0	25.000	5.170	5.109
68	C81	-1.0	26.000	5.909	5.891
69	C81	10.0	1.000	398.375	460.224
70	C81	10.0	1.060	371.736	460.238
71	C81	15.0	1.000	848.816	966.984
72	C81	15.0	2.000	813.701	958.473
73	C81	15.0	2.835	721.676	952.016
74	C81	20.0	1.000	1356.169	1659.323
75	C81	20.0	2.000	1319.843	1635.921
76	C81	20.0	3.000	1295.626	1614.161
77	C81	20.0	4.000	1247.191	1594.044
78	C81	20.0	5.000	1149.111	1575.570
79	C81	20.0	5.082	1109.152	1574.129
80	GW82	2.0	0.000	53.946	33.312
81	GW82	3.0	0.000	95.349	59.810
82	GW82	3.5	0.000	119.103	75.936
83	GW82	3.7	0.000	131.091	82.924
84	GW82	4.0	0.000	146.298	93.981
85	GW82	4.1	0.000	145.854	97.820

Index	Source	Temperature	Salinity	Recession	Agassiz rate
86	GW82	4.2	0.000	166.611	101.736
87	GW82	4.8	0.000	183.594	126.843
88	GW82	5.0	0.000	124.320	135.826
89	GW82	5.1	0.000	122.544	140.433
90	GW82	5.3	0.000	121.101	149.876
91	GW82	5.6	0.000	193.029	164.617
92	GW82	5.8	0.000	201.132	174.828
93	GW82	6.0	0.000	226.107	185.345
94	GW82	6.8	0.000	253.968	230.486
95	GW82	7.0	0.000	279.498	242.538
96	GW82	7.5	0.000	357.198	274.013
97	GW82	9.7	0.000	482.628	435.290
98	SG83	-0.2	30.000	-9.226	17.607
99	SG83	3.0	30.000	204.840	156.178
100	SG83	5.0	30.000	423.745	259.223
101	SG83	-1.8	35.000	-18.630	2.158
102	SG83	1.0	35.000	53.039	86.354
103	SG83	3.0	35.000	211.275	175.185
104	JM84	21.1	35.000	1824.748	1939.468
105	JM84	17.3	35.000	1462.433	1432.396
106	JM84	12.2	35.000	1011.187	853.983
107	JM84	8.3	35.000	662.047	514.070
108	JM84	5.3	35.000	372.196	302.598
109	JM84	4.4	35.000	283.264	249.643
110	JM84	3.6	35.000	204.214	204.008
111	JM84	2.6	35.000	131.751	156.335
112	JM84	1.7	35.000	62.582	115.983
113	JM84	0.8	35.000	6.588	77.571
114	JM84	1.2	35.000	23.056	93.788
115	JM84	21.7	0.000	2019.080	1974.710
116	JM84	20.4	0.000	1847.804	1744.087
117	JM84	18.4	0.000	1501.958	1438.197
118	JM84	17.3	0.000	1337.270	1275.447
119	JM84	13.1	0.000	862.967	760.131
120	JM84	10.2	0.000	523.709	478.304
121	JM84	9.8	0.000	484.184	443.347
122	JM84	8.4	0.000	365.608	337.823

Index	Source	Temperature	Salinity	Recession	Agassiz rate
123	JM84	6.8	0.000	230.564	228.681
124	JM84	6.4	0.000	164.688	208.053
125	JM84	5.7	0.000	108.694	169.720
126	JM84	3.7	0.000	121.869	84.398
127	KM15	1.3	0.000	105.494	19.330
128	KM15	2.3	0.000	163.037	40.456
129	KM15	3.1	0.000	220.579	62.881
130	KM15	3.8	0.000	249.350	86.533
131	KM15	4.2	0.000	287.712	101.736
132	KM15	4.7	0.000	287.712	122.467
133	KM15	5.4	0.000	326.074	154.713

Appendix C

Data from Manitoba experiment

Temperature is in °C, salinity is absolute, duration is in minutes, weights are in g, and recession rates are in kg m^{-2} day^{-1}. Geometry "B" is ball, "C" is cylinder.

Table C.1
Data from Manitoba experiment.

Index	Temperature	Salinity	Geometry	Duration	Start weight	End weight	Recession	Agassiz rate
1	2.8	0.37	B	45	46.7	24.0	121.3671	53.5259
2	23.5	0.37	B	7	43.2	2.2	2404.1598	2280.8116
3	3.9	0.37	B	45	45.6	24.9	110.5089	89.5402
4	10.2	0.37	B	4	44.2	36.3	427.9535	480.2129
5	16.2	0.37	B	4	43.5	25.9	1063.5836	1127.2275
6	19.6	0.37	B	4	45.6	20.1	1626.5271	1614.4748
7	21.6	0.37	B	4	48.2	16.9	2044.4561	1941.8461
8	24.2	0.37	B	4	45.3	12.5	2370.1316	2412.5617
9	5.0	0.37	B	45	44.0	20.5	134.3846	139.2438
10	5.3	0.98	B	45	44.0	19.5	142.0473	155.3398
11	5.0	1.61	B	45	44.4	19.4	144.6342	143.2770
12	5.1	2.23	B	45	47.1	20.5	148.1086	149.9596
13	22.4	0.37	B	4	43.9	14.3	2096.6300	2081.2476
14	25.5	0.37	B	4	45.0	11.7	2451.5230	2667.0518
15	1.6	2.84	B	45	43.0	35.0	39.3471	29.0802
16	26.7	0.37	B	4	43.3	7.2	3011.3744	2913.2867
17	21.4	0.37	B	4	43.1	15.9	1889.1355	1907.7505
18	15.6	0.37	B	4	43.3	26.2	1031.6171	1050.2994
19	4.5	0.37	B	4	44.1	43.2	46.1067	117.2132
20	9.7	0.37	B	4	44.4	36.8	409.2661	438.5593
21	6.1	2.84	B	4	45.1	42.7	122.4985	202.1475
22	13.3	0.37	B	4	43.8	30.0	795.9442	780.5787
23	11.2	2.86	B	4	45.2	35.2	542.7548	566.1745
24	15.5	0.37	B	4	44.7	27.2	1031.8618	1037.7422
25	14.6	2.86	B	4	46.6	31.1	864.6208	909.3554
26	16.8	0.37	B	4	44.7	23.8	1281.3095	1206.8726
27	18.3	0.37	B	4	47.0	22.1	1529.0720	1417.8723
28	16.8	2.87	B	4	44.8	25.4	1166.1906	1167.7175
29	19.6	2.86	B	4	43.8	20.4	1508.3425	1560.0609
30	19.3	2.85	B	4	45.5	21.4	1512.1908	1516.3470
31	21.4	2.90	B	4	43.9	16.6	1860.9128	1835.8985
32	22.3	2.88	B	4	43.2	14.3	2060.7147	1983.0618
33	3.2	3.86	B	45	44.5	27.3	90.1999	75.5250
34	2.4	4.86	B	45	45.7	37.7	37.6206	53.5680
35	2.1	3.36	B	45	47.0	34.4	60.3860	41.9079
36	2.3	5.86	B	45	43.3	32.3	55.3518	53.1993

Index	Temperature	Salinity	Geometry	Duration	Start weight	End weight	Recession	Agassiz rate
37	2.2	4.36	B	45	43.3	31.7	58.7124	46.8251
38	1.8	6.87	B	45	47.9	33.3	70.1972	41.8982
39	2.3	5.38	B	45	48.0	33.6	68.9935	52.0160
40	2.1	6.36	B	45	44.0	32.3	58.5394	48.8078
41	1.7	7.87	B	45	44.7	35.9	42.3571	41.4128
42	2.1	7.36	B	45	45.4	36.7	41.3588	51.1801
43	1.7	8.89	B	45	45.2	36.7	40.4703	43.5921
44	20.6	8.37	B	4	48.1	25.1	1350.5562	1609.6544
45	2.1	8.33	B	45	46.0	33.2	62.5009	53.4929
46	1.7	9.88	B	45	44.6	35.4	44.5144	45.7563
47	6.3	8.31	B	4	46.9	42.3	232.4081	232.2409
48	10.6	8.30	B	4	44.6	35.7	483.1644	519.9688
49	8.4	8.29	B	4	45.0	38.4	348.9748	359.0832
50	12.3	8.34	B	4	44.3	34.3	551.0839	663.8106
51	2.5	10.85	B	45	45.0	30.3	74.4052	72.3928
52	14.4	8.32	B	4	45.1	32.7	689.2155	864.9270
53	18.4	8.30	B	4	48.3	27.3	1201.7061	1320.0586
54	2.5	11.86	B	45	44.9	30.4	73.3784	76.8764
55	2.3	5.36	B	45	44.3	33.4	53.8407	51.9637
56	2.4	12.86	B	45	44.5	33.3	55.2860	74.6390
57	4.1	8.35	B	4	43.9	43.2	35.9154	123.1839
58	2.4	13.86	B	45	46.1	30.7	76.9608	77.4327
59	2.6	9.37	B	45	44.6	30.2	73.1965	71.5747
60	1.0	5.35	B	45	46.3	43.0	14.8056	22.4251
61	2.3	14.85	B	45	44.4	32.2	60.9029	76.7604
62	1.8	10.37	B	45	44.5	35.6	43.0199	49.6742
63	2.1	15.85	B	45	46.1	34.1	58.0655	72.7000
64	1.8	11.38	B	45	44.9	34.6	50.0789	51.9859
65	2.5	16.85	B	45	47.1	27.7	99.1891	89.5774
66	2.4	12.37	B	45	45.7	29.6	81.6102	73.2844
67	0.5	10.86	B	45	46.0	43.5	11.1984	19.5423
68	2.1	17.86	B	45	44.5	28.6	82.2307	78.1546
69	2.1	13.36	B	45	44.3	32.3	59.8952	66.1216
70	0.9	10.85	B	45	49.6	45.0	19.8636	28.8599
71	1.9	14.38	B	45	45.8	36.3	45.1801	62.2953
72	2.0	18.85	B	45	46.5	34.3	58.7452	77.3526
73	7.1	14.35	B	4	44.0	37.7	337.6974	302.5835
74	10.7	14.34	B	4	43.3	32.3	622.7080	547.2107
75	0.4	10.82	B	45	45.2	42.6	11.7964	16.2306
76	14.3	14.36	B	4	44.2	29.4	856.0605	857.9038
77	15.8	14.32	B	4	45.1	29.1	921.5459	1006.6791
78	17.3	14.36	B	4	50.2	28.5	1208.6661	1167.0299
79	18.3	14.30	B	4	44.2	24.2	1225.4709	1280.2732
80	19.3	14.36	B	4	44.7	20.5	1547.3092	1398.5425
81	20.0	14.35	B	4	47.3	25.0	1319.3449	1484.3943
82	2.4	19.86	B	45	47.4	26.3	109.2675	94.8504

Index	Temperature	Salinity	Geometry	Duration	Start weight	End weight	Recession	Agassiz rate
83	0.6	10.86	B	45	46.0	44.6	6.2196	21.4519
84	2.7	20.85	B	45	43.6	21.3	126.6147	109.5418
85	25.1	14.36	B	4	44.5	16.0	1950.6722	2184.8390
86	2.7	21.85	B	45	43.7	23.0	114.8989	112.7530
87	2.4	10.86	B	45	45.8	32.7	64.3665	69.1695
88	2.2	15.35	B	45	43.9	30.4	68.8761	74.7388
89	0.1	14.34	B	45	44.2	43.4	3.6347	14.9036
90	2.3	22.86	B	45	43.7	23.9	108.6969	100.0793
91	1.6	16.36	B	45	45.2	35.2	48.2449	57.5867
92	0.4	14.33	B	45	44.6	41.5	14.2506	20.3708
93	2.3	23.86	B	45	48.2	28.4	99.6332	103.1553
94	1.9	17.36	B	45	43.5	32.7	54.0488	69.9326
95	2.0	18.36	B	45	43.1	28.8	74.6654	76.0283
96	2.1	24.86	B	45	44.2	22.4	121.3904	98.2991
97	7.1	18.31	B	4	45.7	38.3	389.5179	321.7736
98	9.8	18.29	B	4	44.0	32.1	671.1181	500.1295
99	-0.0	14.37	B	45	47.9	46.2	7.3641	0.2699
100	24.2	18.36	B	4	44.1	16.3	1900.5610	2039.1692
101	12.8	19.18	B	4	45.9	32.2	760.2934	744.6871
102	15.6	19.13	B	4	43.3	26.2	1031.6171	1006.0949
103	16.9	19.18	B	4	43.4	23.9	1207.4483	1140.4978
104	0.2	14.35	B	45	49.2	46.9	9.8249	16.8090
105	21.8	19.16	B	4	45.2	20.9	1538.7305	1717.5204
106	2.1	14.33	B	45	44.9	33.5	55.9902	68.6515
107	1.9	25.85	B	45	45.1	26.3	99.1892	93.4350
108	2.6	26.85	B	45	48.3	22.7	137.2387	125.0934
109	23.6	19.15	B	4	44.4	18.7	1689.4647	1957.9303
110	18.8	19.15	B	4	44.7	25.4	1161.1520	1350.6766
111	15.4	19.16	B	4	45.9	29.1	961.4108	986.3727
112	13.8	19.17	B	4	44.4	28.1	954.1880	833.8910
113	12.6	19.12	B	4	44.1	30.4	785.0472	727.0380
114	11.6	19.16	B	4	44.4	32.2	685.1580	643.7501
115	10.3	19.15	B	4	49.2	38.0	575.9681	542.1469
116	1.8	19.16	B	45	43.6	32.9	53.4029	71.2170
117	7.7	19.12	B	4	47.2	39.7	385.9267	362.7436
118	2.4	27.85	B	45	44.5	22.4	122.7421	119.9381
119	-0.1	19.16	B	45	44.2	44.0	0.9045	3.5481
120	2.6	28.85	B	45	43.7	18.2	151.0491	131.8819
121	0.5	19.12	B	45	44.2	40.1	19.1187	31.2992
122	2.6	29.85	B	45	44.3	21.5	128.3230	135.3305
123	1.7	19.16	B	45	46.3	32.4	68.2248	67.7974
124	2.4	30.36	B	45	45.4	22.0	129.6198	128.2437
125	2.2	20.36	B	45	45.2	26.9	95.8332	88.8252
126	2.1	30.85	B	46	47.0	24.0	120.0035	116.9474
127	2.5	21.35	B	45	43.7	26.9	89.0846	103.2347
128	0.1	19.20	B	45	44.6	43.9	3.1587	20.9669

Index	Temperature	Salinity	Geometry	Duration	Start weight	End weight	Recession	Agassiz rate
129	2.7	22.36	B	45	46.7	16.5	178.7247	114.4108
130	1.9	31.35	B	45	44.3	27.4	88.6776	110.0860
131	8.8	22.76	B	4	47.1	37.4	509.0829	457.1559
132	12.6	22.72	B	4	46.7	30.2	927.8852	753.6950
133	15.0	22.76	B	4	46.4	27.0	1130.5955	975.8035
134	17.0	22.68	B	4	43.9	23.2	1287.1745	1180.1308
135	2.1	31.85	B	45	43.6	20.3	134.0796	120.1782
136	23.3	22.75	B	4	44.0	18.2	1714.6238	1947.4826
137	2.6	32.35	B	45	45.3	17.7	162.3597	144.0689
138	1.6	32.86	B	45	46.9	28.5	93.4358	102.3279
139	2.3	22.76	B	45	43.2	23.9	106.4131	99.7638
140	1.6	33.36	B	45	47.5	27.2	104.0176	103.8596
141	2.4	23.35	B	45	45.6	23.4	120.6458	105.5414
142	2.0	24.35	B	45	45.9	34.2	56.6498	92.9205
143	1.2	33.85	B	45	43.9	30.9	65.9940	89.1800
144	1.6	34.36	B	45	44.5	23.4	115.7410	106.9290
145	2.2	25.35	B	45	46.7	24.7	116.6631	103.7687
146	1.6	34.85	B	46	46.3	27.5	95.8775	108.4572
147	2.1	26.35	B	45	48.0	27.6	103.6776	102.8301
148	2.3	27.35	B	45	46.4	29.5	85.2767	114.1075
149	1.5	35.35	B	45	44.2	24.0	110.2840	105.8401
150	1.6	35.85	B	45	46.5	27.3	99.0594	111.6190
151	1.9	36.34	B	45	44.2	20.8	133.0391	126.1852
152	1.9	36.84	B	45	44.5	21.9	126.3210	127.8250
153	6.7	27.45	B	4	46.3	40.2	314.7089	348.9656
154	9.3	27.42	B	4	44.3	34.6	533.0883	527.3866
155	11.4	27.46	B	4	44.8	30.4	820.4761	695.0694
156	13.7	27.46	B	4	47.9	29.4	1039.0169	902.0381
157	15.5	27.46	B	4	45.7	27.3	1074.9003	1081.2292
158	18.1	27.46	B	4	43.3	21.9	1359.8678	1366.8081
159	2.3	37.35	B	45	48.7	20.3	156.4695	147.8354
160	21.2	27.46	B	4	44.1	19.1	1638.4314	1748.6515
161	23.3	27.46	B	4	44.5	17.2	1833.5291	2032.8485
162	2.3	37.85	B	45	45.0	19.4	147.3235	149.6174
163	-0.4	22.81	B	45	44.7	44.3	1.7982	6.0482
164	2.2	38.35	B	45	44.9	17.8	159.7478	146.6844
165	2.0	38.85	B	45	44.2	20.5	135.2892	139.1557
166	-0.2	22.80	B	90	46.6	45.0	3.5282	7.3392
167	1.7	39.35	B	45	44.3	21.8	126.1428	127.3163
168	2.0	22.78	B	45	43.8	30.0	70.7506	88.3659
169	1.6	39.85	B	45	44.9	22.3	125.2464	124.5786
170	-0.4	22.77	B	90	44.8	42.8	4.5437	6.2381
171	0.1	22.75	B	90	47.1	41.4	12.8702	27.7366
172	2.3	28.36	B	45	44.9	24.3	111.4014	119.4730
173	0.5	22.67	B	90	45.4	36.1	22.2214	38.4526
174	2.6	29.36	B	45	47.0	25.5	112.6979	133.6337

Index	Temperature	Salinity	Geometry	Duration	Start weight	End weight	Recession	Agassiz rate
175	2.8	40.36	B	45	45.7	14.4	193.4674	183.6043
176	6.0	40.36	B	4	45.0	39.5	288.1744	386.3248
177	9.1	40.32	B	4	45.4	33.8	636.6545	636.5158
178	11.7	40.35	B	4	45.9	30.6	862.4002	892.0480
179	13.9	40.35	B	4	46.1	27.4	1087.7204	1139.8254
180	15.0	40.35	B	4	47.2	26.2	1226.7382	1274.8549
181	15.9	40.36	B	4	44.6	23.1	1330.5288	1390.8421
182	16.9	40.36	B	4	45.1	22.2	1427.0898	1525.3893
183	19.3	39.78	B	4	45.3	19.8	1637.4689	1851.3005
184	2.3	30.35	B	45	43.5	20.1	135.1458	123.8741
185	5.5	30.36	B	4	47.3	42.8	225.8323	292.7857
186	9.9	30.34	B	4	44.2	33.3	606.7616	599.6019
187	12.2	30.35	B	4	48.3	33.4	802.7956	797.3894
188	14.1	30.36	B	4	45.3	27.0	1076.0599	980.0699
189	17.7	30.36	B	4	47.6	24.4	1378.8114	1374.0035
190	21.0	30.36	B	4	43.4	19.0	1611.5293	1789.9846
191	0.8	22.78	B	90	48.3	35.5	30.0802	46.9156
192	3.2	32.36	B	45	45.2	14.5	190.2996	172.4472
193	6.0	32.36	B	4	46.5	41.5	254.9357	334.8572
194	10.0	32.33	B	4	44.8	35.2	522.6752	627.5297
195	13.0	32.36	B	4	46.8	30.2	932.7790	899.9588
196	15.1	32.35	B	4	45.1	26.3	1115.8788	1117.0648
197	16.5	32.36	B	4	44.2	23.3	1294.6537	1274.3496
198	19.6	32.35	B	4	44.5	20.0	1579.9528	1656.6177
199	2.2	27.47	B	90	48.0	21.0	74.1208	110.3608
200	1.2	27.44	B	90	46.2	29.5	42.2005	71.4794
201	2.3	34.35	B	45	45.4	20.1	143.6943	137.3715
202	5.1	34.35	B	4	45.0	40.8	217.7575	290.6819
203	8.7	34.33	B	4	44.3	34.4	545.0738	541.5930
204	-0.6	27.46	B	90	44.3	41.3	6.9222	10.7345
205	11.5	34.35	B	4	46.2	31.7	806.6610	783.6816
206	13.3	34.35	B	4	44.6	27.0	1040.8942	960.6665
207	15.9	34.35	B	4	44.2	22.9	1325.9741	1246.0059
208	18.2	34.36	B	4	44.3	22.6	1354.7810	1527.9418
209	0.3	27.45	B	90	44.1	30.4	34.8910	40.8735
210	21.0	34.36	B	4	44.4	16.7	1876.5935	1908.2625
211	21.2	35.35	B	4	49.3	21.6	1680.0792	1971.2248
212	18.8	35.35	B	4	46.5	22.1	1504.6028	1634.1300
213	15.7	35.35	B	4	45.0	24.9	1213.2384	1244.1003
214	13.4	35.36	B	4	45.3	28.2	992.6055	987.8563
215	11.9	35.36	B	4	46.7	32.2	799.6977	835.7033
216	9.4	35.36	B	4	44.9	33.5	629.8903	608.7379
217	3.5	35.35	B	45	45.9	13.2	206.1281	199.6806
218	-0.9	27.46	B	90	48.6	48.1	1.0634	7.9807
219	-0.3	27.45	B	90	48.9	41.9	15.5427	13.2687
220	20.8	0.37	B	4	45.7	18.6	1763.7081	1807.2749

Index	Temperature	Salinity	Geometry	Duration	Start weight	End weight	Recession	Agassiz rate
221	2.4	35.56	B	45	45.2	18.3	156.9833	146.1613
222	4.7	35.56	B	4	44.7	40.2	234.9756	273.1284
223	18.2	0.37	B	4	43.6	20.5	1491.3824	1403.2773
224	-0.8	27.35	B	90	44.5	44.0	1.1281	8.5729
225	8.2	35.54	B	4	46.4	35.9	561.1723	513.2094
226	15.2	0.37	B	4	49.7	32.5	924.8126	1000.5235
227	17.7	35.55	B	4	48.2	23.8	1453.3752	1495.2291
228	6.6	0.37	B	4	45.2	42.0	164.0980	222.4211
229	23.1	35.51	B	4	43.9	14.7	2053.9066	2266.4484
230	2.7	0.37	B	45	45.6	29.6	81.1682	50.7047
231	9.1	35.52	B	4	44.8	34.5	564.3436	585.3497
232	2.6	30.36	B	45	43.9	24.3	106.8991	137.0876
233	9.7	0.37	B	4	48.1	41.1	353.8945	438.5593
234	13.9	35.46	B	4	44.0	25.7	1103.7065	1043.0399
235	15.8	35.51	B	4	45.0	23.4	1327.2792	1259.3732
236	14.3	0.37	B	4	44.5	29.0	898.0573	892.9429
237	-0.4	30.36	B	90	44.8	38.0	16.0585	16.8751
238	3.5	0.62	B	45	44.5	20.6	135.8884	76.1159
239	11.2	0.62	B	4	47.5	37.4	528.5062	568.7635
240	2.8	35.71	B	45	45.3	15.5	181.4606	165.7554
241	15.5	0.62	B	4	44.7	26.9	1053.0056	1035.0969
242	18.8	0.62	B	4	45.5	23.2	1367.8565	1486.8747
243	21.9	0.61	B	4	47.3	18.4	1860.4527	1985.5691
244	-0.3	30.35	B	90	46.3	39.9	14.7105	17.7668
245	6.0	35.71	B	4	45.0	39.4	293.6547	355.7000
246	11.4	35.68	B	4	44.4	29.9	833.0574	791.9495
247	15.6	35.70	B	4	49.4	26.3	1324.9061	1239.9883
248	18.3	35.71	B	4	44.8	20.4	1560.8404	1577.9358
249	0.8	30.35	B	90	44.1	26.5	46.7135	66.5492
250	22.8	35.71	B	4	49.1	19.1	1883.7782	2227.7336
251	2.4	0.88	B	45	44.5	33.1	56.3791	43.8978
252	6.2	0.88	B	4	45.4	43.8	80.8026	201.3596
253	13.9	0.88	B	4	43.8	29.1	855.7475	843.6660
254	19.0	0.88	B	4	49.1	24.9	1413.1016	1511.3475
255	18.9	0.87	B	4	45.6	20.3	1609.4020	1496.4677
256	22.2	0.87	B	4	43.8	14.2	2102.3278	2029.0516
257	-1.0	30.37	B	90	44.0	43.6	0.9087	9.9229
258	3.1	1.13	B	45	45.3	26.5	98.8056	64.5338
259	5.2	1.12	B	4	45.4	44.2	60.4198	151.0179
260	8.6	1.12	B	4	49.1	42.8	312.1510	354.7669
261	-0.8	30.43	B	90	47.2	45.3	4.1626	12.7038
262	11.9	1.12	B	4	43.9	31.0	735.9899	633.9032
263	15.8	1.12	B	4	45.6	25.5	1198.8914	1067.1742
264	17.6	1.12	B	4	45.4	23.1	1370.6885	1304.9715
265	0.2	30.40	B	90	47.9	35.0	30.5393	45.7563
266	21.8	1.11	B	4	45.1	18.1	1779.4111	1952.6374

Index	Temperature	Salinity	Geometry	Duration	Start weight	End weight	Recession	Agassiz rate
267	2.7	35.91	B	45	44.3	16.3	169.8419	161.6469
268	5.9	35.92	B	4	45.2	39.1	320.1764	350.3939
269	11.3	35.88	B	4	47.4	31.9	852.6922	785.2229
270	14.0	35.90	B	4	48.0	27.9	1145.5861	1062.0276
271	1.7	30.34	B	90	45.6	22.2	64.5360	100.4280
272	1.2	30.33	B	90	45.8	23.7	59.7339	82.2062
273	20.3	35.91	B	4	44.8	18.6	1718.6948	1860.1515
274	2.0	1.36	B	45	44.3	37.4	32.8836	35.1323
275	1.8	32.32	B	45	42.6	26.6	85.9303	108.9355
276	2.5	36.11	B	45	47.3	20.0	152.7725	152.8275
277	6.8	1.36	B	4	47.7	44.7	148.0064	236.9762
278	7.1	36.11	B	4	43.9	36.1	424.2852	435.0005
279	11.1	1.36	B	4	43.7	34.1	532.5651	558.5849
280	10.6	36.06	B	4	44.6	30.9	777.9681	722.2162
281	13.7	1.36	B	4	49.0	34.2	787.5523	818.5811
282	-0.0	32.37	B	90	44.0	37.4	15.7639	25.3692
283	17.5	1.35	B	4	44.3	21.7	1427.2573	1287.4561
284	16.5	35.98	B	4	46.2	21.6	1530.4671	1354.9167
285	-0.3	32.36	B	90	48.0	41.9	13.6312	20.9398
286	19.6	36.11	B	4	45.1	18.2	1770.2154	1767.1255
287	20.1	1.35	B	4	45.0	18.7	1719.7189	1669.1690
288	-1.0	32.36	B	90	47.0	46.5	1.0875	12.5585
289	2.6	1.61	B	45	44.6	28.8	81.4754	51.0615
290	2.1	36.31	B	45	48.0	21.2	146.7629	135.0102
291	7.9	1.61	B	4	43.5	39.0	239.5183	306.9668
292	8.3	36.31	B	4	44.3	35.4	485.6032	528.0380
293	13.9	1.61	B	4	44.5	29.4	871.2670	839.0879
294	13.9	36.26	B	4	49.5	30.5	1042.7754	1057.6249
295	-0.7	32.35	B	90	44.7	38.1	15.5851	16.0393
296	18.6	1.60	B	4	45.1	21.9	1451.3199	1438.1740
297	17.7	36.30	B	4	46.4	23.7	1373.6512	1515.5434
298	22.3	1.60	B	4	43.9	13.8	2151.1699	2022.5993
299	22.1	36.31	B	4	45.1	16.2	1960.9600	2143.2042
300	0.7	32.35	B	90	43.0	26.6	43.8879	66.6425
301	1.3	32.32	B	90	43.3	23.9	53.4356	88.5471
302	2.2	1.88	B	45	46.1	34.3	56.9939	41.1048
303	1.9	36.45	B	45	46.9	23.0	129.1178	128.7687
304	3.4	36.47	B	4	45.0	41.7	169.8792	199.1090
305	7.5	1.87	B	4	44.5	39.2	279.4502	281.4540
306	5.4	36.45	B	4	44.7	38.7	317.1856	321.1457
307	-1.1	32.35	B	90	44.0	43.3	1.5938	11.0622
308	9.4	1.87	B	4	46.5	38.7	406.7558	415.8279
309	7.9	36.42	B	4	43.8	35.4	460.1440	497.6051
310	14.0	1.87	B	4	45.3	30.4	845.5571	848.5572
311	13.0	36.46	B	4	47.9	30.9	940.6644	964.3814
312	-0.9	32.84	B	90	46.0	45.4	1.3249	13.2991

Index	Temperature	Salinity	Geometry	Duration	Start weight	End weight	Recession	Agassiz rate
313	-0.6	32.83	B	90	45.3	40.6	10.8231	17.3914
314	17.8	36.47	B	4	48.8	21.0	1705.9736	1533.3032
315	18.3	1.86	B	4	44.0	20.5	1511.8271	1390.6048
316	-0.5	32.86	B	90	44.5	38.6	13.8952	20.2168
317	20.0	1.88	B	4	45.0	18.9	1701.7538	1641.1744
318	19.8	36.46	B	4	44.9	18.2	1760.1756	1807.2034
319	0.3	32.76	B	90	45.0	29.9	38.3694	55.4100
320	1.9	32.85	B	45	45.8	25.6	106.8007	117.4427
321	1.5	32.86	B	45	43.2	26.6	88.6942	100.1339
322	1.2	32.84	B	45	45.1	28.7	84.3130	87.3549
323	2.1	2.11	B	45	44.6	33.2	56.2812	39.1320
324	4.5	2.10	B	4	46.5	45.2	64.4519	122.8161
325	7.6	2.10	B	4	45.5	40.6	253.4996	288.4688
326	10.5	2.10	B	4	45.6	36.9	463.7716	505.4524
327	14.1	2.10	B	4	44.9	30.6	812.4955	858.2467
328	-0.8	33.35	B	90	44.0	39.1	11.5367	15.6283
329	20.4	2.09	B	4	44.2	18.6	1688.3500	1698.1132
330	0.3	33.27	B	90	45.5	28.4	43.9515	54.2078
331	-0.5	33.00	B	90	44.6	40.1	10.4598	19.1750
332	1.8	2.36	B	45	45.5	36.3	43.8542	32.5832
333	4.4	2.36	B	4	46.0	45.7	14.8730	115.3072
334	-0.1	33.34	B	90	43.4	33.8	23.7931	26.3704
335	8.4	2.36	B	4	47.8	41.9	297.0718	342.8690
336	11.0	2.36	B	4	46.4	36.0	555.3418	548.7538
337	-0.9	33.19	B	90	44.9	40.5	10.1711	14.5039
338	13.0	2.35	B	4	46.3	32.5	761.2861	739.6719
339	15.7	2.37	B	4	44.3	26.5	1061.2134	1042.1148
340	1.7	33.35	B	45	45.6	26.6	99.5010	108.6188
341	0.7	33.33	B	45	48.2	38.5	44.4775	72.0111
342	19.8	2.36	B	4	43.9	18.4	1691.2334	1600.1711
343	3.7	2.62	B	45	44.0	22.2	121.9110	89.1441
344	6.2	2.61	B	4	43.1	40.9	115.6505	206.8027
345	11.8	2.61	B	4	44.1	33.9	565.0814	621.2844
346	15.0	2.60	B	4	45.9	30.5	868.8990	956.9004
347	17.6	2.62	B	4	43.3	24.8	1134.2605	1282.2490
348	20.1	2.61	B	4	50.1	22.6	1637.0132	1640.0870
349	2.4	33.17	B	4	45.7	45.2	24.9336	137.8180
350	3.3	33.16	B	4	45.6	43.8	90.7687	180.5282
351	4.0	33.13	B	4	49.1	46.3	135.2231	216.4742
352	4.5	33.18	B	4	47.6	43.9	183.7561	249.6198
353	5.4	33.12	B	4	45.0	39.9	266.3452	302.0649
354	7.0	33.18	B	4	44.9	36.5	451.7647	406.4192
355	7.9	33.04	B	4	45.4	36.4	482.5857	469.4995
356	8.8	33.19	B	4	48.6	37.1	598.4462	538.9848
357	9.9	33.19	B	4	45.1	33.0	670.6402	628.1173
358	17.0	33.19	B	4	44.1	21.6	1425.2725	1350.7205

Index	Temperature	Salinity	Geometry	Duration	Start weight	End weight	Recession	Agassiz rate
359	2.2	2.87	B	45	45.6	32.7	63.4832	43.3536
360	6.6	2.86	B	4	48.9	44.5	215.5705	229.8908
361	12.2	2.86	B	4	44.7	32.9	656.7100	658.7630
362	15.3	2.85	B	4	44.4	27.8	974.8754	990.0386
363	20.7	2.84	B	4	43.5	17.6	1744.7380	1726.9745
364	-1.0	33.76	B	90	43.9	41.9	4.6070	14.2039
365	1.8	3.38	B	45	43.8	33.4	51.5777	34.6149
366	2.2	3.37	C	45	44.6	31.2	67.4384	50.4282
367	-0.6	33.73	B	90	44.2	40.4	8.8384	19.6870
368	4.5	3.36	B	4	44.1	43.7	20.4137	126.9793
369	8.9	3.36	B	4	43.9	37.3	355.2727	380.5857
370	1.1	33.67	B	45	44.0	28.5	80.5788	88.1119
371	12.2	3.36	C	4	44.3	32.5	661.3230	745.0829
372	12.3	3.35	B	4	43.9	33.1	603.7824	667.3350
373	-0.1	33.70	B	50	44.3	38.5	24.6461	27.2133
374	15.7	3.34	B	4	47.6	30.9	926.1886	1033.3186
375	0.8	33.70	B	45	44.9	31.6	66.5132	74.4327
376	21.6	3.33	C	4	44.7	16.3	1930.9514	2103.0353
377	20.9	3.31	B	4	47.7	18.9	1834.6670	1746.8493
378	0.4	33.72	B	45	44.0	33.1	54.1228	60.4864
379	2.4	36.85	B	45	44.4	16.9	165.0871	150.7642
380	2.5	36.86	C	45	44.4	13.9	192.4959	176.1906
381	4.6	36.85	B	4	45.3	41.4	200.7878	273.8428
382	5.0	36.83	C	4	44.6	39.7	257.1021	337.6818
383	10.9	36.86	B	4	44.8	31.7	736.8953	760.4100
384	10.9	36.88	C	4	45.0	30.3	837.0580	861.5939
385	19.4	36.85	B	4	43.8	19.0	1632.0365	1763.3401
386	19.0	36.86	C	4	44.4	17.5	1800.0387	1934.1840
387	2.1	33.54	B	45	45.1	24.0	114.3209	129.2060
388	1.9	3.87	B	45	47.8	39.5	37.8589	38.0373
389	2.7	3.87	C	45	42.8	26.7	86.2217	67.7003
390	1.6	37.35	B	45	44.6	24.6	108.0474	116.4011
391	1.7	37.36	C	45	44.2	18.6	150.0756	136.7711
392	6.5	3.86	B	4	45.9	43.5	121.0320	227.4401
393	6.8	3.85	C	4	42.7	37.5	282.1077	277.0509
394	11.5	37.36	B	4	48.9	32.6	880.7938	825.3517
395	11.5	37.36	C	4	43.4	26.8	993.8922	934.8668
396	14.6	3.85	B	4	45.2	31.1	795.2610	903.2249
397	14.4	3.84	C	4	43.3	28.6	863.8522	998.2725
398	20.1	3.83	B	4	48.1	22.7	1534.3446	1614.5524
399	19.5	3.87	C	4	41.8	18.2	1600.5971	1728.8816
400	18.9	37.35	B	4	44.1	19.0	1647.3352	1709.1589
401	19.5	37.35	C	4	42.5	14.8	1971.1263	2032.6347
402	2.1	3.86	B	45	45.4	33.5	58.2164	43.0287
403	2.6	3.85	C	45	44.2	31.2	65.6375	64.2947
404	3.9	37.36	B	4	49.3	45.9	164.4420	230.0354

Index	Temperature	Salinity	Geometry	Duration	Start weight	End weight	Recession	Agassiz rate
405	4.5	37.34	C	4	44.3	40.5	198.5503	306.2776
406	4.7	3.84	B	4	45.0	44.0	50.5754	137.2426
407	5.7	3.84	C	4	42.7	41.0	89.5752	209.1317
408	10.0	3.84	B	4	45.0	37.7	388.2728	465.1738
409	10.2	3.83	C	4	44.5	35.0	519.3853	545.1452
410	13.2	3.82	B	4	44.2	31.4	725.6326	754.8995
411	13.2	3.81	C	4	43.8	29.9	802.5294	855.1567
412	1.8	37.32	B	45	44.5	22.0	125.6009	125.0032
413	21.5	3.80	B	4	43.9	17.8	1746.5120	1828.7493
414	2.0	37.35	C	45	44.6	19.4	145.5333	151.8391
415	20.9	3.85	C	4	44.7	19.0	1677.7255	1964.8551
416	5.4	37.36	B	4	45.3	41.2	211.4186	326.4820
417	6.0	37.34	C	4	44.4	37.7	358.0186	414.8098
418	14.7	37.36	B	4	48.6	29.0	1099.3506	1170.0903
419	14.7	37.36	C	4	44.7	23.1	1335.5749	1325.5950
420	20.5	37.36	B	4	48.1	20.3	1731.5894	1940.8147
421	20.0	37.36	C	4	44.7	15.0	2062.9517	2115.0252
422	20.3	0.37	B	4	45.9	17.7	1856.4014	1725.6207
423	20.0	0.91	B	4	43.8	17.6	1760.1066	1664.1640
424	20.0	1.46	B	4	45.0	16.3	1729.8175	1650.8851
425	20.2	2.01	B	4	44.3	18.8	1675.3974	1669.0639
426	20.4	2.55	B	4	45.5	18.2	1790.2062	1687.3142
427	19.9	3.10	B	4	45.3	19.5	1663.6339	1599.6588
428	19.7	3.64	B	4	45.1	21.0	1525.3648	1559.5418
429	19.4	4.18	B	4	48.0	22.3	1561.4142	1506.5116
430	19.2	4.73	B	4	45.1	21.8	1459.4457	1469.3690
431	19.5	5.26	B	4	44.7	21.6	1455.6628	1502.6911
432	20.1	5.81	B	4	45.1	20.6	1558.9536	1578.3323
433	19.7	6.35	B	4	45.5	22.2	1447.0807	1513.9094
434	21.7	6.89	B	4	46.3	20.2	1652.6040	1791.6533
435	21.4	7.43	B	4	46.0	20.3	1629.2471	1737.6785
436	21.1	7.96	B	4	45.7	20.9	1563.6642	1685.6431
437	21.3	8.50	B	4	44.6	20.4	1550.7557	1705.8593
438	21.0	9.04	B	4	47.4	23.6	1430.1942	1656.0496
439	20.7	9.58	B	4	46.3	23.2	1407.4895	1608.0480
440	20.9	10.12	B	4	44.9	22.0	1433.1789	1629.1709
441	20.4	10.66	B	4	47.4	23.3	1453.4500	1556.6140
442	20.4	11.19	B	4	45.7	22.1	1465.0845	1551.9599
443	20.1	11.73	B	4	45.4	22.1	1450.1463	1508.9463
444	20.6	12.79	B	4	46.0	22.8	1424.0921	1566.8075
445	20.3	13.34	B	4	44.0	21.5	1428.3818	1525.5247
446	20.1	13.87	B	4	47.1	23.3	1438.8723	1498.2171
447	20.7	14.40	B	4	44.6	21.6	1450.6167	1572.5564
448	20.4	14.94	B	4	45.3	21.1	1527.0446	1533.2173
449	20.0	15.47	B	4	46.0	22.7	1432.0022	1482.8377
450	19.7	16.00	B	4	46.2	23.1	1410.3792	1446.2373

Index	Temperature	Salinity	Geometry	Duration	Start weight	End weight	Recession	Agassiz rate
451	20.0	16.54	B	4	45.7	22.2	1457.0322	1483.2815
452	2.4	17.07	B	18	44.5	37.6	84.2819	86.5901
453	5.1	17.05	B	10	44.9	34.4	230.1493	206.4562
454	7.1	17.01	B	10	45.4	27.7	412.8315	315.2286
455	9.2	16.95	B	10	45.6	22.0	587.2756	450.1762
456	10.0	17.06	B	10	44.4	18.5	683.0233	507.8757
457	12.3	17.05	B	10	44.6	14.3	852.8662	689.4494
458	14.3	16.95	B	10	45.9	12.4	964.7237	867.7510
459	18.4	17.03	B	10	47.9	7.8	1256.3544	1295.3089
460	20.2	17.55	B	5	44.2	19.9	1169.0751	1509.8500
461	19.8	17.03	B	10	44.9	3.9	1509.1250	1459.8237
462	21.1	17.55	B	4	47.1	22.2	1525.8927	1622.0523
463	20.7	18.08	B	4	45.2	20.8	1547.1142	1573.2822
464	20.3	18.61	B	4	44.0	21.4	1436.6083	1526.0102
465	20.0	19.14	B	4	43.5	20.9	1452.5548	1492.2080
466	19.5	19.67	B	4	48.3	22.5	1559.8251	1435.6287
467	19.7	20.20	B	4	45.6	21.2	1533.7005	1463.0536
468	19.6	20.73	B	4	47.0	22.1	1529.0720	1455.2499
469	19.6	21.26	B	4	44.2	20.5	1522.0030	1459.8105
470	19.5	21.78	B	4	46.7	22.3	1498.3309	1452.9315
471	19.4	22.31	B	4	44.0	20.8	1486.5138	1446.4977
472	19.8	22.84	B	4	45.2	22.3	1424.0704	1500.0362
473	19.2	23.38	B	4	45.6	22.2	1452.0601	1435.0818
474	18.7	23.91	B	4	48.4	24.0	1447.6437	1383.4421
475	18.4	24.44	B	4	44.9	22.1	1425.1023	1355.7605
476	18.2	24.97	B	4	47.6	23.7	1432.1704	1340.1256
477	18.0	25.45	B	4	44.8	21.1	1501.9635	1324.0380
478	18.6	25.06	B	4	44.9	21.5	1473.9336	1387.3268
479	18.5	25.36	B	4	46.2	22.8	1433.9716	1380.0443
480	18.4	25.86	B	4	45.3	21.6	1485.7824	1375.8962
481	19.3	26.36	B	4	44.6	20.7	1525.3604	1490.0202
482	19.0	26.86	B	4	48.3	23.9	1450.5021	1462.5318
483	18.6	27.36	B	4	44.4	22.0	1407.9483	1423.6963
484	18.6	27.86	B	4	47.3	23.2	1456.3939	1432.5655
485	18.4	28.36	B	4	45.1	20.0	1610.1620	1417.9900
486	18.5	28.86	B	4	46.0	21.4	1537.0153	1439.3754
487	20.1	29.36	B	4	45.1	17.7	1816.5364	1647.9356
488	19.7	29.86	B	4	46.5	19.9	1688.2566	1608.2598
489	20.3	30.36	B	4	46.3	19.6	1704.4963	1697.3422
490	1.9	5.38	B	45	44.3	33.7	52.2127	41.2690
491	20.3	30.86	B	4	44.4	18.4	1716.6541	1709.8064
492	19.7	31.36	B	4	47.3	19.4	1770.9332	1644.0834
493	3.8	5.37	B	10	44.2	39.3	103.4979	101.4809
494	6.3	5.36	B	10	45.0	32.8	271.1980	221.4902
495	19.2	31.86	B	4	44.2	18.6	1688.3500	1592.1438
496	8.5	5.35	B	10	45.0	27.9	399.2869	356.9500

Index	Temperature	Salinity	Geometry	Duration	Start weight	End weight	Recession	Agassiz rate
497	18.8	32.36	B	4	44.5	18.8	1685.5274	1553.5383
498	10.4	5.32	B	10	45.5	25.6	474.6364	499.0077
499	18.4	32.86	B	4	45.8	19.7	1671.0582	1515.2317
500	11.7	5.30	B	10	45.0	22.2	568.8294	609.6370
501	18.0	33.36	B	4	45.3	19.2	1690.0686	1477.2163
502	12.6	5.27	B	10	46.8	20.2	670.8573	692.6647
503	17.8	33.86	B	4	48.8	22.3	1599.6704	1464.4698
504	19.7	5.37	B	4	45.4	21.9	1466.3241	1529.0560
505	19.8	34.35	B	4	45.3	17.6	1835.9151	1740.0754
506	19.4	34.86	B	4	46.2	17.7	1871.2313	1700.6304
507	18.9	35.36	B	4	44.2	18.5	1697.4131	1647.7765
508	18.6	35.86	B	4	48.9	20.7	1735.8773	1622.0888
509	18.5	36.36	B	4	43.8	17.5	1769.5107	1623.3787
510	20.8	36.86	B	4	45.1	16.6	1921.6039	1966.9070
511	20.0	37.36	B	4	48.8	19.2	1860.6672	1866.9269
512	19.5	37.86	B	4	44.2	16.9	1847.0842	1811.6747
513	19.1	38.36	B	4	45.4	17.7	1831.5406	1771.0895
514	18.8	38.86	B	4	44.2	17.6	1780.4893	1744.9095
515	1.4	5.34	B	45	44.8	38.9	27.6570	29.1887
516	3.9	6.87	B	10	47.1	43.5	71.9880	110.2198
517	6.6	6.86	B	10	46.0	33.9	264.1586	243.4313
518	9.1	6.84	B	10	45.4	26.3	452.3532	403.0339
519	10.6	6.87	B	10	48.2	26.4	504.2652	517.3202
520	11.9	6.83	B	4	44.2	33.2	612.9035	627.4768
521	13.0	6.87	B	4	45.4	31.7	766.9703	728.8132
522	14.8	6.85	B	4	44.7	29.8	854.8183	910.7330
523	16.9	6.82	B	4	44.1	27.9	952.7337	1148.2956
524	20.0	6.87	B	4	49.0	25.2	1386.1073	1547.7556
525	20.1	10.86	B	4	45.2	21.5	1488.9821	1515.4969
526	2.5	10.87	B	45	44.6	33.7	53.5623	73.9470
527	2.6	2.37	B	45	45.4	30.6	74.4480	54.2774
528	4.4	10.87	B	10	47.2	39.6	156.5554	146.9163
529	3.5	6.37	B	45	45.1	30.3	74.8510	95.2926
530	4.5	2.36	B	10	44.2	39.1	107.9008	121.5540
531	8.0	10.85	B	10	45.2	26.9	431.2495	339.7961
532	6.8	2.36	B	10	46.3	36.0	220.1679	237.2983
533	5.0	6.35	B	10	47.3	39.5	160.6875	157.3062
534	9.7	10.87	B	10	44.4	21.8	569.6701	455.8854
535	9.5	2.35	B	10	46.9	28.7	415.0285	421.0991
536	8.2	6.37	B	10	45.0	27.1	421.5943	336.8845
537	11.8	10.87	B	10	45.4	18.2	714.0878	621.2412
538	11.4	2.37	B	10	45.3	23.4	536.9222	581.4641
539	10.3	6.37	B	10	46.1	25.2	498.3034	489.5335
540	12.7	10.87	B	4	45.5	31.6	778.3043	699.5699
541	13.2	2.36	B	4	44.9	30.9	793.0839	757.0481
542	12.3	6.37	B	4	45.0	33.9	610.5650	660.5859

Index	Temperature	Salinity	Geometry	Duration	Start weight	End weight	Recession	Agassiz rate
543	14.1	10.87	B	4	45.4	30.2	863.6200	830.3088
544	15.2	2.35	B	4	44.7	26.5	1081.4432	979.1628
545	14.5	6.35	B	4	47.2	31.7	855.6351	877.7166
546	15.8	10.87	B	4	45.1	27.7	1017.0746	1003.6258
547	18.5	2.37	B	4	45.1	21.7	1467.5965	1407.4252
548	18.1	6.37	B	4	46.7	26.7	1166.5676	1298.2948
549	18.7	10.87	B	4	46.7	25.4	1260.5307	1336.1485
550	18.9	2.36	B	4	45.8	20.7	1585.4232	1464.8119
551	18.7	6.37	B	4	46.3	24.9	1277.8785	1376.2700
552	19.1	10.87	B	4	43.3	20.2	1501.5280	1385.6607
553	2.0	33.76	B	45	45.4	21.9	130.3399	124.0291
554	1.8	16.56	B	45	45.4	32.4	64.2586	66.0050
555	4.0	33.76	B	10	46.3	35.5	231.8724	221.9452
556	1.8	14.37	B	45	45.0	32.0	64.7100	60.5112
557	3.4	16.56	B	10	47.4	41.5	119.5423	125.2606
558	4.0	14.37	B	10	45.7	38.8	144.6765	142.5492
559	8.5	33.70	B	10	45.1	20.7	620.2064	517.0473
560	7.2	16.56	B	10	45.2	27.5	414.3965	316.3388
561	7.0	14.37	B	10	45.2	29.1	370.6219	294.2332
562	8.7	16.56	B	10	46.8	24.1	545.0604	411.2653
563	8.6	14.37	B	10	45.9	25.5	485.5144	393.9074
564	7.0	33.70	B	10	44.7	25.1	473.3156	406.9909
565	10.3	16.56	B	10	47.5	20.5	674.2580	524.7058
566	10.6	14.37	B	10	44.8	21.1	600.7854	536.8742
567	9.2	33.70	B	10	46.0	19.8	668.9097	572.3668
568	11.6	16.56	B	4	44.9	31.9	729.2717	626.1111
569	12.0	14.37	B	4	46.5	34.7	636.9128	649.1011
570	10.7	33.70	B	4	46.4	32.7	753.7613	699.3963
571	12.8	16.56	B	4	45.5	30.9	823.1145	727.0876
572	13.6	14.37	B	4	45.8	31.4	805.9555	789.6074
573	12.6	33.76	B	4	48.8	31.3	958.0447	877.9213
574	14.0	16.56	B	4	44.8	29.2	899.7698	835.1190
575	14.8	14.37	B	4	45.2	29.0	933.2752	903.5632
576	13.9	33.77	B	4	45.6	26.1	1155.2481	1010.2752
577	14.9	16.56	B	4	45.3	28.8	951.7642	920.7890
578	16.3	14.37	B	4	45.6	28.1	1014.4287	1056.3406
579	15.7	33.77	B	4	47.3	24.6	1349.2170	1207.8797
580	16.4	16.56	B	4	45.4	25.6	1181.6043	1072.3860
581	18.3	14.37	B	4	47.2	27.3	1148.6269	1277.9072
582	18.0	33.76	B	4	47.2	21.5	1587.6424	1484.6796
583	18.4	16.56	B	4	44.1	24.1	1227.9881	1291.7128
584	18.5	14.37	B	4	44.6	25.4	1156.1059	1301.1863
585	18.2	33.76	B	4	47.5	22.4	1529.2836	1510.0328
586	18.5	16.56	B	4	45.3	23.6	1326.8237	1303.1911
587	2.4	40.86	B	45	46.0	16.6	174.7928	167.6437
588	4.6	40.86	B	10	45.2	30.2	341.4498	291.8217

Index	Temperature	Salinity	Geometry	Duration	Start weight	End weight	Recession	Agassiz rate
589	7.4	40.86	B	10	45.0	22.5	559.2243	493.1513
590	9.4	40.86	B	10	45.5	17.9	727.1582	666.6462
591	11.2	40.86	B	4	45.6	31.3	802.4062	843.9328
592	12.7	40.86	B	4	44.7	27.1	1038.8924	1006.9698
593	16.4	40.86	B	4	47.0	22.3	1512.9915	1468.6269
594	2.0	42.01	B	45	46.2	21.0	140.4498	152.3637
595	3.3	42.01	B	10	47.5	36.5	232.0123	219.7532
596	6.1	42.01	B	10	46.1	27.5	432.2965	401.6352
597	7.3	42.01	B	10	47.6	24.8	539.5110	494.9455
598	9.1	42.01	B	10	44.2	16.9	738.8337	652.1930
599	10.2	42.01	B	10	45.0	14.1	869.5864	758.4804
600	11.4	42.01	B	4	45.4	29.5	909.8207	883.3022
601	12.5	42.01	B	4	45.7	28.4	998.8602	1005.8031
602	16.4	42.01	B	4	48.3	24.3	1420.0542	1502.5167
603	17.7	42.01	B	4	44.8	19.4	1647.3341	1689.7163
604	19.9	42.01	B	4	45.2	17.6	1830.9137	2031.1708
605	17.6	0.37	B	4	44.6	23.6	1289.0771	1314.2389
606	2.2	42.01	B	45	45.4	17.5	164.8519	162.0292
607	2.5	43.27	B	45	46.8	15.8	185.5736	181.8578
608	0.6	0.37	B	45	45.5	47.5	-8.6435	9.4001
609	4.4	43.27	B	10	44.7	31.2	303.8610	291.8242
610	1.8	20.97	B	45	45.1	29.7	78.4023	77.5995
611	7.1	43.27	B	10	44.9	24.5	493.8603	489.4175
612	0.8	0.37	B	90	47.2	50.6	-7.1783	12.0170
613	3.9	20.97	B	10	45.0	36.4	184.5028	163.1874
614	9.3	43.27	B	10	46.6	17.8	750.9227	686.2962
615	7.7	20.97	B	10	46.7	26.9	462.5863	370.3864
616	11.2	43.27	B	4	46.1	30.5	877.3355	882.2432
617	10.2	20.97	B	10	45.4	19.2	677.8254	543.4592
618	12.8	43.27	B	4	45.3	26.3	1122.2357	1065.8954
619	17.5	20.97	B	4	46.7	25.9	1223.8026	1215.7759
620	18.0	43.27	B	4	45.5	19.2	1696.1228	1780.4272
621	1.4	0.37	B	90	48.6	38.6	22.8698	21.6868
622	2.4	19.16	B	45	44.3	25.3	102.0287	94.4593
623	0.1	1.37	B	90	44.1	50.4	-13.5493	4.4373
624	4.8	19.16	B	10	45.8	36.1	206.2633	198.3421
625	7.2	19.16	B	10	48.0	31.1	372.1436	329.5324
626	9.6	19.16	B	10	44.5	22.2	558.3476	488.0258
627	13.1	19.16	B	4	48.9	34.6	755.2174	768.1071
628	14.0	19.16	B	4	45.0	31.1	786.9424	849.5130
629	0.5	1.37	B	90	45.0	49.7	-10.0292	8.9266
630	14.7	19.15	B	4	45.0	29.0	924.4251	915.4129
631	1.3	1.38	B	90	46.3	36.4	23.4751	21.4273
632	15.4	19.15	B	4	44.3	27.1	1018.1553	983.7047
633	18.9	19.16	B	4	45.4	23.8	1318.4186	1360.0882
634	18.5	20.96	B	4	46.3	25.1	1262.0335	1327.1667

Index	Temperature	Salinity	Geometry	Duration	Start weight	End weight	Recession	Agassiz rate
635	5.3	20.97	B	10	44.6	32.7	265.5613	231.6813
636	15.0	21.19	B	4	44.6	26.5	1077.6166	959.2638
637	7.7	20.97	B	10	47.5	27.3	466.9759	370.3848
638	0.3	2.37	B	90	45.6	53.8	-17.2325	7.0877
639	1.9	44.75	B	45	44.2	16.8	165.4380	157.4728
640	1.4	2.38	B	90	44.7	35.5	22.1527	24.9886
641	3.3	44.75	B	10	44.8	34.4	227.6953	231.7283
642	6.7	44.75	B	10	46.0	25.1	499.2865	468.9883
643	9.0	44.75	B	10	45.5	17.4	743.0092	675.2184
644	11.0	44.75	B	4	46.6	31.3	851.8044	884.5462
645	12.6	44.75	B	4	44.9	26.4	1094.2945	1072.0931
646	14.1	44.75	B	4	46.1	25.2	1246.0118	1264.1593
647	19.2	44.75	B	4	44.3	17.6	1784.6273	2034.5789
648	1.9	46.00	B	45	45.6	17.1	168.8225	162.0536
649	4.1	46.00	B	10	45.8	34.1	253.9914	286.6504
650	6.2	46.00	B	10	44.7	25.9	451.3323	438.3877
651	0.1	3.35	B	90	45.0	52.8	-16.5507	5.1442
652	8.3	46.00	B	10	44.4	18.2	691.9413	622.1743
653	9.8	46.00	B	4	48.2	32.1	878.8153	773.0548
654	11.3	46.00	B	4	45.5	29.6	907.9976	940.3122
655	0.8	3.37	B	90	44.7	42.2	5.8466	15.2989
656	13.4	46.00	B	4	47.4	29.1	1031.6441	1201.8917
657	15.2	46.00	B	4	44.7	23.8	1286.3978	1451.6310
658	0.1	4.34	B	90	45.6	49.5	-8.4562	5.6010
659	16.1	46.00	B	4	44.8	22.1	1419.1631	1585.3315
660	0.3	4.36	B	90	48.5	50.5	-4.1665	8.3814
661	19.4	46.00	B	3	44.6	22.5	1838.4696	2125.8753
662	1.0	4.36	B	90	44.7	34.1	25.9812	20.1998
663	1.6	22.86	B	45	44.4	27.9	85.8447	75.4913
664	3.8	22.86	B	15	44.3	31.1	200.5538	166.0046
665	0.0	6.82	B	90	45.1	47.0	-4.1747	5.4767
666	5.6	22.29	B	15	44.6	24.9	318.3011	253.9109
667	7.9	22.29	B	15	46.2	15.7	551.8075	390.9682
668	10.0	22.28	B	10	47.7	20.8	668.4295	537.4828
669	1.1	6.82	B	90	48.4	39.8	19.5454	26.0081
670	12.8	22.16	B	4	44.0	29.7	824.1171	763.7134
671	-0.1	8.30	B	90	44.0	46.2	-4.8790	-1.1613
672	0.4	8.31	B	90	46.2	39.9	14.5066	13.5931
673	0.1	10.63	B	90	44.5	40.6	9.0776	10.0757
674	-0.3	10.60	B	90	45.3	44.3	2.2374	-1.3285
675	-0.3	10.60	B	90	45.1	45.1	0.1559	-1.3296
676	-0.3	10.60	B	90	45.1	45.4	-0.5559	-1.3297
677	0.3	12.25	B	90	44.6	38.8	13.6778	16.0093
678	-0.4	12.20	B	90	47.1	47.0	0.2383	-1.0426
679	0.3	13.25	B	90	44.8	39.5	12.3774	17.2533
680	0.3	15.23	B	90	44.6	38.4	14.6893	19.9187

Index	Temperature	Salinity	Geometry	Duration	Start weight	End weight	Recession	Agassiz rate
681	-0.6	15.23	B	90	44.9	45.1	-0.4014	-0.0176
682	-0.1	17.20	B	90	47.7	43.7	8.9673	1.8896
683	-0.7	17.16	B	90	45.1	45.2	-0.1558	0.8594
684	0.9	19.36	B	90	44.9	32.6	30.5236	43.8128
685	-0.3	19.36	B	90	44.5	41.4	6.9993	3.2063
686	-0.8	19.32	B	90	45.3	45.4	-0.1332	1.9517
687	0.0	21.36	B	90	47.2	40.8	14.5020	21.2419
688	-0.5	21.36	B	90	45.1	40.9	9.8250	4.3931
689	-0.8	21.36	B	90	44.8	44.7	0.2016	3.3319
690	-1.2	23.36	B	90	45.4	45.5	-0.1773	2.9443
691	-0.6	23.36	B	90	45.0	43.0	4.4846	5.8768
692	0.0	23.33	B	90	47.2	38.2	21.0200	24.5477
693	-0.4	23.36	B	90	48.6	41.6	15.5860	6.8523
694	-0.6	25.06	B	90	45.1	40.2	11.2462	7.6482
695	-1.2	25.07	B	90	44.9	44.2	1.5048	3.9030
696	0.2	25.05	B	90	44.7	36.2	20.5954	33.7450
697	-1.1	26.36	B	90	47.2	47.3	-0.3456	5.4420
698	-0.4	26.36	B	90	46.1	39.6	14.9724	10.5770
699	-0.2	26.36	B	90	48.0	38.6	21.5432	12.0140
700	-1.3	28.36	B	90	45.1	45.4	-0.6890	5.1013
701	-0.5	28.36	B	90	44.5	39.8	10.9114	12.5193
702	0.0	28.36	B	90	46.6	34.5	28.9916	34.2540
703	-0.6	30.36	B	90	44.9	37.9	16.4374	14.3365
704	-1.0	31.36	B	90	46.1	43.1	6.6916	10.8285
705	-1.5	31.30	B	90	47.6	47.8	-0.3861	4.5071
706	-1.1	31.31	B	90	44.6	44.1	1.1261	9.5276
707	-0.7	31.36	B	90	47.7	42.8	10.7889	14.5672
708	-0.3	31.36	B	90	45.8	36.2	22.9913	19.4988
709	-1.5	32.36	B	90	44.5	44.7	-0.4936	5.0201
710	-0.9	32.36	B	90	45.0	39.4	13.1935	13.2621
711	-0.7	32.36	B	90	46.9	41.5	12.0889	15.9776
712	-0.2	32.36	B	90	46.9	34.3	30.1681	22.7251
713	-1.1	33.36	B	90	46.0	43.0	6.8157	11.5073
714	-0.5	33.36	B	90	45.9	34.9	26.3918	20.4017
715	-1.3	34.36	B	90	45.4	41.7	8.5287	9.2962
716	-0.7	34.36	B	90	45.6	36.2	22.2993	18.9740
717	0.1	34.36	B	90	45.5	31.2	35.7004	51.6199
718	-0.8	35.36	B	90	44.9	38.3	15.5026	18.8210
719	-0.4	35.36	B	90	46.7	34.0	30.7808	25.7793
720	0.1	35.36	B	90	47.8	28.5	48.8228	54.2288
721	-1.7	36.36	B	90	45.3	44.2	2.5300	3.4426
722	-1.3	36.33	B	90	46.8	43.3	7.8715	10.9224
723	-0.6	36.36	B	90	44.8	35.1	23.2759	24.0895
724	-1.9	37.35	B	90	46.1	46.0	0.3297	-0.2235
725	-1.3	37.35	B	90	46.6	43.8	6.3405	11.8067
726	-1.0	37.36	B	90	46.8	40.0	15.4631	17.8526

Index	Temperature	Salinity	Geometry	Duration	Start weight	End weight	Recession	Agassiz rate
727	-1.2	37.36	B	90	47.5	34.7	30.5126	13.8230
728	-1.8	38.36	B	90	45.3	45.1	0.4892	1.9989
729	-1.2	38.35	B	90	46.1	42.3	8.7857	14.8571
730	-0.6	38.35	B	90	43.8	31.7	30.5073	27.8442
731	-0.2	38.35	B	90	47.0	31.9	36.9144	36.5665
732	-2.1	39.35	B	90	45.8	45.4	0.7077	-4.5510
733	-1.7	39.35	B	90	46.3	43.8	5.5273	4.5015
734	-1.3	39.36	B	90	46.1	39.1	16.2088	13.6424
735	-0.5	39.35	B	90	46.9	31.8	37.1010	32.1321
736	0.2	39.35	B	90	45.6	25.4	53.6862	68.8967
737	-2.1	40.36	B	90	44.5	44.0	1.1504	-4.7110
738	-1.5	40.35	B	90	44.4	39.5	11.4649	9.7257
739	-0.7	40.35	B	90	47.6	34.9	29.9948	29.3744
740	-2.3	41.35	B	90	45.5	44.8	1.6252	-9.8913
741	-1.4	41.34	B	90	49.9	38.9	24.8800	12.9907
742	-0.9	41.35	B	90	44.8	37.2	17.8768	26.0394
743	-0.4	41.35	B	90	46.8	30.4	41.0427	39.2960
744	-1.7	42.35	B	90	45.0	42.1	6.5686	5.7092
745	-2.1	42.35	B	90	44.5	44.1	0.7668	-5.0178
746	0.6	42.35	B	90	46.4	20.9	71.1741	92.9619
747	19.3	0.37	C	4	45.7	19.6	1672.5713	1773.0082
748	19.9	0.37	C	4	44.2	18.4	1705.2334	1879.2685
749	18.8	30.33	B	4	44.8	20.8	1524.5165	1503.7220
750	19.4	30.36	B	4	43.9	18.1	1713.8652	1579.5093
751	20.1	30.36	B	4	44.3	18.1	1735.9864	1669.1743
752	20.8	30.22	B	4	44.2	17.0	1833.4957	1757.8322
753	19.7	30.36	B	4	43.9	18.8	1653.5756	1617.6127
754	20.4	30.36	B	4	46.4	21.3	1567.3222	1708.3927
755	20.9	30.23	B	4	44.3	20.5	1525.3878	1771.3764
756	19.1	30.36	B	4	43.9	19.4	1599.4649	1541.7191
757	19.7	30.36	B	4	44.6	18.9	1683.7065	1617.6328
758	19.2	30.36	B	4	45.1	21.0	1524.0320	1554.2411
759	19.3	30.36	B	4	45.1	19.4	1663.6445	1566.8476
760	19.9	30.36	B	4	47.6	21.7	1590.8938	1643.2968
761	20.5	30.36	B	4	48.2	22.1	1592.8036	1721.5199
762	19.8	30.36	B	4	44.5	20.1	1574.9688	1630.4233
763	19.0	30.35	B	4	45.0	22.4	1410.8474	1529.1363
764	20.1	30.36	B	4	44.3	19.7	1596.2211	1669.1926
765	19.2	30.24	B	4	43.4	20.3	1503.5130	1551.5232
766	1.6	2.00	B	45	47.0	41.5	24.8172	28.4706
767	19.0	30.36	B	4	44.5	20.6	1528.2413	1529.2519
768	19.1	30.36	B	4	44.4	18.4	1712.7147	1541.7192
769	1.2	2.21	B	45	44.7	38.4	29.7336	20.8393
770	-0.7	22.41	B	90	45.2	45.3	-0.3779	4.5504
771	18.4	30.36	B	4	47.8	23.0	1497.0007	1455.3872
772	19.4	30.36	B	4	44.6	20.5	1542.7719	1579.4642

Index	Temperature	Salinity	Geometry	Duration	Start weight	End weight	Recession	Agassiz rate
773	19.3	30.36	B	4	46.4	21.7	1531.4829	1566.8436
774	19.4	30.36	B	4	44.2	20.0	1558.8377	1579.4528
775	0.4	24.13	B	45	46.4	41.4	22.4639	38.0956
776	3.5	24.13	B	22	44.8	27.3	183.5588	157.1576
777	6.1	24.14	B	22	44.6	14.5	374.5586	291.2960
778	8.4	24.14	B	15	43.8	16.1	508.2697	432.6332
779	10.1	24.15	B	10	43.5	19.2	640.1726	554.9889
780	11.4	24.16	B	5	46.4	31.1	681.7504	661.6723
781	-0.8	22.41	B	90	44.6	44.9	-0.7213	4.1312
782	12.7	24.16	B	5	43.6	26.7	810.7734	772.3657
783	-0.6	22.42	B	90	43.5	43.8	-0.4918	4.9789
784	14.1	24.16	B	5	44.2	25.2	923.4526	900.3303
785	-0.8	22.42	B	90	43.2	41.0	5.1476	4.1372
786	18.8	30.36	B	4	44.2	18.8	1672.3021	1504.4376
787	-0.9	22.39	B	646	40.4	31.8	3.0799	3.4858
788	15.9	24.17	B	5	45.0	23.2	1073.4408	1078.1457
789	19.3	24.17	B	5	45.1	20.3	1266.7603	1454.9213
790	19.2	30.36	B	4	43.1	19.2	1573.0966	1554.2616
791	20.3	30.36	B	4	46.1	20.2	1641.4157	1695.3855
792	19.4	30.24	B	4	44.4	18.8	1678.1577	1576.7615
793	18.9	30.12	C	4	46.2	18.5	1795.4873	1712.2850
794	19.2	30.36	B	4	45.0	20.7	1543.9839	1554.2511
795	18.7	30.25	C	4	45.3	19.9	1631.5750	1687.4061
796	19.0	30.36	B	4	43.7	18.5	1744.4062	1529.2439
797	18.6	30.24	C	4	44.5	18.5	1822.2335	1673.4251
798	-0.9	22.36	B	500	43.5	39.5	1.7362	3.6724
799	20.4	30.36	B	4	43.8	19.9	1732.2219	1708.3619
800	20.0	30.25	C	4	44.4	17.4	1902.6660	1873.1212
801	20.4	30.13	B	4	44.2	20.0	1570.9185	1702.6424
802	20.4	30.02	C	4	44.0	16.1	2103.4874	1925.6744
803	20.0	30.36	B	4	43.2	18.1	1831.7728	1656.2414
804	19.6	30.25	C	4	45.5	17.5	2035.9871	1814.9560
805	1.2	25.71	C	45	43.4	28.1	86.1471	77.6386
806	19.7	30.36	B	4	46.5	19.6	1756.8696	1617.6103
807	19.3	30.24	C	4	43.9	15.8	1984.3950	1771.7284
808	-0.9	22.31	B	549	44.2	39.8	1.7718	3.8392
809	20.7	30.36	B	4	44.2	19.0	1654.6017	1748.0050
810	20.2	30.25	C	4	44.4	16.9	1860.3412	1902.4561
811	20.6	30.36	B	4	43.8	19.1	1628.6686	1734.7519
812	20.0	30.23	C	4	44.8	17.1	1864.1567	1872.7456
813	18.9	30.36	B	4	43.9	19.7	1571.7640	1516.8131
814	18.5	30.24	C	4	44.6	17.7	1790.9144	1659.5073
815	19.3	30.36	B	4	48.2	21.1	1669.7001	1566.8227
816	18.8	30.22	C	4	44.4	18.5	1705.2895	1700.8466
817	1.2	25.43	B	45	43.6	30.0	69.9409	67.8360
818	1.6	25.37	C	45	43.9	24.2	107.7176	93.2235

Index	Temperature	Salinity	Geometry	Duration	Start weight	End weight	Recession	Agassiz rate
819	-0.9	22.24	B	738	44.3	37.7	1.8910	3.7939
820	19.4	30.36	B	4	44.5	19.8	1601.5448	1579.4669
821	18.9	30.24	C	4	44.6	17.0	1854.1680	1715.1822
822	3.2	25.44	B	15	47.8	37.1	149.3676	148.4746
823	4.2	25.39	C	15	44.0	29.0	231.8317	221.4855
824	5.9	25.45	B	15	43.6	23.9	323.9782	286.7527
825	6.5	25.36	C	15	44.1	19.8	420.0829	364.2474
826	7.3	25.46	B	10	44.8	26.0	447.3586	371.8172
827	7.6	25.37	C	10	43.8	24.0	487.7648	442.5387
828	8.1	25.46	B	10	43.4	23.4	497.0615	424.5312
829	8.4	25.37	C	10	43.8	22.0	551.3462	503.4238
830	12.1	25.48	B	5	45.5	28.5	785.9126	732.5473
831	19.4	25.49	B	5	43.9	19.2	1293.8437	1485.8135
832	19.7	30.36	B	4	44.5	18.2	1736.3373	1617.6378
833	19.2	30.23	C	4	44.1	16.4	1894.4100	1757.3687
834	19.8	30.36	B	4	43.6	19.6	1570.1352	1630.4442
835	19.3	30.24	C	4	44.4	17.0	1852.3213	1771.8801
836	21.0	30.36	B	4	43.4	16.7	1823.0898	1788.0619
837	20.5	30.23	C	4	44.5	15.3	2019.3375	1946.5203
838	20.1	30.36	B	4	43.8	17.8	1739.3596	1669.1707
839	19.7	30.24	C	4	44.3	17.5	1791.8833	1829.1122
840	20.0	30.36	B	4	50.0	22.0	1684.4020	1656.2295
841	19.5	30.23	C	4	43.4	15.9	1904.9482	1800.0824
842	20.0	30.36	B	4	44.3	19.0	1657.4957	1656.2269
843	19.5	30.24	C	4	43.9	17.1	1814.3853	1800.4400
844	-0.9	22.36	B	603	44.6	39.2	1.8820	3.8805
845	19.2	30.36	B	4	44.2	19.3	1627.2573	1554.2564
846	18.8	30.24	C	4	44.3	17.8	1768.5001	1701.3308
847	1.2	26.30	B	45	44.2	31.9	61.8024	70.0794
848	1.6	26.25	C	45	44.4	28.0	85.5103	95.9992
849	3.0	26.25	B	15	45.2	35.3	143.5378	142.4901
850	4.1	26.21	C	15	44.0	27.6	258.6246	219.8154
851	5.2	26.26	B	15	43.6	23.9	324.4146	251.6589
852	5.8	26.17	C	15	44.7	20.2	418.3394	322.6822
853	6.6	26.27	B	15	44.8	19.4	439.1461	332.9051
854	7.1	26.16	C	15	44.3	15.1	540.9875	411.6572
855	7.6	26.28	B	10	44.4	23.9	502.7929	396.5670
856	8.0	26.19	C	10	44.3	21.0	594.4160	478.8034
857	8.6	26.29	B	10	44.6	20.5	616.2557	464.8762
858	8.8	26.18	C	10	43.5	17.4	703.6563	541.7987
859	9.8	26.30	B	10	43.6	17.1	720.8446	553.0218
860	9.9	26.18	C	10	44.0	14.9	815.6659	634.0143
861	18.9	30.36	B	4	44.0	19.5	1599.2054	1516.8051
862	18.5	30.25	C	4	44.5	17.3	1830.4099	1659.6996
863	11.4	26.31	B	5	44.4	30.3	648.6069	680.9786
864	10.9	26.25	C	5	44.4	25.4	919.6170	724.0461

Index	Temperature	Salinity	Geometry	Duration	Start weight	End weight	Recession	Agassiz rate
865	20.6	30.36	B	4	44.6	17.8	1777.0348	1734.7418
866	20.2	30.24	C	4	44.0	15.7	1953.3419	1902.2071
867	19.6	30.36	B	4	42.9	18.9	1592.8077	1604.8430
868	19.1	30.25	C	4	44.8	17.4	1827.1893	1743.6702
869	19.8	30.36	B	4	45.0	19.2	1675.1604	1630.4358
870	19.4	30.24	C	4	44.6	17.2	1843.9403	1786.1660
871	20.5	30.36	B	4	44.6	19.7	1613.5550	1721.5359
872	20.0	30.25	C	4	43.5	16.2	1881.9084	1873.1227
873	20.3	30.36	B	4	43.5	17.8	1726.1791	1695.2662
874	19.8	30.25	C	4	43.8	17.5	1775.8925	1843.8926
875	20.9	30.36	B	4	44.4	18.6	1698.4228	1774.6732
876	20.4	30.25	C	4	43.1	15.0	1985.8848	1932.0683
877	1.6	29.67	B	45	44.4	26.0	97.6355	94.5791
878	1.8	29.59	C	45	43.8	22.7	117.2955	115.9480
879	3.4	29.09	B	15	45.2	32.5	187.1137	171.6664
880	4.4	29.03	C	15	43.1	24.8	298.5102	251.3021
881	5.5	29.13	B	15	43.9	23.2	343.0448	283.3212
882	6.1	29.03	C	15	43.7	19.1	430.7370	360.7768
883	6.9	29.14	B	15	44.2	18.4	455.1834	369.4278
884	7.3	29.02	C	15	43.4	13.4	576.5199	447.3615
885	7.9	29.15	B	15	43.9	14.9	542.6336	436.6957
886	8.1	29.02	C	10	44.7	19.7	646.8199	509.4284
887	9.7	29.04	C	10	43.9	15.2	799.3800	644.2187
888	11.1	29.17	B	10	45.5	14.7	852.8321	684.0670
889	11.1	29.03	B	10	45.5	14.7	852.8321	682.6363
890	11.0	28.90	C	10	43.4	13.2	878.1568	762.1122
891	19.5	30.13	B	4	44.7	20.2	1574.1165	1586.7708
892	19.1	30.02	C	4	43.9	17.7	1759.9535	1737.9010
893	19.3	29.88	B	4	46.9	22.2	1518.0869	1556.0737
894	18.9	29.77	C	4	44.2	18.4	1706.5750	1703.6623
895	19.6	29.91	B	4	45.3	18.2	1781.4898	1594.5168
896	19.2	29.79	C	4	43.6	18.3	1683.1021	1746.4084
897	19.7	30.36	B	4	47.9	21.6	1617.6459	1617.6312
898	19.3	30.25	C	4	44.9	17.3	1840.4943	1771.9764
899	20.7	30.36	B	4	44.9	18.1	1765.6889	1748.0133
900	20.3	30.25	C	4	44.4	16.4	1905.1990	1917.2229
901	20.8	30.36	B	4	43.7	18.0	1711.9414	1761.3255
902	20.4	30.25	C	4	44.6	17.1	1845.8518	1932.2157
903	19.5	30.36	B	4	44.7	19.7	1619.0035	1592.1371
904	19.1	30.26	C	4	44.1	19.4	1617.7050	1743.7847
905	1.1	29.65	B	45	44.5	30.6	70.3667	75.2314
906	0.9	29.59	C	45	43.4	27.7	82.6940	76.6828
907	2.2	30.22	B	15	43.9	35.1	129.4821	121.0787
908	3.4	30.18	C	15	44.9	30.1	225.2051	199.3046
909	4.8	30.22	B	15	44.2	25.1	308.6883	249.1200
910	5.6	30.13	C	15	44.4	21.1	395.4419	333.7447

Index	Temperature	Salinity	Geometry	Duration	Start weight	End weight	Recession	Agassiz rate
911	6.5	30.22	B	15	44.7	19.2	443.6869	350.5485
912	6.9	30.11	C	15	44.5	14.8	553.0886	425.5730
913	7.6	30.22	B	15	45.0	17.7	483.1652	423.6433
914	8.0	30.10	C	15	44.2	11.4	651.4741	510.6003
915	8.4	30.22	B	15	43.8	12.0	627.7557	480.4894
916	8.7	30.08	C	10	44.9	17.6	724.0546	568.0256
917	9.8	30.22	B	10	44.2	16.9	736.4403	587.4262
918	9.9	30.11	C	10	46.0	15.2	844.7468	673.2053
919	10.4	30.22	B	5	47.8	33.2	629.8001	636.1603
920	10.5	30.16	C	5	48.6	30.7	791.1741	729.2896
921	11.6	30.23	B	5	45.8	27.6	844.3780	738.8665
922	11.6	30.15	C	5	45.6	24.7	1006.4824	835.9534
923	12.9	30.23	B	5	44.2	24.2	978.4709	858.0048
924	12.9	30.14	C	5	46.8	24.3	1076.1354	970.6596
925	19.0	30.36	B	4	43.2	18.1	1688.3544	1529.3766
926	18.6	30.26	C	4	43.9	17.7	1752.2446	1673.8900
927	16.3	30.23	B	5	46.8	20.2	1343.0366	1208.2732
928	16.0	30.11	C	5	46.6	18.7	1438.5300	1328.9169
929	18.8	30.36	B	4	43.4	21.4	1406.7614	1504.4201
930	18.4	30.27	C	4	45.0	18.4	1742.1676	1646.4329
931	-1.0	22.86	B	735	43.1	33.5	2.9311	3.5842
932	-1.0	22.73	B	731	43.1	30.4	4.0330	3.4958

Appendix D

Matlab code for glacier density model

```
warning('off', 'all')
StartTime = datetime
clearvars
close all

% Define formats.
format shortG
FontSize = 16;
TileTitleSize = 20;
SubTitleSize = 22;
TitleSize = 24;
MarkerSize = 80;
LineWidth = 2;

% Path to save file.
MainPath = 'C:\Users\onegr\Documents\University\MSc\MATLAB';
ThesisPath = "../My work/00 Current/Latex thesis/";
TextOutput = sprintf("%sGlacierOutput.txt", ThesisPath);
Now = datetime;
str = sprintf("%% Model output generated at %s.", Now);
writelines(str, TextOutput)


% Define constants.
rho_Ih = 916.7;
rho_firn = 830;
rho_snow = 550;
g = 9.81;
R = 8.314;
TC0 = 273.16; % conversion from C to K
```

```
31
32 % Other definitions.
33 wgs84 = wgs84Ellipsoid("m");
34
35
36 % Ad-hoc parameter for bubble pressure.
37 AdHoc = 0.36;
38 str = sprintf("\\newcommand{\\AdHoc}{%0.2f} %% ad hoc parameter", ...
39     AdHoc);
40 writelines(str, TextOutput, WriteMode="append")
41
42
43 %% GISP2 profiles
44 % Density data (Gow et al. 1997)
45 GISPTester = [76 .830
46     250 .9141
47     500 .919
48     1000 .92
49     1500 .9205
50     2000 .9203
51     2250 .9197
52     2500 .919
53     2750 .918
54     3000 .9172];
55 GISPTester = table(GISPTester(:, 1), 1000*GISPTester(:, 2));
56 GISPTester = renamevars(GISPTester, ...
57     GISPTester.Properties.VariableNames, ...
58     {'Depth', 'Density'});
59
60 % Temperature data (Cuffey et al. 1995)
61 GISPTemp = readtable("../Data/GISP2_t.txt");
62 GISPTemp = renamevars(GISPTemp, GISPTemp.Properties.VariableNames, ...
63     {'Depth', 'T'});
```

```
64
65 % Display.
66 E = figure;
67 set(gcf, 'Position', get(0, 'Screensize'))
68 tiledlayout flow
69 nexttile
70 scatter(GISPTester.Depth, GISPTester.Density, MarkerSize, 'k', 'filled')
71 xlim([0 3053])
72 xlabel('Depth (m)')
73 ylabel('Density (kg/m3)')
74 grid on
75 set(gca, 'FontSize', FontSize)
76 title('Density (Gow et al., 1997)', 'FontSize', TileTitleSize, ...
77     'FontWeight', 'bold')
78
79 nexttile
80 scatter(GISPTemp.Depth, GISPTemp.T, MarkerSize, 'k', 'filled')
81 xlim([0 3053])
82 xlabel('Depth (m)')
83 ylabel('Temperature (C)')
84 grid on
85 set(gca, 'FontSize', FontSize)
86 title('Temperature (Cuffey et al., 1995)', 'FontSize', TileTitleSize, ...
87     'FontWeight', 'bold')
88
89 sgtitle('Density and temperature in GISP2 ice core', 'FontSize', ...
90     TitleSize, 'FontWeight', 'bold')
91 saveas(E, "../My work/00 Current/Latex thesis/GISP2.png")
92
93
94
95
96 %%
```

```
97  % ====================================================================
98  % Values used for test.
99  % ====================================================================
100 A = 0.12;
101 TC = -32;
102 HASL = 3200;
103 rho_init = 285;
104 Z = 3053;
105 t_inf = -15;
106 z_ice = 1400;
107 t_ductile = -27;
108 rho_ice = 920.5;
109 z_inf = 3000;
110 rho_inf = 917.2;
111 % ====================================================================
112
113 %% Parameters.
114 % A = input("Accummulation rate (m water/day): ");
115 % TC = input("Mean annual temperature (C): ");
116 % HASL = input("Altitude of glacier surface (m): ");
117 % rho_init = input("Initial density of snowpack: ");
118 % Z = input("Thickness of glacier (m): ");
119 % t_inf = input("Temperature at bottom of glacier (C): ");
120 % z_ice = input("Depth of ductile transition (m): ");
121 % t_ductile = input("Temperature of ductile transition (C): ");
122 % rho_ice = input("Maximum density of ice (kg/m3): ");
123 % z_inf = input("Depth of last density point (m): ");
124 % rho_inf = input("Density at last point (kg/m3): ");
125
126 T_inf = t_inf + TC0;
127
128 % Writing parameters to file for LaTeX.
129 str = sprintf("\\newcommand{\\AccRate}{%0.2f} %% accumulation rate", ...
```

```
130     A);
131 writelines(str, TextOutput, WriteMode="append")
132 str = sprintf("\\newcommand{\\TC}{%0.0f} %% mean annual temperature", ...
133     TC);
134 writelines(str, TextOutput, WriteMode="append")
135 str = sprintf("\\newcommand{\\HASL}{%0.0f} %% height of surface", ...
136     HASL);
137 writelines(str, TextOutput, WriteMode="append")
138 str = sprintf("\\newcommand{\\rhoinit}{%0.0f} %% density of snow pack", ...
139     rho_init);
140 writelines(str, TextOutput, WriteMode="append")
141 str = sprintf("\\newcommand{\\ZZ}{%0.0f} %% depth of bottom", ...
142     Z);
143 writelines(str, TextOutput, WriteMode="append")
144 str = sprintf("\\newcommand{\\tinf}{%0.0f} %% bottom temperature", ...
145     t_inf);
146 writelines(str, TextOutput, WriteMode="append")
147 str = sprintf("\\newcommand{\\zice}{%0.0f} %% depth of ductile transition", ...
148     z_ice);
149 writelines(str, TextOutput, WriteMode="append")
150 str = sprintf("\\newcommand{\\tductile}{%0.0f} %% temperature of ductile tr.", ...
151     t_ductile);
152 writelines(str, TextOutput, WriteMode="append")
153 str = sprintf("\\newcommand{\\rhoice}{%0.1f} %% max density of ice", ...
154     rho_ice);
155 writelines(str, TextOutput, WriteMode="append")
156 str = sprintf("\\newcommand{\\zinf}{%0.0f} %% depth of last point", ...
157     z_inf);
158 writelines(str, TextOutput, WriteMode="append")
159 str = sprintf("\\newcommand{\\rhoinf}{%0.1f} %% density of last point", ...
160     rho_inf);
161 writelines(str, TextOutput, WriteMode="append")
162
```

```
163
164 % ======== Define Herron-Langway profile. ========
165 % Coefficients from Arrhenius plots.
166 k10 = 11;
167 k20 = 1.016e4;
168 k11 = 575;
169 k21 = 2.14e4;
170
171 % We need to change the units of density to be consistent with Herron &
172 % Langway's usage.
173 TK = TC + TC0;
174 Rho_ice = rho_ice / 1000;
175 Rho_firn = rho_firn / 1000;
176 Rho_snow = rho_snow / 1000;
177 Rho_init = rho_init / 1000;
178
179 % Create Herron-Langway function for snow layer.
180 syms Z0(z)
181 Z0 = exp((Rho_ice * k10 * exp(-k20 / R / TK) * z) + log(Rho_init ...
182     / Rho_ice));
183
184 syms Rho1(z)
185 Rho1 = rho_ice * Z0 / (1 + Z0);
186
187 % Calculate snow-firn transition depth.
188 Z0_target = Rho_snow / (Rho_ice - Rho_snow);
189 eqn0 = (Z0 == Z0_target);
190 z_snow = double(vpasolve(eqn0, z));
191 str = sprintf("\\newcommand{\\zsnow}{%0.0f} %% depth of firn transition", ...
192     z_snow);
193 writelines(str, TextOutput, WriteMode="append")
194
195 % Create Herron-Langway function for firn layer.
```

```
196 syms Z1(z);
197 Z1 = exp((Rho_ice * k11 * exp(-k21 / R / TK) * (z - z_snow) / sqrt(A)) ...
198     + log(Rho_snow / (Rho_ice - Rho_snow)));
199
200 syms Rho2(z)
201 Rho2 = rho_ice * Z1 / (1 + Z1);
202
203 % Calculate firn-ice transition depth.
204 Z1_target = Rho_firn / (Rho_ice - Rho_firn);
205 eqn1 = (Z1 == Z1_target);
206 z_firn = double(vpasolve(eqn1, z));
207 str = sprintf("\\newcommand{\\zfirn}{%0.0f} %% depth of pore closure", ...
208     z_firn);
209 writelines(str, TextOutput, WriteMode="append")
210
211 % Display results.
212 fprintf('Height of snow-firn transition: %0.0f\n', z_snow);
213 fprintf('Height of firn-ice transition: %0.0f\n', z_firn);
214
215 % Keep track.
216 z_vect = [0 z_snow z_firn z_ice];
217 rho_vect = [rho_init rho_snow rho_firn rho_ice];
218
219
220 %% Brittle layer.
221 % Define terms.
222 C_firn = log(rho_ice / rho_firn - 1);
223 C_snow = log(rho_ice / rho_snow - 1);
224
225 k = (C_snow - C_firn) / (z_firn - z_snow);
226 z0 = z_firn + C_firn / k;
227
228 syms Rho3(z)
```

```
Rho3 = rho_ice / (1 + exp(-k * (z - z0)));


%% Ductile layer.
% Make temperature profile.
DeltaT = t_inf - TC;
DeltaThick = Z - z_ice;

syms tz(z)
tz = DeltaT / DeltaThick * (z - z_ice) + t_ductile;

% Set the point where the brittle and ductile profiles meet.
Intercept = eval(subs(Rho3, z, z_ice));

% Make linear density profile.
syms Rho4(z)
Rho4 = (z - z_ice) * (rho_inf - Intercept) / (z_inf - z_ice) + Intercept;


%% Now make a big function.
syms BigRho(z)
BigRho = piecewise(z <= z_vect(2), Rho1, ...
    z_vect(2) < z <= z_vect(3), Rho2, ...
    z_vect(3) < z <= z_vect(4), Rho3, ...
    z > z_vect(4), Rho4);


%% Display
for h1 = 1:height(GISPTester)
    GISPTester.Model(h1) = eval(subs(BigRho, z, GISPTester.Depth(h1)));
end
Corr = corrcoef(GISPTester.Density, GISPTester.Model);
R2 = Corr(1, 2)^2;
```

```
262 str = sprintf("\\newcommand{\\glacierfit}{%0.4f} %% R2 of glacier model", ...
263     R2);
264 writelines(str, TextOutput, WriteMode="append")
265
266 F = figure;
267 tiledlayout(2, 1)
268 for tile = 1:2
269     nexttile
270     P = fplot(BigRho, [0 Z], 'k');
271     P.LineWidth = LineWidth;
272     hold on
273     scatter(GISPTester.Depth, GISPTester.Density, MarkerSize, 'k', 'filled')
274     grid minor
275     grid on
276     xlabel('Depth (m)')
277     ylabel('Density (kg m^{-3})')
278     ylim([rho_init 25*ceil(rho_ice/25)])
279     set(gca, 'FontSize', FontSize)
280     yline(550, 'b', 'LineWidth', LineWidth)
281     xline(z_snow, 'b', 'LineWidth', LineWidth)
282     yline(830, 'r', 'LineWidth', LineWidth)
283     xline(z_firn, 'r', 'LineWidth', LineWidth)
284     xline(z_ice, 'g', 'LineWidth', LineWidth)
285     legend('Model', 'GISP2 data', 'Snow-firn transition', '', ...
286         'Pore closure', ...
287         '', 'Ductile transition', 'Location', 'southeast')
288     switch tile
289         case 1
290             title('Full height', 'FontSize', TileTitleSize, ...
291                 'FontWeight', 'bold')
292             ylim([0 950])
293         case 2
294             title('Ice layers', 'FontSize', TileTitleSize, 'FontWeight', ...
```

```
295                     'bold')
296                 ylim([rho_firn 925])
297             end
298         end
299         sgtitle('Full glacier density model', 'FontSize', TitleSize, ...
300             'FontWeight', 'bold')
301         set(gcf, 'Position', get(0, 'Screensize'))
302         saveas(F, "../My work/00 Current/Latex thesis/GlacierProfile.png")
303
304
305         %% Overburden pressure profile.
306         % Calculate atmospheric pressure from the surface altitude and temperature.
307         % EAM_Barometric is listed later in this appendix.
308         p_atm = EAM_Barometric(HASL, TC);
309         str = sprintf("\\newcommand{\\patm}{%0.0f} %% surface pressure", ...
310             p_atm);
311         writelines(str, TextOutput, WriteMode="append")
312
313         % Integrate each section of model and calculate corrections at boundaries.
314         Pr1 = p_atm + g * int(Rho1, 0, z);
315         p_snow = eval(subs(Pr1, z, z_snow));
316
317         Pr2 = g * int(Rho2, z_snow, z);
318         p_corr = eval(subs(Pr2, z, z_snow));
319         Pr2 = Pr2 - p_corr + p_snow;
320         p_firn = eval(subs(Pr2, z, z_firn));
321
322         Pr3 = g * int(Rho3, z_firn, z);
323         p_corr = eval(subs(Pr3, z, z_firn));
324         Pr3 = Pr3 - p_corr + p_firn;
325         p_ice = eval(subs(Pr3, z, z_ice));
326
327         Pr4 = g * int(Rho4, z_ice, z);
```

```
328 p_corr = eval(subs(Pr4, z, z_ice));
329 Pr4 = Pr4 - p_corr + p_ice;
330
331
332 % Make full piecewise function.
333 syms BigP(z)
334 BigP = piecewise(z <= z_vect(2), Pr1, ...
335     z_vect(2) < z <= z_vect(3), Pr2, ...
336     z_vect(3) < z <= z_vect(4), Pr3, ...
337     z > z_vect(4), Pr4);
338
339 G = figure;
340 set(gcf, 'Position', get(0, 'Screensize'))
341 tiledlayout(1, 3)
342 nexttile
343 Q1 = fplot(BigP, [0 Z], 'k');
344 Q1.LineWidth = LineWidth;
345 grid minor
346 grid on
347 xlabel('Depth (m)')
348 ylabel('Pressure (Pa)')
349 set(gca, 'FontSize', FontSize)
350 title('Overburden pressure', 'FontSize', TileTitleSize, 'FontWeight', ...
351     'bold')
352
353
354 %% Bubble pressure profile.
355 % Calculate pore closure pressure from the surface altitude and pore
356 % closure temperature and depth.
357 p_close = EAM_Barometric(HASL-z_firn, TC);
358 str = sprintf("\\newcommand{\\pclose}{%0.1f} %% pressure at pore closure", ...
359     p_close);
360 writelines(str, TextOutput, WriteMode="append")
```

```
361
362
363 % Calculate the temperature below the pore closure, assuming it varies
364 % linearly with depth from the pore closure temperature to the temperature
365 % at the ductile transition.
366 syms T(z)
367 T = piecewise(z <= z_firn, TC, ...
368     z >= z_ice, tz, ...
369     TC + (z - z_firn) * (t_ductile - TC) / (z_ice - z_firn));
370
371 % Now get the in-situ ice Ih density as a function of overburden pressure.
372 % Functions starting with "gsw_" are available in the GSW Toolbox.
373 syms RhoGSW(z)
374 RhoGSW = gsw_rho_ice(T, (BigP - 101325)/1e4);
375
376 % Density deficit.
377 syms RhoDef(z)
378 RhoDef = RhoGSW - BigRho;
379
380 nexttile
381 Q2 = fplot(RhoDef, [z_firn Z], 'k');
382 Q2.LineWidth = LineWidth;
383 grid minor
384 grid on
385 xlim([0 Z])
386 xlabel('Depth (m)')
387 ylabel('Density deficit (kg m^{-3})')
388 set(gca, 'FontSize', FontSize)
389 title('Density deficit', 'FontSize', TileTitleSize, 'FontWeight', ...
390     'bold')
391
392
393 % Equation of Gow 1968.
```

```
394 syms BubblePress(z)
395 assume(z, "positive")
396 BubblePress = piecewise(z <= z_firn, p_atm, ...
397     (RhoGSW - rho_firn) / (RhoGSW - BigRho) * ...
398     BigRho * p_close / rho_firn);
399
400 nexttile
401 Q2 = fplot(BubblePress, [0 Z], 'k');
402 Q2.LineWidth = LineWidth;
403 grid minor
404 grid on
405 yline(30*101325, ':k', 'LineWidth', LineWidth)
406 xline(316, ':k', 'LineWidth', LineWidth)
407 xline(z_ice, ':r', 'LineWidth', LineWidth)
408 xlabel('Depth (m)')
409 ylabel('Pressure (Pa)')
410 set(gca, 'FontSize', FontSize)
411 title('Air pressure in bubbles', 'FontSize', TileTitleSize, 'FontWeight', ...
412     'bold')
413 legend('Bubble pressure', '30 atm', '316 m', 'Ductile transition')
414
415 saveas(G, "../My work/00 Current/Latex thesis/BubblePress.png")
416
417
418 %%
419 % Detail.
420 H = figure;
421 Q4 = fplot(AdHoc*BubblePress/101325, [z_firn z_firn+400], 'k');
422 Q4.LineWidth = LineWidth;
423 grid minor
424 grid on
425 yline(1, 'b', 'LineWidth', LineWidth)
426 xline(120, 'b', 'LineWidth', LineWidth)
```

```
427 yline(20, 'c', 'LineWidth', LineWidth)
428 xline(235, 'c', 'LineWidth', LineWidth)
429 yline(27, 'r', 'LineWidth', LineWidth)
430 xline(360.5, 'r', 'LineWidth', LineWidth)
431 ylim([0 32])
432 xlabel('Depth (m)')
433 ylabel('Pressure (atm)')
434 set(gca, 'FontSize', FontSize)
435 title('Air pressure in bubbles', 'FontSize', TileTitleSize, 'FontWeight', ...
436     'bold')
437 set(gcf, 'Position', get(0, 'Screensize'))
438 legend('Modelled bubble pressure', ...
439     '1 atm, 120 m', '', ...
440     '20 atm, 235 m', '', ...
441     '27 atm,  360.5 m', '', ...
442     'Location', 'southeast')
443
444 saveas(H, "../My work/00 Current/Latex thesis/BubblePressDetail.png")
445
446
447 %% ====================================================================
448 % Application at sea.
449 % ====================================================================
450
451 % Load ORAS5 data.
452 load("../Data/Olat.mat")
453 load("../Data/Olon.mat")
454 load("../Data/ORAS-bathy.mat")
455 load("../Data/Depth.mat")
456
457 % ====================================================================
458 % Values used for test.
459 % ====================================================================
```

```
460 z_sail = 80;
461 del_z = 200;
462 Lat = 69+7/60;
463 Lon = -52-6/60;
464 YY = 1958;
465 MM = 5;
466
467 % Write test data to LaTeX.
468 str = sprintf("\\newcommand{\\Lat}{%0.2f} %% test latitude", ...
469     Lat);
470 writelines(str, TextOutput, WriteMode="append")
471 str = sprintf("\\newcommand{\\Lon}{%0.2f} %% test longitude", ...
472     Lon);
473 writelines(str, TextOutput, WriteMode="append")
474 str = sprintf("\\newcommand{\\YY}{%d} %% test year", ...
475     YY);
476 writelines(str, TextOutput, WriteMode="append")
477 str = sprintf("\\newcommand{\\MM}{%d} %% test month", ...
478     MM);
479 writelines(str, TextOutput, WriteMode="append")
480 str = sprintf("\\newcommand{\\zsail}{%d} %% height in glacier", ...
481     z_sail);
482 writelines(str, TextOutput, WriteMode="append")
483 str = sprintf("\\newcommand{\\delz}{%d} %% size of iceberg", ...
484     del_z);
485 writelines(str, TextOutput, WriteMode="append")
486
487
488 %% Select test site.
489 % Lat = input("Latitude of test location: ");
490 % Lon = input("Longitude of test location: ");
491
492 %% Select test month.
```

```
% YY = input("Year of test: ");
% MM = input("Month of test: ");

% Locate on ORAS5 and check bathymetry.
LatPts = find(Olat >= floor(Lat) & Olat <= ceil(Lat));
LonPts = find(Olon >= floor(Lon) & Olon <= ceil(Lon));
TryPts = intersect(LatPts, LonPts);
TryDist = TryPts;
for n1 = 1:length(TryDist)
    pt = TryPts(n1);
    dist = distance(Olat(pt), Olon(pt), Lat, Lon, wgs84);
    TryDist(n1) = dist;
end
pt = TryPts(find(TryDist == min(TryDist)));
[row,col] = ind2sub(size(Bathymetry),pt);
LimLayer = Bathymetry(pt);
DepthLim = Depth(LimLayer);
str = sprintf("Available depth at test point (m): %0.0f", DepthLim);
disp(str)
str = sprintf("\\newcommand{\\depthlim}{%0.0f} %% available depth", ...
    DepthLim);
writelines(str, TextOutput, WriteMode="append")

% Set last layer.
Layer = min(find(Depth > del_z));

%% Select iceberg on glacier profile.
% z_sail = input("Height of top of iceberg in glacier (m): ");
% del_z = input("Vertical dimension of iceberg (m): ");

% Limit iceberg height to bathymetry. (This can be expanded later to allow
% icebergs to ground.)
if del_z > DepthLim
```

```
526     disp("The iceberg vertical dimension has been reduced to the available depth.")
527     del_z = DepthLim;
528 end
529 z_keel = z_sail + del_z;
530 
531 % Calculate the mass of the iceberg by integrating the density between the
532 % top and bottom.
533 BergMass = eval(int(BigRho, z_sail, z_keel));
534 str = sprintf("Mass of iceberg (kg/m2): %d", BergMass);
535 disp(str)
536 
537 % Load ORAS5 temperature and salinity.
538 if YY > 2014
539     Type = "OPER";
540 else
541     Type = "CONS";
542 end
543 
544 TPath = "D:/Data/ORAS/Temperature/votemper_control_monthly_highres_3D_";
545 SPath = "D:/Data/ORAS/Salinity/vosaline_control_monthly_highres_3D_";
546 str = sprintf("%s%0.4d%0.2d_%s_v0.1.nc", TPath, YY, MM, Type);
547 Tem = ncread(str, "votemper");
548 str = sprintf("%s%0.4d%0.2d_%s_v0.1.nc", SPath, YY, MM, Type);
549 Sal = ncread(str, "vosaline");
550 
551 % Populate data table.
552 Temperature = squeeze(Tem(row, col, 1:Layer));
553 Salinity = squeeze(Sal(row, col, 1:Layer));
554 
555 Ocean = table(Depth(1:Layer), Temperature, Salinity);
556 Ocean = renamevars(Ocean, "Var1", "Depth");
557 H1 = height(Ocean);
558 
```

```
559 for h1 = 1:H1
560     if h1 == 1
561         Ocean.Thickness(h1) = Ocean.Depth(h1);
562         Ocean.Pressure(h1) = 101325;
563     else
564         Ocean.Thickness(h1) = Ocean.Depth(h1) - Ocean.Depth(h1-1);
565         Ocean.Pressure(h1) = Ocean.Pressure(h1-1) + ...
566             Ocean.Mass(h1-1) * g;
567     end
568     Ocean.Density(h1) = gsw_rho_t_exact(Ocean.Salinity(h1), ...
569         Ocean.Temperature(h1), ...
570         (Ocean.Pressure(h1) - 101324)/1e4);
571     if h1 == 1
572         Ocean.Mass(h1) = Ocean.Depth(h1) * Ocean.Density(h1);
573         Ocean.TotalMass(h1) = Ocean.Mass(h1);
574     else
575         Ocean.Mass(h1) = (Ocean.Depth(h1) - Ocean.Depth(h1-1)) * ...
576             Ocean.Density(h1);
577         Ocean.TotalMass(h1) = Ocean.TotalMass(h1-1) + Ocean.Mass(h1);
578     end
579
580     % Melt rate.
581     Ocean.Agassiz(h1) = MB_Agassiz(Ocean.Salinity(h1), ...
582         Ocean.Temperature(h1)+TC0, 0);
583 end
584
585 % Density curve in the sea.
586 Fit = fit(Ocean.Depth, Ocean.Density, 'poly9');
587 syms WaterDens(y)
588 WaterDens = y.^[9 : -1 : 0] * coeffvalues(Fit)';
589
590
591 % Pressure curve in the sea.
```

```
592 WaterPress = int(WaterDens, y);
593
594 % Buoyancy.
595 syms Buoy(y)
596 assume(y, "positive")
597 Buoy = int(WaterDens, 0, y);
598 Keel = vpasolve(Buoy == BergMass, y, [0 Inf]);
599 Sail = del_z - Keel;
600 str = sprintf("Iceberg's keel depth (m): %d", Keel);
601 disp(str)
602 str = sprintf("Iceberg's sail height (m): %d", Sail);
603 disp(str)
604
605 % Now we need to add layers above the surface to accommodate the iceberg
606 % sail.
607 temp = Ocean(1:5, :);
608 temp(:, :) = array2table(NaN);
609 temp.Depth = linspace(0, -Sail, 5)';
610 temp.Agassiz(:) = 0;
611 temp.Thickness(:) = Sail / 5;
612 temp.Pressure(:) = 101325;
613 Ocean = vertcat(temp, Ocean);
614 Ocean = sortrows(Ocean, "Depth");
615 Ocean.Depth = eval(Ocean.Depth);
616 clearvars temp
617
618 H1 = height(Ocean);
619 for h1 = 1:H1
620     if Ocean.Depth(h1) < Keel
621         Ocean.BergHeight(h1) = Ocean.Thickness(h1);
622     elseif Ocean.Depth(h1-1) < Keel
623         Ocean.BergHeight(h1) = Keel - Ocean.Depth(h1-1);
624     else
```

```
625             Ocean.BergHeight(h1) = NaN;
626         end
627         ypt = z_sail + Sail + Ocean.Depth(h1);
628         denspt = eval(subs(BigRho, z, ypt));
629         Ocean.BergDens(h1) = denspt;
630         prespt = eval(subs(BubblePress, z, ypt));
631         Ocean.BubblePress(h1) = prespt;
632     end
633 
634     % Density curve inside iceberg.
635     Fit = fit(Ocean.Depth, Ocean.BergDens, 'poly9');
636     syms BergDens(y)
637     BergDens = y.^[9 : -1 : 0] * coeffvalues(Fit)';
638 
639     % Recession.
640     Ocean.Recession = Ocean.Agassiz ./ Ocean.BergDens;
641 
642 
643     %%
644     % Display
645     l = figure;
646     tiledlayout flow
647     nexttile
648     scatter(30*Ocean.Recession, Ocean.Depth, MarkerSize, 'k', 'filled')
649     set(gca, 'YDir', 'reverse')
650     yline(0, '--b', 'LineWidth', LineWidth)
651     grid minor
652     grid on
653     ylabel('Depth (m)')
654     xlabel('Recession (m month^{-1})')
655     legend('Recession', 'Surface')
656     set(gca, 'FontSize', FontSize)
657     title('Agassiz recession', 'FontSize', TileTitleSize, ...
```

```
658     'FontWeight', 'bold')
659
660 nexttile
661 scatter(Ocean.BubblePress, Ocean.Depth, MarkerSize, 'k', 'filled')
662 hold on
663 plot(Ocean.Pressure, Ocean.Depth, ':', 'LineWidth', LineWidth)
664 yline(0, '--b', 'LineWidth', LineWidth)
665 set(gca, 'YDir', 'reverse')
666 grid minor
667 grid on
668 ylabel('Depth (m)')
669 xlabel('Pressure (Pa)')
670 legend('Bubble pressure', 'Hydrostatic pressure', 'Surface')
671 set(gca, 'FontSize', FontSize)
672 title('Pressure profile', 'FontSize', TileTitleSize, ...
673     'FontWeight', 'bold')
674
675 set(gcf, 'Position', get(0, 'Screensize'))
676 saveas(I, "../My work/00 Current/Latex thesis/AblModel.png")
677
678
679 %% Wall shear
680 J = figure;
681 set(gcf, 'Position', get(0, 'Screensize'))
682
683 % Display bubble pressure.
684 nexttile
685 fplot(BubblePress, [0 1400], 'k', 'LineWidth', LineWidth)
686 xlabel('Depth (m)')
687 ylabel('Pressure (Pa)')
688 set(gca, 'FontSize', FontSize)
689 grid minor
690 title("Bubble pressure", 'FontSize', TileTitleSize, 'FontWeight', ...
```

```
691     'bold')
692 % Set the horizontal radius of bubbles.
693 r_o = 1e-3; % m3
694
695 % Calculate density of air at pore closure. AP_bubbles is listed later in
696 % this appendix.
697 rho_air = AP_bubbles(p_close, TC);
698
699 % Calculate the number density of bubbles.
700 N_o = (1 - (rho_firn - rho_air) / (rho_lh - rho_air)) * 3 / ...
701     (4 * pi * rho_firn * r_o^3);
702
703 % Calculate volume of air at pore closure.
704 V_a = 1/rho_firn - (rho_firn - rho_air) / (rho_lh - rho_air) / rho_firn;
705
706 % Calculate the vertical diameter.
707 syms r_v(z)
708 r_v = r_o + 3 * V_a * z / (4 * pi * r_o^2 * N_o * (z_firn - z_ice));
709
710 % Display vertical radius.
711 nexttile
712 fplot(r_v, [0 1400], 'k', 'LineWidth', LineWidth)
713 xlabel('Depth (m)')
714 ylabel('Radius (m)')
715 set(gca, 'FontSize', FontSize)
716 grid minor
717 title("Vertical radius", 'FontSize', TileTitleSize, 'FontWeight', ...
718     'bold')
719
720 % Calculate the outward force.
721 delP = BubblePress - subs(WaterPress, y, z);
722
723 % Display the outward force.
```

```
724 nexttile
725 fplot(delP, [0 1400], 'k', 'LineWidth', LineWidth)
726 xlabel('Depth (m)')
727 ylabel('Pressure (Pa)')
728 set(gca, 'FontSize', FontSize)
729 grid minor
730 title("Outward force", 'FontSize', TileTitleSize, 'FontWeight', ...
731     'bold')
732
733 % Calculate the wall thickness.
734 r_o = 1e-3; % assumed starting radius of bubble
735 alpha = r_v / r_o;
736 nu = 0.33; % Poisson's ratio
737 sig_max = 1e6; % tensile strength of ice
738
739 Numerator = 3 * delP * r_v^2;
740 Denominator = (3 + 2 * alpha^2 + 3 * alpha^4);
741 Ratio = Numerator / Denominator;
742
743 BreakPt = sqrt(-(1 + nu * alpha^2) * Ratio / sig_max);
744
745 nexttile
746 fplot(BreakPt, [0 1400], 'k', 'LineWidth', LineWidth)
747 xlabel('Depth (m)')
748 ylabel('Wall thickness at failure (m)')
749 set(gca, 'FontSize', FontSize)
750 grid minor
751 title("Wall thickness", 'FontSize', TileTitleSize, 'FontWeight', ...
752     'bold')
753
754 saveas(J, "../My work/00 Current/Latex thesis/WallShear.png")
755
756
```

```
%% Buoyancy effect
% Creating all the functions.
% Set the height range for the plots.
Range = [z_sail+eval(Sail)+8 z_sail+eval(Keel)];

% Change the depth scale for the water equation.
WaterPress = subs(WaterPress, y, z - z_sail - eval(Sail));
WaterDens = subs(WaterDens, y, z - z_sail - eval(Sail));

% Calculate the density of air.
rho_air = AP_bubbles(p_close, TC);

% Calculate the volume of ice Ih in a unit volume at pore closure.
V_h = ((rho_firn * 1) - rho_air) / (rho_Ih - rho_air);

% Volume of air
V_air = 1 - V_h;

% Mass of air
m_a = rho_air * V_air;

% Mass of ice Ih
m_h = (rho_firn * 1) - m_a;

% Calculate the volume of air in 830 kg of melt.
syms V_out(z)
V_out = BubblePress * V_air / WaterPress;

% Density of air in melt.
rho_out = AP_bubbles(WaterPress, 0);

% Mass of air.
m_out = rho_out * V_out;
```

```
790
791 % Mass of water.
792 m_w = (1 * rho_firn) - m_out;
793
794 % Density of water in melt.
795 syms rho_w(z)
796 rho_w = 1137*exp(9.071e-7 * z) - 137.1*exp(-2.959e-5 * z);
797
798 % Volume of water in melt.
799 V_w = m_w / rho_w;
800
801 % Volume of melt.
802 V_melt = V_out + V_w;
803
804 % Calculate the density of melt.
805 syms RhoMelt(z)
806 RhoMelt = (m_w + m_out) / (V_w + V_out);
807
808 % Calculate the buoyancy of melt.
809 syms BuoyBubMelt(z)
810 BuoyBubMelt = g * (RhoMelt - WaterDens) / RhoMelt;
811 syms BuoyFlatMelt(z)
812 BuoyFlatMelt = g * (rho_w - WaterDens) / rho_w;
813
814
815 % Plot 1: partition.
816 K = figure;
817 set(gcf, 'Position', get(0, 'Screensize'))
818 tiledlayout(2, 3)
819 nexttile
820 fplot(V_out/rho_firn*1000, Range, 'k', 'LineWidth', LineWidth)
821 grid minor
822 xlabel('Depth (m)')
```

```
ytickformat("%0.1f")
ylabel('Volume (m^3)')
set(gca, 'FontSize', FontSize)
title('Volume of air', 'FontSize', TileTitleSize, 'FontWeight', ...
    'bold')

nexttile
fplot(m_out/rho_firn*1000, Range, 'k', 'LineWidth', LineWidth)
grid minor
xlabel('Depth (m)')
ylabel('Mass (kg)')
set(gca, 'FontSize', FontSize)
title('Mass of air', 'FontSize', TileTitleSize, 'FontWeight', ...
    'bold')

nexttile
fplot(rho_out, Range, 'k', 'LineWidth', LineWidth)
grid minor
xlabel('Depth (m)')
ytickformat("%0.1f")
ylabel('Density (kg m^{-3})')
set(gca, 'FontSize', FontSize)
title('Density of air', 'FontSize', TileTitleSize, 'FontWeight', ...
    'bold')

nexttile
fplot(V_w/rho_firn*1000, Range, 'k', 'LineWidth', LineWidth)
grid minor
xlabel('Depth (m)')
ytickformat("%0.3f")
ylabel('Volume (m^3)')
set(gca, 'FontSize', FontSize)
title('Volume of water', 'FontSize', TileTitleSize, 'FontWeight', ...
```

```
    'bold')

nexttile
fplot(m_w/rho_firn*1000, Range, 'k', 'LineWidth', LineWidth)
grid minor
xlabel('Depth (m)')
ylabel('Mass (kg)')
set(gca, 'FontSize', FontSize)
title('Mass of water', 'FontSize', TileTitleSize, 'FontWeight', ...
    'bold')

nexttile
fplot(rho_w, Range, 'k', 'LineWidth', LineWidth)
grid minor
xlabel('Depth (m)')
ytickformat("%0.1f")
ylabel('Density (kg m^{-3})')
set(gca, 'FontSize', FontSize)
title('Density of water', 'FontSize', TileTitleSize, 'FontWeight', ...
    'bold')

sgtitle('Contributions of air and water in 1000 kg of melt', ...
    'FontSize', TitleSize, 'FontWeight', 'bold')

saveas(K, "../My work/00 Current/Latex thesis/Partitions.png")


%%
% Plot 2: buoyancy.
L = figure;
set(gcf, 'Position', get(0, 'Screensize'))
tiledlayout(1, 3)
nexttile
```

```
889 fplot(BuoyBubMelt, Range, 'k', 'LineWidth', LineWidth)
890 grid minor
891 xlabel('Depth (m)')
892 ylabel('Buoyancy (N)')
893 set(gca, 'FontSize', FontSize)
894 set(gca, 'YDir', 'reverse')
895 title('With bubbles', 'FontSize', TitleSize, 'FontWeight', 'bold')
896
897 nexttile
898 fplot(BuoyFlatMelt, Range, 'k', 'LineWidth', LineWidth)
899 grid minor
900 xlabel('Depth (m)')
901 ylabel('Buoyancy (N)')
902 ytickformat("%0.4f")
903 set(gca, 'FontSize', FontSize)
904 set(gca, 'YDir', 'reverse')
905 title('Without bubbles', 'FontSize', TitleSize, 'FontWeight', 'bold')
906
907
908 nexttile
909 fplot(BuoyBubMelt / BuoyFlatMelt, Range, 'k', 'LineWidth', LineWidth)
910 grid minor
911 xlabel('Depth (m)')
912 ylabel('Ratio')
913 set(gca, 'FontSize', FontSize)
914 title('Bubbles over flat', 'FontSize', TitleSize, 'FontWeight', 'bold')
915
916 sgtitle('Buoyancy in bubbly and flat melt', ...
917     'FontSize', TitleSize, 'FontWeight', 'bold')
918
919 saveas(L, "../My work/00 Current/Latex thesis/Buoyancy.png")
920 EndTime = datetime
```

```
function P_bar = EAM_Barometric(h, T)

P_b = 101325; % sea level pressure (Pa)
T_b = T + 273.16; % temperature at sea level (K)
L_b = -0.0065; % standard temperature lapse rate (K/m)
h_b = 0; % height at bottom of atmospheric layer (m)
R = 8.31432; % gas constant
g_0 = 9.80665; % acceleration due to gravity
M = 0.0289644; % molar mass of air (kg/mol)

A = 1 + (h - h_b) * L_b / T_b;
B = -g_0 * M / R / L_b;

P_bar = P_b * A^B;

end
```

```
function Picard08 = AP_bubbles(p_in_Pa, t_in_C)

% This function calculates the bubble density versus depth in a glacier,
% based on Picard et al. (2008).

% Mole fraction of CO2. Current is 0.0004, set whatever you want.
xco2 = 0.0003;

% Relative humidity (100% because the air in a bubble in a glacier is
% always going to be saturated.
h = 1;

% Temperature.
T = t_in_C + 273.16;

```

```
16 % Set all the empirical parameters.
17 k1 = 3.48374;
18 k2 = 1.4446;
19 k3 = 0.0004;
20 k4 = 0.378;
21
22 l1 = 1.00062;
23 l2 = 3.14e-8;
24 l3 = 5.6e-7;
25
26 A = 1.2378847e-5;
27 B = -1.9121316e-2;
28 C = 33.93711047;
29 D = -6.3431645e3;
30
31 a0 = 1.58123e-6;
32 a1 = -2.9331e-8;
33 a2 = 1.1043e-10;
34
35 b0 = 5.707e-6;
36 b1 = -2.051e-8;
37
38 c0 = 1.9898e-4;
39 c1 = -2.376e-6;
40 d = 1.83e-11;
41 e = -0.765e-8;
42
43 % Calculate vapour pressure at saturation.
44 psv = exp((A * T * T) + B * T + C + D / T);
45
46 % Calculate mole fraction of water.
47 xv = h * (l1 + l2 * p_in_Pa + l3 * t_in_C * t_in_C) * psv / p_in_Pa;
48
```

```
49 % Calculate compressibility coefficient.
50 z1 = a0 + a1 * t_in_C + a2 * t_in_C * t_in_C;
51 z2 = (b0 + b1 * t_in_C) * xv;
52 z3 = (c0 + c1 * t_in_C) * xv * xv;
53 z4 = (z1 + z2 + z3) * p_in_Pa / T;
54 Z = 1 - z4 + (d + e * xv * xv) * p_in_Pa * p_in_Pa / T / T;
55
56 % Calculate density.
57 Picard08 = 1e-3 * (k1 + k2 * (xco2 - k3)) * ( 1 - k4 * xv) * p_in_Pa / Z / T;
58
59 % fprintf('rho_air = %d\n', Picard08);
60 end
```